

**Search for invisible decays of the Higgs boson
produced via vector boson fusion at the ATLAS
detector with 139 fb^{-1} of integrated luminosity**

Dissertation
zur Erlangung des Doktorgrades
an der Fakultät für Mathematik, Informatik und Naturwissenschaften
Fachbereich Physik
der Universität Hamburg

vorgelegt von
Pablo Andres Rivadeneira Bracho

Hamburg 2022

Gutachter/innen der Dissertation::	Dr. Krisztian Peters Prof. Dr. Elisabetta Gallo
Zusammensetzung der Prüfungskommission:	Dr. Krisztian Peters Prof. Dr. Elisabetta Gallo Prof. Dr. Caren Hagner Prof. Dr. Georg Weiglein Prof. Dr. Freya Blekman
Vorsitzender der Prüfungskommission:	Prof. Dr. Caren Hagner
Datum der Disputation:	March 28 th , 2022
Vorsitzender Fach-Promotionsausschuss Physik:	Prof. Dr. Wolfgang J. Parak
Leiter des Fachbereichs Physik:	Prof. Dr. Günter H. W. Sigl
Dekan der Fakultät MIN:	Prof. Dr. Heinrich Graener

Abstract

Dark Matter composes a significant part of the Universe. Despite the experimental evidence, its fundamental nature is still an open question. If dark matter interacts with the Higgs boson, it could be produced in a particle collider and it would escape undetected. This manuscript presents a search for invisible decays of the Higgs boson using 139 fb^{-1} of proton-proton collision data taken with the ATLAS detector at a center-of-energy of $\sqrt{s} = 13 \text{ TeV}$ at the Large Hadron Collider. This analysis targets the vector boson fusion Higgs boson production mode using a final state with two highly energetic jets with a wide separation between them in the longitudinal axis. The analysis strategy, background estimate, statistical treatment and results are presented in the following pages. Since jets are key objects in this search, additionally, the ATLAS jet energy calibration chain, and new algorithms for the subtraction of energy contributions from multiple soft interactions in the proton-proton collision are presented.

The background-only hypothesis is tested, in the absence of an excess over the Standard Model predictions an upper limit on the branching ratio of invisible Higgs boson decays is set at 95% CL. In the Standard Model this branching ratio is 0.12%. Evidence of a larger branching ratio would point to a decay into new particles. The observed upper limit is 0.145 while 0.103 was expected. This result is interpreted using Higgs-portal models to set exclusion limits on the cross section of a possible interaction between dark matter particles and a nucleon. Furthermore, upper limits for a scalar mediator with different masses than the Standard Model Higgs boson are obtained as a function of the mediator mass.

Zusammenfassung

Dunkle Materie macht einen signifikanten Teil des Universums aus. Trotz der experimentellen Hinweise ist ihre grundlegende Natur noch immer eine offene Frage. Wenn dunkle Materie mit dem Higgs-Boson wechselwirkt, könnte diese in einem Teilchenbeschleuniger erzeugt werden und würde den Detektor unentdeckt verlassen. In dieser Arbeit wird eine Suche nach unsichtbaren Zerfällen des Higgs-Bosons unter Verwendung von 139 fb^{-1} Proton-Proton-Kollisionsdaten präsentiert, die mit dem ATLAS-Detektor bei einer Schwerpunktsenergie von $\sqrt{s} = 13 \text{ TeV}$ am Large Hadron Collider gemessen wurden. Die Analyse zielt auf den Produktionsmechanismus der Vektorboson-Fusion des Higgs-Bosons und einem Endzustand mit zwei hochenergetischen Jets mit einem großen Abstand zwischen ihnen in der Längsachse. Die Analyse-Strategie, die Untergrundabschätzung, die statistische Analyse und die Resultate werden vorgestellt. Da Jets Schlüsselobjekte bei dieser Suche sind, werden zusätzlich die ATLAS-Strategie der Jet-Energiekalibrierung und neue Algorithmen für die Subtraktion von Energiebeiträgen aus vielen weichen Wechselwirkungen bei den Proton-Proton-Kollisionen präsentiert.

Die pure Untergrund-Hypothese wird getestet. Wenn es dabei keine Überschreitung der Vorhersagen des Standardmodells gibt, wird eine obere Grenze für das Verzweigungsverhältnis der unsichtbaren Higgs-Boson-Zerfälle auf 95% CL bestimmt. Im Standardmodell liegt dieses Verzweigungsverhältnis bei 0.12%. Evidenz für ein größeres Verzweigungsverhältnis würde auf einen Zerfall in neue Teilchen hindeuten. Die beobachtete Obergrenze beträgt 0.145, während 0.103 erwartet wurde. Dieses Ergebnis wird mit Hilfe von Higgs-Portal-Modellen interpretiert, um Ausschlussgrenzen für den Wirkungsquerschnitt einer möglichen Wechselwirkung zwischen Teilchen der dunklen Materie und einem Nukleon festzulegen. Außerdem werden Obergrenzen für unsichtbare Zerfälle von skalaren Mediatoren mit anderen Massen als dem Standardmodell-Higgs-Boson als Funktion der Mediator-Masse ermittelt.

Contents

Abstract	iii
Zusammenfassung	v
1 Introduction	1
1.1 Author's contributions	2
2 Theory framework	5
2.1 The Standard Model	5
2.1.1 Gauge theories and fundamental interactions	6
2.1.2 Standard Model Lagrangian	8
2.1.3 Electroweak interaction	9
2.1.4 The Higgs Mechanism	12
2.1.5 Quantum chromodynamics	14
2.2 Higgs boson at hadron colliders	14
2.2.1 Higgs boson production	15
2.2.2 Higgs boson decays	16
2.3 Open questions to the Standard Model	17
2.3.1 Neutrino oscillation	18
2.3.2 Matter-antimatter asymmetry	18
2.3.3 Energy density in the Universe	18
2.4 Dark matter	19
2.5 Dark matter detection experiments	21
2.5.1 Direct detection	22
2.5.2 Indirect detection	23
2.5.3 Collider searches	24
2.6 Interpretation of DM models	27
2.6.1 Higgs-portal DM model	27
3 The ATLAS experiment at the Large Hadron Collider	31
3.1 The Large Hadron Collider	31
3.1.1 Luminosity	32
3.2 The ATLAS detector	33
3.2.1 Magnet system	35
3.2.2 Inner Detector	36
3.2.3 Calorimeter	38

3.2.4	Muon spectrometer	41
3.2.5	Trigger and data acquisition system	44
3.3	The high luminosity LHC	45
3.4	Reconstruction of physics objects	47
3.4.1	Tracks	47
3.4.2	Vertices	47
3.4.3	Jets	48
3.4.4	Electrons and photons	50
3.4.5	Muons	52
3.4.6	E_T^{miss}	53
3.4.7	Overlap removal	54
3.5	Monte Carlo simulation	54
3.5.1	MC simulation chain	55
4	Jet energy calibration	57
4.1	Pile-up correction	57
4.1.1	Area based correction	58
4.1.2	Residual pile-up correction	59
4.2	Monte Carlo based Jet Energy Scale and η calibration	60
4.3	Global sequential calibration	61
4.4	<i>In situ</i> calibration	61
4.4.1	η intercalibration	62
4.4.2	Z+jets and γ +jets calibration	62
4.4.3	Multijet balance	62
4.5	New developments on the Pile-up correction	62
4.5.1	Comparison of p_T median density definitions	63
4.5.2	Residual correction first step: energy correction to truth scale	65
4.5.3	Inclusive N_{PV}, μ pile-up scale	66
4.5.4	Average N_{PV}, μ pile-up scale	66
4.5.5	Alternative approach: Average pile-up scale after area correction	68
4.5.6	Study of the residual pile-up correction in EMTopo jets with a cell-time cut	68
5	Analysis strategy	73
5.1	Introduction	73
5.2	Data and simulation	75
5.2.1	Dataset and triggers	75
5.2.2	Simulation	76
5.3	Event selection	78
5.3.1	Jet radiation variable definition	80
5.3.2	Forward jet vertex tagger variable definition	80
5.3.3	Event cleaning	81
5.3.4	Signal region	81
5.3.5	$W \rightarrow l\nu$ control region	82
5.3.6	Fake electrons in the $W \rightarrow e\nu$ control region	83
5.3.7	Fake muons in the $W \rightarrow l\nu$ control region	83

5.3.8	$Z \rightarrow \mu l$ control region	83
5.3.9	High $\Delta\phi_{jj}$ validation region	84
6	Background estimates	85
6.1	QCD multijet background	85
6.1.1	Rebalance and Smear estimate of multijet background	87
6.1.2	R+S systematic uncertainties on the m_{jj} shape	88
6.1.3	Normalisation in mid E_T^{miss} mid m_{jj} and low m_{jj} control regions and non-closure uncertainty	88
6.1.4	Cross check of multijet normalisation using $f_{JVT} < 0.5$	90
6.1.5	Multijet Prediction	94
6.1.6	Multijet m_{jj} shape in the signal region	94
6.1.7	Pile up control region multijet estimate	95
6.2	V + jets estimate	102
6.2.1	Z CR	105
6.2.2	W CR	106
7	Systematic uncertainties	115
7.1	Experimental uncertainties	115
7.1.1	Luminosity	115
7.1.2	Trigger	115
7.1.3	Lepton reconstruction	115
7.1.4	Jets	116
7.1.5	Missing transverse momentum	116
7.2	Theoretical uncertainties	116
7.2.1	V + jets uncertainties	116
7.2.2	Signal uncertainties	118
8	Results	119
8.1	Statistical treatment	119
8.2	High $\Delta\phi_{jj}$ validation region fit	121
8.3	Control region only fit	123
8.4	SR+CR fit	123
8.5	Interpretation of the \mathcal{B}_{inv} upper limit	126
8.6	Sensitivity projections for the HL-LHC	130
9	Conclusions	133
	Bibliography	135
A	List of triggers	149
A.1	Lepton triggers	149
A.2	E_T^{miss} triggers	150
B	ABCD multijet estimate	151
B.1	ABCD method	151

B.2	m_{jj} vs E_T^{miss}	151
B.3	m_{jj} vs fJVT	152
List of Figures		155
List of Tables		161

Introduction

Matter is composed of fundamental particles which interact between them to produce all the phenomena we observe. Yet nevertheless, we only understand a small fraction of the matter in the Universe while there are still several open questions to be answered. The Standard Model (SM) is the theory that describes the fundamental particles and their interactions. In this theory, the building blocks of nature (fermions) interact by exchanging force mediators (bosons). The Higgs boson was the missing part of the SM until its discovery in 2012. It is a manifestation of the Higgs field, responsible for the generation mechanism of the mass of W and Z bosons. With the discovery of the Higgs boson, the SM is complete. However, phenomena like matter-antimatter asymmetry, CP violation, neutrino oscillations, dark matter and dark energy are examples of Beyond the Standard Model (BSM) physics.

Dark matter (DM) is a form of matter which does not have electromagnetic interactions. All the evidence of its existence has been found through astronomical observations. First, it was inferred that the visible amount of mass is not enough to explain the rotation dynamics of galaxies [1]. Further evidence of DM is also found in galaxy clustering [2], and in the cosmic microwave background [3]. Despite all this evidence the fundamental nature of dark matter is still unknown.

The particles DM is made of are still to be discovered and understood. There are many possible theoretical models to describe dark matter. One of the best motivated ones is the theory of weakly interacting massive particles (WIMPs) [4, 5]. In general, a WIMP is a new fundamental particle which interacts via gravity and BSM forces as weak as the weak nuclear force. This thesis will focus on this kind of DM.

There are three different ways to search for WIMPs: direct and indirect detection, and production at colliders. Direct detection experiments look for WIMP-nucleus collisions in detectors. Indirect detection experiments search for decay or annihilation products of WIMPs in regions of the space expected to have a high density of DM. In a collider experiment, dark matter particles could be produced. Given the weak interactions between DM and SM particles, DM would escape the detector and produce an imbalance in the measured transverse momentum of the detected particles. This momentum imbalance in addition to the SM objects produce a signature which can be used to detect the production of DM.

Since dark matter is massive, interaction with a Higgs field is conceivable. A potential scenario of interest [6–18] is that the Higgs boson might decay into a pair of DM particles. These models are

called Higgs-portal models. A strategy to search for the production of DM particles at the LHC is to produce the Higgs boson and to look for its invisible decays.

The Higgs production process of interest in this analysis is the Vector boson fusion (VBF) [19, 20]. In this mechanism a quark from each of the incoming protons radiates a vector boson which interact or "fuse" to generate a Higgs boson. The initial quarks are slightly deflected and hadronize producing two collimated cones of particles named jets. The VBF channel is characterised by a pair of highly energetic jets widely separated in the longitudinal axis. Such a particular signature is exploited in the analysis making VBF the most sensitive channel to search for invisible decays of the Higgs boson. In this analysis we search for an excess over the SM prediction of events with two jets and missing transverse momentum in the final state. The absence of an excess would translate into an upper limit on the invisible decays of the Higgs boson assuming the SM cross section [21]. In the SM, this branching ratio is 0.12%. Evidence of a higher branching ratio would point to decays into BSM particles. The upper limit reported by the ATLAS collaboration in a previous iteration of this analysis is 28% expected and 37% observed [22]. The latest result from the CMS collaboration is an observed upper limit of 18% while 10% was expected [23].

Jets are the most important objects in this search. Given the complexity of the reconstruction and calibration of jets, there are several uncertainties associated with these objects. It is crucial to have jets properly understood and calibrated. Jets in ATLAS pass through a calibration chain designed to correct the jet energy to that of the jets reconstructed at particle level. Part of this thesis will focus on the development of a new method to remove the dependence of the reconstructed jet momentum on the multiple soft interactions originated in the proton-proton collisions.

This thesis manuscript is organised as follows. Chapter 2 introduces the theoretical framework of the Standard Model and open questions in fundamental physics. This chapter will focus on the Higgs physics and Higgs-portal models. Then, dark matter and WIMPS will be described in more detail. Also, the principles of DM detection will be covered in this chapter. Chapter 3 is an overview of the LHC and the ATLAS experiment. Here, the reconstruction of physics objects and the Monte Carlo (MC) simulations used in the analysis will be discussed. Chapter 4 will focus on the calibration of jets. Given the relevance of these objects in the analysis, a detailed explanation of the calibration is presented. This chapter summarises the full calibration chain of jets in ATLAS while focusing on the new developments for correcting the effect of multiple collisions in the same bunch crossing on the jet momentum. The analysis strategy is introduced in Chapter 5. The data and simulation, and event selection are described in this Chapter. The background estimates are described in Chapter 6 and their systematic uncertainties are introduced in Chapter 7. The statistical treatment, and results are presented in Chapter 8. Finally, the conclusions are presented in Chapter 9.

1.1 Author's contributions

The ATLAS experiment involves more than three thousand researchers from all around the world. These scientists collaborate to the operation, maintenance and upgrade of the detector, data processing, reconstruction and calibration of physics objects, simulation, physics analysis and many other

activities. Without the joint effort of all them, it would be impossible to perform any kind of search for new particles. Therefore, the studies documented in this thesis are ultimately attributed to the full collaboration. The author contributions are summarised in the following paragraphs.

Regarding the calibration of jets, I worked on the residual pile-up calibration as the main researcher and developer. My contributions were to re-design and optimize the existing software, and validate it against the consolidated results. I developed an upgraded algorithm for the calibration with the objective to mitigate the jet p_T dependence on the pile-up simultaneously over a number of variables. I tested a few calibration approaches, then I did optimization and performance studies in order to decide for the best method. In addition, I have contributed to study the pile-up dependence and to derive corrections for variations of the ATLAS Monte Carlo used in studies of the jet constituents, and in the simulations of the upgraded version of the LHC, the High Luminosity LHC. At the end, necessary inputs for the next steps of the ATLAS jet calibration chain were provided for each one of the different studies performed.

In the search of invisible Higgs boson decays I was one of the main analysers. I contributed to the optimization of the signal region definition studying the sensitivity of the analysis as a function of the kinematic cuts on variables like the missing transverse momentum and the angle between leading jets, the experimental systematic uncertainties, and theory uncertainties on the V+jets background. I also studied the efficiency of ATLAS on the primary vertex reconstruction in the VBF analysis phase space. I also contributed to the estimate of the QCD multijet background and studied the correlation between Z+jets and W+jets processes. I have validated the QCD multijet background estimate, derived a non-closure correction together with a corresponding systematic uncertainty, evaluated the impact of the systematic uncertainties on the shape of the distributions, and compared the two different methods used in the analysis to predict this particular background. In addition, I developed an alternative estimate as a cross check of the nominal prediction.

From the analysis presented in this manuscript, these publications emerged or have been submitted for publication:

- Search for invisible Higgs boson decays with vector boson fusion signatures with the ATLAS detector using an integrated luminosity of 139 fb^{-1} [24].
- Search for invisible Higgs-boson decays in events with vector-boson fusion signatures using 139 fb^{-1} of proton-proton data recorded by the ATLAS experiment [25].

Theory framework

"What is the Universe made of?" is one of the big questions in the history of humanity. From the philosophical debates in ancient cultures to modern science, humans have developed many models to explain the nature we observe. With the development of technology and science, the Standard Model of particle physics, a theory that describes the fundamental particles of nature and their interactions arose. However, there are still open questions that escape our understanding. In particular, there is a fraction of the Universe composed of a type of matter which does not have electromagnetic interactions. This new type of matter is called dark matter (DM). Nowadays it is known that DM corresponds to 25% of the universe while the "ordinary" matter is only 5% of the content of the Universe.

This chapter discusses the Standard Model of particle physics and the open questions in fundamental physics. General descriptions of the Standard Model, gauge theories and the SM Lagrangian are presented in Sections 2.1 to 2.1.2. The electroweak interaction and the Higgs mechanism are treated in more detail in Sections 2.1.3 and 2.1.4, respectively. The strong interaction is introduced in Section 2.1.5. The open questions in fundamental physics are summarised in Section 2.3. In particular, dark matter and the DM search methods are core concepts for the studies presented in this manuscript. A general description of DM and the different ways to search for it are introduced in Sections 2.4 and 2.5, respectively. A summary of Higgs boson physics at the LHC is shown in Section 2.2. Theoretical models for DM and the interpretation of these models in the context of the ATLAS experiment are discussed in Section 2.6.

2.1 The Standard Model

The Standard Model (SM) of particle physics [26–29] is the theory that describes the fundamental particles in nature and the interactions between them. The SM is a Quantum Field Theory (QFT) that describes particles as quantized excitations of fundamental fields. It is composed by a set of related theories that describe different interactions: Quantum Electrodynamics (QED), flavour dynamics, and Quantum Chromodynamics (QCD). The SM is currently the best description we have of the subatomic world and it has been successfully tested for decades. Experimental observation of the W and Z bosons, the quarks, the gluons and the Higgs boson are confirmations of SM predictions [30–38].

In the SM, there are two types of particles defined by their spin quantum number: fermions and bosons. Fermions, the building blocks of matter, have a half-integer spin and interact via the gauge bosons which are the force carriers and have an integer spin. The Higgs boson is the only particle with a spin of 0. Figure 2.1 summarises the particle content of the SM.

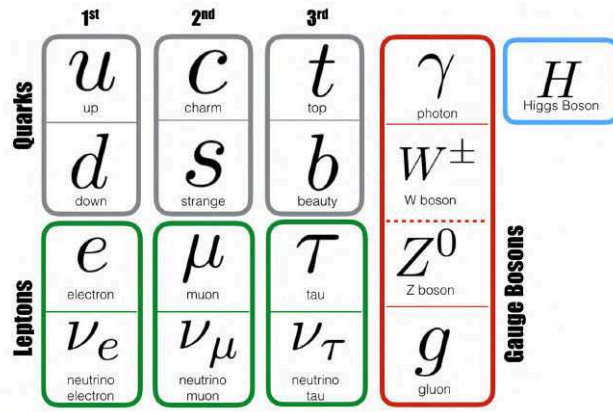


Figure 2.1: Elementary particles of the Standard Model [39]

Fermions are composed by six leptons, six quarks and their corresponding antiparticles. These particles can be grouped in three *generations* with different mass. There are three charged leptons (electron, muon, tau), each one with an associated neutral neutrino (ν_e, ν_μ, ν_τ). Also, there are three generations of quarks with a positive charge $+2/3$ (up, charm, and top) and three with a negative charge $-1/3$ (down, strange, bottom). Due to the property of quantum confinement, quarks cannot exist alone and need to be bound in composed particles called hadrons. Hadrons are subdivided in two categories: mesons are particles composed of an even number of quarks, usually two, and baryons are made of an uneven number of particles, usually three. The most common hadrons in nature are protons and neutrons.

There are four known fundamental interactions in nature: electromagnetic, weak, strong and gravity. Gravity is not described in the SM, a force carrier (graviton) has been proposed but no experimental evidence of such particle has been found. Leptons and quarks interact via the electromagnetic and weak forces. Quarks also interact via strong force. All these interactions are mediated by the exchange of a vector boson, electromagnetism is mediated by photons (γ), the weak interaction is mediated via W and Z bosons, and the strong interaction is mediated via gluons (g). The Higgs boson is responsible for the mechanism that originates the mass of the W and Z bosons, the electroweak symmetry breaking. A list of the bosons and their fundamental properties is presented in Table 2.1.

2.1.1 Gauge theories and fundamental interactions

Historically, in classical mechanics, particles are understood as localized entities and we are interested to know its position as a function of time. In particle physics, the fundamental interaction are described within a new paradigm: the fields. A field is an entity that permeates a region in the space and we are

Boson	Force	Mass [GeV]	Charge [e]	Spin
Photon (γ)	electromagnetic	0	0	1
W^\pm	weak	80.4	± 1	1
Z^0	weak	91.2	0	1
Gluon (g)	strong	0	0	1
Higgs (H)	-	125.2	0	0

Table 2.1: List of bosons in the Standard Model and their fundamental properties.

interested to calculate one or more field variables ϕ_i as a function of position and time. The field variables might be any physics observable such as the temperature or electromagnetic field.

Gauge theories are formulated as a "Lagrangian" L (or a Lagrangian density \mathcal{L}) from which we can obtain the dynamics of a system. In non-relativistic mechanics the Lagrangian is a function of the space coordinates and their time derivatives. The fundamental law of motion is given by the Euler-Lagrange equation:

$$\frac{d}{dt} \frac{\partial L}{\partial \dot{q}_i} = \frac{\partial L}{\partial q_i}. \quad (2.1)$$

In the case of a relativistic theory, the Lagrangian density is a function of the fields and their derivatives on the spacial and time coordinates $\partial_\mu \phi_i \equiv \partial \phi_i / \partial x^\mu$. We say that in this case space and time are treated "equally". The Euler-Lagrange equation generalizes as:

$$\partial_\mu \left(\frac{\partial \mathcal{L}}{\partial (\partial_\mu \phi_i)} \right) = \frac{\partial \mathcal{L}}{\partial \phi_i} \quad (i = 1, 2, 3, \dots). \quad (2.2)$$

Another difference is that in classical mechanics, the Lagrangian of a system can be obtained as the difference between the kinetic and the potential energy, while in relativistic mechanics the Lagrangian is postulated as an axiom. After postulating a Lagrangian, the laws of dynamics are derived and they can be experimentally tested.

Local Gauge invariance

To illustrate the concept of gauge invariance, let's take the following example of the Dirac Lagrangian which describes a free particle of spin 1/2:

$$\mathcal{L} = i\hbar c \bar{\psi} \gamma^\mu \partial_\mu \psi - mc^2 \bar{\psi} \psi, \quad (2.3)$$

where ψ represents the Dirac field spinor, $\bar{\psi} = \psi^\dagger \gamma^0$ is the Dirac adjoint, and γ^μ represents the Dirac matrices. Such Lagrangian is invariant under a global gauge transformation (also called phase transformation) defined as

$$\psi \rightarrow e^{i\theta} \psi, \quad (2.4)$$

with the phase θ being a real number. If θ is dependant on the space-time position we call it a local

gauge transformation. As a convention, the phase θ is factored out a term $-(q/\hbar c)$, thus we can write the transformation as

$$\psi \rightarrow e^{-iq\lambda(x)/\hbar c} \psi. \quad (2.5)$$

The Dirac Lagrangian is not invariant under a local gauge transformation. If we demand the Lagrangian to be invariant under this transformation, one needs to add a term containing a new vector field A (gauge field) that couples to ψ . Furthermore, when adding a new field, another term describing the free field has to be added in the Lagrangian. Thus the Lagrangian should be written as:

$$\mathcal{L} = [i\hbar c \bar{\psi} \gamma^\mu \partial_\mu \psi - mc^2 \bar{\psi} \psi] - (q \bar{\psi} \gamma^\mu \psi) A_\mu - \left(\frac{1}{16\pi} F^{\mu\nu} F_{\mu\nu} \right), \quad (2.6)$$

where the gauge field A should transform under local gauge transformation following the rule $A \rightarrow A + \partial_\mu \lambda$, and $F^{\mu\nu} = \partial^\mu A^\nu - \partial^\nu A^\mu$. It can be proved that the vector field A has to be massless in order to conserve the local gauge invariance. It goes beyond the scope of this thesis but it can be proved that the Lagrangian in Equation 2.6 can generate the complete theory of electrodynamics.

The idea of requiring a Lagrangian to be invariant under a specific transformation and the mathematics behind may seem abstract but the potential of this formalism is extremely powerful and can be generalized to the other interactions. The dynamics of a system can be obtained demanding a symmetry of the Lagrangian under a local gauge transformation from certain groups. Formally, the theory of electrodynamics is invariant under the group $U(1)$. The same formalism applied under the groups $SU(2)$ and $SU(3)$ generate the theories of electroweak and strong interactions respectively.

2.1.2 Standard Model Lagrangian

The Standard Model is a Quantum Field Theory (QFT) constructed under the gauge symmetry group:

$$SU(3)_C \otimes SU(2)_L \otimes U(1)_Y, \quad (2.7)$$

where U corresponds to the unitary group and SU to the special unitary group. The group $SU(3)$ generates the theory of Quantum Chromodynamics. This field is responsible for the strong interaction and is mediated via gluons. The gluons have 8 different states defined by different colour and anti-colour states. On the other hand, $SU(2) \otimes U(1)$ generates the electromagnetic and weak interactions which are unified into the electroweak (EWK) force. This force is mediated via 4 boson fields: photon (γ), W^\pm and Z^0 .

The theories that make the SM can be expressed as a Lagrangian that describes the dynamics of each interaction. Each of these theories are described in Sections 2.1.3 to 2.1.5. The SM Lagrangian can be expressed as the sum of these Lagrangians:

$$\mathcal{L} = \mathcal{L}_{\text{EWK}} + \mathcal{L}_{\text{Higgs}} + \mathcal{L}_{\text{QCD}} + \mathcal{L}_{\text{Yukawa}}. \quad (2.8)$$

The summed Lagrangian can be condensed in the following form:

$$\mathcal{L} = \frac{1}{4}F_{\mu\nu}F^{\mu\nu} + i\bar{\psi}\mathcal{D}\psi + h.c. + \bar{\psi}_i y_{ij} \psi_j \phi + h.c. + |D_\mu \phi|^2 - V(\phi), \quad (2.9)$$

where $\mathcal{D} = \gamma^\mu D_\mu$. The first term, $F^{\mu\nu}$, describes the dynamics of all bosons except the Higgs boson. The second term, $i\bar{\psi}\mathcal{D}\psi$, includes the free fields Lagrangian and the interaction between fermions and the bosons carrying the electroweak and strong forces. The third term, $\bar{\psi}_i y_{ij} \psi_j \phi$, describes the interaction between matter particles and the Higgs field. The $h.c.$ in the Lagrangian means the hermitian conjugate of the previous term and it is needed to cancel out complex values that can appear when doing calculations (i.e. the Lagrangian remains real-valued). The fifth term, $|D_\mu \phi|^2$ describes the coupling between the bosons of the weak interaction (W^\pm, Z) and the Higgs field. Finally, the term $V(\phi)$ is the Higgs potential responsible for the electroweak symmetry breaking.

Detailed explanations of the electroweak interaction and the Higgs mechanism are presented in Sections 2.1.3 and 2.1.4, respectively. The theory of quantum chromodynamics is introduced in Section 2.1.5.

2.1.3 Electroweak interaction

Historically, the electromagnetic and weak interactions were treated as two different forces. The Electroweak interaction is the unification of these two forces and it is described within the Weinberg–Salam theory [27, 40, 41]. This chapter introduces the electromagnetic and weak forces, and their unification.

Electrodynamics

In classical mechanics, the electromagnetic interaction is a force carried by the electric and magnetic fields. It is described by the Maxwell laws of electromagnetism, a theory which treats electricity and magnetism as different manifestations of the same phenomenon. Electromagnetism was the first unification of physics theories in history. This theory is also consistent with special relativity and it was, in fact, one of its main inspirations. With the advent of quantum mechanics at the beginning of the 20th century, electrodynamics was the first theory to be adapted into this framework. The quantum theory of electrodynamics was postulated and perfected by Tomonaga, Feynman and Schwinger in the 1940s.

Quantum electrodynamics (QED) is the theory of electromagnetic phenomena at a quantum scale. It is the oldest, the simplest and the most successful theory of physics dynamics. Within this description, all electromagnetic phenomena can be reducible to a interaction between two charged particles mediated by the exchange of a photon. As shown in Section 2.1.1, if we impose the free fermion Lagrangian to be invariant under local gauge transformations of the group $U(1)$, the complete theory of electrodynamics is generated. The QED Lagrangian can be written as:

$$\mathcal{L}_{\text{QED}} = \bar{\psi}(i\gamma^\mu \partial_\mu - m)\psi + e\bar{\psi}\gamma^\mu A_\mu\psi - \frac{1}{4}F^{\mu\nu}F_{\mu\nu}, \quad (2.10)$$

where ψ represents the fermion field spinor, and $\bar{\psi} = \psi^\dagger$ is known as the Dirac adjoint. γ^μ represent

the Dirac matrices. A corresponds to the electromagnetic field and it transforms as $A \rightarrow A + \partial_\mu \lambda$. $F^{\mu\nu}$ is the field strength tensor and it is defined as $F^{\mu\nu} = \partial^\mu A^\nu - \partial^\nu A^\mu$.

In the framework of perturbation theory, the transition amplitude between states can be calculated as a series expansion. Each term of this perturbative expansion can be graphically represented with a Feynman diagram. The QED interaction at first order can be graphically expressed in the Feynman diagram shown in Figure 2.2. Reading from left to right, the diagram can be interpreted as an upcoming charged particle e , emitting (or absorbing) a photon γ , and exiting. More complicated processes can be expressed simply by patching together two or more vertices of the QED interaction. Examples of different electrodynamic processes are shown in Figures 2.3 and 2.4.

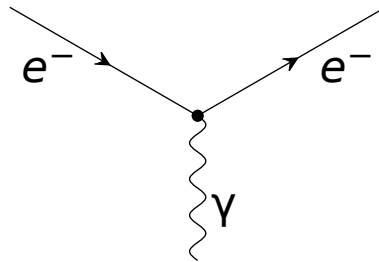


Figure 2.2: Interaction vertex of quantum electrodynamics.

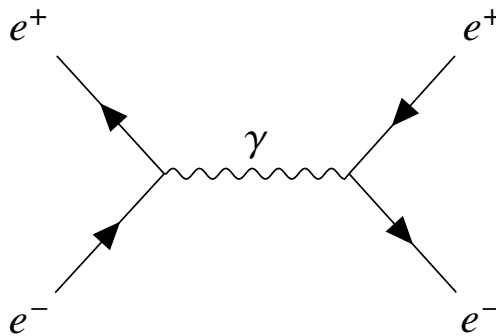


Figure 2.3: Example of a QED process. An electron and an anti-electron annihilate to produce a photon which later decays into a electron anti-electron pair.

Weak interaction

The first evidence of a weak interaction was the nuclear beta decay where the process $n \rightarrow p + e^-$ was observed. Since $m_e \ll m_n, m_p$ the electron was expected to be monoenergetic. However, a continuous energy spectrum was measured experimentally. To explain this process Fermi and Pauli postulated the existence of a new neutral particle carrying part of the decay energy, the neutrino. Further evidences of a weak interaction were found studying the decay of the pion, the muon and the neutron.

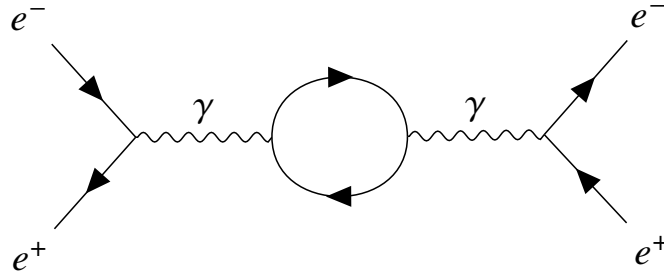


Figure 2.4: Example of one loop QED processes.

In contrast to the electromagnetism, the weak interaction does not conserve flavour. For this reason the theory describing the weak force is called *flavourdynamics*. The weak interaction also violates parity (P) and charge conjugation (C) symmetry, as well as CP and T. The weak processes are classified according to the matter particles involved as leptonic (e.g. $\mu^+ \rightarrow e^+ + \bar{\nu}_\mu + \nu_e$), semi-leptonic (e.g. $\tau^+ \rightarrow \rho^+ + \bar{\nu}_\tau$) and hadronic (e.g. $K^0 \rightarrow \pi^+ + \pi^-$). All quarks and leptons interact via the weak force. This interaction is better understood within the theory of the electroweak interaction. A description of the electroweak unification is presented in the following section.

Electroweak unification

The electroweak interaction is the unification of electromagnetism and the weak force. Although these two forces appear different at low energies, they are two different aspects of the same force. The Electroweak unification was postulated by Sheldon Glashow, Abdus Salam, and Steven Weinberg in the Glashow-Weinberg-Salam (GWS) theory and experimental confirmation was found in the discovery of neutral currents in neutrino scattering and the discovery of the W and Z bosons.

The electroweak theory is a gauge theory invariant under local transformation of the group $SU(2)_L \otimes U(1)_Y$. The first component, $SU(2)_L$, introduces the weak isospin fields (W^1, W^2, W^3) while the $U(1)$ group introduces the weak hypercharge field B . These are not physical fields yet, the observed physical bosons (γ, W^\pm, Z) are produced by the spontaneous symmetry breaking of the electroweak symmetry.

The formalism of the electroweak interaction requires to split the fermionic fields into right-handed and left-handed fields defined as:

$$\psi_{R,L} = \frac{1}{2}(1 \pm \gamma^5)\psi, \quad (2.11)$$

where γ^μ ($\mu \in [0, 4]$) are the Dirac gamma matrices, $\gamma^5 \equiv i\gamma^0\gamma^1\gamma^2\gamma^3\gamma^4$, and $\frac{1}{2}(1 + \gamma^5)$ are the chirality operators. The Lagrangian of the electroweak interaction before the electroweak symmetry breaking can be written as:

$$\mathcal{L}_{\text{EWK}} = \sum_f \left(\bar{\psi}^f i\gamma^\mu \partial_\mu \psi^f + g \bar{\psi}^f \gamma^\mu \frac{\sigma_i}{2} W_\mu^i \psi^f + g' \bar{\psi}^f \gamma^\mu \frac{Y}{2} B_\mu \psi^f - \frac{1}{4} W_a^{\mu\nu} W_{\mu\nu}^a \right) - \frac{1}{4} B^{\mu\nu} B_{\mu\nu}, \quad (2.12)$$

where the sum is done over the fermion fields, g and g' are the coupling constants of the weak and electromagnetic interaction, σ_i represents the Pauli matrices, and Y is the weak hypercharge. B_μ corresponds to the B boson field and W_μ^i to the three W boson fields ($i = 1, 2, 3$). The field strength tensors are defined as $W_{\mu\nu}^i = \partial_\mu W_\nu^i - \partial_\nu W_\mu^i + g \epsilon_{ijk} W_\mu^j W_\nu^k$, and $B_{\mu\nu} = \partial_\mu B_\nu - \partial_\nu B_\mu$.

It is important to mention that no mass term for the W and B fields is introduced because this terms would break the electroweak symmetry by mixing right and left-handed fields. The observed physical fields are obtained by mixing the W , and B fields as follows:

$$\begin{aligned} W^\pm &= \frac{1}{\sqrt{2}}(W^1 \pm W^2), \\ Z &= W^3 \cos \theta_W - B \sin \theta_W, \\ A &= W^3 \sin \theta_W + B \cos \theta_W, \end{aligned} \quad (2.13)$$

where W^\pm and Z are the boson fields of the weak force, A is the photon field and θ_W is called the weak mixing angle.

2.1.4 The Higgs Mechanism

To preserve the electroweak symmetry, bosons have to be massless. However this is not in agreement with the experimental observations. Thus, the electroweak symmetry has to be broken. This is accomplished via the Higgs Mechanism also known as the Spontaneous Symmetry Breaking (SSB), where the symmetry group $SU(2) \otimes U(1)$ breaks down to $U(1)$.

To account for the masses of the electroweak gauge bosons, a new field ϕ has to be introduced. Let's consider it as a complex $SU(2)$ doublet of the form:

$$\phi = \begin{pmatrix} \phi^+ \\ \phi^0 \end{pmatrix}, \quad (2.14)$$

where ϕ^+ is a field with positive charge and ϕ^0 is an electric neutral field. The Lagrangian corresponding to this doublet can be written as:

$$\mathcal{L}_{\text{Higgs}} = (D_\mu \phi)^\dagger (D_\mu \phi) - V(\phi), \quad (2.15)$$

where D_μ is the covariant derivative and $V(\phi)$ is the Higgs potential defined as:

$$V(\phi) = \mu^2 \phi^\dagger \phi + \lambda (\phi^\dagger \phi)^2. \quad (2.16)$$

There are two free parameters, λ has to be positive because otherwise the potential would not have a

ground state and μ^2 can be either positive or negative. If $\mu^2 > 0$, the potential $V(\theta)$ has its minimum at $\phi^\dagger = \phi^0 = 0$. Alternatively, if $\mu^2 < 0$, there is an infinite number of degenerated ground states at $\phi^\dagger \phi = -\mu^2/2\lambda \equiv v^2/2$.

For simplicity, one can choose a minimum as:

$$\phi = \frac{1}{\sqrt{2}} \begin{pmatrix} 0 \\ v \end{pmatrix}, \quad (2.17)$$

where v is the vacuum expectation value (VEV) of ϕ . In order to use the Feynman calculus, the Higgs field is expanded around the minimum,

$$\phi' = \frac{1}{\sqrt{2}} \begin{pmatrix} 0 \\ v + h \end{pmatrix}. \quad (2.18)$$

The Higgs field Lagrangian can then be written as:

$$\mathcal{L}_{Higgs} = (D_\mu \phi)^\dagger (D_\mu \phi) - \frac{1}{2}(-2\mu^2)h^2 - \lambda v h^3 - \frac{1}{4}\lambda h^4. \quad (2.19)$$

The mass of the Higgs field can be extracted from the second term of the Lagrangian:

$$m_H = \sqrt{-2\mu^2} = v\sqrt{2\lambda}. \quad (2.20)$$

Now we need to determine the mass of the W and Z bosons. Expanding the first term with the electroweak covariant derivative,

$$D_\mu \phi = \left(\partial_\mu - ig \frac{\sigma_i}{2} W_\mu^i - ig' \frac{Y}{2} B_\mu \right) \phi \quad (2.21)$$

the mass term of the electroweak bosons can be extracted expanding the expression:

$$\left| \left(-ig \frac{\sigma_i}{2} W_\mu^i - ig' \frac{Y}{2} B_\mu \right) \phi \right|^2 = \left(\frac{vg}{2} \right)^2 W_\mu^+ W_\mu^- + \frac{1}{2} \left(\frac{v\sqrt{g^2 + g'^2}}{2} \right)^2 Z_\mu^2 + \frac{1}{2} \cdot 0 \cdot A_\mu^2 \quad (2.22)$$

and the masses of the bosons are:

$$m_{W^+} = m_{W^-} = \frac{vg}{2} \quad (2.23)$$

$$m_Z = \frac{v\sqrt{g^2 + g'^2}}{2} \quad (2.24)$$

$$m_\gamma = 0. \quad (2.25)$$

On the other hand, the masses of the fermions are generated via the Yukawa coupling between the fermion fields and the Higgs field:

$$\mathcal{L}_{\text{Yukawa}} = \sum_f -g_Y^f \left(\bar{p} \bar{s}_L^f \phi \psi_R^f + \psi \bar{\psi}_R^f \bar{\phi} \psi_L^f \right). \quad (2.26)$$

Therefore the masses of the fermions are:

$$m_f = \frac{v g_Y^f}{\sqrt{2}} \quad (2.27)$$

2.1.5 Quantum chromodynamics

Quantum chromodynamics (QCD) is the theory of the strong interaction. It is a non-abelian gauge theory invariant under the symmetry group $SU(3)$. In this theory, particles carrying a *colour charge*, i.e. quarks and gluons, interact via the exchange of gluons. One of the main characteristics of the strong interaction is that the coupling constant in reality changes with the separation between the particles being smaller at small distances and stronger when particles are separated. As a consequence, at small distances the particles are basically free (asymptotic freedom) while if we try to separate them, as the distance increases the energy grows to the point that a quark-antiquark pair is produced making impossible to have colour charged particles isolated. Thus, these particles can only exist in composed particles with a null colour charge.

The Lagrangian of quantum chromodynamics is

$$\mathcal{L}_{QCD} = \bar{\psi}_i (i\gamma^\mu (D_\mu)_{ij} - m\delta_{ij}) \psi_j - \frac{1}{4} G_{\mu\nu}^a G_a^{\mu\nu}, \quad (2.28)$$

where ψ_i is the quark field in the fundamental representation of the $SU(3)$ group and the indexes i and j run from 1 to 3. The symbol $G_{\mu\nu}^a$ represents the gauge invariant gluon field strength tensor given by

$$G_{\mu\nu}^a = \partial_\mu A_\nu^a - \partial_\nu A_\mu^a + g f^{abc} A_\mu^b A_\nu^c, \quad (2.29)$$

where A_μ^a are the gluon fields, indexed by a, b and c running from 1 to 8, and f_{abc} are the structure constants of $SU(3)$. The variables m and g correspond to the quark mass and coupling of the theory, respectively. Another particularity of QCD is that in addition to the interaction between quarks and gluons, gluons can also interact with themselves. This can be reflected in term $A_\mu^b A_\nu^c$ which describes the coupling between gluons. This property makes the dynamics of the strong interaction more diverse. The first order Feynman diagrams for the strong interaction are shown in Figure 2.5 and 2.6.

2.2 Higgs boson at hadron colliders

The LHC was designed and built as a Higgs factory. With the discovery of the Higgs boson in 2012, the next step was to study the properties and decay modes of this particle. Since then several analyses have been performed to measure the interaction couplings between the Higgs boson and the other SM particles. The different production modes of the Higgs boson are summarised in Section 2.2.1 and the decay modes are introduced in Section 2.2.2. A detailed review of the Higgs boson properties

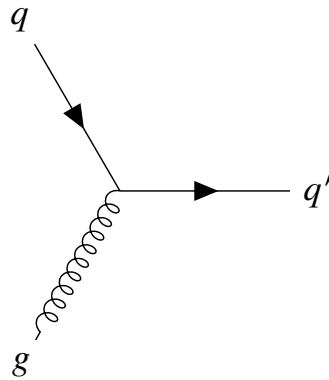


Figure 2.5: Tree level Feynman diagram for the interaction between two quarks mediated by a gluon.

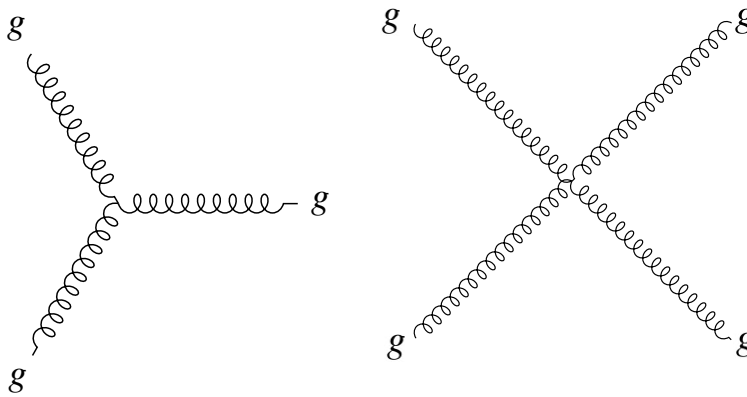


Figure 2.6: Feynman diagrams for the coupling between three gluons (left) and four gluons (right).

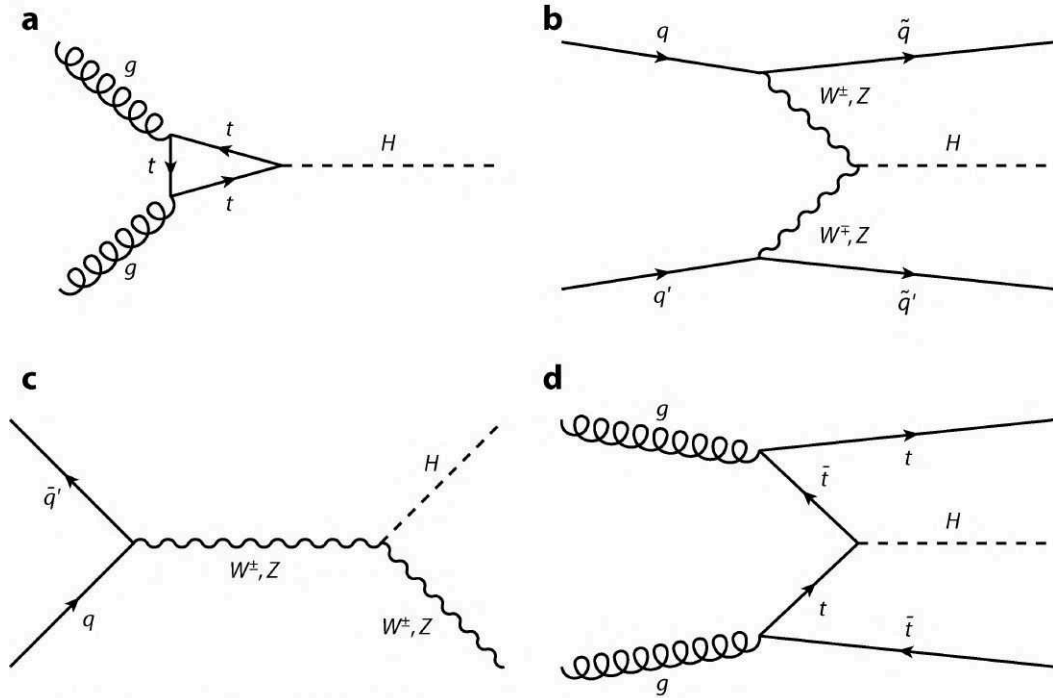
measured at the LHC can be found in [42].

2.2.1 Higgs boson production

At the LHC there are four dominant production modes for the Higgs boson: gluon-gluon fusion (ggF), vector boson fusion (VBF), production in association with a vector boson (VH) and with heavy quarks ($b\bar{b}H, t\bar{t}H, tH$). The Higgs production cross section of these different channels as a function of the center-of-mass energy in pp collisions is shown in Figure 2.8. The lowest level Feynman diagrams of these processes are shown in Figure 2.7.

- Gluon-gluon fusion (ggF): the gluon pair couples to the Higgs boson via a fermion loop. This is the dominant production mode at the LHC Run 2.
- Vector boson fusion (VBF): either two W or two Z bosons "fuse" to produce a Higgs particle. This is the process used in the search for invisible decays in Chapter 5 and has a particular signature of two hard jets in the final state.

- Production in association with a vector boson (VH): in this process a vector boson is produced and it radiates a Higgs boson.
- Production in association with heavy quarks: this is the result of the interaction between the Higgs boson and the quarks, in particular with the top and bottom quarks.



 Murray W, Sharma V. 2015. Annu. Rev. Nucl. Part. Sci. 65:515–54

Figure 2.7: Lowest level Feynman diagrams of the Higgs production modes at the LHC [42].

2.2.2 Higgs boson decays

The Higgs boson interacts with all fermions and the electroweak bosons, and has a lifetime of $\tau = 1.56 \times 10^{-22}$. In order to have a complete understanding of the Higgs boson it is necessary to measure all its partial decay modes. The fraction of decays in a particular decay mode is described by the branching ratio (BR) defined as the relation between the decay width (Γ) of the mode under study and the total decay width:

$$BR(H \rightarrow X_j) = \frac{\Gamma(H \rightarrow X_j)}{\sum_i \Gamma(H \rightarrow X_i)} \quad (2.30)$$

where X_j corresponds to the final state under study, and $\sum_i \Gamma(H \rightarrow X_i)$ is the sum over all final states i . The Higgs boson dominant decays at the LHC are $H \rightarrow b\bar{b}$, $H \rightarrow WW^*$, and $H \rightarrow \tau^+\tau^-$ followed by $H \rightarrow ZZ^*$ and $H \rightarrow \gamma\gamma$. A summary of the branching fraction for the main Higgs decay modes at the LHC is shown in Figure 2.9.

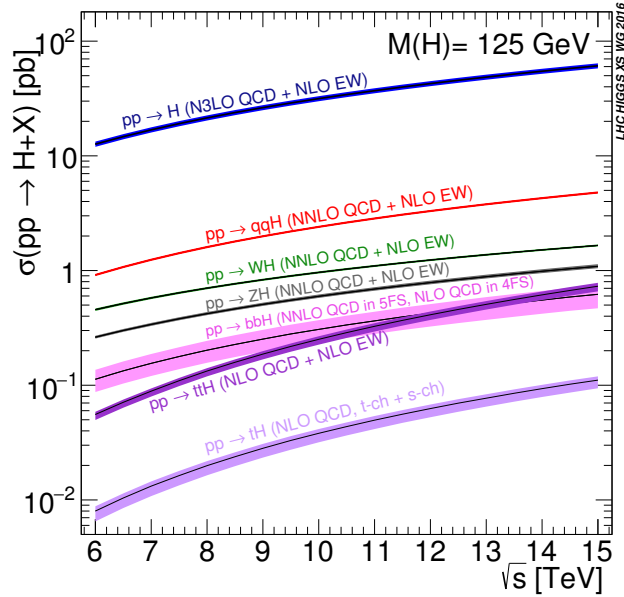


Figure 2.8: Higgs boson production cross section as a function of the center-of-mass energy in pp collisions for $m_H = 125$ GeV[20].

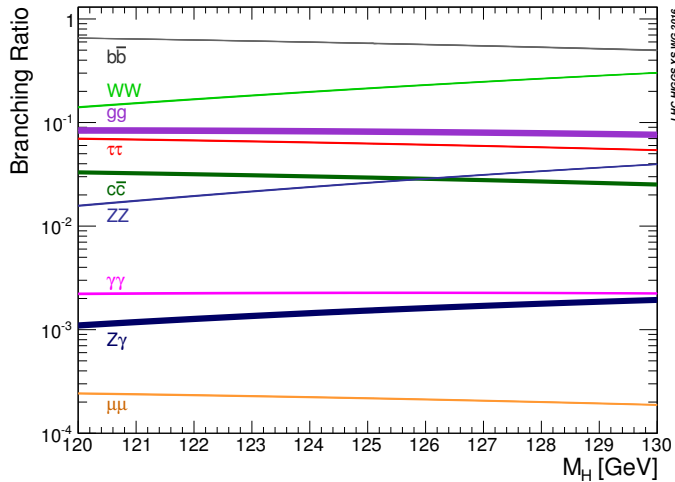


Figure 2.9: Summary of the branching fractions for the main Higgs decay modes at the LHC [20].

2.3 Open questions to the Standard Model

Despite the success of the standard model, there is experimental evidence and theoretical motivation that the SM is just an approximation at low energy of a more complete theory. For example, evidence of beyond Standard Model (BSM) physics are the evidence of dark matter and dark energy, neutrino oscillations, and matter-antimatter asymmetry. On the theoretical side, scientist are puzzle about the vast difference between the mass scale of the weak nuclear force and gravity (known as the hierarchy

problem), and the large number of parameters (19) measured experimentally without relation between them found so far. Furthermore, the SM does not explain gravity. A more complete theory is needed to integrate the gravitational force in a theory of all interactions.

To explain the evidence of new physics, theorists have developed many different BSM models. However, without discovery of any BSM particle so far, some models are rolled out and there is no clear favorite to solve the open problems in physics. It is the role of the current physicist to dig into the predictions of these models and find out which is the one that describes nature the best. A summary of the BSM phenomena and some of the postulated solutions is presented below.

2.3.1 Neutrino oscillation

Neutrino oscillation is the quantum mechanical phenomenon in which a neutrino created with a specific lepton flavour can be measured at a later stage in a different lepton flavour. The probability that the neutrino lepton flavour changes varies as it propagates through space. The first evidence of neutrinos oscillations was found in the Super-Kamiokande [43] and the Sudbury neutrino observatories [44]. This evidence implies that at least two of the neutrinos are massive. In contrast, the SM assumes that neutrinos are massless. There are several experiments measuring the properties of neutrinos nowadays. Exclusion upper limits on the squared difference between the neutrinos masses Δm_{21}^2 and Δm_{31}^2 has been measured to be $(7.53 \pm 0.18) \times 10^{-5} \text{ eV}^2$ and $(2.44 \pm 0.06) \times 10^{-3} \text{ eV}^2$, respectively [45].

2.3.2 Matter-antimatter asymmetry

In the SM, for each particle there is a corresponding antiparticle. When two antiparticles interact, they annihilate each other producing energy. For each interaction process between particles there is a mirrored process involving antiparticles. The matter-antimatter asymmetry problem refers to the imbalance of these two types of matter in the observed Universe. A BSM approach is needed to resolve this problem since equal amounts of matter and antimatter were produced in the Big Bang and there is no explanation for the generation of this imbalance in the SM.

2.3.3 Energy density in the Universe

The cosmic microwave background (CMB) is electromagnetic radiation remnant from an early stage in the evolution of the universe. A map of the anisotropies of the CMB at microwave and infrared frequencies was measured by the Planck space observatory with high sensitivity and small angular resolution. This map is showed in Figure 2.10. Planck measured several cosmological parameters including the energy composition of the Universe [46]. It was measured that the Universe is made of $\sim 5\%$ of ordinary matter, $\sim 27\%$ of Dark matter and $\sim 68\%$ of Dark Energy.

Dark matter is non-baryonic matter which only interacts weakly. Therefore, this matter it cannot be observed using modern telescopes. Experimental evidence of DM has been found through astrophysical observations of the rotation curve of galaxies, the dynamics of galaxy clustering, and the cosmic

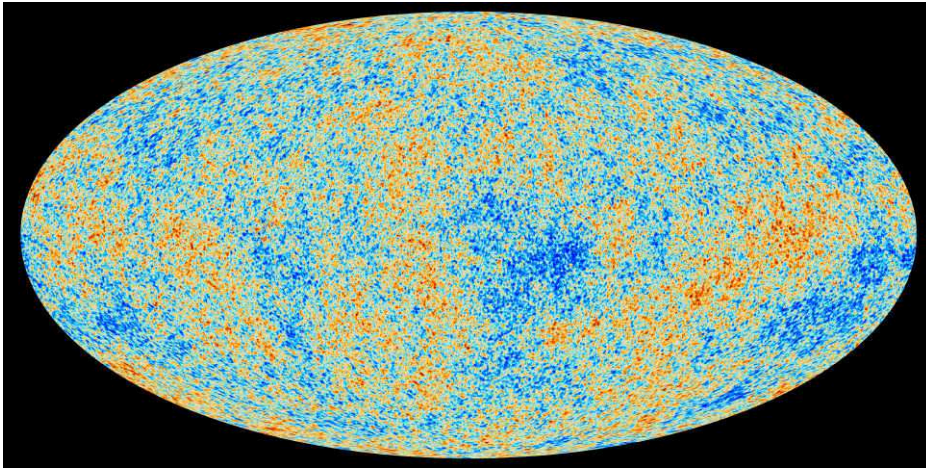


Figure 2.10: Map of the cosmic microwave background. It shows tiny temperature fluctuations that correspond to regions of slightly different densities [47].

microwave background. A summary of the evidence, characteristic, and DM detection methods is presented in Sections 2.4 and 2.5.

2.4 Dark matter

Most of matter in the Universe is found in a form that does not have electromagnetic interactions. The fundamental nature of dark matter (DM) is still a mystery to science but there is evidence of its existence since almost a century ago. The first indication of dark matter is attributed to Zwicky [1]. He measured the rotation velocity of galaxies in the Coma cluster and found that the computed velocity cannot be explained by the visible amount of matter.

A comparison of the rotation velocity of the galaxy NGC 3198 as a function of the distance to the galactic centre is shown in Figure 2.11. It shows that the observed data agrees with a model which includes more matter than what is visible. Other experimental evidences of DM are found in the dynamics of galaxy clusters. For example, an image of the cluster 1E 0657-56 is shown in Figure 2.12. This cluster was formed after the collision of two large clusters of galaxies. It can be observed that most of the matter is separated from the "normal" matter as an evidence of the null electromagnetic interaction of DM. The most precise evidence as of now comes from the cosmic microwave background (CMB). Measurements by the Planck experiment have reported that $\sim 27\%$ of the Universe is made of DM.

Several theoretical models have been developed to describe dark matter. One of the best motivated ones (and the one discussed in this manuscript) are weakly interacting massive particles (WIMPs). In general, a WIMP is a new fundamental particle which interacts via gravity and BSM forces as weak as the weak nuclear force. The mass of WIMPs is assumed to be in the GeV to TeV range.

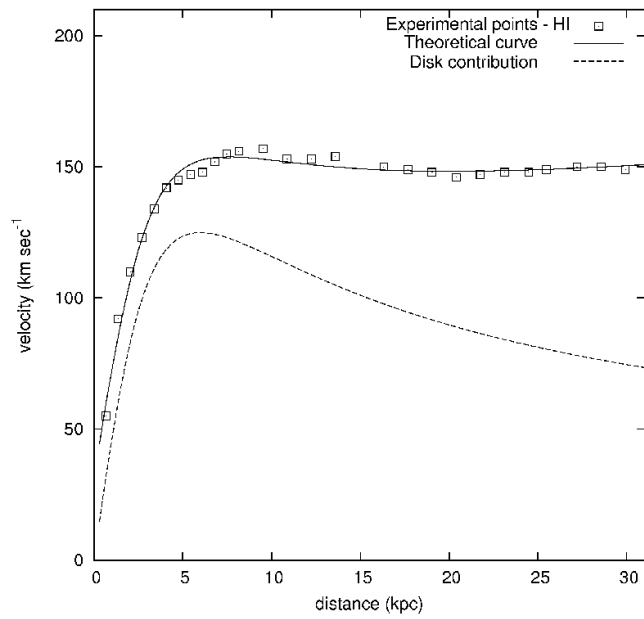


Figure 2.11: Rotational velocity v versus distance r from the galactic centre, for the galaxy NGC 3198. Squares (\square) are the velocities determined from HI observations [48] while the dashed line is the prediction from visible matter.

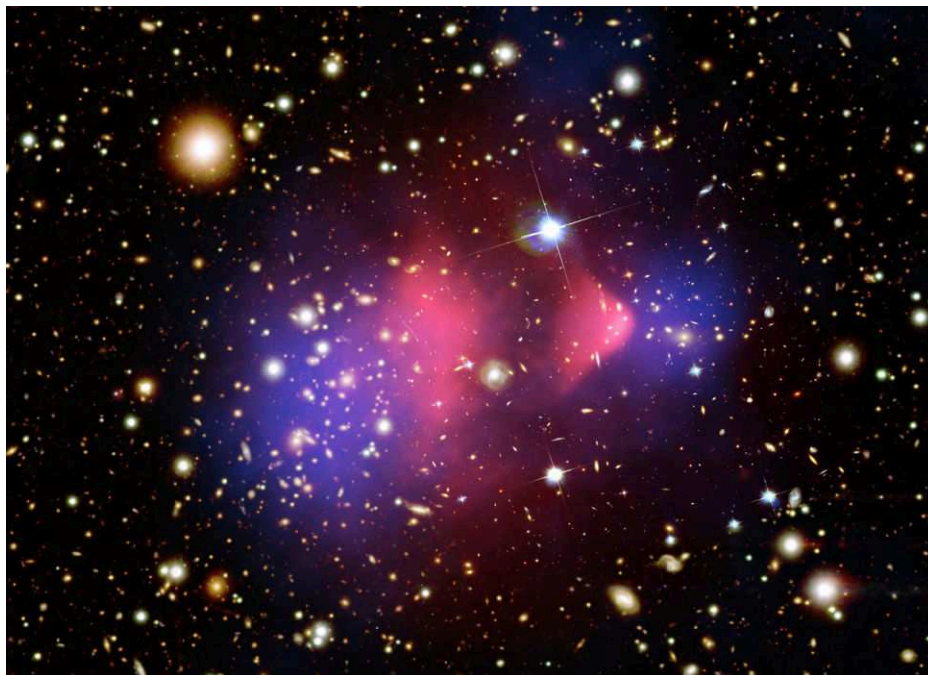


Figure 2.12: Picture of the bullet cluster taken by the Chandra X-ray observatory. Baryonic matter is illustrated in pink and the DM distribution deduced from gravitational lensing is displayed in blue.

Other DM candidates are axions, dark photons and sterile neutrinos [45]. There are also attempts to explain the cosmological observations with modified dynamics so that there is no need for a dark matter component. One of the most popular of these models is the modified newtonian dynamics. This model can explain the dynamic properties of galaxy rotation but has failed to explain phenomena like gravitational lensing and the properties of galaxy formation.

2.5 Dark matter detection experiments

The strategies to search for new physics strongly depend on the DM model we want to test. In particular two types classes of DM have attracted the attention of the experimental particle physics community: WIMPs and axions. A strong international effort has been devoted to detect these particles. This thesis manuscript, and in particular this chapter, will focus on the WIMP detection experiments.

There are three ways to search for WIMP dark matter particles: direct, indirect and collider searches. Direct detection experiments look for WIMP-nucleus collisions in detectors on the Earth. Indirect detection experiments search for decay or annihilation products of WIMPs in regions of the space expected to have a high density of DM. In a collider experiment, dark matter particles could be produced. Given the weak interactions between DM and SM particles, DM particles would escape the detector and produce an imbalance in the measured momentum of the detected particles. This momentum imbalance in addition to other SM objects produce a signature which can be used to indirectly detect the production of DM. These three strategies can be read from the hypothetical interaction vertex between two SM particles and two DM particles shown in Figure 2.13. Detailed overviews of dark matter searches are found in [49–51].

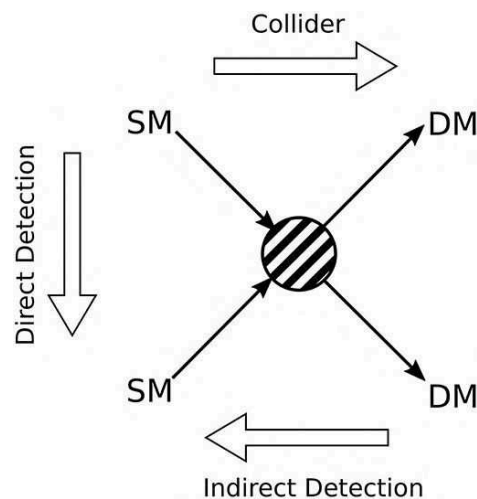


Figure 2.13: Illustration of DM searches. If one take the direction of time from up to down we have the vertex for direct detection, if the time arrow points to the left we have the indirect detection vertex, and if the time arrow points to the right we have the collider search vertex.

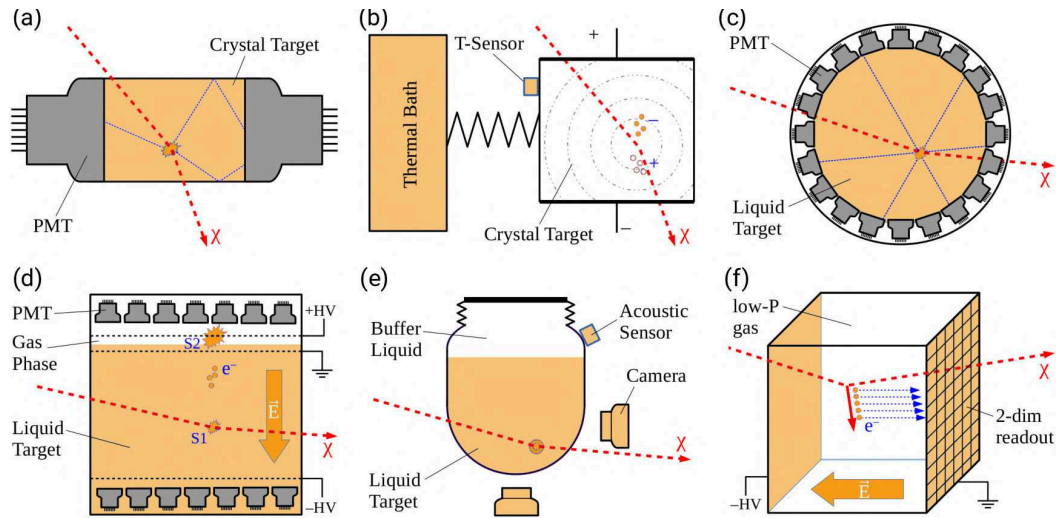


Figure 2.14: Working principle of common detector types for the direct WIMP search: (a) scintillating crystal, (b) bolometer (here with additional charge-readout), (c) single-phase and (d) dual-phase liquid noble gas detectors, (e) bubble chamber, (f) directional detector [50].

2.5.1 Direct detection

The scientific objectives of direct detection (DD) experiments are: (i) to detect a direct interaction of a DM particle with a detector, and (ii) to determine its mass and interaction cross section, or else (iii) to experimentally exclude the broadest accessible ranges of both quantities. If the mass of the WIMPs is in the range of 10 to 1000 GeV/c^2 , a nucleon-DM scattering would produce a nuclear recoil energy in the range of 1 to 100 keV. This energy can be measured using modern detector technologies as Time Projection Chambers (TPCs), scintillation detectors (NaI, CaF_2), and heat detectors (Bolometers). Most detectors are sensitive to at least two different signals from the nuclear recoil and use the combined information to reject background events. Detecting WIMP recoils on electrons has also been proposed, but the electron recoil energy would be of the order of sub-eV energies, below the threshold of most direct detection detectors.

A usual direct detection detector works as follows. A target mass, typically liquefied noble gases or scintillators is used as the interaction active medium. Large detector sizes are needed because of the low interaction rate between DM and the SM particles. The recoil energy is mostly transferred into heat. A small fraction of the recoil energy can cause the excitation of an atom, producing then either a photon or an electron depending on the active medium. This small signal is then detected with photomultipliers or by measuring the temperature and charge of the medium. Illustrations of the working principles of common detector types for direct WIMP searches are shown in Figure 2.14.

Direct detection experiments aim to reduce background such that a small number of signal events observed in the experiment correspond to a high statistical significance. Examples of background sources are the cosmic muons, radioactive isotopes in the vicinity of the detector and detector artifacts. Backgrounds are reduced using several strategies often called as "low background techniques". These techniques include positioning the experiment in deep-underground laboratories to reduce the

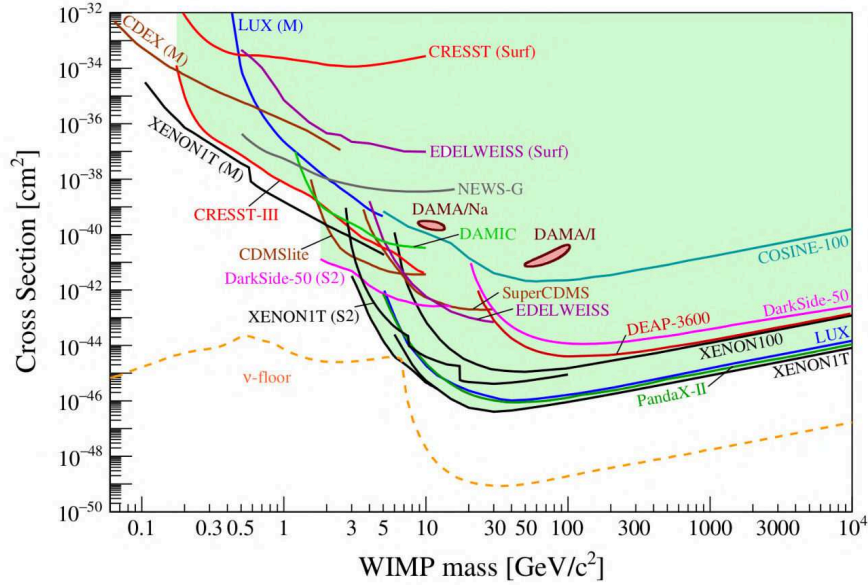


Figure 2.15: Current status of searches for spin-independent elastic WIMP-nucleus scattering assuming the standard parameters for an isothermal WIMP halo. The neutrino floor (ν – floor) corresponds to a limit at which the background from solar neutrinos is irreducible defining a sensitivity edge for current direct detection experiments [50].

cosmic background, shielding of the experiment, detector and target materials are selected and purified from radioactive and trace contaminations, and fiducialisation of the detector volume, within others.

So far, no conclusive evidence of DM-nucleon scattering has been found. The DAMA/LIBRA experiment reported an observation [52] but the DM nature of this observation is in tension with a large number of results. The status of spin-independent WIMP-nucleon scattering assuming the standard parameters for an isothermal WIMP halo ($\rho_0 = 0.3 \text{ GeV/cm}^3$, $v_0 = 220 \text{ km/s}$, $v_{esc} = 544 \text{ km/s}$) is shown in Figure 2.15.

2.5.2 Indirect detection

DM particles can gravitationally accumulate in astrophysical objects such as stars, galaxy centres and in the Sun and the Earth. Indirect dark matter searches scan the sky for any excess of standard model particles or antiparticles produced from dark matter annihilation or decay. These experiments are directed at regions of the space where the DM density is expected to be high, e.g. the galactic centre. There are indirect DM searches using neutrinos (IceCube, KM3Net, Super-K), x-rays (Micro-X, NuStar), gamma-rays (Fermi, HAWC), micro (Planck, WMAP) and radio waves (GreenBank, EDGES), and cosmic rays (HAWC, Auger).

Signals which could be produced by DM have been reported by several projects. Examples of possible DM signatures are an excess of GeV gamma rays reported by Fermi-LAT [53], an antiproton

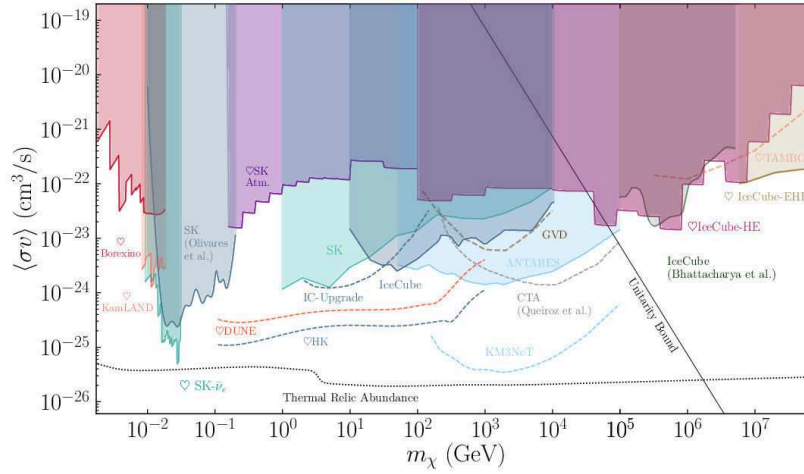


Figure 2.16: Summary of 90% C.L. limits (shaded) and projected sensitivities (dashed) to the dark matter annihilation cross section, assuming s-wave annihilation [57].

excess observed at AMS-02 [54, 55], and the 3.5 keV X-ray line found in the spectrum of galaxy clusters [56]. However, alternative astrophysical explanations to these signals have been proposed and their origin remains unclear. A summary of the current limits on the cross section vs mass of the WIMP is shown in Figure 2.16.

2.5.3 Collider searches

If dark matter would interact with SM particles more than only gravitationally, it could be produced in a particle collider. Three types of analyses are performed in the search for dark matter: measurements of electroweak observables with high precision, where any deviation from the SM prediction might indicate the loop level contribution from BSM particles, searches for narrow resonances, where the DM mediators produced at the collider decay back into a pair of SM particles, and searches for events with imbalanced total momentum, where the DM pair produced in association with SM particles escapes the detector without leaving a trace.

This thesis manuscript focuses on a search for DM in events where a pair of DM particles escape the detector. At the LHC, the total momentum in the plane transverse to the collision is zero. Thus, the escape of the DM particles would produce an imbalance in the measured total transverse momentum. This imbalance can be interpreted as the momentum of all invisible particles such as neutrinos or dark matter particles. It can be measured adding the momentum vector of all the visible particles. The module of this quantity is called the "missing transverse energy" and it is defined as:

$$E_T^{\text{miss}} = \left| - \sum_i \vec{p}_{T_i} \right| \quad (2.31)$$

where i is added over all the visible particles. This type of analysis are called $E_T^{\text{miss}} + X$ searches. The signal characteristic generated in this type of events is illustrated in Figure 2.17. The invisible

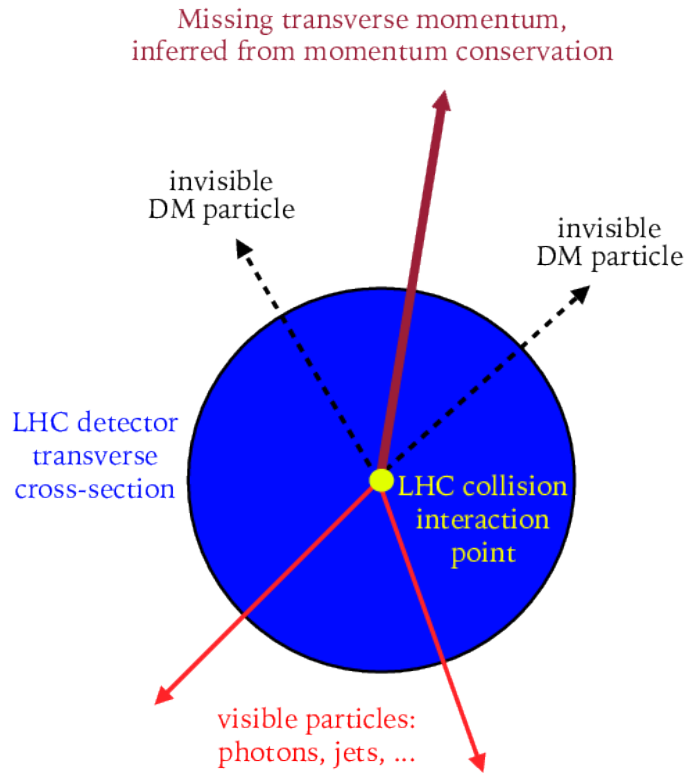


Figure 2.17: Illustration of the signal generated in $E_T^{\text{miss}} + X$ events. The visible particles recoil against the E_T^{miss} produced by the invisibles particles scaping the detector [58].

particles escape the detector recoiling against the visible particles which are used to discriminate these type of events.

In $E_T^{\text{miss}} + X$ searches, the DM should recoil against SM particles in order to be detectable. Otherwise, there would be no missing transverse energy in the event because there would be a pair of DM particles moving in back to back directions. A discovery would be claimed if an excess of events over the SM background prediction is found in the experimental data taken with the ATLAS detector. Examples $E_T^{\text{miss}} + X$ searches using a Higgs boson are [59–61], a jet [62, 63], a photon [64, 65], a leptonically decaying Z boson [66, 67], a hadronically decaying W or Z [63, 68, 69], and a heavy-flavour quark pair [70, 71]. A selection of ATLAS exclusion limits for different scenarios are shown in Figures 2.18. These results use the simplified model interpretation that is described in Section 2.6.

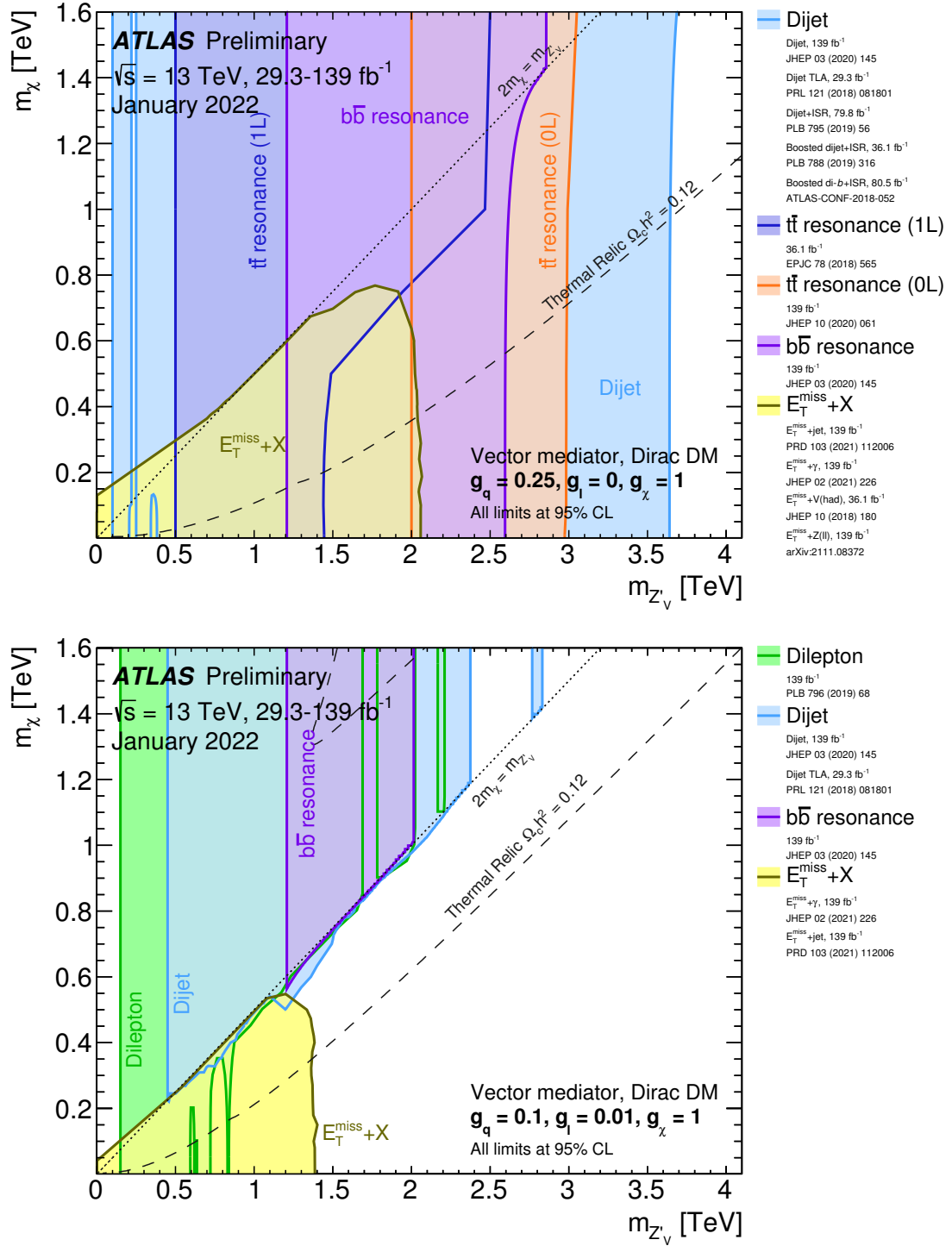


Figure 2.18: DM constraints in a scenario with couplings $g_q = 0.25, g_l = 0, g_x = 1$ on top and $g_q = 0.1, g_l = 0.01, g_x = 1$ on the bottom [72].

2.6 Interpretation of DM models

When performing a search for DM, it is crucial to have a theoretical framework that allows for comparison between data and prediction, and also between results of different experiments. Three approaches can be applied to build such theoretical models: effective field theories (EFT), simplified models and complete theories. In Chapter 5, the EFT interpretation will be used to connect the upper limit on invisible decays of the Higgs with the DM-nucleon cross section in the context of Higgs-portal models [6–18, 73].

When a BSM mediator is heavy compared with the collision energy, the DM-SM interaction can be described by one effective scale Λ , and one dark matter mass m_χ . In this case, the complicated high energy interactions (the mediators) are conveniently integrated out, and the DM production can be described by EFTs in a more model-independent way. At the LHC energies, one may hope that such description is sufficient. EFTs provide a framework to systematically explore a wide range of possible physics.

When the interaction physics is kinematically accessible, one should replace the EFT description with a complete model specifying the details of the interaction between the DM and the SM. Complete theories provide a full description of the SM extension and usually are UV complete up to some large scale. These theories are able to provide precise predictions for the fields of particle and astroparticle physics, and cosmology while providing a connection to compare results from different experiments. However, complete theories make use of many free parameters complicating the process of extracting physics conclusions from a finite number of measurements. Furthermore, any conclusion obtained is model dependant. Some of the more popular complete theories are Supersymmetric theories. Unfortunately no evidence of any beyond Standard Model have been found so far in the experiments.

Simplified models are an intermediate step between EFTs and complete theories. These models consider a mediator between DM and the SM particles and are characterised by a few number of parameters describing the mass of the DM particle, the strength of its interactions, and the mass of the mediator. The DM interactions are described by the coupling strengths between DM and the mediator (g_{DM}), and between the mediator and SM quarks (g_q), and leptons (g_l). When reporting results using a simplified model interpretation, exclusion limits on the phase space of the DM mass - mediator mass are set for specific values of the coupling constants.

2.6.1 Higgs-portal DM model

Higgs-portal models consider that DM couples to the SM only through an interaction with the Higgs boson. Experimentally, the dark sector would be accessible only via the Higgs production and its possible subsequent decay into DM. We can consider three possibilities for DM, either it consists of scalar particles S, vectors (V) or Majorana fermions χ . The Lagrangian corresponding to each of the three scenarios are the following:

$$\begin{aligned}
 \Delta\mathcal{L}_S &= \frac{1}{2}m_S^2 S^2 - \frac{1}{4}\lambda_S S^4 - \frac{1}{4}\lambda_{hSS} H^\dagger H S^2 \\
 \Delta\mathcal{L}_V &= \frac{1}{2}m_V^2 V_\mu V^\mu + \frac{1}{4}\lambda_V (V_\mu V^\mu)^2 + \frac{1}{4}\lambda_{hVV} H^\dagger H V_\mu V^\mu \\
 \Delta\mathcal{L}_f &= -\frac{1}{2}m_f \bar{\chi}\chi - \frac{1}{4}\frac{\lambda_{hff}}{\Lambda} H^\dagger H \bar{\chi}\chi,
 \end{aligned} \tag{2.32}$$

where S, V or f are the DM fields, λ_{hSS} , λ_{hVV} , and λ_{hff}/Λ are the corresponding coupling constants, and v is the vacuum expectation value of the SM Higgs doublet. The Lagrangians are requested a Z_2 parity to ensure the stability of the DM particles. The hidden sector could contain several particles, but for the interpretation of searches at the LHC it is generally sufficient to only assume one for simplicity. After the electroweak symmetry breaking, the masses of the DM would be:

$$\begin{aligned}
 M_S &= m_S^2 + \frac{1}{2}\lambda_{HSS} v^2 \\
 M_V &= m_V^2 + \frac{1}{2}\lambda_{HVV} v^2 \\
 M_f &= m_f^2 + \frac{1}{2}\frac{\lambda_{Hff}}{\Lambda} v^2,
 \end{aligned} \tag{2.33}$$

If the DM particles are light enough ($M_{DM} < (1/2)m_H$), the Higgs boson might decay into a pair of DM particles and leave the ATLAS detector undetected. The decay width of invisible Higgs boson decays is defined as:

$$\Gamma_H^{\text{inv}} = \frac{BF(H \rightarrow \text{invisible})}{1 - BF(H \rightarrow \text{invisible})} \times \Gamma_H, \tag{2.34}$$

where Γ_H is the Higgs boson total decay width in the SM. Following Reference [15], the Higgs partial decay widths into invisible DM particles for the three cases under study is given by:

$$\begin{aligned}
 \Gamma_{h \rightarrow SS}^{\text{inv}} &= \frac{\lambda_{HSS}^2 v^2 \beta_S}{64\pi m_H} \\
 \Gamma_{h \rightarrow VV}^{\text{inv}} &= \frac{\lambda_{HVV}^2 v^2 m_H^3 \beta_V}{256\pi M_V^4} \left(1 - 4\frac{M_V^2}{m_H^2} + 12\frac{M_V^4}{m_H^4} \right) \\
 \Gamma_{h \rightarrow ff}^{\text{inv}} &= \frac{\lambda_{Hff}^2 v^2 m_H \beta_f^3}{32\pi \Lambda^2},
 \end{aligned} \tag{2.35}$$

where $\beta_X = \sqrt{1 - 4m_x^2/m_H^2}$ and m_x is the mass of the DM particle. In the Higgs-portal model, the Higgs boson is assumed to be the only mediator in the WIMP-nucleon scattering. The WIMP-nucleon cross section can be written as:

$$\begin{aligned}
\sigma^{SI} &= \frac{\lambda_{HSS}^2}{16\pi m_H^4} \frac{m_N^4 f_N^2}{(m_S + m_N)^2}, \\
\sigma^{SI} &= \frac{\lambda_{HVV}^2}{16\pi m_H^4} \frac{m_N^4 f_N^2}{(m_V + m_N)^2}, \\
\sigma^{SI} &= \frac{\lambda_{Hff}^2}{4\pi \Lambda^2 m_H^4} \frac{m_N^4 m_f^2 f_N^2}{(m_f + m_N)^2},
\end{aligned} \tag{2.36}$$

where m_N is the nucleon mass, and f_N is the form factor associated to the Higgs boson-nucleon coupling. Both the invisible decay width and the WIMP-nucleon cross section depend on the coupling constant squared. Using equations 2.34, 2.35, and 2.36, we can translate an upper limit on the branching fraction of invisible Higgs boson decays into an upper bound on the scattering cross section between nucleons and WIMPs. The concept of Higgs-portal models can be generalized to an undiscovered Higgs-like scalar field as the link between the SM and a hidden sector. Experimental analyses that use the interpretation of the Higgs-portal always have the option to probe other mediator masses.

The ATLAS experiment at the Large Hadron Collider

This chapter introduces the Large Hadron Collider and the ATLAS experiment at CERN. The LHC experiment is described in Section 3.1. A general description of the ATLAS experiment is provided in Section 3.2. The upcoming upgrade of the experiment, the high luminosity LHC, is introduced in Section 3.3. The trigger and data acquisition systems are presented in Section 3.2.5, followed by the reconstruction of physical objects in Section 3.4. Finally, the Monte Carlo simulation is discussed in Section 3.5.

3.1 The Large Hadron Collider

The Large Hadron Collider (LHC) [74–76] is the most energetic particle accelerator in the world and it is operated by the European Organization for Nuclear Research (CERN). The experiment is located near Geneva at an average depth of 100 meters inside a tunnel of 26.7 km circumference that was built for the Large Electron-Positron Collider (LEP) [77, 78], the predecessor of the LHC. The LHC is designed to accelerate protons up to an energy of 7 TeV and heavy ions to 2.56 TeV (energy per nucleon). This thesis manuscript will focus only on proton-proton collisions.

The particles collide in four interaction points where dedicated detectors are located: A Large Ion Collider Experiment (ALICE) [79], a Large Hadron Collider beauty (LHCb) [80], a Compact Muon Solenoid (CMS) [81], and A Toroidal LHC ApparatuS (ATLAS) [82]. ALICE focuses on understanding the quark-gluon-plasma in dedicated heavy-ion runs at the LHC. LHCb focuses on the study of interactions containing a b quark to investigate the differences between matter and antimatter. In contrast to these two detectors with a specific objective, CMS and ATLAS are general purpose experiments covering a broad band of the physics program at the LHC.

To reach the desired energy, the protons need to pass through the CERN accelerator complex illustrated in Figure 3.1. First, protons are obtained by ionising hydrogen atoms and accelerated to an energy of 750 keV using Radio Frequency (RF) cavities. Next, the protons go through the LINAC 2 reaching an energy of 50 MeV and are subsequently injected to the Proton Synchrotron Booster (PSB)

going up to an energy of 1.4 GeV. Later, the protons are inserted into the Proton Synchrotron (PS) and the Super Proton Synchrotron (SPS) where they are accelerated to an energy of 26 GeV and 450 GeV to finally be injected into the LHC.

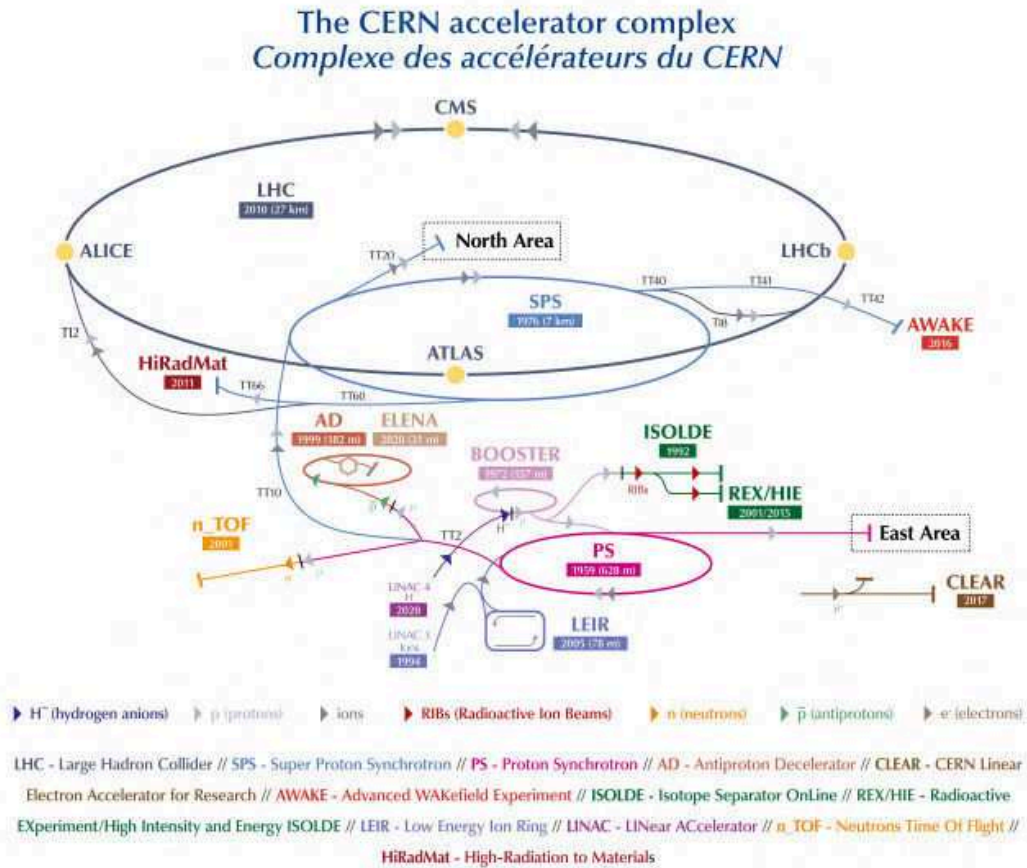


Figure 3.1: Illustration of the CERN LHC accelerator complex [83].

3.1.1 Luminosity

Particle colliders are usually characterised by their beam energy. Besides the energy, the number of useful interactions is very important, in particular when studying rare processes with a small cross section. The quantity that describes the ability of a particle accelerator to produce the required number of interactions is called luminosity [84], and it is defined as the proportionality factor between the rate of events per second dN/dt and the cross section as written in Equation 3.1.

$$\frac{dN}{dt} = \sigma \mathcal{L} \quad (3.1)$$

$$N = \sigma \int \mathcal{L} dt \quad (3.2)$$

Integrating Equation 3.1 we can obtain the expression for the number of expected events as a function of the experiment running time written in Equation 3.2. The term $\int \mathcal{L} dt$ is called integrated luminosity, and it is often measured in inverse barns ($1\text{b} = 10^{-24}\text{cm}^{-2}$). Therefore, having an expression of the luminosity as a function of time one can measure or estimate the expected number of events. Such an expression can be obtained considering that the beam is divided in groups of protons called bunches. These proton bunches are separated 25 ns in time. Assuming a Gaussian profile in the proton distribution inside the beam, the luminosity can be computed as:

$$\mathcal{L} = \frac{N_b^2 n_b f_{\text{rev}} \gamma}{4\pi \epsilon_n \beta^*} F(\theta), \quad (3.3)$$

where N_b^2 is the number of particles per bunch, n_b is the number of bunches per particle beam, f_{rev} is the revolution frequency in the accelerator, $\gamma = 1/\sqrt{1 - v^2/c^2}$ is the Lorentz factor defined by the particle speed v and the speed of light c , and $F(\theta)$ is a geometric factor due to the crossing angle between the beams at the interaction point. In the denominator, ϵ is the beam emittance defined as the smallest opening you can squeeze the beam through and β^* is the so-called amplitude function and is defined by the width of the beam and the emittance. The LHC is equipped with dedicated luminometers used to continuously monitor the luminosity conditions. The integrated luminosity delivered by the LHC, recorded by ATLAS and good for physics are shown in Figure 3.2. ATLAS uses several detectors to measure the luminosity being LUCID-2 the main luminosity monitor [85, 86].

Due to the high luminosity of the LHC, multiple pp interactions per bunch crossing may occur. These interactions are usually split into the hard scatter (HS) process and the multiple soft interactions (pile-up). As a consequence, signals from different interactions might be recorded when reconstructing a triggered event. This is called pile-up and can be divided into in-time pile-up when signals are from soft interactions in the same bunch crossing and out-of-time pile-up when signals come from the surrounding bunches. Out-of-time pile-up is associated with the mean number of interactions per bunch crossing μ while the in-time pile-up is associated with the reconstructed number of primary vertices N_{PV} . A more detailed explanation of pile-up and the required calibration to remove these energy contributions are presented in Section 4.1. The μ distribution in the LHC Run 2 data taking period is shown in Figure 3.3.

3.2 The ATLAS detector

The ATLAS detector is a general purpose experiment located at one of the four interaction points of the LHC. It is designed to cover an extensive physics program in proton proton (pp) and heavy ion collisions. This research program includes a wide range of SM measurements and BSM searches such as precise Higgs coupling measurements and searches for DM and supersymmetry. The detector has a cylindrical shape with 44 m of length, 25 m in diameter and covers a solid angle of almost 4π around the interaction point.

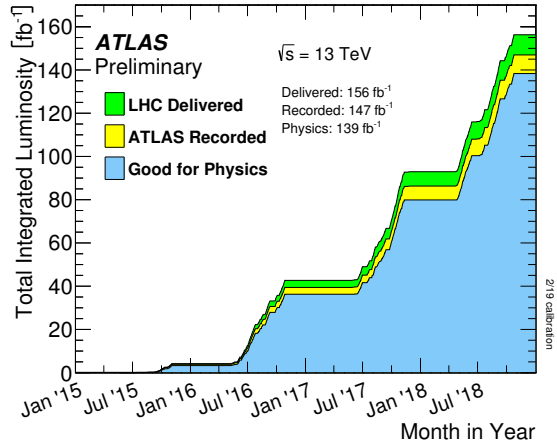


Figure 3.2: Integrated luminosity as a function of time delivered by the LHC (green), recorded by ATLAS (yellow), and Good for physics (blue) [87].

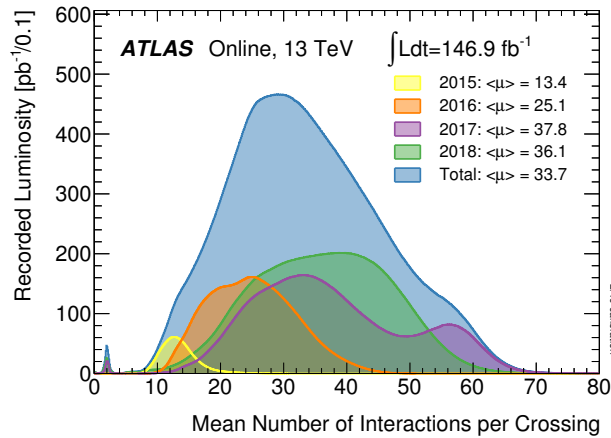


Figure 3.3: Mean number of interaction per bunch crossing at LHC Run 2 [88].

ATLAS uses a coordinate system centred at the interaction point. The z-axis is defined along the beam axis and its positive direction points counter-clockwise around the LHC ring in a right-handed coordinate system. The x-y plane is the plane perpendicular to the beam pipe with the x-axis pointing towards the centre of the LHC. Spherical coordinates are used with the polar angle θ measured with respect to the z axis and the azimuthal angle ϕ measured on the x-y plane. The pseudorapidity variable is defined as $\eta = -\ln(\theta/2)$ such that the differences in pseudorapidity between two objects $\Delta\eta$ is a Lorentz invariant. Another variable commonly used is the angular distance defined as $\Delta R = \sqrt{(\Delta\eta)^2 + (\Delta\phi)^2}$.

The ATLAS detector is composed by three sub-detector systems designed to measure different properties of the particles. The Inner Detector (ID) is responsible for the reconstruction of the

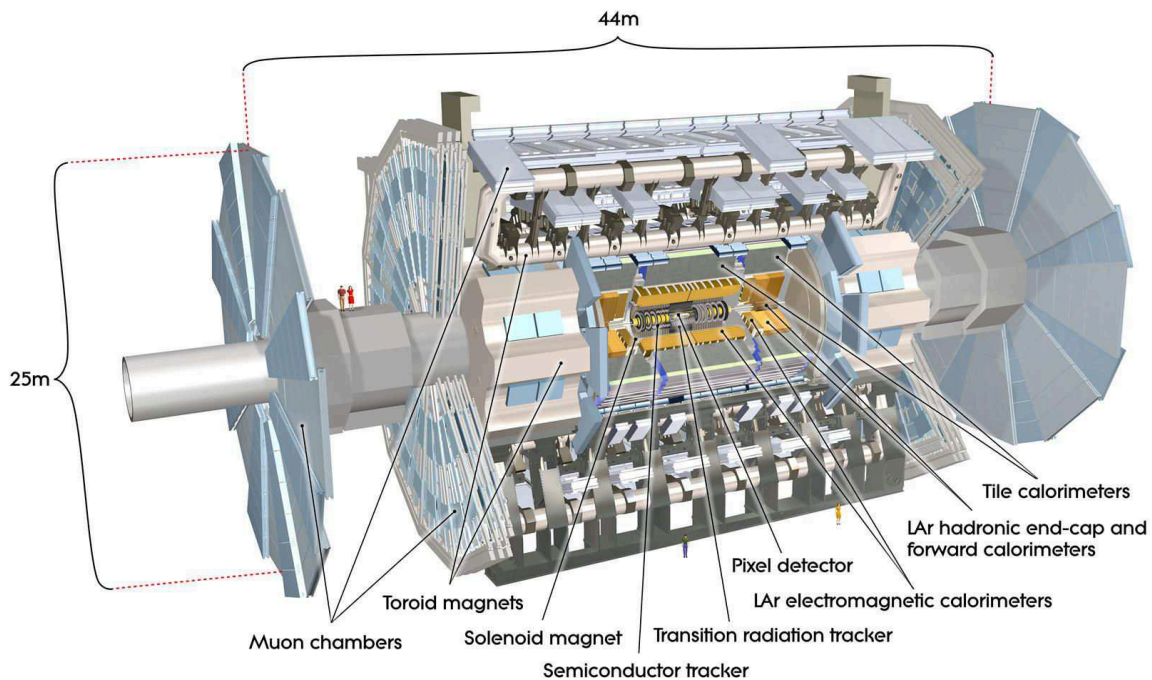


Figure 3.4: Illustration of the ATLAS detector [82] with its different subsystems.

trajectories of charged particles, the electromagnetic and hadronic calorimeter system measures the energy of electrons, photons and hadrons, and at the most external part the muon spectrometer is used to reconstruct the trajectory and energy of muons. The detector is immersed in a magnet system placed to bend the trajectories of charged particles allowing the measurement of the particle momentum perpendicular to the magnetic field. Given the high collision rate, a dedicated trigger and data acquisition system is needed to store only the information of processes of interest. A more detailed explanation of these different components of the ATLAS experiment, the trigger and data acquisition is presented in Sections 3.2.1 to 3.2.5. An illustration of the ATLAS detector and its components is shown in Figure 3.4.

3.2.1 Magnet system

The ATLAS magnet system is designed to bend the trajectories of charged particles allowing the measurement of their momentum. It is composed by a central solenoid magnet surrounding the inner tracker, and a toroid magnet system for the muon spectrometer. The Central Solenoid (CS) is built up from a single layer coil wound in a supporting cylinder and provides a 2 T magnetic field aligned with the beam axis. The toroid magnet system consists of an air-core Barrel Toroid (BT) and two air-cored End-Cap Toroids (ECT). Each of these components has eight coils assembled radially and symmetrically around the beam axis. They provide a magnetic field of 4T in the muon spectrometer. An illustration of the ATLAS magnet system is shown in Figure 3.5.

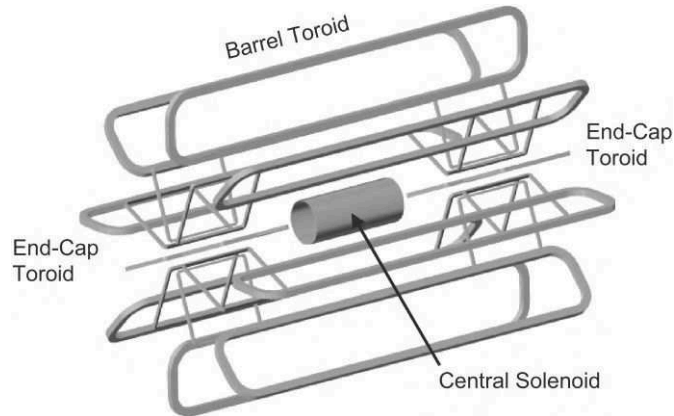


Figure 3.5: Illustration of the ATLAS magnet system composed of the Central Solenoid, the Barrel Toroid and the End-Cap Toroids [89].

3.2.2 Inner Detector

The Inner Detector (ID) is the innermost layer of ATLAS and consist of three different systems of sensors immersed in a magnetic field parallel to the beam axis. The ID is used to reconstruct the trajectory, momentum and charge of charged particles produced in the pp collision. The ID components are: Pixel Detector (PD), Semiconductor Tracker (SCT), Transition Radiation Tracker (TRT), and the newest element is the Insertable B-Layer added to recover the loss of sensitivity due to radiation damage. All the elements of the ID span a pseudorapidity range $|\eta| < 2.5$. The ID and its substructure are illustrated in Figure 3.6 and a more detailed illustration of the ID in the central region is shown in Figure 3.7.

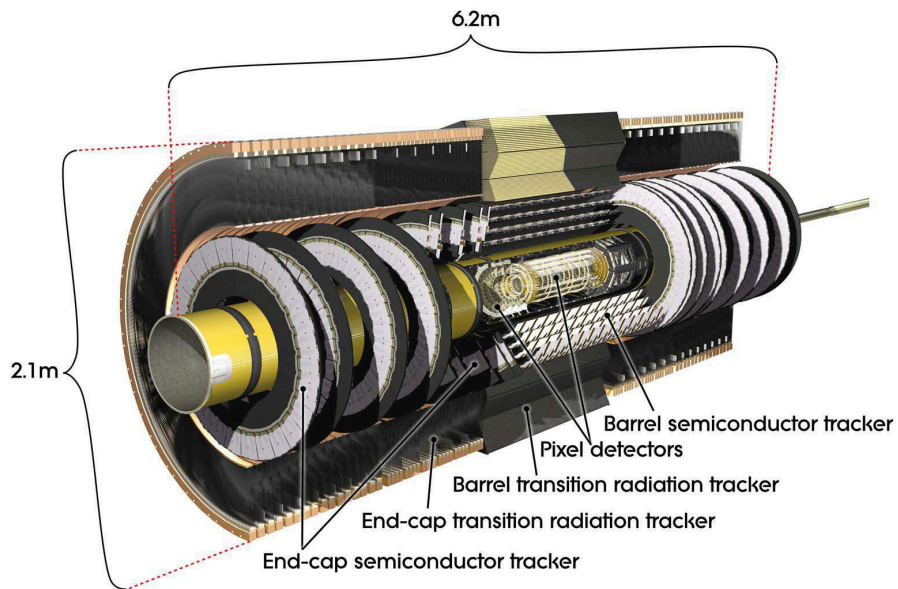


Figure 3.6: Illustration of the ATLAS inner detector and its subcomponents [90].

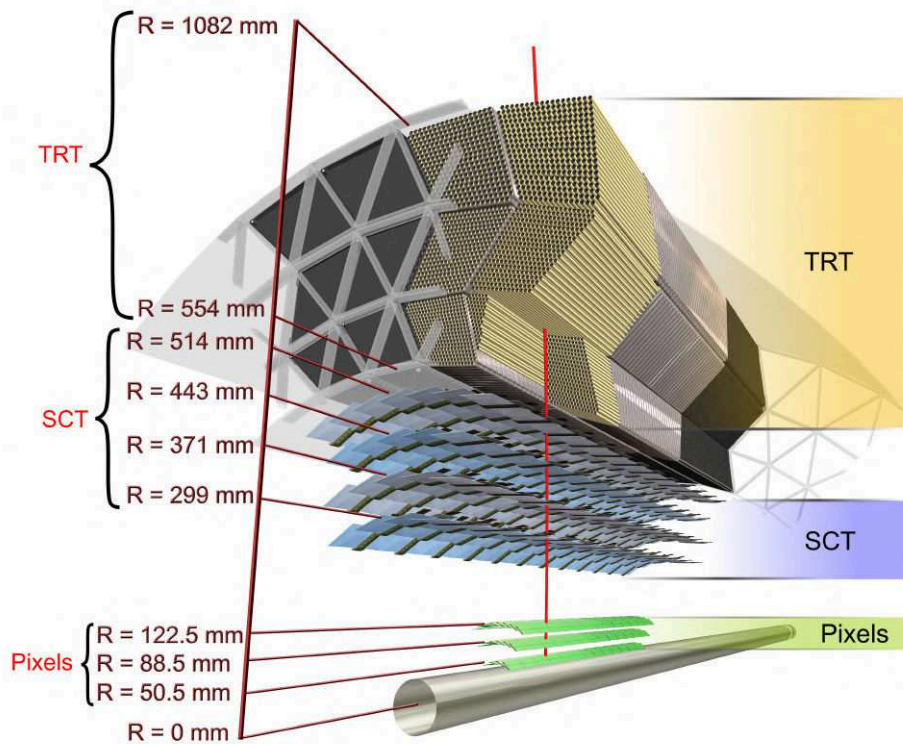


Figure 3.7: Illustration of the central region of the ATLAS Inner Detector showing the Pixel Detector (PD), the Semi-Conductor Tracker (SCT), the Transition Radiation Tracker (TRT), and the new Insertable B-Layer (IBL) [90].

Pixel Detector

The Pixel Detector [91] is the innermost element of the inner detector. It is designed to provide at least three points in the trajectory of a charged particle emanating from the collision region. The active region of the pixel detector is composed of three barrel layers and three disk layers at each end of the barrel region. The basic building block of the active part of the pixel detector is a module that is composed of silicon sensors, front-end electronics and flex-hybrids with control circuits. The total number of pixels in the system is approximately 67 million in the barrel and 13 million in the endcaps, covering a total active area of about 1.7 m^2 . The Pixel Detector provides a spatial resolution of $10 \mu\text{m}$ per layer in the $R - \phi$ plane transverse to the beam and $115 \mu\text{m}$ along the z -axis.

The Insertable B-Layer (IBL) [92, 93] is the innermost layer of the Pixel Detector. It was installed during the LHC shutdown between the Run 1 and Run 2 with the purpose to recover the loss in sensitivity due to radiation damage. The IBL is composed of 8 million pixels providing a spatial

resolution of $8 \mu\text{m}$ in the $R - \phi$ plane and $40 \mu\text{m}$ along the z-axis. The IBL improves the quality of the impact parameter reconstruction for tracks, the vertexing and b-tagging performance and allows a robust reconstruction against pile-up.

Semiconductor Tracker

The Semiconductor Tracker (SCT) [94] is a precision silicon microstrip detector located in the middle layer of the inner detector covering the region $|\eta| < 2.5$. The SCT has four double layers of silicon strip sensors in the barrel region and nine disks in each endcap. Strips in each layer or disk provide two strip measurements at a stereo angle which are combined to obtain space-points. The SCT typically provides eight strip measurements (four space-points) for particles originating in the beam-interaction region, allowing the reconstruction of trajectories with a spacial resolution of $17 \mu\text{m}$ in the $R - \phi$ plane and $580 \mu\text{m}$ along the z-axis.

Transition Radiation Tracker

The Transition Radiation Tracker (TRT) [95, 96] is the outermost element of the inner detector and covers the region $|\eta| < 2.0$. The TRT is composed of 370,000 cylindrical drift tubes of 4 mm diameter filled with a mix of Xe, CO₂, and O₂ to increase the electron drift velocity, and for photons-quenching. It is designed to provide robust tracking information with stand-alone patten recognition, to enhance the momentum resolution by providing track measurements points up to the solenoid radius and to provide a fast level-2 trigger. By integrating the transition-radiation signature, the TRT also provides stand-alone electron/pion separation.

3.2.3 Calorimeter

Calorimeters are detectors designed to absorb the energy of particles coming from a collision. When a particle crosses the calorimeter, its interaction with the detector produces a shower of secondary particles. The energy deposited by the charged particles of the shower in the active part of the calorimeter can be detected in the form of light or charge and used to measure the energy of the incident particle. Calorimeters are usually divided into electromagnetic calorimeters, used to measure electrons and photons through their electromagnetic interactions, and hadronic calorimeters, used to measure hadrons through their strong interactions. Further, they can be classified into sampling calorimeters and homogeneous calorimeters. ATLAS counts with a sampling calorimeter system consisting of layers of an absorbing high-density material that stops incoming particles, interleaved with layers of an active medium used to measure their energy. The ATLAS calorimeter is composed of the Liquid Argon (LAr) Calorimeter designed to absorb electrons, photons and hadrons, and the Tile Hadronic Calorimeter designed to stop hadrons such as protons and neutrons. An illustration of the ATLAS calorimeter system is shown in Figure 3.8.

Two types of showers are generated in the calorimeters depending on the nature of the incoming particle: electromagnetic and hadronic. The development of the electromagnetic shower is dominated by bremsstrahlung, and electron-positron pair production. It can be described in terms of the radiation

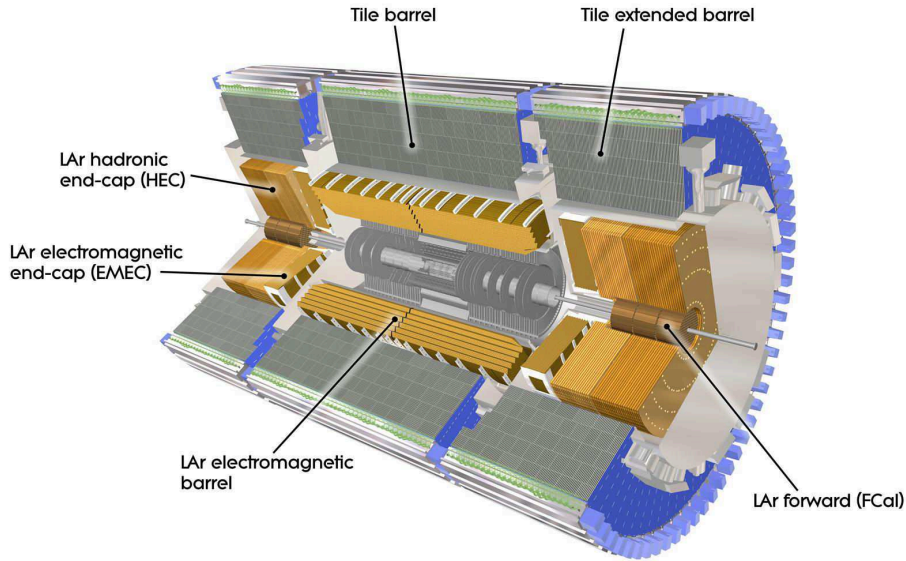


Figure 3.8: Illustration of the ATLAS calorimeter [97].

length (X_0) defined as mean distance over which a high-energy electron loses all but $1/e$ of its energy by bremsstrahlung. The radiation length is a characteristic of the material and can be approximated as

$$X_0 \text{ g/cm}^{-2} = \frac{716 \text{ g cm}^{-2} A}{Z(Z+1) \ln(287/\sqrt{Z})}, \quad (3.4)$$

where Z is the atomic number and A is the mass number of the nucleus. On the other hand, the hadronic shower is dominated by inelastic collisions with the dense material. In this case the shower can be described by the hadronic interaction length λ defined as the mean distance travelled by a hadronic particle before undergoing an inelastic nuclear interaction. Ideally, the radiation length and the hadronic interaction length have to be small to fully contain the particle energy within a compact calorimeter.

The fractional resolution of calorimeters can be expressed as a function of the total energy as:

$$\frac{\sigma_E}{E} = \frac{N}{E} \oplus \frac{S}{\sqrt{E}} \oplus C, \quad (3.5)$$

where N represents the noise of the measurements, S stands for the stochastic uncertainty, and C is a constant term corresponding to the non-uniformities in the detector. The \oplus symbol indicates a quadratic sum.

Liquid Argon Calorimeter

The LAr Calorimeter [98, 99] surrounds the ATLAS inner detector and spans the region $|\eta| < 4.9$. It measures the energy of electrons, photons and hadrons using liquid argon as active material. The

detector consists of layers of metal (either tungsten, copper or lead) that absorb incoming particles producing a particle shower. These secondary particles ionise the LAr in between the metal layers creating ionised charges which are directed by a high voltage to create electric signals in the electrodes. In the barrel and endcaps the LAr calorimeter has more than 22 radiation lengths to assure the containment of the electromagnetic shower.

The LAr calorimeter is subdivided into four parts: an electromagnetic barrel (EMB), an electromagnetic endcap calorimeter (EMEC), a hadronic end cap (HEC) calorimeter, and a forward calorimeter (FCAL). The system formed by the EMB and the EMEC is the electromagnetic calorimeter (ECal) covering the region $|\eta| < 3.2$. The EMB covers the region $|\eta| < 1.475$ and the EMEC the region $1.375 < |\eta| < 3.2$. The electromagnetic calorimeter is designed following an accordion geometry with alternating layers of lead as the absorber and liquid argon as the active medium. An illustration of the ECal layers is shown in Figure 3.9. The fractional resolution of the ECal in the barrel region is measured as

$$\frac{\sigma_E}{E} = \frac{10.1\%}{\sqrt{E}} \oplus 0.2\%, \quad (3.6)$$

and in the endcap region

$$\frac{\sigma_E}{E} = \frac{12.1\%}{\sqrt{E}} \oplus 0.4\%. \quad (3.7)$$

The HEC and the FCAL cover the regions $1.5 < |\eta| < 3.2$ and $3.1 < |\eta| < 4.9$ respectively. Together with the Tile Calorimeter they form the ATLAS Hadronic Calorimeter (HCal). The HEC uses plates of copper over four longitudinal layers as absorber while the FCAL has a first layer of copper, and a second and third layers made of tungsten. The measured energy resolution of the HEC is:

$$\frac{\sigma_E}{E} = \frac{70.6\%}{\sqrt{E}} \oplus 5.8\%, \quad (3.8)$$

and the measured energy resolution of the FCAL is:

$$\frac{\sigma_E}{E} = \frac{94.2\%}{\sqrt{E}} \oplus 7.5\%. \quad (3.9)$$

Tile hadronic calorimeter

The Tile Calorimeter (TileCal) [100, 101] surrounds the LAr calorimeter and measures the energy of hadronic particles which do not deposit all of their energy in the LAr Calorimeter. It covers the region $|\eta| < 3.2$ and is composed of layers of steel as absorber and plastic scintillating tiles as active medium. The tile calorimeter is made up of about 460,000 plastic scintillator tiles working in sync and it is subdivided in three components: a central component in the region $|\eta| < 1.0$, and two extended barrels covering the range $1.5 < |\eta| < 3.2$. The tileCal plays an important role in the measurement of jet and missing energy, jet substructure, electron isolation, and triggering.

As particles hit the layers of steel, a shower of new particles is produced from the inelastic scattering

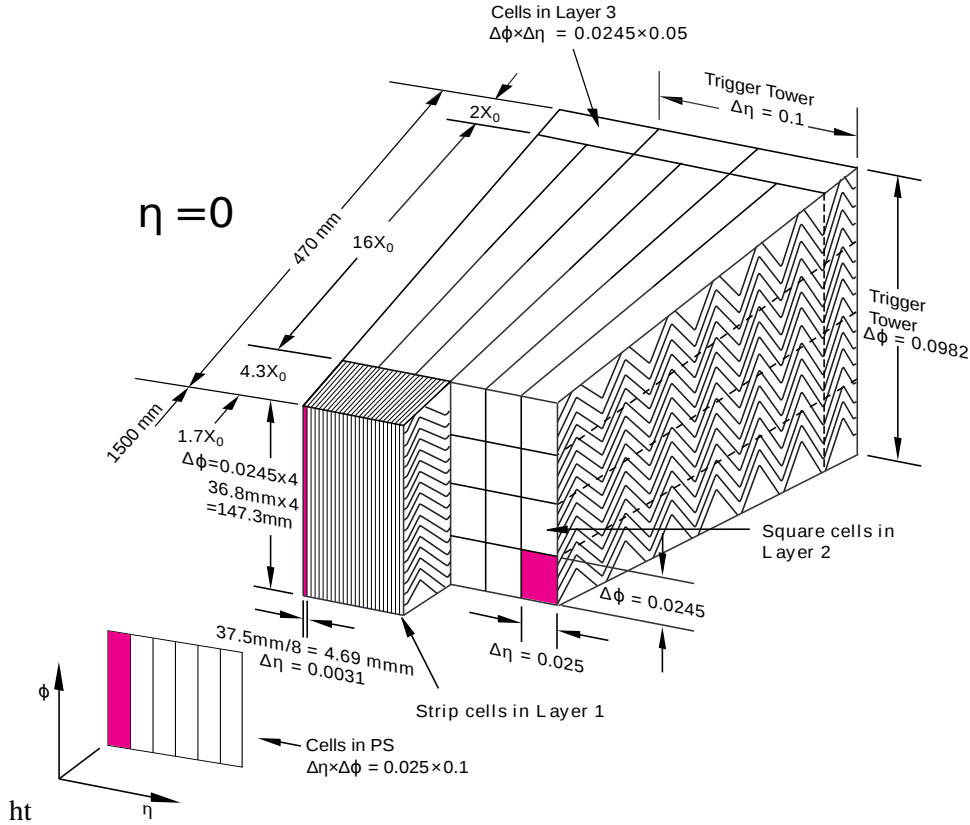


Figure 3.9: Illustration of the LAr calorimeter layers in the barrel [82].

between the hadrons and the nuclei of the material. These particles interact with the plastic scintillators producing photons. The photons are then read out by wavelength shifting fibers, which transport the signals to photomultiplier tubes (PMTs). A sketch of the tile calorimeter system is shown in Figure 3.10. PMTs can multiply the current produced by the incident photons by a factor as much as 10^8 producing a usable signal for the reconstruction of physics objects which is proportional to the original particle's energy. The resolution of the tile calorimeter can be parametrized as:

$$\frac{\sigma_E}{E} = \frac{52.0\%}{\sqrt{E}} \oplus 3.0\%. \quad (3.10)$$

3.2.4 Muon spectrometer

Muons do not produce a particle shower in the calorimeters. Consequently, its energy is not fully contained and a dedicated muon system is needed to measure the momentum and trajectory of these particles. The ATLAS muon spectrometer [102, 103] is the outermost and the largest part of the ATLAS detector. It surrounds the calorimeters and covers the region $|\eta| < 2.7$ with a cylindrical shape of 22 m in diameter and 45 m in length. This sub-detector consists of a barrel and two endcap sections immersed in a magnetic field generated by the toroid magnets in ATLAS (see Section 3.2.1). Four different technologies are used in the muon spectrometer: a Thin Gap Chamber (TGC) [104]

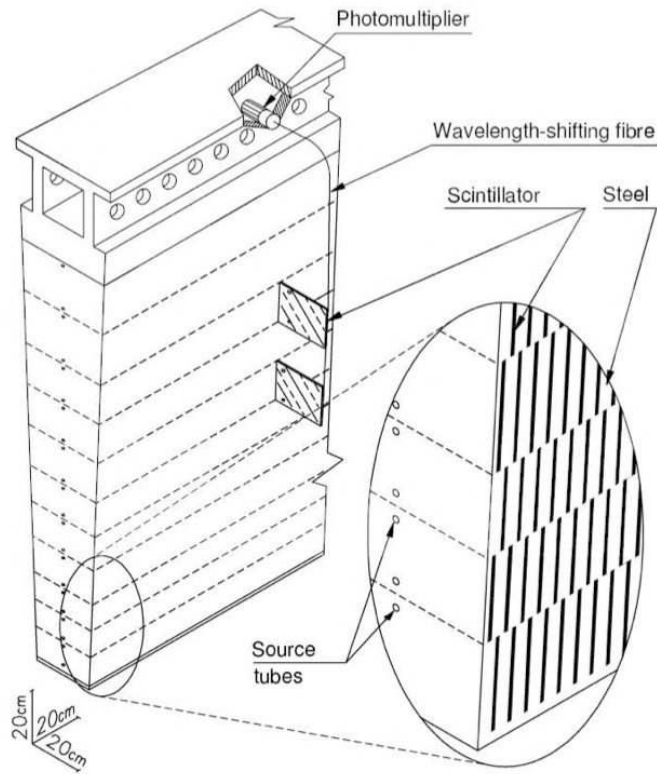


Figure 3.10: Sketch of the structure and readout system of the tile calorimeter [82].

and a Resistive Plate Chamber (RPC) [105] are used for triggering in the endcaps and the barrel, respectively, while Monitored Drift Tubes (MDT) [106], and Cathode Strip Chambers (CSC) are used for precision measurements of the muon dynamics. The ATLAS muon spectrometer is illustrated in figure 3.11.

Thin Gap Chambers

The Thin Gap Chambers provide fast tracking information at the region $|\eta| < 2.4$ for triggering and also to determine the azimuthal coordinate ϕ of muons. Each TGC unit is a multi-wire proportional chamber consisting of two parallel cathode plates filled with a highly quenching gas mixture of CO₂ and n-C₅H₁₂, and wires placed in between serving as anodes. A potential of 2.9 kV is applied across the wires. When a muon crosses the TGC, the gas is ionised and the resulting ions and electrons are accelerated by the electric field and collected in the closest wire. The pulses from the different wires are used to reconstruct the muon trajectories. One of the advantages of TGCs is their high gain mode which provide large saturated signals. These signals are relatively insensitive to mechanical variations allowing the construction of large highly efficient detectors. Another characteristic is the narrow time spread of signals allowing for a timing resolution of ~ 4 ns.

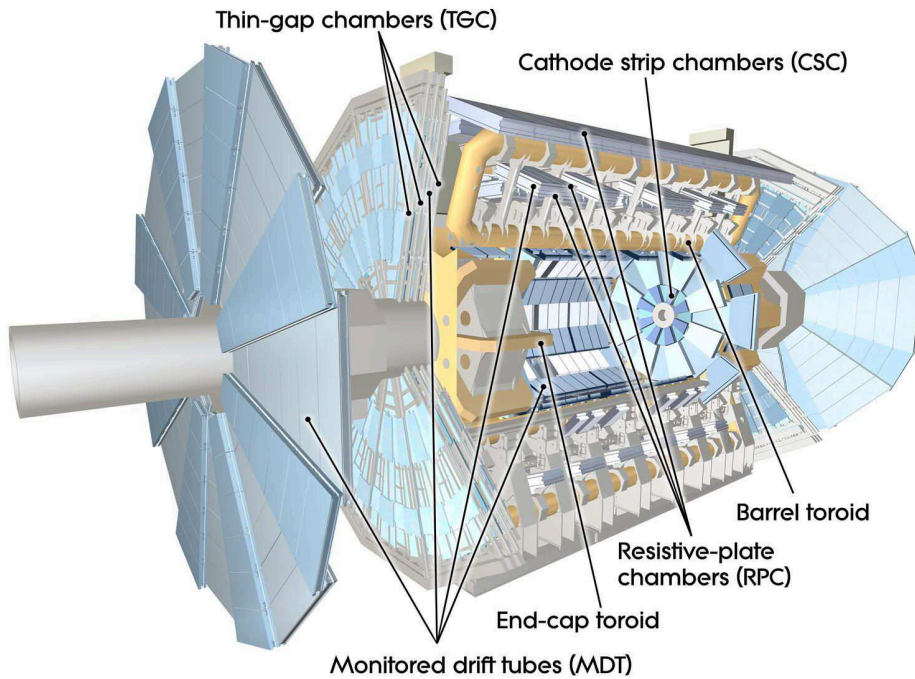


Figure 3.11: Illustration of the ATLAS muon spectrometer [107].

Resistive Plate Chambers

Resistive Plate Chambers (RPCs) provide fast tracking information at the central region of $|\eta| < 1.05$. RPCs in ATLAS are used for first-level muon triggering and for the measurement of the coordinate in the non-bending direction in the barrel region of the muon spectrometer. Two RPCs are installed in the barrel middle station providing the low- p_T trigger, and another chamber is installed on the outer barrel for high- p_T triggering. The operation principle of RPCs is the same as for the TGCs, and these two sub-detectors provide the muon information in the non-bending direction.

Monitored Drift Tubes

Drift chambers are multi-wire detectors which differ from the TGCs and RPCs in that the timing of the current pulses of the wires is precisely measured. Taking into account that the ions need some time to drift to the nearest wire, one can infer the distance at which the particle passed the wire. The ATLAS MDT chambers consist of six layers of drift tubes, arranged such that three layers are mounted on each side of a support structure. The basic detection cell of MDTs is a drift tube of 3 cm diameter containing a stretched wire within a gas volume. When a muon or any charged particle passes through the volume, it ionises the gas and produces an electric current in the wire. The MDT chambers provide precision tracking for charged-particles in the plane defined by the beam axis (z) and the radial distance to the beam (r) in the pseudorapidity range $|\eta| < 2.7$. In the innermost wheel in the end-cap region at $2.0 < |\eta| < 2.7$ the expected flux of particles is higher than 100 Hz/cm^2 and cathode strip chambers are installed because of their higher granularity.

Cathode Strip Chambers

The Cathode Strip Chambers complement the MDT in the region $2.0 < |\eta| < 2.7$ providing tracking of muons in this region with higher rate capacity and better timing resolution compared to the MDT chambers. The system consists of two endcaps, with 16 chambers in each endcap. Each chamber contains 4 precision layers and 4 transverse layers achieving a spatial resolution of $60 \mu\text{m}$ in the CSC plane and 5 mm in the non-bending direction.

3.2.5 Trigger and data acquisition system

In Run-2, the LHC produced around 1.7 billion collisions per second in the ATLAS detector. This data contains information of all sub-detector systems as well as the reconstructed collision products taking about 1.5 MB of disk space and a relatively long CPU time per event. To reduce the flow of data to manageable levels, ATLAS uses a two-level event selection system which determines the events that are interesting for physics studies.

The ATLAS trigger is a two level system consisting of a hardware-based level 1 (L1) trigger which uses information from the calorimeters and muon spectrometer. The L1 trigger provides a fast selection and identifies regions of interest (RoI) in the $\eta - \phi$ plane, followed by a software-based high level trigger (HLT). In addition to the calorimeters and muon spectrometer, the L1 trigger uses information from the inner detector. It works on the RoIs applying a stricter criterion than the L1 decision. The L1 trigger reduces the bunch crossing rate to 100 kHz and the HLT reduces the rate further down to around 1 kHz. A schematic of the ATLAS trigger and data acquisition system is shown in Figure 3.12.

The ATLAS detector uses several different triggers designed to select specific event topologies. For example, there is a trigger to select events containing at least one jet, one muon, or large missing transverse momentum depending on the physics motivation. The ATLAS collection of triggers is called the trigger menu and changes according to the LHC running conditions.

Even after the trigger decision the available data space might not be enough to record all the triggered events. In these cases, a "pre-scale" selection criteria is applied to the events that pass the trigger selection in order to face this limitation. A fraction of these events is randomly discarded. To compensate for the loss of events, the pre-scale has to be taken into account when comparing data and simulation. For example, a trigger with a pre-scale of 4 would record only one fourth of the total events satisfying the trigger selection criteria and the remaining events need to be scaled up by a factor of 4.

Trigger turn-on curves

Because of the fast response of the trigger system, the variables measured at this level have a lower resolution than the reconstructed objects that enter the dataset. Consequently, there are events that should be triggered, but the trigger value of a particular variable is below the required threshold to pass the trigger. To study this phenomenon, we use the efficiency ϵ of the trigger defined as the ratio between the events that pass the trigger selection over the total number of events. This efficiency can be parametrized as an error function called the trigger turn on function:

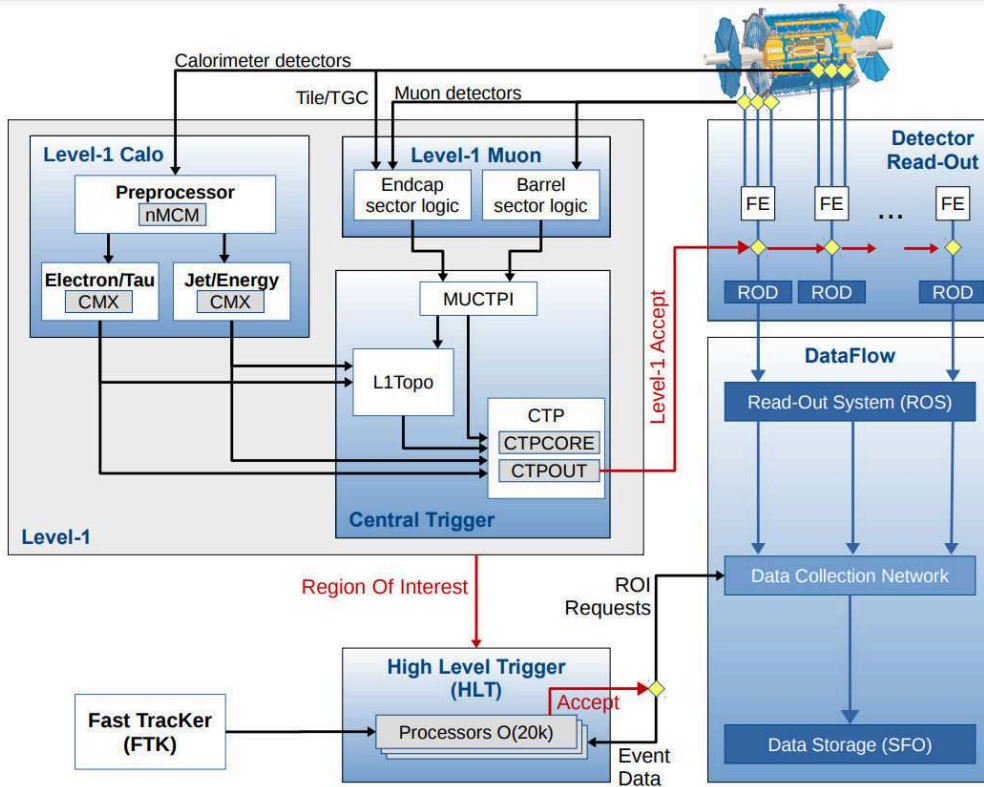


Figure 3.12: Schematic representation of the ATLAS trigger and data acquisition system. The level-1 trigger consist of the L1 Calo, the L1 Muon, and the L1 Topo. Events passing the L1 trigger are passed to the software based high-level trigger to be finally saved in the Data Storage.

$$\epsilon(T, i) = \frac{\text{Number of events in bin } i \text{ passing } T}{\text{Number of events in bin } i} = \frac{p_2}{2} \cdot \left[1 + \text{erf}\left(\frac{x_i - p_0}{\sqrt{2}p_1}\right) \right], \quad (3.11)$$

where x_i is the value of the trigger variable in bin i . The free parameters a and b are usually used to model the trigger efficiency with a fit. In the limit $x_i \rightarrow \infty$, the efficiency is constant and equal to a .

3.3 The high luminosity LHC

The high luminosity Large Hadron Collider (HL-LHC) is the next planned upgrade to the LHC. Its objective is to increase the luminosity by a factor of 10 compared to the LHC's design value in order to increase the potential for new physics discoveries. The HL-LHC will deliver pp collisions at a center-of-mass energy of 14 TeV with an integrated luminosity of 3000 fb^{-1} for both the ATLAS and CMS experiments. The planned timeline for the development of the HL-LHC is shown in Figure 3.13. The research and development of the needed technologies is in progress and physics experiments are expected to start taking data in 2028.



Figure 3.13: Plan for the development of the HL-LHC. Run 3 is expected to start in 2022 followed by a long shutdown (LS3) for the installation of the HL-LHC. Physics runs at HL-LHC are expected to start in 2027.

The development of the HL-LHC depends on several accelerator and detector innovations. To increase the instantaneous luminosity, the beam size at the collision point and the spacing between proton bunches need to be reduced. The following innovations are planned for the accelerator complex:

- Quadrupole magnets with a strength of 12 Tesla.
- Dipole magnets with a strength of 11 Tesla.
- Crab cavities to tilt and project the beam in the required direction.
- Beam optics system to maintain the intensity at a constant level.
- Larger cryogenics plants.
- Machine protection and collimators to reduce potential damage in the machine.
- Superconducting power lines to supply the required energy.

On the detector side, the following developments are planned for the ATLAS Phase-II upgrade [108]:

- The Inner Tracker will be replaced to improve the momentum resolution and extend the $|\eta|$ coverage from $|\eta| < 2.5$ to $|\eta| < 4.0$.
- The Calorimeter system will be upgraded with new frontend and readout electronics to withstand the increased radiation conditions.
- A large fraction of the muon spectrometer readout and trigger electronics will be replaced to enable higher trigger rates and longer latencies.

- The trigger and data acquisition system will be upgraded to deal with the increased frequency.
- To reduce background from pile-up jets, a High-Granularity Timing Detector (HGTD) will be installed. This will allow precise measurements of the timings of charged particles in the region $2.4 < |\eta| < 4.0$

In order to understand the physics potential of the upgraded experiments, sensitivity studies of the performance of the ATLAS detector in the HL-LHC conditions are required. My contributions of sensitivity projections for the search of invisible Higgs boson decays are summarised in Section 8.6.

3.4 Reconstruction of physics objects

The signals generated in pp collisions are energy deposits in the calorimeters and hits in the trackers. This information is used to reconstruct physics objects such as jets, photons, electrons, muons, etc. Some particles escape the detector and cannot be reconstructed (e.g. neutrinos). These invisible particles produce an imbalance in the measured total transverse momentum and their momenta is added into the missing transverse momentum.

The reconstructed objects are divided into two types: basic objects including tracks, vertices and topological clusters (topoclusters), and composite physics objects as electrons, muons, and jets. The basic objects are used as inputs for the reconstruction of the composite objects. This chapter summarises the ATLAS reconstruction procedure for each of these objects. Section 3.4.3 introduces the jets and its different reconstruction algorithms, electrons and photons are presented in Section 3.4.4, muons in Section 3.4.5, and E_T^{miss} in Section 3.4.6.

3.4.1 Tracks

Tracks are reconstructed trajectories of charged particles. They are obtained by connecting the hits in the different layers of the Inner Detector or the Muon Spectrometer. Starting from a seed containing three hits in the inner detector, the trajectories of charged primary particles are reconstructed by extrapolating the track into the TRT (inside-out algorithm). In contrast, secondary particles trajectories are obtained by extrapolating inwards the tracks starting from the TRT (outside-in algorithm). All tracks are required to have $p_T > 400$ MeV and $|\eta| < 2.5$ and are parametrized by a set of five parameters, $(d_0, z_0, \phi, \theta, q/p_T)$ where d_0 and z_0 are the transverse and longitudinal impact parameters, ϕ and θ are the azimuthal and polar angle of the tracks and q/p_T is the ratio between the charge and the transverse momentum.

3.4.2 Vertices

Vertices are the points where the collisions or decays occur. The vertices reconstruction is done in two steps: the vertex finding and the vertex fitting. In the vertex finding, a set of vertex candidates are defined from the tracks. All vertices are required to have at least two tracks. Then, the precise z -coordinate is obtained from an iterative χ^2 fit. The vertex with the largest sum of squared transverse

momenta of all tracks associated is referred to as the primary vertex (PV).

3.4.3 Jets

A jet can be defined as a collimated spray of stable particles arising from the fragmentation and hadronisation of a parton (quark or gluon) after a collision. The jet reconstructions start from a set of inputs which are clustered and then calibrated. In practice, a jet is defined by the chosen inputs and clustering algorithm.

Topological clusters

When the incident particles cross the calorimeter, they leave energy deposits which are grouped into clusters of topologically connected calorimeter cells. The cluster starts from a set of seed cells called 'proto-clusters'. Next, in the "collect" step, cells adjacent to the proto-clusters are added to them if they exceed a certain threshold on the signal significance. This step is repeated until there are no neighboring cells surpassing the significance threshold. These proto-clusters are split according to the distribution of local signal maxima in order to form the final topoclusters.

Sequential Clustering Algorithms

Assuming that particles within jets have small differences in transverse momenta, it is possible to group them according to this quantity. Sequential clustering algorithms [109] provide a method to group the basic inputs into complex objects called clusters. In these type of algorithms the distance between two particles is defined as:

$$d_{ij} = \min(p_{Ti}^a, p_{Tj}^a) \times \frac{R_{ij}^2}{R} \quad (3.12)$$

where a is an exponent corresponding to a particular algorithm. R_{ij} is the distance in the $\eta - \phi$ space defined by $R_{ij}^2 = (\eta_i - \eta_j)^2 + (\phi_i - \phi_j)^2$ and R is the radius parameter which determines the size of the jet. In the ATLAS collaboration, different types of jets are defined according to their R value. The jets used in all the studies presented in this manuscript are called "small" R jets and are defined as $R = 0.4$.

A second distance variable is the momentum space distance between the beam axis and a particle i defined as:

$$d_{i,B} = p_{Ti}^a \quad (3.13)$$

The clustering algorithm works as follows. First, the minimum of the entire set d_{ij}, d_{iB} is computed. If d_{ij} is the minimum then particles i and j are combined into one particle (ij). If d_{iB} is the minimum i is labeled as a final jet and removed from the list of particles. This process is repeated until all particles are part of a jet. The distance between two jet axes R_{ij} is required to be greater than R .

There are two particular cases of sequential clustering of interest for the studies in this manuscript: the k_t and anti- k_t [110] algorithms.

- k_t : The value of a is 2 in this case, resulting in the distances

$$d_{ij} = \min(p_{Ti}^2, p_{Tj}^2) \times \frac{R_{ij}^2}{R} \quad (3.14)$$

$$d_{iB} = p_{Ti}^2 \quad (3.15)$$

From this equation one can conclude that this algorithm is dominated by low p_T particles. The algorithm prefers to cluster soft particles first, resulting in an area that can fluctuate considerably and a jet that is susceptible to the soft pile-up interactions. Because of these characteristics, the k_t clustering algorithm is used when determining the per event pile-up activity in Section 4.1.1.

- *Anti* - k_t : The value of a in this case is -2, giving the following equations:

$$d_{ij} = \min\left(\frac{1}{p_{Ti}^2}, \frac{1}{p_{Tj}^2}\right) \times \frac{R_{ij}^2}{R} \quad (3.16)$$

$$d_{iB} = \frac{1}{p_{Ti}^2} \quad (3.17)$$

From Equation 3.16 one can conclude that this algorithm prefers to cluster hard particles first. The area then hardly fluctuates and the jets are less susceptible to the soft pile-up interactions than in the k_t algorithm. The *Anti* - k_t results in an algorithm that is the best at resolving jets, but it is not the best for studying the jet substructure.

Topological and Particle Flow jets

Different sets of variables can be used as inputs in the clustering algorithms. Within the ATLAS collaborations, the term "jet collection" is used to define the objects obtained from a particular set of inputs. For the LHC Run 1 topoclusters were used as the nominal inputs, defining the EMTopo jet collection [111]. For the LHC Run 2, a new jet collection called particle flow (PFlow) [112] was developed and chosen as nominal. PFlow jets use the tracks from the inner detector in addition to the topoclusters as inputs to the clustering algorithm. The particle flow (PFlow) algorithm suppresses calorimeter energy deposits arising from charged pile-up particles and takes the momentum estimation from tracks whenever the tracker resolution is better than the calorimeter resolution. The main advantages of the PFlow jet collection in comparison with EMTopo is a better energy and angular resolution, and smaller sensitivity to pile-up interactions.

Both PFlow and EMTopo jets were used for different studies in this manuscript. They will be specified in the corresponding sections.

3.4.4 Electrons and photons

Electrons and photons deposit most of their energy in the electromagnetic calorimeter and can be distinguished using information from the inner detector. A common electron signature includes 12 hits in the tracker. Thus, the reconstruction of electrons is limited to the coverage area of the ID ($|\eta| < 2.47$). An illustration of the electron trajectory through the detector is shown in Figure 3.14.

The reconstruction consists of four different steps: Cluster reconstruction, track association, track refit, and candidate reconstruction. These steps are described below:

- **Seed cluster reconstruction:** The $\eta \times \phi$ space of the EM calorimeter is divided into a grid of 200×256 elements (towers) of size $\Delta\eta \times \Delta\phi = 0.25 \times 0.25$. All the energy deposits in each element are added to compute the tower energy. A sliding window algorithm [113] is then used to seed electromagnetic-energy cluster candidates with a summed transverse energy E_T of 2.5 GeV. The clusters have a fixed size of 3×5 towers in $\eta \times \phi$. Finally, duplicated seed clusters are removed.
- **Track association:** After the clusters are defined, they are associated with the reconstructed ID tracks. A distance of $|\Delta\eta| < 0.05$ and $|\Delta\phi| < 0.1$ is required for a successful matching. If more than one track are matched, the track with the smallest ΔR is chosen. The association is then refined by taking the energy losses due to bremsstrahlung into account. The matched tracks are required to be originating from the primary vertex with $d_0/\sigma_{d_0} < 5$ and $|z_0 \sin \theta| < 0.05$ mm.
- **Candidate reconstruction:** extended clusters are formed around the seed clusters in a window of size 3×7 and 5×5 in the $\eta - \phi$ plane, for the barrel and the endcap, respectively. The cluster energy is then calibrated using multivariate techniques based on data and simulated samples. The energy of the final electron candidate is taken from the calibrated energy of the extended-window cluster, and η and ϕ are taken from the track best matched to the original seed cluster.

In order to discriminate between real electrons and background, a multivariate likelihood (LH) method is applied. The LH discriminant takes clusters and tracks information as input. Three levels of identification are defined within the collaboration: Loose, Medium, and Tight, in order of increasing background rejection. The LH discriminant uses the same information for the three working points, but different selection values are applied. The main selection requirements are the following,

- **Loose:** cuts on the shower shape variables of the first and second layers of the ECal and the hadronic leakage variables.
- **Medium:** cuts on the track quality in the IBL and the Pixel Detector, the TRT high-threshold fraction, the track-cluster matching and the transverse impact parameter d_0 , in addition to a tighter version of the Loose selections.
- **Tight:** cuts on the track quality in the TRT, the ratio between the cluster energy and the track momentum and the photon conversion suppression variables, in addition to a tighter version of the Medium selection

In addition to the standard Loose, Medium, and Tight working points, there is a variation of the Loose working point called "LooseBLayer" which has at least one hit in the IBL on top of the Loose

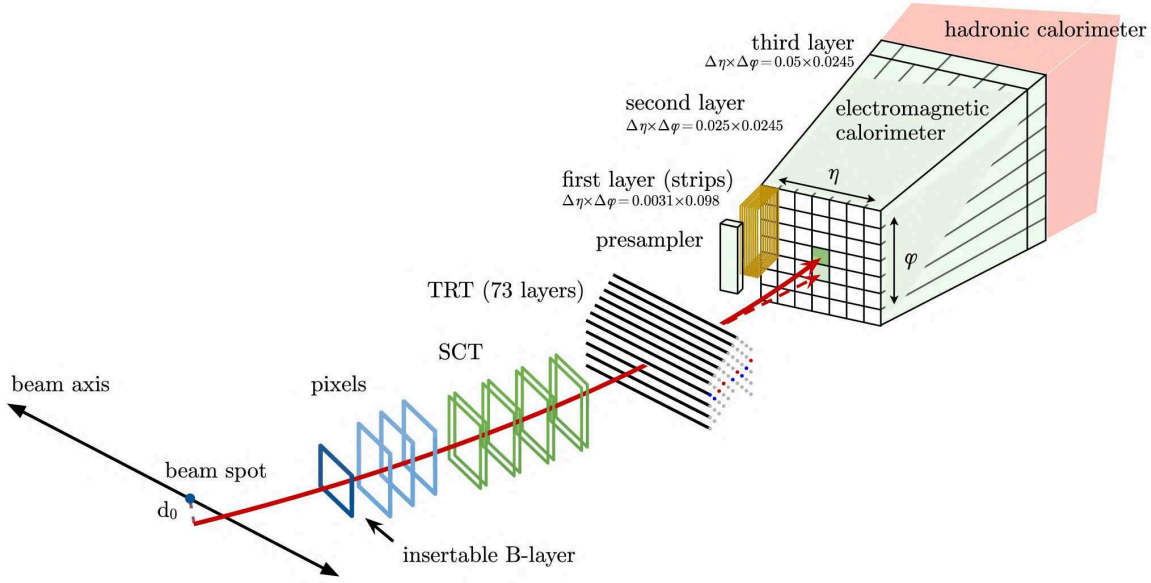


Figure 3.14: A schematic illustration of the path of an electron through the detector [114]. The red trajectory shows the hypothetical path of an electron, which first traverses the tracking system (pixel detectors, then silicon-strip detectors and lastly the TRT) and then enters the electromagnetic calorimeter. The dashed red trajectory indicates the path of a photon produced by the interaction of the electron with the material in the tracking system

selection.

There is a background component from electrons originating in hadronic showers. Motivated by the fact that the signal electrons are expected to be isolated while the electrons from weak decays are mixed with other shower products, isolation conditions are required to be satisfied in order to mitigate this background. Two types of variables are used to quantify the energy of particles around the reconstructed electrons: the track isolation ($p_T^{\text{varcone0.2}}$, $p_T^{\text{varcone0.3}}$), and the calorimeter isolation energy ($E^{\text{cone0.2}}$). The track isolation $p_T^{\text{varcone0.2}}$ and $p_T^{\text{varcone0.3}}$ are defined as the sum of the transverse momenta of all the tracks around the candidate electrons in a cone with a variable radius dependant on the E_T , $R = \min\{0.2, 10 \text{ GeV}/E_T\}$, and $R = \min\{0.3, 10 \text{ GeV}/E_T\}$ correspondingly. The calorimeter isolation energy $E^{\text{cone0.2}}$ is defined as the sum of the transverse energies of all the calorimeter cells in a cone of size $R = 0.2$ around the candidate electron.

Based on the track isolation and calorimeter isolation variables, several isolation working points are defined within the ATLAS collaboration. Only the "FixedCutLoose" working point is used in the studies presented in Chapter 5. This working point requires $p_T^{\text{varcone0.3}}/p_T < 0.15$, and $E^{\text{cone0.2}} < p_T < 0.20$.

In the search for invisible Higgs boson decays in Chapter 5, we need to make a further differentiation between electrons coming from a Z or a W boson, and we define two categories, Signal and Veto electrons, based on the LH and isolation working points. The main definitions are given by:

- **W signal electron:** Must pass $p_T > 30$ GeV and the “TightLH” likelihood based identification criteria. Furthermore, “FixedCutLoose” isolation criteria with an efficiency of 95% for true electrons with $p_T > 25$ GeV and 99% for true electrons with $p_T > 60$ GeV are applied. For $p_T > 200$ GeV, the isolation is tightened to “FixedCutHighPtCaloOnly” due to large multijet contributions. A longitudinal impact parameter requirement of $|z_0 \sin(\theta)| < 0.5$ mm as well as a transverse impact parameter requirement of $|d_0|/\sigma(d_0) < 5$ is applied to ensure that the electron track is consistent with having originated at the primary vertex [115].
- **Z signal electron:** Must pass “LooseBLayer” likelihood based identification criteria. Furthermore, “FixedCutLoose” isolation criteria with an efficiency of 95% for true electrons with $p_T > 25$ GeV and 99% for true electrons with $p_T > 60$ GeV are applied. This is less pile-up dependant than the “Gradient” isolation. A longitudinal impact parameter requirement of $|z_0 \sin(\theta)| < 0.5$ mm as well as a transverse impact parameter requirement of $|d_0|/\sigma(d_0) < 5$ is applied to ensure that the electron track is consistent with having originated at the primary vertex [115].
- **Veto electron:** Must pass the “LooseBLayer” likelihood based identification criteria. No isolation nor impact parameter requirements are made.

3.4.5 Muons

In ATLAS, muons are reconstructed using information from the tracks in the Inner Detector, the Muon spectrometer, and also energy clusters in the calorimeter. Four types of muons are defined according to the sub-detector information, and the combination algorithms used in the reconstruction. These are defined as follows:

- **Combined** muons are defined from tracks reconstructed independently of the ID and the MS and combined in a global fit. In general, this category has the highest muon purity in comparison to the other definitions.
- **Segment-tagged** muons are defined with the ID tracks which are extrapolated to the MS. This category is mainly used in regions with limited muon spectrometer coverage when muons might cross only one layer of the MS.
- **Calorimeter-tagged** muons are defined by matching an ID track to a calorimeter energy deposit compatible with a minimum ionizing particle. This definition is optimized to enhance the acceptance in the region $|\eta| < 0.1$ which is not covered by the MS.
- **Extrapolated** muons are defined from MS tracks compatible with the interaction point. This definition extends the acceptance to the region $2.5 < |\eta| < 2.7$ which is not covered by the ID.

There are four muon identification working points defined within the ATLAS collaboration: Loose, Medium, Tight and High- p_T . The Loose and Medium working points are used in Chapter 5. These two categories are defined as follows:

- **Loose:** All muon types are included. This category maximizes the reconstruction efficiency while providing good quality muon tracks.

- **Medium:** Only combined and extrapolated muons are included. This category minimizes the systematic uncertainties on the muon reconstruction and calibration.

In addition, isolation requirements need to be fulfilled in order to reduce the background of muons originating from hadronic showers. The same variables as in the case of electrons are used to select isolated muons: $p_T^{\text{varcone0.3}}$ and $E^{\text{cone0.2}}$. These variables are defined in Section 3.4.4. Different working points are defined from different selection cuts on these two variables. Only one of these working points is used for the studies in this manuscript: FixedCutLoose (FCLoose) defined by $p_T^{\text{varcone0.3}}/p_T < 0.15$ and $E^{\text{cone0.2}}/p_T < 0.30$.

Different definitions are used in Chapter 5 for the muons produced by a W or a Z . Also, a different category is defined for Veto muons. The W and Z signal muons, and the Veto muons are defined as follows:

- **W signal muon:** Must pass $p_T > 30$, “Medium” track quality, and the “FCLoose” isolation criteria with an efficiency of 96% for true muons with $p_T > 25$ GeV and 99% for true muons with $p_T > 60$ GeV are applied. A longitudinal impact parameter requirement of $|z_0 \sin(\theta)| < 0.5$ mm as well as a transverse impact parameter requirement of $|d_0|/\sigma(d_0) < 3$ is applied to ensure that the muon track is consistent with having originated at the primary vertex [116].
- **Z signal muon:** Must pass “Loose” track quality, and the “FCLoose” isolation criteria with an efficiency of 96% for true muons with $p_T > 25$ GeV and 99% for true muons with $p_T > 60$ GeV are applied. A longitudinal impact parameter requirement of $|z_0 \sin(\theta)| < 0.5$ mm as well as a transverse impact parameter requirement of $|d_0|/\sigma(d_0) < 3$ is applied to ensure that the muon track is consistent with having originated at the primary vertex [116].
- **Veto muon:** No isolation, nor overlap removal, nor impact parameter requirements are made.

3.4.6 E_T^{miss}

Not all objects can be reconstructed in the ATLAS detector. For example, neutrinos escape the detector without interacting. Also, BSM particles would escape the detector without producing a signal. These invisible particles produce an imbalance in the measured transverse momentum of the visible objects. The E_T^{miss} is defined as the negative of the vectorial sum of the momentum of all visible objects: electrons, muons, photons, and jets, as well as tracks associated to the primary vertex but not matched to any object,

$$E_T^{\text{miss}} = - \sum_i \vec{p}_{Ti}, \quad (3.18)$$

where i runs over all visible objects. The vector defined in Equation 3.18 is called the missing transverse momentum while its magnitude is called missing transverse energy. The missing transverse momentum can be divided into two components, the hard component ($\vec{E}_T^{\text{miss,hard}}$) is the vectorial sum of all the reconstructed particles and jets in the event, and the soft component ($\vec{E}_T^{\text{miss,soft}}$) is the vectorial sum of all the tracks or topoclusters that cannot be matched to any physics object.

$$E_{\text{T}}^{\vec{\text{miss}}} = \vec{E}_{\text{T}}^{\text{miss,hard}} + \vec{E}_{\text{T}}^{\text{miss,soft}}. \quad (3.19)$$

Two different approaches are used in ATLAS to compute the soft term. The calorimeter soft term (CST) is defined from the calorimeter topoclusters that cannot be associated to any physics object. On the other hand, the track soft term (TST) is defined from the tracks matched to the primary vertex that are not matched to physics objects. In the studies presented in this manuscript the TST definition is used.

Several working points are defined in order to suit the needs of the different analyses. In Chapter 5 the Loose working point is used. This category requires jets with $p_{\text{T}} > 20$ GeV and $|\eta| < 4.5$. In addition, jets with $p_{\text{T}} < 60$ GeV and $|\eta| < 2.4$ are required to pass the Jet Vertex Tagger (JVT) [117] with a JVT score larger than 0.59.

A variable related to the $E_{\text{T}}^{\vec{\text{miss}}}$ is the missing hadronic activity defined as the absolute value of the negative vectorial sum of p_{T} of the hard scatter and pile-up jets:

$$E_{\text{T}}^{\text{jet,no-jvt}} = - \left| \sum_i \vec{p}_{\text{T}}^{\text{jet}_i} \right|, \quad (3.20)$$

where i runs over all jets in the event (hard scatter and pile-up).

3.4.7 Overlap removal

During the reconstruction, it is possible that an object meets the identification requirements of two different objects. This effect is called overlap and is especially prevalent in jets because they spread in a wide cone with many constituents. In order to determine the nature of the reconstructed object and to avoid double counting its energy, an overlap removal is employed. In particular, the overlap removal is important for the calculation of $E_{\text{T}}^{\vec{\text{miss}}}$ because different physical object are used in the computation of this variable.

Electrons almost always also fit the criteria for a jet, since the jet algorithms search for energy deposits in both calorimeters. When a jet's and an electron's angular direction coincide within $\Delta R = 0.2$, the electron is kept and the jet is removed. In contrast, if an electron is within $\Delta R = 0.4$ of a jet without fitting the jet criterion, the electron candidate is likely to be a charged hadronic object produced in the particle shower. In this case the jet is kept and the electron is discarded.

When a muon and a jet within $\Delta R = 0.4$ of each other are found, they are resolved in one of these two ways: If the jet has less than three associated tracks, it is removed and the muon is kept. If the jet has three or more associated tracks, the jet is kept and the muon is discarded.

3.5 Monte Carlo simulation

In order to test the SM or any beyond Standard Model, one needs to generate predictions that are directly comparable to the experimental data. This purpose is achieved with Monte Carlo simulations which are the link between the experiment and theory in high-energy particle physics. The simulation

process is a challenging activity within the ATLAS collaboration because of the complex physics environment and the computational necessities and limitations. Thus, it is also important to understand the limitations and uncertainties of the MC simulations. Section 3.5.1 introduces the process of Monte Carlo simulations. The simulated samples used in the analysis are described in Section 5.2.2.

3.5.1 MC simulation chain

Because of the complex and diverse physics processes involved in the pp collisions the MC simulation is performed in several steps that describe the different phenomena. First, the hard scattering is simulated at a fixed order perturbation theory. At this step it is important to describe the proton substructure via the Parton Distribution Functions (PDFs). The products of the collision decay forming a cascade of particles (particle shower) which are simulated in a second step using the colour string model [118] or other phenomenological models. The interactions of the partons that did not participate in the hard scattering (underlying event) is added to the event. Finally, the colour-charged partons are bound into colourless states using the string model [119] in the hadronisation processes. This simulation chain is illustrated in Figure 3.15. A complete description of the MC simulation techniques can be found in References [120–123].

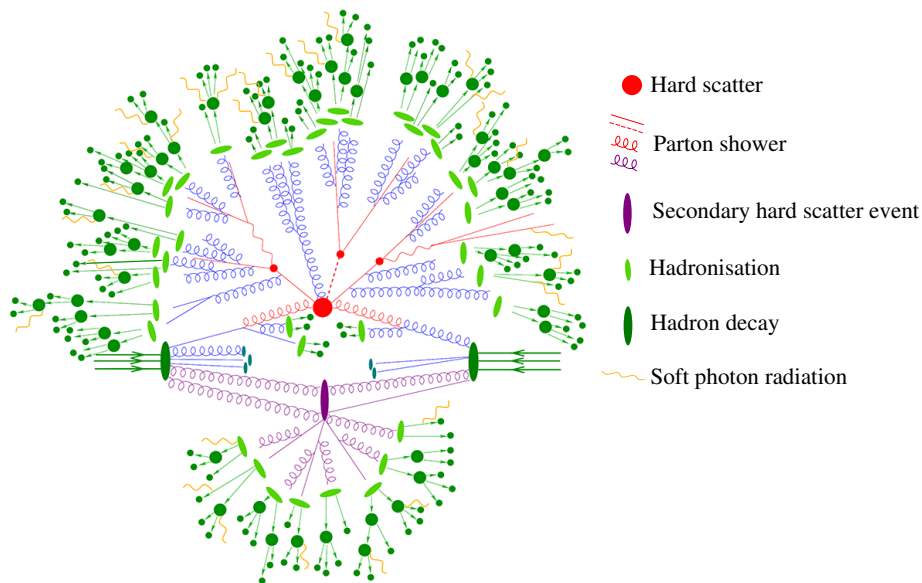


Figure 3.15: Illustration of the different processes occurring (and simulated) in a pp collision [122]. The hard scatter event is shown as a red blob in the center, the purple blob indicates a secondary hard scatter event, the red and purple tree structures represent the parton shower, the hadronisation processes are represented with green blobs and hadron decays with dark green blobs. Soft photon radiation is illustrated as yellow lines.

After the physics of the particle collision is ready we need to simulate the detector geometry and the interaction of the particles with the detector. There are two options for this purpose. The full simulation describes the detailed interaction of the particles with the detector material as they pass through. The other option is a fast simulation that makes use of parametrized models to describe the

response of the detector. The full simulation is in general more accurate, but it is highly computational consuming while the fast simulation can be two or three orders of magnitude faster. The nominal ATLAS simulation samples use the full simulation of the detector using `GEANT 4` [124]. The fast simulation is used as an alternative for some particular studies with the `AtlFast-II` software [125, 126]. In the last step, the simulated detector energy deposits are converted into a digital format (digitization) so that data and simulation are directly comparable.

Jet energy calibration

Jets are cones of particles produced by the hadronisation of quarks and gluons generated in the pp collision. At the ATLAS detector, jets are measured as energy deposits in the calorimeters and are reconstructed using the anti- k_t algorithm [110] with radius parameter $R = 0.4$ (or 1.0) (See Section 3.4.3). After the reconstruction, a Monte Carlo based calibration is applied followed by a data driven *in situ* calibration. The MC based calibration corrects the jet energy to the particle-level scale while the *in situ* calibration accounts for differences between data and simulation. The different steps of the MC based calibration are introduced in Sections 4.1 to 4.3, the *in situ* calibration is described in Section 4.4, and the author's developments on the pile-up correction are presented in Section 4.5.

The MC calibration starts removing the energy contributions from multiple proton-proton interactions in the bunch crossing. This is done in two steps: a subtraction based on the area of the jet, and a residual correction which is parametrized as a function of the number of reconstructed primary vertices (N_{PV}) and the mean number of interactions per bunch crossing (μ). Next, an MC based jet energy scale (JES) correction is applied. Afterwards, the global sequential calibration improves the resolution of the jet momenta and its uncertainties removing the dependence on several observables which are defined from the tracking, calorimeter, and muon chamber detector systems. Finally, an *in situ* calibration is needed to correct for the remaining differences between data and MC. This calibration is derived using well-measured reference objects such as photons, Z bosons, and calibrated jets. The ATLAS jet energy calibration chain is illustrated in Figure 4.1.

4.1 Pile-up correction

At the LHC Run 2, the proton-proton (pp) beam reached a center-of-mass energy of $\sqrt{s} = 13$ TeV, with an instantaneous luminosity peak of $21.4 \times 10^{33} \text{ cm}^{-2} \text{ s}^{-1}$, and an integrated luminosity of 148.5 fb^{-1} . Under these conditions, the mean number of pp collisions per bunch crossing (μ) is 34.2. The soft interactions, additional to the hard scattering, generate signals in the ATLAS calorimeters that overlap with those produced from the hard-scatter process. This contribution is known as in-time pile-up. In addition, the bunch crossing intervals of 25 ns introduce a sensitivity of the ATLAS calorimeter to signals produced in the collisions of surrounding bunch crossings. This contribution is named out-of-time pile-up. Because of the bipolar shape of the calorimeter response, in-time

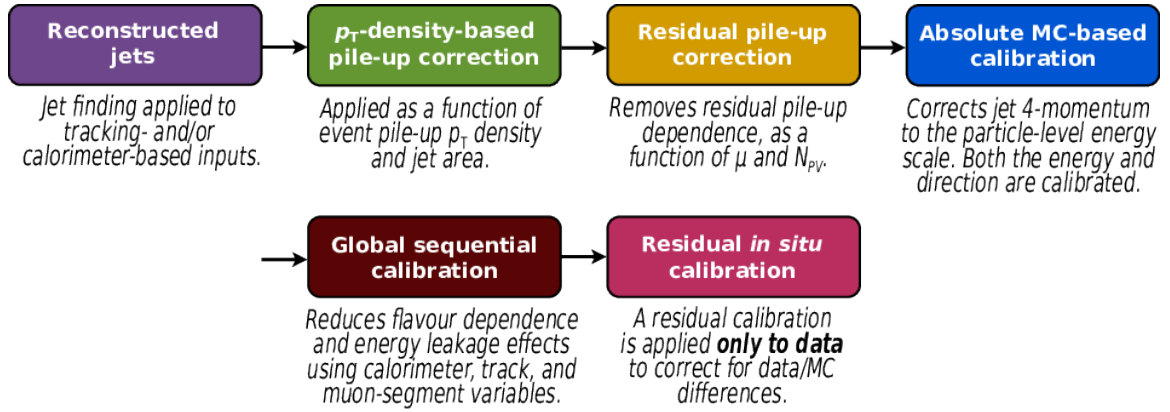
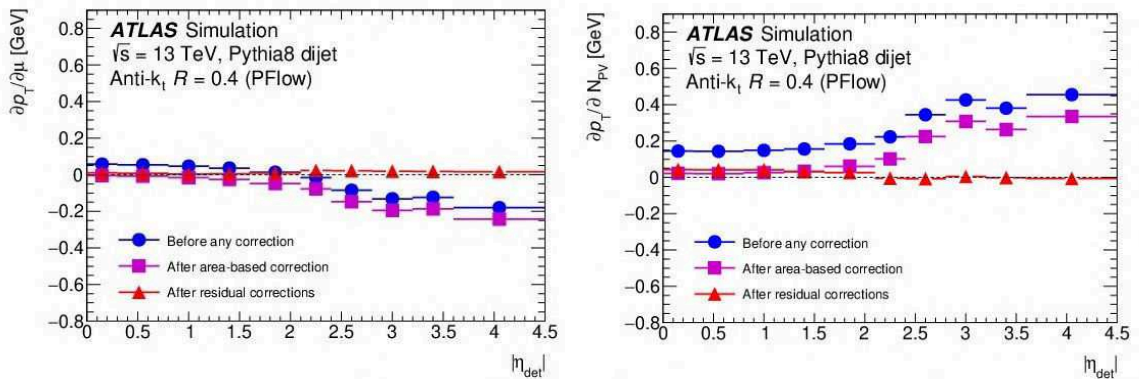


Figure 4.1: ATLAS jet energy calibration chain [127]

pile-up produces positive contributions to the measured energy of the jets while out-of-time pile-up contributes negatively. In order to remove the dependence of the reconstructed momentum of the jets on the pile-up conditions, an area-based correction is applied followed by a residual subtraction [128–130]. A comparison of the jet p_T dependence on μ and N_{PV} at three different stages of the jet calibration chain are shown in Figure 4.2: before the pile-up correction, after the area-based correction and after the residual correction. Detailed explanations of the area based correction and the residual subtraction are presented in Section 4.1.1 and Section 4.1.2, respectively.


 Figure 4.2: Jet transverse momentum dependence on μ (left) and N_{PV} (right) before the pile-up correction, after the area-based correction and after the residual correction [127]

4.1.1 Area based correction

The pile-up correction in the ATLAS jet calibration chain starts with an area based correction. The jet area is a measure of the susceptibility of the jet to pile-up. Assuming the pile-up as a uniform and diffuse background, the p_T median density (p_T/A) can be considered as an estimate of the pile-up

activity in the event. Thus, the pile-up contribution to the energy of the jet can be computed as the product of the jet area times the p_T median density.

The jet area is evaluated overlaying a dense, uniform population of neutral, infinitesimally soft ($p_T = O(10^{-100} \text{ GeV})$) ghost particles in the event. The jet area four-momentum is obtained summing over the four-momenta of the ghost constituents as:

$$A_j = \frac{1}{\nu_g < g_t >} \sum_{g_i \in j} g_i, \quad (4.1)$$

where $\nu_g < g_t >$ is the transverse momentum density of the ghosts. The transverse component of the area four-momentum is the area of the jet. Intuitively this area can be thought as the scalar obtained from counting the number of ghosts associated to a jet and dividing by the ghost number density. This definition provides a method to compute the area of any jet including non-circular ones.

The median p_T density in the event is defined as

$$\rho = \text{median} \left\{ \frac{p_{T,i}^{jet}}{A_i^{jet}} \right\}, \quad (4.2)$$

where the index i enumerates the jets found when clustering the event with the k_T algorithm [131, 132]. The use of the k_T algorithm is motivated by its sensitivity to soft radiation. No cut on the lower p_T is used in the calculation of ρ since the goal is to quantify the predominantly soft pile-up background.

4.1.2 Residual pile-up correction

After the area based correction, a residual correction is needed to remove the remaining pile-up dependence. The residual subtraction is a method to remove the PU contributions using the number of primary vertex (N_{PV}), as an estimator of in-time pile-up, and the mean number of interactions per bunch crossing (μ), as an estimator of out-of-time pile-up. These two corrections are applied following Equation 4.3.

$$p_T^{\text{corr}} = p_T^{\text{reco}} - \rho \times A - \partial p_T / \partial N_{PV} \times (N_{PV} - 1) - \partial p_T / \partial \mu \times \mu \quad (4.3)$$

The standard ATLAS residual correction is derived as follows. First, the average difference between the jet p_T after the area correction and the truth jet p_T ($\Delta p_T^{\text{area-truth}}$) is plotted as a function of N_{PV} in bins of μ , the truth scale jet transverse momentum (p_T^{truth}) and η . This distribution is fitted with a linear function and the slope of this function is taken as the dependence $\partial p_T / \partial N_{PV}$ per μ bin. These derivatives are plotted as a function of μ and averaged between bins. The value of the average derivative is taken as the p_T dependence on N_{PV} and depends on p_T^{truth} and η . The same procedure but exchanging N_{PV} by μ is done to compute the derivative $\partial p_T / \partial \mu$. From now this method would be referred as 1D correction in order to discriminate it from the new developments described in Section 4.5.

The derivatives $\partial p_T/\partial N_{PV}$ and $\partial p_T/\partial \mu$ are observed to have a logarithmic dependence on p_T^{truth} . Logarithmic fits are performed in the range $20 < p_T^{\text{truth}} < 200$ for each bin of η . In each η bin, the value of the logarithmic fit at 25 GeV is taken as the nominal correction. This is the p_T region where the pile-up effects are most relevant. The differences between the nominal pile-up dependence and the logarithmic fits over the p_T spectrum are taken as a p_T dependant systematic uncertainty in the residual pile-up dependence. Finally, a piecewise linear function is fitted over the per (η) bin values of $\partial p_T/\partial N_{PV}$ and $\partial p_T/\partial \mu$. This reduces the effect of statistical fluctuations and allows the correction to be continuous over the full η range.

This method has the disadvantage that no correlation between μ and N_{PV} is taken into consideration. Evidence of a clear correlation between these two variables is shown in Figure 4.3. Furthermore, the derivatives $\partial p_T/\partial \mu$ and $\partial p_T/\partial N_{PV}$ depend on the p_T of the jet. This led to a p_T dependant systematic uncertainty in the current precision recommendations. For this reason there is interest to develop a new method which subtracts the pile-up contribution as function of p_T , μ , N_{PV} , and η simultaneously. Section 4.5 shows the studies performed over different options to derive such a simultaneous correction.

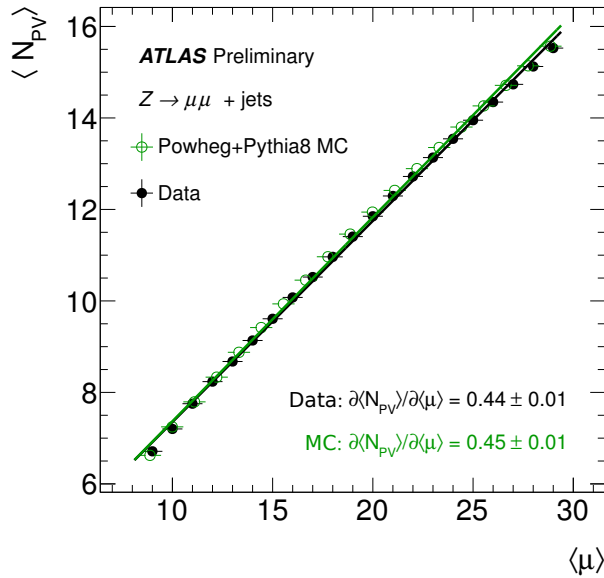


Figure 4.3: Mean number of primary vertices as a function of μ for Z+jets in data and MC [129].

4.2 Monte Carlo based Jet Energy Scale and η calibration

The Monte Carlo based Jet Energy Scale (JES) corrects the four momentum of the reconstructed jet to the particle-level scale while the η calibration corrects the direction of the jet. This way the jet four-momentum is compensated for the calorimeter response, energy losses in dead material, shower products outside the jet radius, and biases in the jet η reconstruction.

The JES is derived after the application of the pile-up correction as follows. The average jet energy response \mathcal{R} , defined as the mean of a Gaussian fit to the core of the $E^{\text{reco}}/E^{\text{truth}}$ distribution, is measured in bins of E^{truth} and η^{det} . The average response is fitted as a function of E^{reco} using the numerical inversion procedure described in [133]. Then, the jet calibration factor is taken as the inverse of the average energy response.

A bias in the reconstructed jet η is measured as a significant deviation from zero in the difference between the truth and the reconstructed jet ($\eta^{\text{reco}} - \eta^{\text{truth}}$). Such biases are larger when a jet covers two calorimeter regions with different geometry or technology with different energy responses. This causes a side of a jet to artificially increase its energy relative to the other side. The η calibration is derived as the difference $\eta^{\text{reco}} - \eta^{\text{truth}}$ parametrized as a function of E^{truth} and η^{det} . Then, a numerical inversion procedure is done to derive the corrections as a function of E^{reco} . This calibration alters the jet p_{T} and η , not the full four-momentum.

4.3 Global sequential calibration

After applying the MC JES, in a given $(p_{\text{T}}^{\text{truth}}, \eta^{\text{det}})$ bin, the jet response can vary from jet to jet depending on their flavour and energy distribution of the constituent particles, their transverse distribution, and the variations of the jet dynamics in the detector. Moreover, the jet particle composition and shape depend on the initiating particles (quarks or a gluons). These per jet variations enlarge the jet resolution ($\sigma_{\mathcal{R}}$) given by the standard deviation of a Gaussian fit to the jet p_{T} response distribution. To improve the resolution, a global sequential calibration (GSC) is applied based on observables computed from information of the jet development in the calorimeter.

The global sequential calibration (GSC), is a series of corrections to mitigate the effect of the per jet fluctuations on the jet response. The GSC is based on observables such as the longitudinal structure of the energy depositions within the calorimeters, tracking information associated with the jet, and information related to the activity in the muon chambers behind a jet. For each observable, a four-momentum correction is derived as a function of $p_{\text{T}}^{\text{truth}}$ and η^{det} by inverting the reconstructed jet response in MC events. The GSC improves the jet p_{T} resolution ($\sigma_{\mathcal{R}}$) and associated uncertainties by applying these independent corrections sequentially to the jet four-momentum.

4.4 *In situ* calibration

The last step in the calibration chain is an *in situ* correction to cover the differences between data and MC simulation caused by mismodelling of the detector materials, and the physics processes. The *in situ* correction is derived by balancing the p_{T} of a target jet against other well-measured reference objects, such as a photon, a Z boson or a collection of well-calibrated jets. The *in situ* jet response is defined as the average ratio between the jet p_{T} and the reference object p_{T} . The calibration is taken from the double ratio between the *in situ* response in data and in MC as defined in Equation 4.4 and is transformed from a function of reference object p_{T} to a function of the jet p_{T} using a numerical inversion.

$$c = \frac{R_{in\ situ}^{data}}{R_{in\ situ}^{MC}} \quad (4.4)$$

There are three steps of the *in situ* calibration. First, the η intercalibration corrects the energy scale of forward jets ($0.8 < |\eta| < 4.5$) to match those of central jets ($|\eta| < 0.8$) using the p_T balance in dijet events. Second, the hadronic recoil in an event is balanced against the p_T of a calibrated Z boson or photon. Finally, the multijet balance uses a system of well calibrated low p_T jets to calibrate a single high p_T jet.

4.4.1 η intercalibration

To compensate for the different jet response in the central and forward regions of the detector, forward jets ($0.8 < |\eta| < 4.5$) are balanced against central jets in a dijet system. Dijet topologies with exactly two jets back to back in ϕ are selected. In these topologies the imbalance between the central and forward region can be attributed to detector effects. A detailed description of the method can be found in Ref. [127].

4.4.2 Z+jets and γ +jets calibration

In this step the hadronic activity in the event is balanced with the p_T of a well-calibrated photon or Z boson. This calibration relies on the energy of the photon or electrons and muons from the Z decay to be well measured. These three objects are well understood in the ATLAS experiment and they have small uncertainties associated to their energy scale [116, 134]. The Z/γ +jet correction is derived in the central region ($|\eta| < 0.8$). Since this is computed after the η intercalibration, it can be applied in the full acceptance of the ATLAS detector. Using the Z +jet and γ +jet methods it is possible to calibrate jets with a p_T up to 1 TeV and 1.2 TeV, respectively. A detailed description of the method can be found in Ref. [127].

4.4.3 Multijet balance

The final step of the *in situ* correction is to calibrate hard jets with a p_T above the range of the Z/γ +jet correction. In the multijet balance, events are selected with a single high- p_T jet balanced against a system of lower- p_T jets (the recoil system). The jets in the recoil system are calibrated up to the Z/γ +jet correction ensuring that these are well-calibrated. The leading jet is left at the scale of the η intercalibration. The response of the system is defined as the average ratio between the p_T of the leading jet and the p_T of the recoil system. The correction is then derived mapping this response as a function of the uncalibrated leading jet p_T . A detailed description of the method can be found in Ref. [127].

4.5 New developments on the Pile-up correction

The method for the residual correction described in Section 4.1.2 has the disadvantage that no correlation between μ and N_{PV} is taken into consideration. Furthermore, the derivatives $\partial p_T / \partial \mu$ and

$\partial p_T / \partial N_{PV}$ depend on the p_T^{truth} of the jet. This led to a p_T^{truth} dependant systematic uncertainty in the current ATLAS precision recommendations. An example of the $\partial p_T / \partial \mu$ and $\partial p_T / \partial N_{PV}$ dependence on p_T^{truth} are shown in Figure 4.5. The developments for an updated method which subtracts the pile-up contribution as function of p_T , μ , N_{PV} , and η simultaneously are summarised in this section.

The idea behind the new residual pile-up correction is illustrated in Figure 4.4. The truth level jet p_T (p_T^{truth}) can be used as a reference to compute a simultaneous correction dependant on N_{PV} , μ , η and p_T^{reco} . In a given $(p_T^{\text{truth}}, \eta^{\text{truth}})$ bin, the jet p_T after the area based correction (p_T^{area}) corresponding to different N_{PV} , μ bins are shifted to the truth scale as a common reference. Then they can be shifted back to a pile-up scale in a second step. Different options were tested using the truth level as the final scale after the residual pile-up correction as well as shifting the jet p_T back to pile-up scales defined in different ways. Also, a different approach which does not use the truth scale as reference was tested. The pros and cons of these different methods are summarised in Sections 4.5.2 to 4.5.5. Additionally, a comparison of the pile-up dependence using different definitions of ρ is presented in Section 4.5.1, and a method for removing the out-of-time pile-up at the jet constituents level is shown in Section 4.5.6.

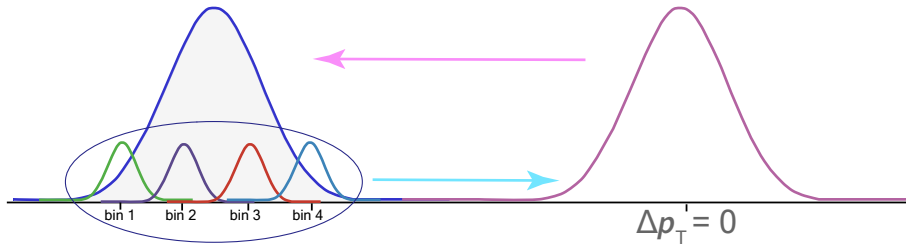


Figure 4.4: Illustration of the residual calibration. In a given $(p_T^{\text{truth}}, \eta^{\text{truth}})$ bin, the p_T of the jets corresponding to different N_{PV} , μ bins are shifted to the truth scale as a common reference, and they can be shifted back to a pile-up scale in a second step.

4.5.1 Comparison of p_T median density definitions

The p_T median density ρ used to be defined from the same objects as the PFlow jets. These PFlow objects are chosen such that they point to the primary vertex. As a consequence, ρ depends on the topology of the hard scatter. The systematic uncertainty associated to this dependence is one of the dominants at low jet p_T where the pile-up corrections are larger. The different components of the jet energy scale systematic uncertainty are shown in Figure 4.6. The uncertainty from the topology dependence and the residual pile-up dependence are added in quadrature and are shown as the pile-up component.

One way to remove the ρ topology dependence is to change the definition of ρ . Instead of using the PFlow objects, ρ can be computed from a side band $2 < |z_0 \sin \theta| < 4$ mm around the primary vertex. Following the implementation of the new ρ pile-up side band (ρ^{PUSB}) definition, the performance of the pile-up correction using the two definitions was tested. The pile-up dependence after the residual correction is shown in Figure 4.7. It can be observed that the change in the definition of ρ does

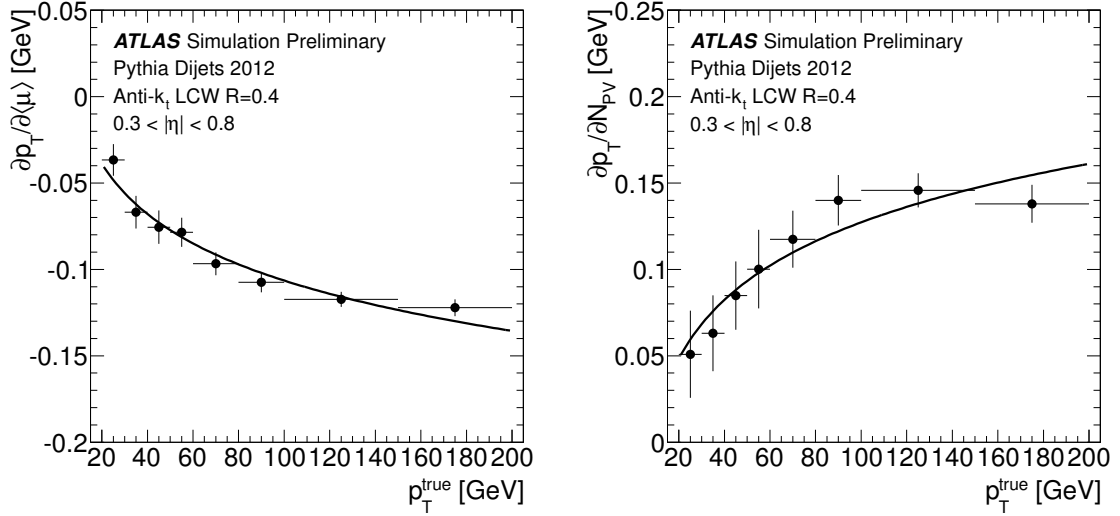


Figure 4.5: $\partial p_T/\partial\mu$ and $\partial p_T/\partial N_{PV}$ dependence on p_T^{truth} after the pile-up correction [127].

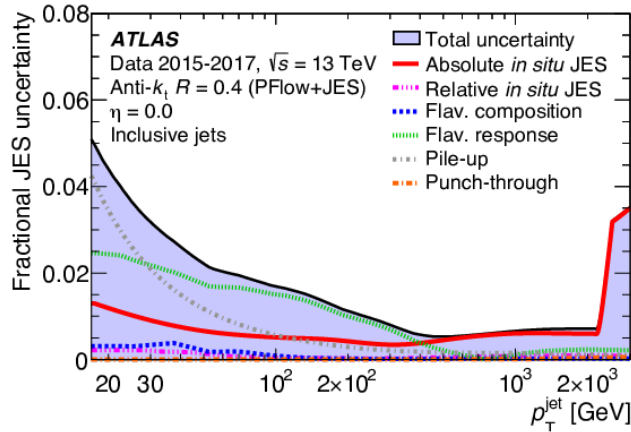


Figure 4.6: Fractional jet energy scale systematic uncertainty components for $R=0.4$ jets as a function of η at $p_T = 60$ GeV, reconstructed from particle-flow objects. The total uncertainty, determined as the quadrature sum of all components, is shown as a filled region topped by a solid black line. Flavour-dependant components shown here assume a dijet flavour composition. Taken from [127].

not affect the pile-up dependence after the pile-up correction. On the other hand, it has been tested that the change in the ρ definition reduces the event topology uncertainty by a factor of ~ 2 , making ρ^{PUSB} the best choice to use. This change of the ρ definition will be implemented in the simulated samples used across the ATLAS collaboration in the next update of the ATLAS reconstruction software.

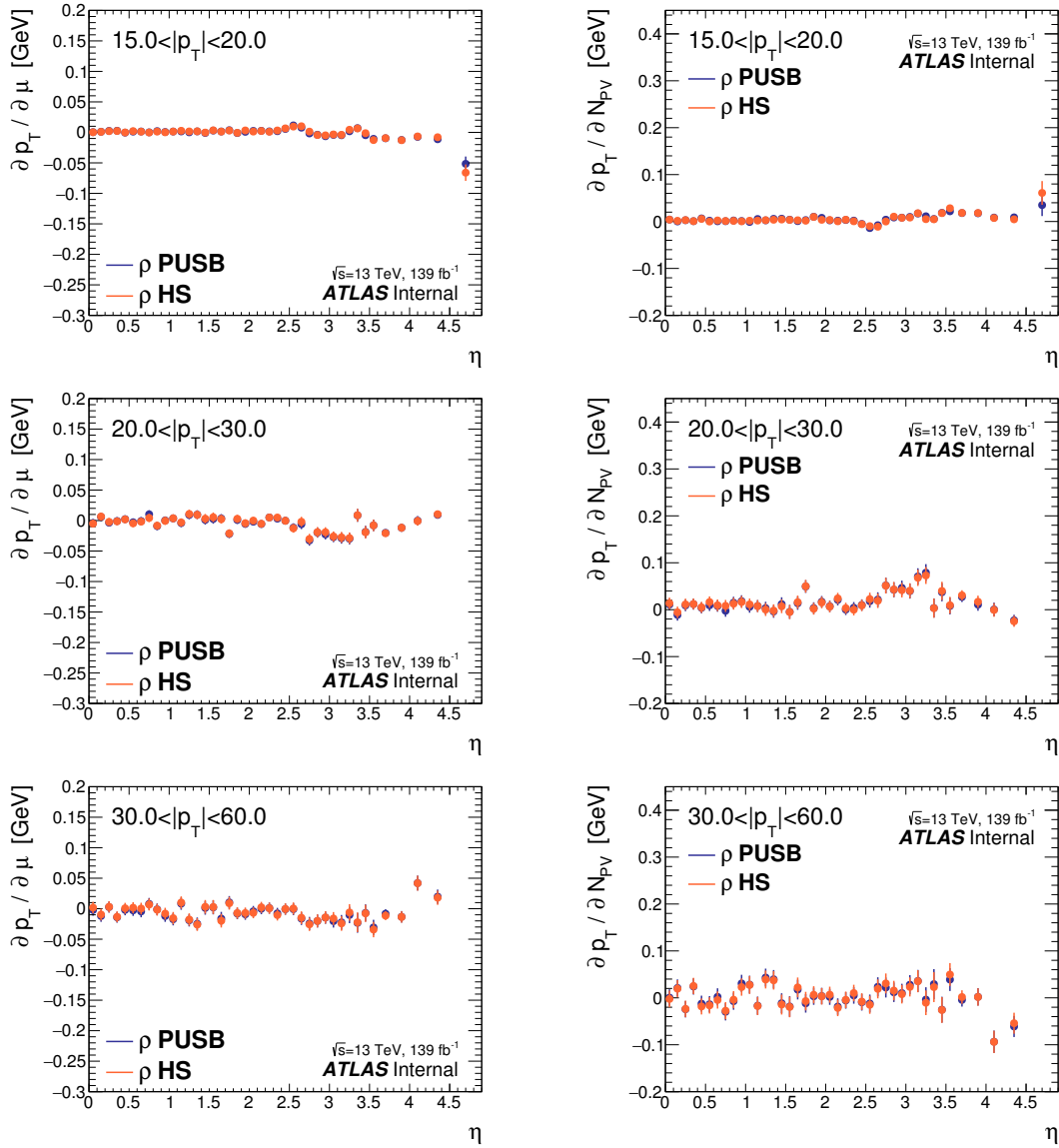


Figure 4.7: Comparison of the pile-up dependence after the residual correction between the old and the new ρ definition. It can be seen that the two definitions produce compatible results in terms of pile-up dependence.

4.5.2 Residual correction first step: energy correction to truth scale

As a first step of the correction, the p_T^{truth} is used as a reference to compute a correction given by the average difference between the p_T^{area} and p_T^{truth} ($\Delta p_T^{\text{area-truth}}$). This average difference, $\Delta p_T^{\text{area-truth}}$, is fitted as a function of p_T^{area} using a linear plus logarithmic function, in bins of N_{PV} , μ , and η^{truth} . The jet transverse momentum after the correction (p_T^{calib}) is given by Equation 4.5. At this stage the jet p_T is moved from the pile-up scale to the truth scale.

$$p_T^{\text{calib}} := p_T^{3\text{D}} = p_T^{\text{reco}} - \rho \times A - \Delta p_T^{\text{area-truth}}(N_{\text{PV}}, \mu, \eta, p_T^{\text{area}}) \quad (4.5)$$

This correction removes the pile-up dependence and is stable as function of p_T^{truth} as can be observed in Figure 4.8 (option 1). On the other hand, by construction, the pile-up correction changes the jet energy scale. There is a dedicated energy scale correction applied in the next step of the calibration chain. This motivates the study of adding a second term to the correction which moves the p_T of the jets back to the pile-up scale. Different definitions for this second term were tested and are described in Section 4.5.3 and Section 4.5.4.

4.5.3 Inclusive N_{PV}, μ pile-up scale

One option to define the second term of the residual correction is to shift back the p_T of the jets by the average difference $\Delta p_T^{\text{area-truth}}$ as a function of p_T^{truth} , but inclusive in N_{PV} and μ . This dependence is fitted with a linear function and the correction is obtained evaluating these linear functions on the $p_T^{3\text{D}}$ after applying the first term of the correction. The jet p_T after calibration is given by Equation 4.6. It can be observed in Figure 4.8 (option 2) that adding this second term does not affect jet p_T dependence on the pile-up.

$$p_T^{\text{calib}} = p_T^{\text{reco}} - \rho \times A - \Delta p_T^{\text{area-truth}}(N_{\text{PV}}, \mu, \eta, p_T^{\text{area}}) + \Delta p_T^{\text{area-truth}}(\eta, p_T^{3\text{D}}) \quad (4.6)$$

On the other hand, adding and subtracting large amounts of p_T can produce large tails in the p_T spectrum, generating jets with negative momentum. A comparison of the p_T distributions in the forward region ($\eta > 2.5$) at low p_T^{truth} ($15 < p_T^{\text{truth}} < 30$ GeV) for the different calibration options is shown in Figure 4.9. It can be observed that for a p_T^{truth} between 15 and 20 GeV, a large fraction of jets with negative p_T^{calib} is present, giving conceptual challenges to the calibration.

4.5.4 Average N_{PV}, μ pile-up scale

A second option to recover the pile-up scale is to use the average $\langle N_{\text{PV}} \rangle, \langle \mu \rangle$ as reference. In this case, for a given η bin, the correction is given by the difference between the average $\langle p_T^{\text{area}} \rangle$ and the p_T^{truth} , where $\langle p_T^{\text{area}} \rangle$ is evaluated at $\langle N_{\text{PV}} \rangle$ and $\langle \mu \rangle$. For this definition, the same fits derived for the first term of the correction can be used. The jet p_T after this correction is defined in Equation 4.7.

$$p_T^{\text{calib}} = p_T^{\text{reco}} - \rho \times A - \Delta p_T^{\text{area-truth}}(N_{\text{PV}}, \mu, \eta, p_T^{\text{area}}) + \Delta p_T^{\text{area-truth}}(\langle N_{\text{PV}} \rangle, \langle \mu \rangle, \eta, p_T^{\text{area}}) \quad (4.7)$$

Figure 4.8 (option 3) shows that this option does not perform as good as the other two methods. When adding a correction which is constant over N_{PV}, μ but varies with p_T^{area} , some pile-up dependence is introduced. The same effect has been reported when applying the MC jet energy scale correction.

A comparison of the performance of the different tested corrections is shown in Figure 4.8. The inclusive N_{PV}, μ method subtracts the pile-up dependence, but the shift back to the pile-up scale

produces long tails in the jet p_T^{calib} spectrum causing a significant fraction of jets with negative p_T^{calib} in the forward region. The average $\langle N_{\text{PV}} \rangle$, $\langle \mu \rangle$ method reduces the amount of jets with negative p_T^{calib} but the pile-up mitigation is not as good as the other options. Applying only the first term of the correction does not produce jets with negative p_T (by construction), and the pile-up mitigation is as good as the inclusive pile-up option. The MC JES after applying this correction was studied and no objections were found for this method. Therefore, this was defined as the new residual pile-up correction. This correction is then propagated to the next steps of the jet calibration chain.

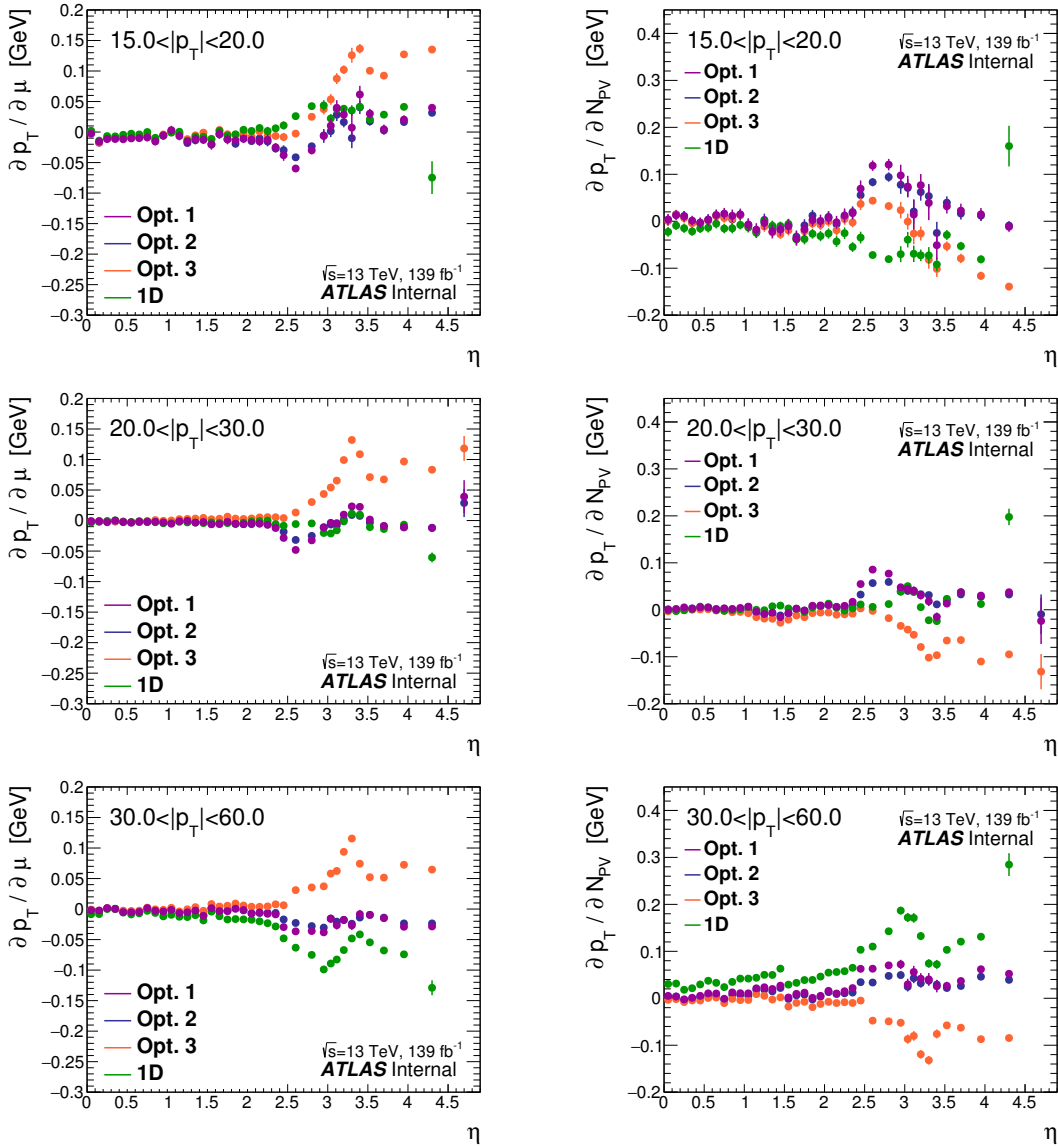


Figure 4.8: Dependence of p_T on μ (left) and N_{PV} (right) after the different residual corrections. In the legend, option 1 corresponds to the first term of the correction, option 2 corresponds to the inclusive N_{PV} , μ method, and option 3 is the $\langle \mu \rangle$, $\langle N_{\text{PV}} \rangle$ method. The previous method described in Section 4.1 is labeled as 1D.

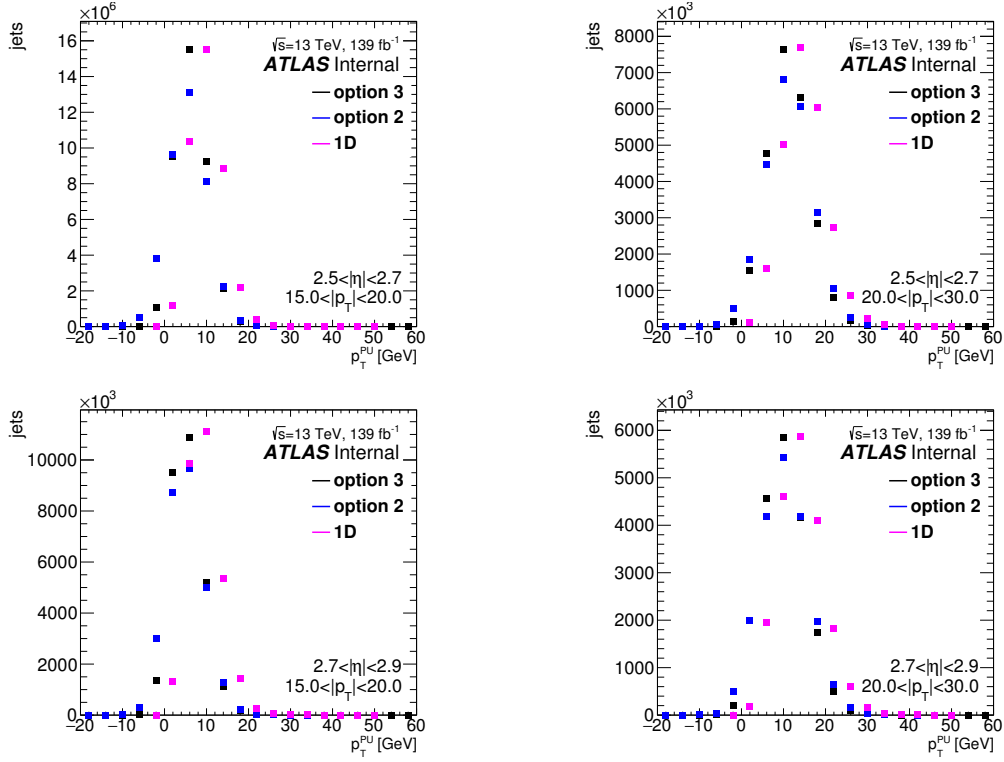


Figure 4.9: Examples of p_T^{calib} distribution in the forward region. Option 0 shows a large amount of jets with negative p_T^{calib} . Option 4 has less amount of jet with negative p_T^{calib} . 1D correction does not have jets with negative p_T^{calib}

4.5.5 Alternative approach: Average pile-up scale after area correction

Another approach to avoid adding and subtracting large amounts of momentum, is to use the p_T^{area} evaluated at the average N_{PV} and μ as reference instead of p_T^{truth} . For a jet in an event, the correction would be given by the difference between the p_T^{area} evaluated in the corresponding N_{PV} , μ , and the p_T^{area} evaluated at the average N_{PV} and average μ , as defined in Equation 4.8. This approach was tested but due to statistical limitations and difficulties in modelling the behavior of the correction as a function of p_T^{area} it was decided not to proceed with this approach.

$$p_T^{\text{calib}} = p_T^{\text{reco}} - \rho \times A + (\langle p_T^{\text{area}}(\eta^{\text{truth}}, N_{\text{PV}}, \mu) \rangle - \langle p_T^{\text{area}}(\eta^{\text{truth}}, \langle N_{\text{PV}} \rangle, \langle \mu \rangle) \rangle) \quad (4.8)$$

4.5.6 Study of the residual pile-up correction in EMTopo jets with a cell-time cut

A different method to remove the out-of-time pile-up is to apply a timing cut at the calorimeter cell level. This time cut would remove the energy contributions from interactions in the surrounding bunches. An example of the distribution of the calorimeter energy deposits over time is shown in Figure 4.10. It can be observed that applying a timing cut would remove the contributions from

out-of-time pile-up.

Simulated EMTopo dijet samples were produced in three different variations: the nominal ones without any timing cut (TimeCutNone), and two different versions with a time cut $|t| > 12.5$ ns. One called TimeCutSeed in which the cells failing the cut are prevented from being the cluster seed but they are allowed to be included in the cluster, and a second one called TimeCutSeedExtended where the cells failing the cut are forbidden from entering the cluster at any level.

The pile-up dependence in jets at the constituent scale is shown in Figure 4.11. It can be observed how the dependence on μ is reduced in the samples with the time cut applied. In the central region the dependence is reduced by a factor of 2 for the TimeCutSeedExtended case. 1D Pile-up corrections were derived and applied to each of these three variations correspondingly. The pile-up dependence after the area-based correction and the residual correction are shown in Figure 4.12 and Figure 4.13, respectively. It can be observed that the pile-up dependence after the residual correction is compatible between the three cases. Hence, a time cut is not necessary at the reconstruction level since the pile-up correction will remove the out-of-time pile-up dependence.

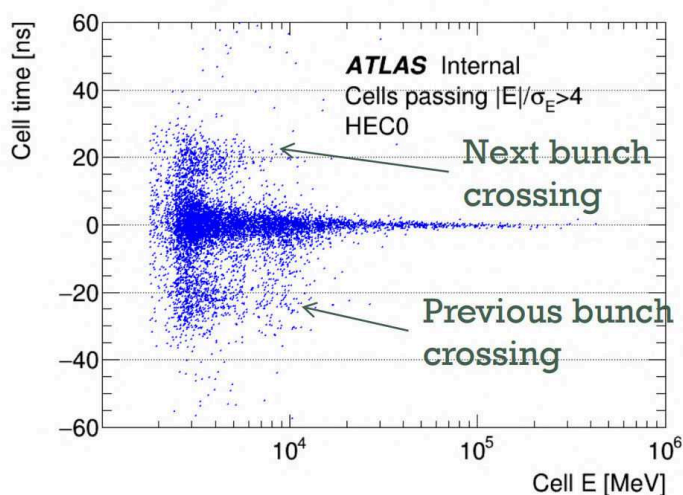


Figure 4.10: Distribution of the calorimeter energy deposits in time. It can be observed that applying a timing cut would remove the contributions from out-of-time pile-up.

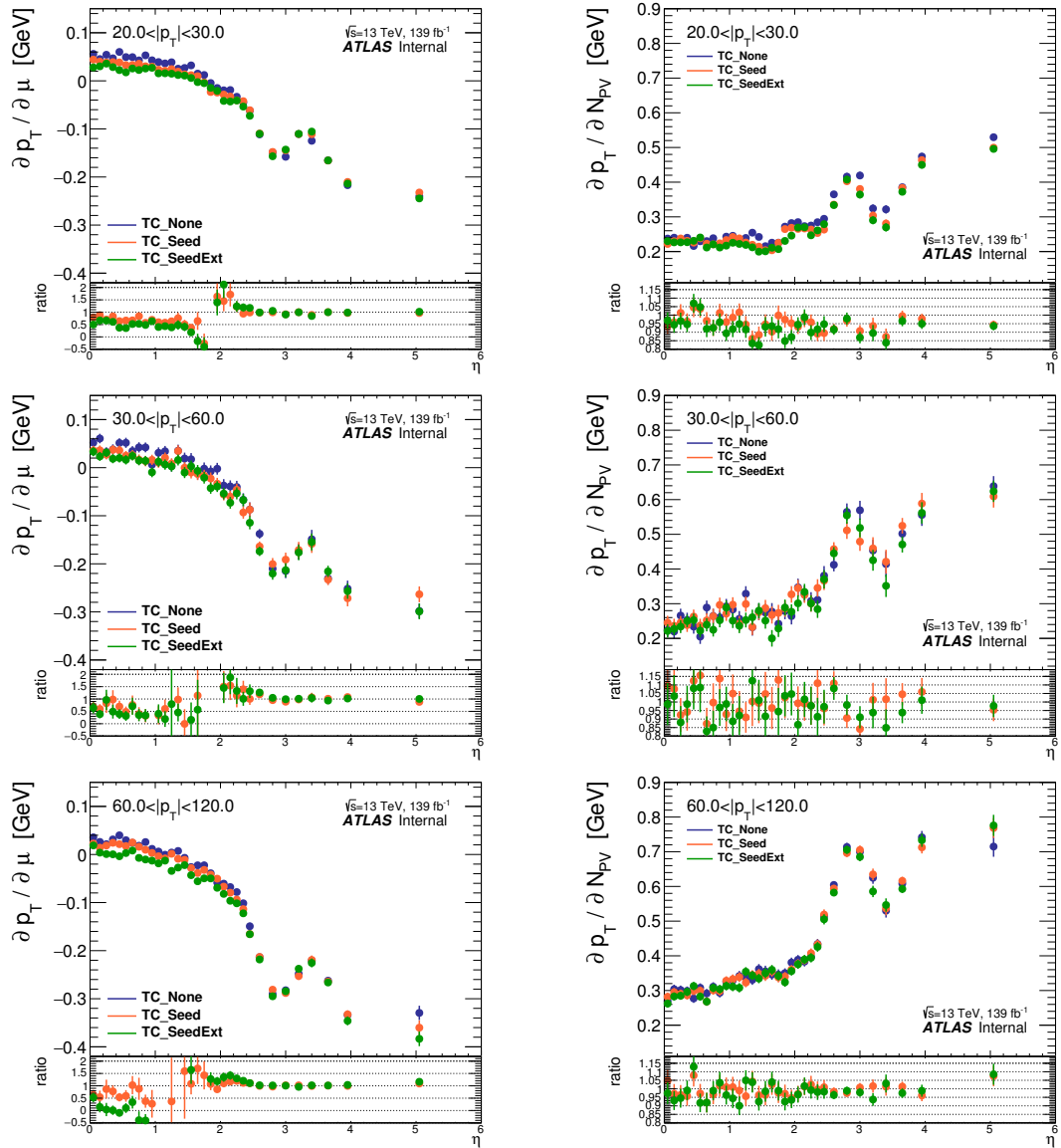


Figure 4.11: Pile-up dependence before any pile-up correction in the different time cut variations.

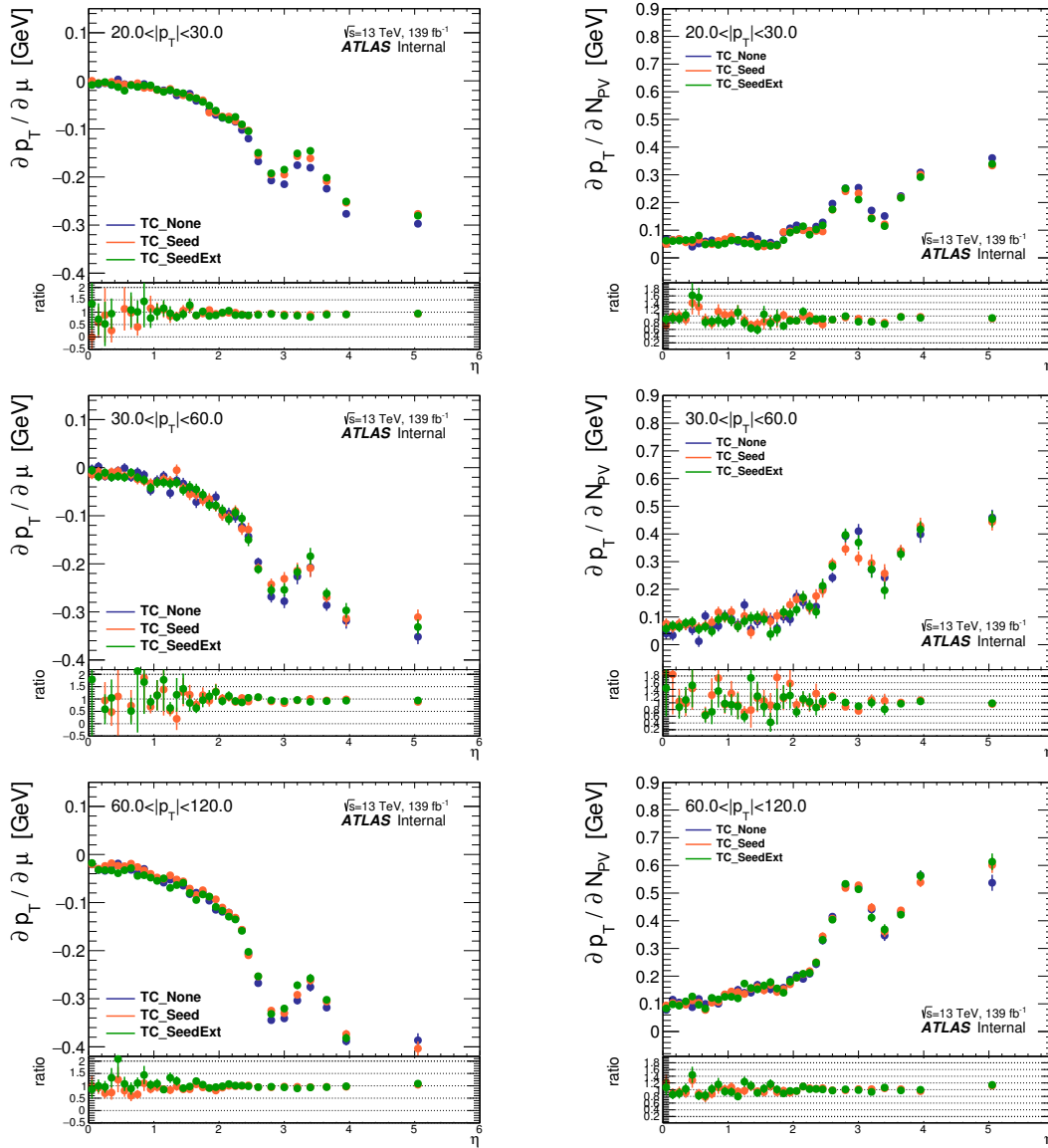


Figure 4.12: Pile-up dependence after area-based correction in the different time cut variations.

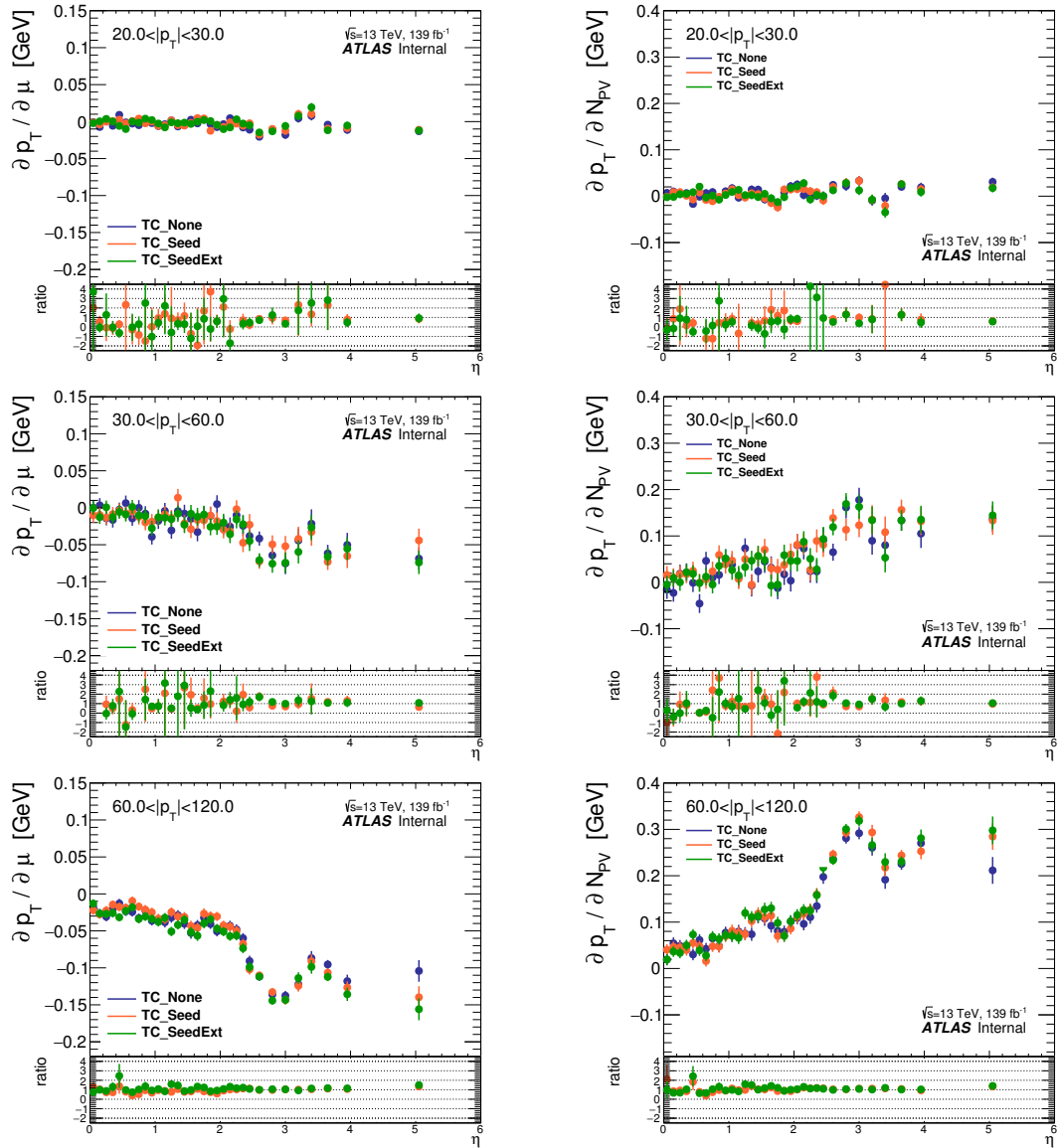


Figure 4.13: Pile-up dependence after residual pile-up correction in the different time cut variations.

Analysis strategy

This chapter presents the strategy search for invisible Higgs boson decays. Section 5.1 provides a general description of the project. Section 5.2 describes the data and simulation used, and the event selection is detailed in Section 5.3. The background estimates are summarised in Chapter 6. The treatment of systematic uncertainties is presented in Chapter 7, the description of the statistical treatment and the likelihood fit and the final results are presented in Chapter 8.

5.1 Introduction

As discussed in Section 2.3, there is astrophysical evidence that most of the matter in the Universe is present in a form that does not have electromagnetic interactions called dark matter. On the other hand, there is no suitable candidate for DM in the Standard model. Thus, an extension to the SM is needed in order to explain the nature of dark matter. If DM is made of particles, one possibility is that it interacts with the Higgs boson as described in Section 2.6.1. At the LHC, it is possible to search for this kind of matter through the momentum imbalance that they would produce. This note presents a search for invisible decays of a Higgs boson produced principally via the Vector Boson Fusion (VBF) mechanism.

A precise measurement of the branching ratio of invisible Higgs boson decays (\mathcal{B}_{inv}) would allow us to directly compare with the standard model prediction. A branching ratio higher than the SM prediction would point to BSM physics. However, this branching ratio for invisible decays of the Higgs boson has not been established yet with a high level of precision. The SM \mathcal{B}_{inv} on invisible decays of the Higgs boson is 0.12% while a previous round of publications from the ATLAS and CMS collaborations have reported observed (expected) upper limits on this branching ratio of 0.26 (0.17) [135] and 0.19 (0.15) [136] respectively. The latest and most sensitive result from the CMS collaboration is an observed upper limit of 18% while 10% was expected [23].

The VBF Higgs production mode is the most sensitive channel for this measurement, and consequently it is the main channel used in this analysis. There is also a sizable contribution from ggF to the signal region considered. No interference between these two production modes is considered. The Feynman diagram for the VBF production mode is shown in Figure 5.1.

At the LHC Run 2, an increased sensitivity to these invisible decays is expected but also we

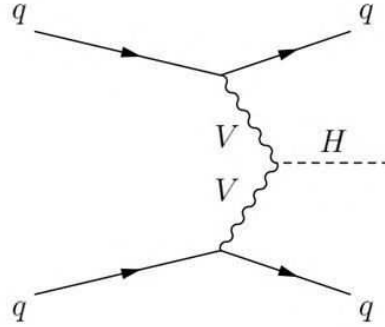
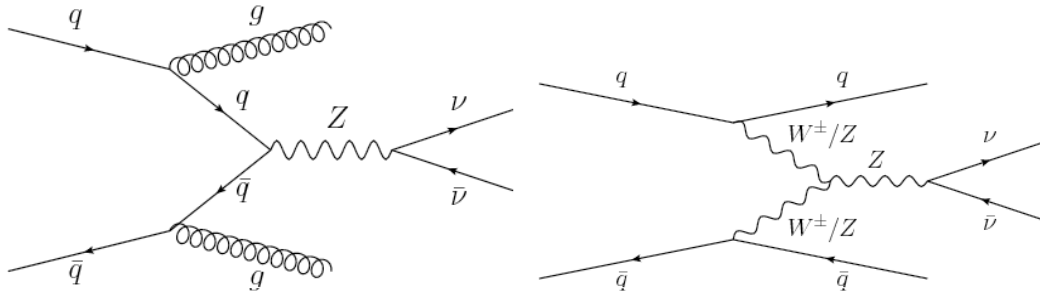


Figure 5.1: Higgs production via Vector-Boson Fusion.

face some limitations. Higher pile-up conditions, increased multijet background and challenges in the understanding of the systematic uncertainties are also expected. The analysis exploits the VBF topology in order to maximize the signal vs background rejection. In the VBF Higgs production mode, two jets with a large transverse momentum and a wide separation in $\Delta\eta_{jj}$ are expected. In addition, the search for invisible decays motivates a selection requirement on the E_T^{miss} . The missing transverse momentum should recoil against the VBF jets, this motivates a requirement on the azimuthal angular distance between the two leading jets $\Delta\phi_{jj}$. In this phase space, the main backgrounds are $Z \rightarrow \nu\nu$ and $W \rightarrow \ell\nu$ where the charged lepton is lost. Example Feynman diagrams for the $Z \rightarrow \nu\nu$ background are shown in Figure 5.2. Events with a single weak boson production in association with jets will be denoted as $V + \text{jets}$.


 Figure 5.2: Example Feynman diagrams for the $Z \rightarrow \nu\nu$ background in the signal region from (left) strong production of order α_{EWK}^2 and (right) electroweak production of order α_{EWK}^4 .

The $V + \text{jets}$ background is modelled using MC simulation. To reduce the impact of systematic uncertainties, we use the transfer factor (TF) method. In this approach, a $Z \rightarrow \ell\ell$ control region (CR) is used to constrain the $Z \rightarrow \nu\nu$ background. Similarly, a $W \rightarrow \ell\nu$ CR where the charged lepton is reconstructed is used to constrain the $W \rightarrow \ell\nu$ background with the lepton being lost. There is a small but significant contribution from QCD multijet events. Due to difficulties in estimating this background and the large uncertainties associated to it, a data driven (pile-up control region) and a Rebalance and Smear methods are used. In addition, data driven methods were developed to estimate a background component in the W CRs where a jet is misidentified as a lepton.

The upper limit on the branching ratio of invisible decays of the Higgs boson is computed using a maximum likelihood fit. The limit is set at 95% confidence level (CL) using asymptotic formulae for a CLs frequentist approach [137–139]. The likelihood function is constructed from the observed events in data, the yields of signal and backgrounds taken from their individual estimates and scaled by free parameters, and nuisance parameters to account for statistical, and systematic uncertainties. We assume the SM Higgs boson production cross section, but no other dependence on other Higgs boson decay BRs.

5.2 Data and simulation

5.2.1 Dataset and triggers

The analysis is performed using ATLAS data collected in 2015-2018 when the LHC delivered pp collisions at $\sqrt{s} = 13$ TeV. The total integrated luminosity is 147 fb^{-1} . Only events recorded during stable beam conditions and with all ATLAS sub-systems fully operating are considered. The total integrated luminosity good for physics is 139 fb^{-1} with an uncertainty of 1.7%.

Events are required to have a primary vertex with at least two associated tracks. The primary vertex is defined as the vertex with the largest $\sum p_T^2$, where the sum is over all tracks with transverse momentum $p_T > 0.4$ GeV that are associated with the vertex.

The data used for this analysis have been recorded using several event triggers. The SR data is collected using E_T^{miss} triggers [140]. The HLT thresholds were raised several times during the Run 2 data taking to reduce the trigger rate because this rate increases with the number of pile-up interactions. In 2015 these thresholds were 70 GeV, and they increased to 110 GeV in 2017-2018. E_T^{miss} triggers are not fully efficient for $E_T^{\text{miss}} < 200$ GeV, a set of trigger scale factors are applied as a function of the offline E_T^{miss} when the data and MC turn on functions do not agree. The transfer factors are computed as the ratio between the trigger efficiency in data and MC for each data taking period individually, and it is fitted with the functional form:

$$t_s = \frac{1}{2} \cdot \left[1 + \text{erf}\left(\frac{x - p_0}{p_1 \sqrt{2}}\right) \right], \quad (5.1)$$

where p_0 and p_1 are floating parameters in the fit, x corresponds to the offline E_T^{miss} and erf is the error function.

The data for the W and Z control regions was recorded with the unrescaled single and dilepton triggers that have the lowest p_T thresholds [141, 142]. The thresholds for single lepton triggers vary from 20 to 26 GeV for the tightest lepton identification working point. For dilepton triggers, the thresholds are usually lower with a looser identification working point. E_T^{miss} triggers are also used in the muon control regions in order to enhance the muon efficiency. These triggers reject events based on the momentum imbalance in the calorimeter energy deposits. Muons do not shower in the calorimeter and thus behave similar to invisible particles at this level. The rebalance and smear multijet estimate uses jet triggered events with thresholds on jet p_T ranging from 15 GeV up to ~ 400 GeV [143]. These

Process	cross section (pb)
VBF	3.782
ggF	48.58

Table 5.1: Inclusive cross section for the production of the Higgs boson. Taken from the LHC Higgs Yellow Report [144].

events are unrescaled to recover a smooth jet p_T spectrum.

The complete list of used triggers can be found in Appendix A. In order to avoid bias from the analysis team, a blind analysis strategy is followed. Data in regions with more than 20% of signal-to-background ratio was blinded until the analysis strategy was frozen, and the collaboration approved the unblinding of data.

5.2.2 Simulation

Signal MC samples

The invisible Higgs boson decay signal can be produced via gluon-gluon fusion (ggF) or Vector Boson fusion (VBF). Both of these processes are simulated using POWHEG interfaced with PYTHIA8 for hadronisation and showering. The simulation is generated at a Higgs boson mass of 125 GeV and the calculations are done up to NLO in α_S . The invisible Higgs boson decay is generated by forcing the Higgs boson to decay into two Z bosons, which are then forced to decay into neutrinos. The Higgs boson production cross section [21, 144] is shown in Table 5.1. In addition, VBF samples with heavier Higgs masses were also generated with the same parameters as the main signal sample but varying the Higgs mass in a range of 50 – 2000 GeV. These samples are used for heavy scalar mediator interpretations.

Background MC samples

The main backgrounds in the SR are $Z \rightarrow \nu\nu$ and $W \rightarrow \ell\nu$ events where the charged lepton is lost. Furthermore, $Z \rightarrow \ell\ell$ and $W \rightarrow \ell\nu$ with the charged lepton reconstructed define CRs to constrain the backgrounds in the SR. The $V + \text{jets}$ background simulation is split into two components based on the order of the electroweak coupling constant α_{EWK} . The “strong-produced” component is of order α_{EWK}^2 and the “electroweak” component (EWK) is of order α_{EWK}^4 . The interference terms of the order α_{EWK}^3 are negligible.

The $V + \text{jets}$ strong-produced background processes are modeled using SHERPA 2.2.7 [145] filtered in m_{jj} at matrix element level to enhance the statistical precision, merged with inclusive SHERPA 2.2.1 samples. The NNPDF3.0 NNLO PDF set [146] is used. The strong $V + \text{jets}$ production is computed at NLO up to two partons in the final state and LO for up to four partons in the final state. These calculations use the Comix [147] and OpenLoops [148] matrix element generators. Parton shower matching is done with the ME+PS@NLO prescription [149]. The strong $V + \text{jets}$ production samples are normalised at NNLO [150]. The electroweak $V + \text{jets}$ production is divided into single boson

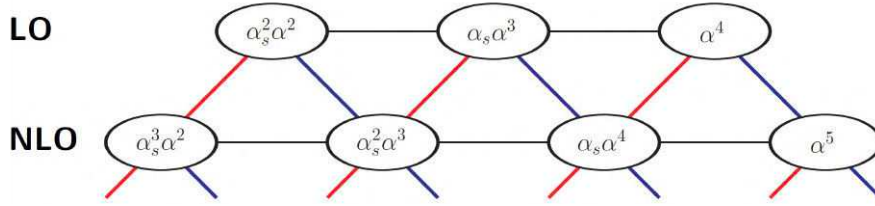


Figure 5.3: Orders of α_{EWK} and α_s up to NLO production of $V + \text{jets}$ processes.

and diboson production. These components are modelled at NLO using HERWIG 7.2.1 [151] and the VBFNLO [152] external matrix element. Diboson production processes are simulated at NLO in QCD for zero or one additional partons and at LO for up to three extra partons. Loop-induced diboson production is generated at LO for up to one additional parton.

Compared to previous iterations of this analysis, the MC statistical precision was improved by a factor of 2 due to an increase in the $V + \text{jets}$ sample size. The $Z + \text{jets}$ MC is additionally reweighted so that the ratio of cross sections between $Z + \text{jets}$ and $W + \text{jets}$ matches a NLO QCD and NLO EWK theoretical calculation in the VBF phase space. The reweighting procedure is described in Section 5.2.2.

There are additional backgrounds from top quark processes and QCD multijets, though these are very small relative to the $V + \text{jets}$. The top backgrounds (both pair production and single-top) are simulated using POWHEG, interfaced with PYTHIA for hadronisation, showering and event generation to describe the b decays involved. Due to the large cross section of QCD multijet processes, the effective luminosity in simulation is substantially smaller than the amount in data. Thus, it is not possible to use simulation to estimate this background. Two methods were developed to face this limitation: the "Rebalance and Smear" technique and a forward JVT control region.

Corrections to $V + \text{jets}$ processes

In this search, corresponding $Z + \text{jets}$ and $W + \text{jets}$ control regions are defined to constrain the $V + \text{jets}$ background in the signal region. The $Z \rightarrow \ell\ell$ event yield in the CR is much smaller compared to the $Z \rightarrow \nu\nu$ component in the SR because of the small $Z \rightarrow \ell\ell$ branching ratio and the lepton acceptance of the ATLAS detector. To exploit the better statistical precision of the $W \rightarrow \ell\nu$ CR, these events can be used to constrain the $Z \rightarrow \nu\nu$ background in the SR. This approach requires a precise knowledge of the ratio between the $Z + \text{jets}$ and $W + \text{jets}$ cross sections ($R_{\text{TH}}^{Z/W}$) and it is motivated by the strong correlation between the Z and W processes. A similar approach was followed in a search for dark matter with $E_{\text{T}}^{\text{miss}}$ and one jet in the final state [62, 153]. For this analysis, dedicated NLO QCD and NLO electroweak calculations based on radiative corrections in the phase space of a VBF-like signature were performed [154].

Figure 5.3 shows all orders in α_{EWK} and α_s for the different production diagrams of $V + \text{jets}$ processes at full NLO in strong and electroweak production. The ATLAS strong $V + \text{jets}$ production MC used in the analysis includes terms in the order of $O(\alpha_s^2 \alpha_{\text{EWK}}^2)$ for up to 4 partons in the final

state, and $\mathcal{O}(\alpha_s^3 \alpha_{\text{EWK}}^2)$ for up to 2 partons in the final state. For electroweak production, terms in the order $\mathcal{O}(\alpha_{\text{EWK}}^4)$ in a VBF approximation are used. The Z + jets MC is reweighted as a function of m_{jj} so that the ratio of cross sections between Z + jets and W + jets matches the NLO QCD and NLO EWK theoretical calculations. The Z + jets differential cross section is scaled by a factor given by the double ratio $\mathcal{R}_{\text{TH}}^{Z/W} / \mathcal{R}_{\text{MC}}^{Z/W}$ between the $\mathcal{R}_{\text{TH}}^{Z/W}$ ratio computed theoretically and this ratio computed on the ATLAS MC $\mathcal{R}_{\text{MC}}^{Z/W}$. The final Z + jets cross section used in the analysis is:

$$\frac{d}{dx} \frac{d}{d\vec{y}} \sigma^Z(\vec{\epsilon}_{\text{MC}}, \vec{\epsilon}_{\text{TH}}) := \frac{d}{dx} \frac{d}{d\vec{y}} \sigma_{\text{MC}}^Z(\vec{\epsilon}_{\text{MC}}) \left[\frac{\mathcal{R}_{\text{TH}}^{Z/W}(x, \vec{\epsilon}_{\text{TH}})}{\mathcal{R}_{\text{MC}}^{Z/W}(x, \vec{\epsilon}_{\text{MC}})} \right], \quad (5.2)$$

where

$$\mathcal{R}_{\text{TH}}^{Z/W} = \frac{\frac{d}{dx} \sigma_{\text{TH}}^Z(\vec{\epsilon}_{\text{TH}})}{\frac{d}{dx} \sigma_{\text{TH}}^W(\vec{\epsilon}_{\text{TH}})}, \quad (5.3)$$

is the ratio between Z and W cross sections in a selection close to the SR, σ_{MC}^V and σ_{TH}^V ($V = Z, W$) are the V + jets production cross section in the MC and from the NLO theoretical calculation, respectively. The correction is derived as a function of x (in this case $x = m_{\text{jj}}$), and \vec{y} denotes other kinematic variables included in the MC simulation, $\vec{\epsilon}_{\text{MC}}$ denotes the set of experimental uncertainties and modeling uncertainties from sources independent on the variable x , and finally, $\vec{\epsilon}_{\text{TH}}$ denotes the set of theoretical uncertainties associated with the correction (described in Section 7.2.1).

The value of the corrections for strong and electroweak production processes are shown in Figures 5.4 and 5.5. The correction to the simulated strong Z + jets prediction is below 5%. For the electroweak Z + jets prediction it varies between 20% at low m_{jj} and 5% at high m_{jj} values. The main reason for those significant corrections at low m_{jj} are missing NLO s channel contributions [155] as well as the missing interference between s and t channel contributions of the used simulated samples.

Pile up reweighting

The MC simulation is performed for a fixed number of interactions per bunch crossing (μ) which generally does not agree with the distribution in data. To correct for this, a set of weights is derived from the data as a function of μ and applied to the MC [156]. This procedure is known as the pile-up reweighting. The weights are derived such that the total normalisation remains unchanged, and a systematic uncertainty is derived varying the reweighting in order to cover the uncertainty on the ratio between the predicted and measured inelastic cross section in the fiducial volume.

5.3 Event selection

This section summarises the event selection applied to the analysis. The event cleaning is defined in Section 5.3.3. The definition of some important variables used in the analysis is introduced in Sections 5.3.1 to 5.3.2. The definition of the analysis signal region (SR) is presented in Section 5.3.4 Control regions (CRs) are used for the V + jets background estimate, the W CR is introduced in Sections 5.3.5

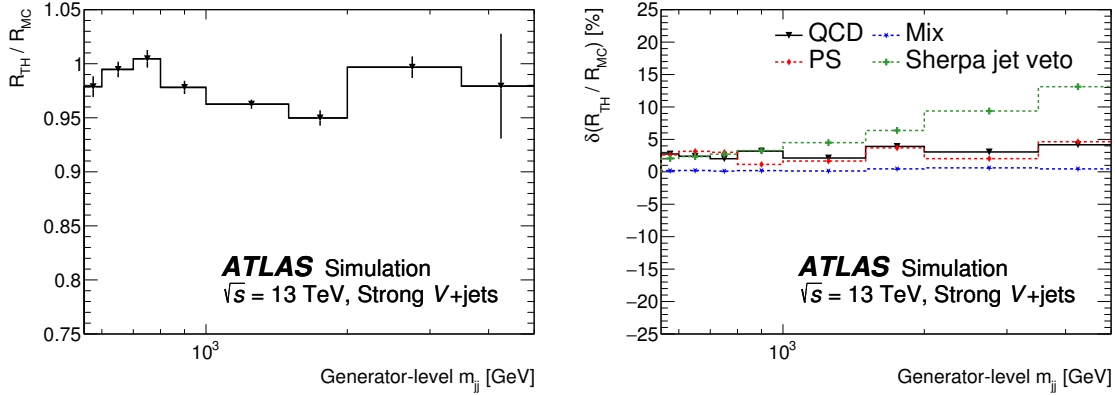


Figure 5.4: Correction applied on strong $V + \text{jets}$ MC (left) and its systematic uncertainties (right). "QCD" refers to the change of the ratio induced by the NLO QCD corrections, "Mix" shows the difference of additive and multiplicative application of the NLO QCD and NLO electroweak corrections, "PS" stands for the uncertainties attributed to the parton shower, and "Sherpa jet veto" denotes the difference between the ratios with and without a jet veto being applied.

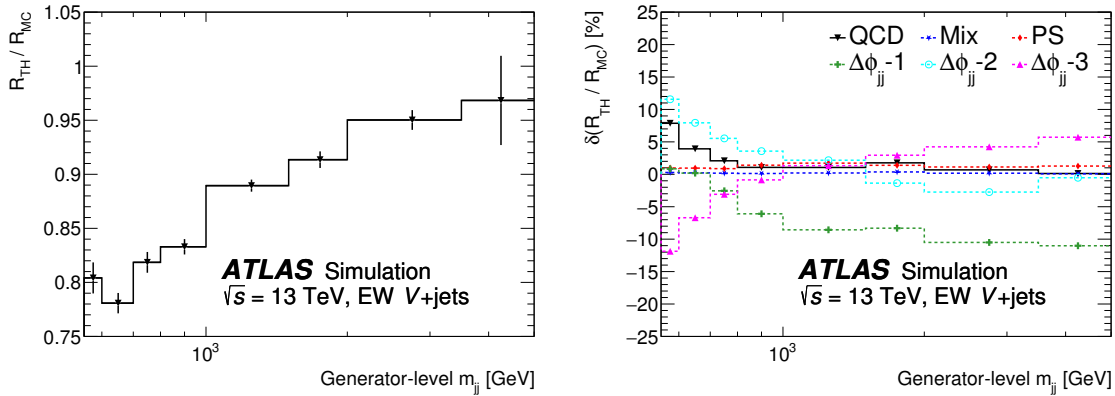


Figure 5.5: Correction applied on electroweak $V + \text{jets}$ MC (left) and its systematic uncertainties (right). "QCD" refers to the change of the ratio induced by the NLO QCD corrections, "Mix" shows the difference of additive and multiplicative application of the NLO QCD and NLO electroweak corrections, "PS" stands for the uncertainties attributed to the parton shower, and the three " $\Delta\phi_{jj} - [1, 2, 3]$ " uncertainties quantify the impact of the $\Delta\phi_{jj}$ dependence on the correction and are evaluated in the ranges of (0-1, 1-2, >2).

to 5.3.7 and the Z CR is explained in Section 5.3.8. A detailed explanation of the $V + \text{jets}$ background estimate is found in Section 6.2.

5.3.1 Jet radiation variable definition

Because there is no colour flow in our signal, we expect very little radiation between the two tagged jets. This motivates the application of a third jet veto in order to remove the QCD and W/Z strong backgrounds which usually have central radiation. On the other hand, events with more than two jets are also of interest of the search and can improve the sensitivity of the analysis if the backgrounds are properly rejected. To achieve this goal we use a variable called centrality (C_3) [157] defined as:

$$C_3 = \exp\left(-\frac{4}{(\eta_1 - \eta_2)^2}\left(\eta_3 - \frac{\eta_1 + \eta_2}{2}\right)^2\right), \quad (5.4)$$

where the subscripts indicate the 1st, 2nd and 3rd highest p_T jets. The centrality variable quantifies if the third jet is central between the two leading jets. If the third jet is perfectly centred between the two tag jets the variable has a value of 1. When the third jet is aligned with one of the leading jets, the value is $1/e$. If the jet is infinitely farther forward in η than the tagged jets, the variable tends to 0. For a fourth jet, the centrality C_4 is defined analogously.

In addition to the centrality, we can characterize the third (or fourth) jet by the relation between its mass and the mass of the tagged jets. We expect the extra jet to be final state radiation from the tagged jets of the signal, therefore the mass of the third jet has to be smaller than the one of the tagged jets. To assure this, we make use of the m_{rel}^3 defined as:

$$m_{\text{rel}}^3 = \frac{\min\{m_{j1j3}, m_{j2j3}\}}{m_{jj}} \quad (5.5)$$

For a fourth jet, the variable m_{rel}^4 is defined analogously.

5.3.2 Forward jet vertex tagger variable definition

The forward jet vertex tagger (fJVT) [158] is a multivariate discriminator designed such that the closer to one, the more probable it is that the jet is a pile-up jet. The closer to zero, the more probable the jet comes from the hard scatter. The fJVT discriminant for a given forward jet with respect to the vertex i , is defined as the normalized projection of the missing transverse momentum on the forward jet transverse momentum (\vec{p}_T^{fj}):

$$\text{fJVT}_i = \frac{\vec{E}_T^{\text{miss}} \cdot \vec{p}_T^{fj}}{|\vec{p}_T^{fj}|^2} \quad (5.6)$$

The fJVT value is defined as $\text{fJVT} = \max_i(\text{fJVT}_i)$. The forward jet is tagged as a pile-up jet if the fJVT value is above certain threshold. A tight (loose) working point is defined such that jets are tagged as pile-up if the fJVT is above 0.2 (0.5).

5.3.3 Event cleaning

There is a background component which does not originate in the pp collisions but is produced from other sources such as cosmic radiation, noisy calorimeter cells, or beam-halo proton interactions. This non-collision background is removed using information from calorimeter signal quality, shape observables of the energy deposits and track properties based on the charged energy fraction [159, 160]. Because jets are the final state objects in this analysis, a tight jet cleaning working point is chosen. This ensures an efficiency of selecting jets from pp collisions of 95% for a jet p_T of 20 GeV and 99.5% at 100 GeV. The event cleaning is performed after the JVT and fJVT selection requirements.

5.3.4 Signal region

The VBF Higgs boson production channel has a particular signature with two high energetic jets with a wide gap in pseudorapidity and large mass of the dijet system. This motivates the introduction of kinematic cuts on the p_T of the two leading jets $p_T(j_1, j_2) > 80, 50$ GeV, $\Delta\eta_{jj} > 3.8$ and $m_{jj} > 0.8$ TeV. All jets are required to have $p_T > 20$ GeV. To ensure that the jets are produced in the hard scatter, the JVT and fJVT discriminators are used. For jets in the central region of the detector ($|\eta| < 2.5$) and $p_T < 60$ GeV, a JVT score above 0.2 is required. If the leading or the subleading jet have $|\eta| > 2.5$ and $p_T < 120$ GeV it is required fJVT < 0.2 (Very Tight) if $E_T^{\text{miss}} < 200$ GeV and fJVT < 0.5 (Loose criteria) elsewhere. To be orthogonal to other searches, it is required that not more than one of the jets are b -tagged.

To suppress the V + jets background, the SR events should contain no "Veto" electrons, no "Veto" muons, neither photons. There is a background component of $W \rightarrow \mu\nu$ events in which the muon is not identified but a track is found. This component is reduced by requiring $E_T^{\text{soft}} < 20$ GeV. To reject the multijet background which accumulates at low E_T^{miss} values and to be in the trigger turn on plateau, the E_T^{miss} is required to be above 160 GeV. Two E_T^{miss} regions are defined: $160 < E_T^{\text{miss}} < 200$ GeV and $E_T^{\text{miss}} > 200$ GeV. QCD multijet events tend to be back-to-back, thus a $\Delta\phi_{jj} < 2.0$ cut is applied to reject this background. To remove multijet events where fake E_T^{miss} is produced by a failed pile-up identification a requirement on the missing hadronic activity (H_T^{miss}) is applied based on the E_T^{miss} value. If $E_T^{\text{miss}} > 200$ GeV, $H_T^{\text{miss}} > 180$ GeV is required, if $160 < E_T^{\text{miss}} < 200$ GeV, $H_T^{\text{miss}} > 140$ GeV is required.

Vetoing additional jet activity is an efficient way to discriminate between the signal and backgrounds. The SR is split into events with two jets and events with more than two jets. The majority of the signal region events fall into the category with only two jets in the final state. Events with a third jet with $p_T > 25$ GeV are rejected from this category. Another category with 3 or 4 jets is used to increase the statistical precision resulting in a gain of signal sensitivity. The extra jets are expected to come from initial state radiation (ISR) or final state radiation (FSR). This is guaranteed by applying cuts on the centrality $\max\{C_3, C_4\} < 0.6$ and the relative mass $\max\{m_{\text{rel}}^3, m_{\text{rel}}^4\} < 0.05$.

To exploit the dependence of the signal-to-background ratio on certain variables the signal region is split into 16 analysis bins corresponding to different $\Delta\phi_{jj}$, m_{jj} , E_T^{miss} , and n_{jet} ranges. The $n_{\text{jet}} > 2$ category is split into three m_{jj} bins (1.5 TeV–2.0 TeV, 2.0 TeV–3.5 TeV, > 3.5 TeV). The remaining

two jet events are split in two E_T^{miss} bins ($160 < E_T^{\text{miss}} < 200$ GeV and $E_T^{\text{miss}} > 200$ GeV). Events with $160 < E_T^{\text{miss}} < 200$ GeV are placed in the same three m_{jj} bins as the FSR events. If $E_T^{\text{miss}} > 200$ GeV, events are split into two $\Delta\phi_{jj}$ bins ($|\Delta\phi_{jj}| < 1.0$ and $1.0 \leq |\Delta\phi_{jj}| < 2.0$) and five m_{jj} bins (0.8 TeV–1.0 TeV, 1.0 TeV–1.5 TeV, 1.5 TeV–2.0 TeV, 2.0 TeV–3.5 TeV, > 3.5 TeV). An illustration of this binning strategy is shown in Figure 5.6.

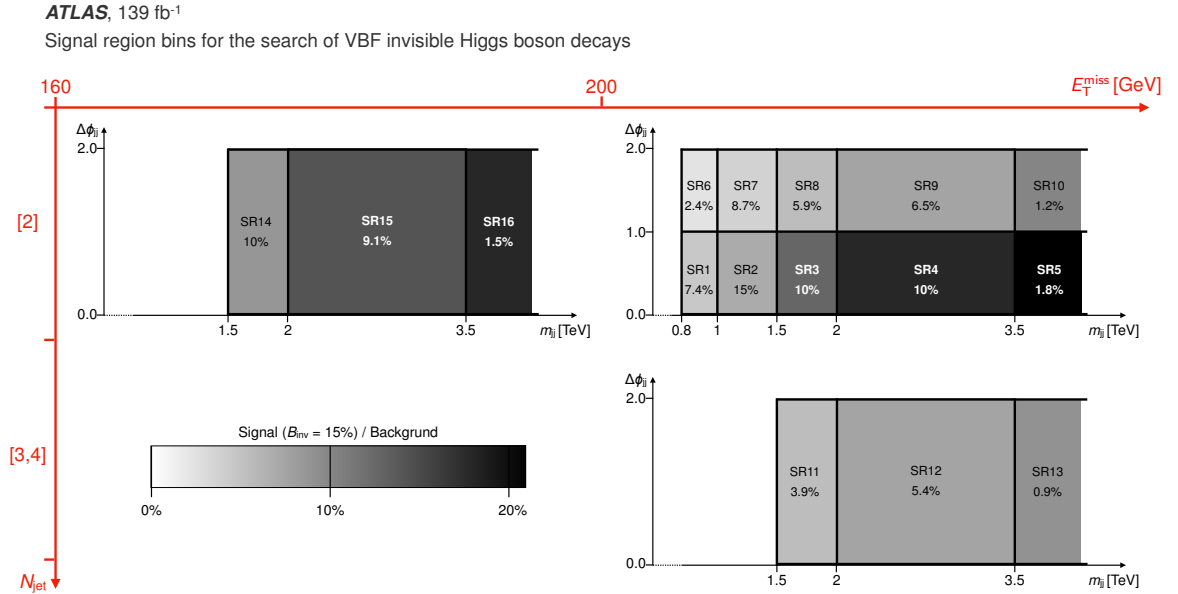


Figure 5.6: Illustration of the binning strategy in the signal region. The shading indicates the signal-to-background ratio, assuming a branching fraction of the invisible Higgs boson decays of $\mathcal{B}_{\text{inv}} = 0.15$. In each bin, the relative contribution of the invisibly decaying Higgs boson signal with respect to the total signal yield in the SR is reported as a percentage.

5.3.5 $W \rightarrow l\nu$ control region

A W control region is defined for each of the signal region bins. To obtain a region pure in W +jets the zero lepton selection is replaced by the requirement to have exactly one lepton. The $W \rightarrow e\nu$ CR uses single electron triggers and $W \rightarrow \mu\nu$ uses an "OR" between the E_T^{miss} triggers used in the signal region and the single and dimuon triggers. The lepton is required to have $p_T > 30$ GeV in order to be on the single lepton trigger efficiency plateau. The lepton selection is summarised in Table 5.2.

The jet selection is kept the same as for the signal region. To obtain a E_T^{miss} spectrum compatible with the definition in the SR, the E_T^{miss} is corrected by vectorially adding the lepton p_T . This method is described in Ref. [161].

There is a contribution of multijet events misidentified as an electron or a muon in the W CR. These "fake" backgrounds need a particular data driven estimate. Also, selection cuts have been designed to remove these contributions. The selection to suppress fake electrons in the $W \rightarrow e\nu$

region is explained in Section 5.3.6, and the suppression of fake muons in the $W \rightarrow \mu\nu$ is presented in Section 5.3.7.

5.3.6 Fake electrons in the $W \rightarrow e\nu$ control region

To reduce the contribution from misidentified electrons in the $W \rightarrow e\nu$ region we make use of the E_T^{miss} significance variable defined as:

$$S_{\text{MET}} = \frac{E_T^{\text{miss}}}{\sqrt{\sum E_T}} = \frac{E_T^{\text{miss}}}{\sqrt{p_T(j1) + p_T(j2) + p_T(el)}}, \quad (5.7)$$

where the E_T^{miss} value in the numerator is the E_T^{miss} excluding the visible lepton. This variable is defined to quantify if the E_T^{miss} is a result of a jet misidentified as an electron. Events are required to have $E_T^{\text{miss}}/\sqrt{\sum E_T} > 4.0 \sqrt{\text{GeV}}$ in order to remove the fake electron background.

5.3.7 Fake muons in the $W \rightarrow l\nu$ control region

Analogously to the case of the misidentified electrons, we need to find a variable that allow us to reject the fake muons background. In this case we use the transverse mass (m_T) defined as:

$$m_T = \sqrt{2p_T^\mu E_T^{\text{miss}} [1 - \cos(\phi_\mu - \phi_{E_T^{\text{miss}}})]} \quad (5.8)$$

This variable depends on the p_T of the muon and the E_T^{miss} as well as on the angle between these two objects. It is designed such that events have small m_T as a result of the misidentified muon coming from a jet and no real transverse momentum. The E_T^{miss} value in Equation 5.8 refers to the E_T^{miss} including the visible lepton. A $m_T > 20$ GeV selection is applied to reject the fake muon background.

5.3.8 $Z \rightarrow \mu l$ control region

Similarly to the W CR, a Z control region is defined for each of the 16 signal region bins defined in Section 5.3.4. The $Z \rightarrow \ell\ell$ CR is defined by replacing the lepton veto with the requirement to have a lepton pair of the same flavour and opposite sign. The dielectron channel is triggered with an "OR" of the single lepton triggers and dielectron triggers. The dimuon channel is triggered by an "OR" between the E_T^{miss} triggers, the single muon and dimuon triggers.

In order to be in the single lepton trigger efficiency plateau, the leading lepton is required to have $p_T > 30$ GeV. The invariant mass of the dilepton system is required to be in the range $|m_Z - m_{ll}| < 25$ GeV where m_Z is the mass of the Z boson and m_{ll} is the mass of the dilepton system. The lepton requirements for both the Z and W control regions are summarised in Table 5.2.

The jet selection is kept the same as for the signal region. To obtain a E_T^{miss} spectrum compatible with the definition in the SR, the E_T^{miss} is corrected by vectorially adding the p_T of both leptons. This method is described in Ref. [161]. There are contributions from diboson, triple boson production and VBF $H \rightarrow W^*W$ or $H \rightarrow \tau\tau$ in this CR. To remove these backgrounds, events are required to have $E_T^{\text{miss}} < 70$ GeV, where the leptons are included in the calculation of the missing transverse momentum.

Table 5.2: Lepton selections

Cut	$W \rightarrow e\nu$	$W \rightarrow \mu\nu$	$Z \rightarrow \ell\ell$
Lepton Flavours	e^-/e^+	μ^-/μ^+	$e^-, e^+/\mu^-, \mu^+$
“Veto” muons and electrons	1	1	2
“Signal” muons and electrons	1	1	2
$p_T(\ell_1)$	>30 GeV	>30 GeV	>30 GeV
$p_T(\ell_2)$	–	–	>4.5 GeV
$ M(\ell\ell) - M_Z $	–	–	<25 GeV
$E_T^{\text{miss}}/\sqrt{\sum E_T}$	> 4.0 $\sqrt{\text{GeV}}$	–	–
m_T	–	> 20 GeV	–
E_T^{miss} (with leptons)	–	–	< 70 GeV

5.3.9 High $\Delta\phi_{jj}$ validation region

A validation region is defined analogously to the SR1-SR10 with the only difference that the $\Delta\phi_{jj}$ cut is inverted ($|\Delta\phi_{jj}| > 2.0$). Minimal signal contamination is expected in this region, allowing for the validation of the different background estimates.

Background estimates

About 95% of the background processes in the VBF phase space are $V + \text{jets}$: $Z \rightarrow \nu\nu$ and $W \rightarrow \ell\nu$ where the lepton escapes undetected. There is a small component of diboson and $t\bar{t}$ production which are estimated from MC simulation. There is also a contribution from multijet events which is estimated using data driven techniques. This particular background is important due to the large uncertainties associated to its estimate. The QCD multijet estimate is discussed in Section 6.1, and the $V + \text{jets}$ estimate is discussed in Section 6.2.

6.1 QCD multijet background

The analysis SR is designed to reject QCD multijet events by requiring large values of E_T^{miss} . However, sizable amounts of E_T^{miss} can be produced because of experimental effects such as fluctuations in the jet detector response, very energetic jets not being contained within the calorimeter, and misidentification of whether a jet is originating from the hard scatter or from pile-up interactions. Such events are extremely rare and have large uncertainties associated with it. The ATLAS Monte Carlo simulation does not provide enough statistical precision to estimate of this background. Therefore, data driven methods are required for this particular background.

Two methods were developed to estimate the multijet background: a Rebalance and Smear (R+S), and a pile-up CR method. R+S emulates the experimental effects explained above and provides the full event dynamics while the pile-up CR makes use of a multijet enriched pile-up CR to obtain an estimate of the multijet event yield in each of the SR bins. The final pre-fit estimate consists of a combination of the results from these two methods as summarised in Table 6.1. The R+S and its validation is described in Sections 6.1.1 to 6.1.6, and the pile-up CR is explained in Section 6.1.7. There is a number of CRs used in the multijet estimate. They are summarised in Table 6.2. An additional multijet estimate using an ABCD method developed at an early stage of the analysis is presented in Appendix B. Because of technical limitations this method was not used in the final estimate, but it was a first step towards the novel pile-up CR method.

SR bins	Pile up CR	Rebalance and Smear
1-5 (high E_T^{miss} , low $\Delta\phi_{\text{jj}}$)	1 CR per bin	-
6-10 (high E_T^{miss} , high $\Delta\phi_{\text{jj}}$)	1 inclusive CR for normalisation	m_{jj} shape
11-13 (high E_T^{miss} , incl. $\Delta\phi_{\text{jj}}$, $2 < N_{\text{jets}} < 5$)	-	Shape and normalisation
14-16 (low E_T^{miss} , incl. $\Delta\phi_{\text{jj}}$)	1 CR per bin	-

Table 6.1: The usage of MJ estimates by SR bins. A - indicates that the method is not used.

Region	Definition	Binned	Purpose
MJ CR	$100 \text{ GeV} < E_T^{\text{miss}} < 200 \text{ GeV}$ and $m_{\text{jj}} > 400 \text{ GeV}$ $N_{\text{jet}} = 2$, $\Delta\eta_{\text{jj}} > 2.5$ no requirement on $E_T^{\text{jet,no-jvt}}$	no	Determine HS-only and HS+PU composition
low- m_{jj} CR	$150 \text{ GeV} < E_T^{\text{miss}} < 200 \text{ GeV}$ $2 \leq N_{\text{jet}} \leq 4$, $200 \text{ GeV} < m_{\text{jj}} < 800 \text{ GeV}$ $\Delta\eta_{\text{jj}} > 2.5$, ($ \eta^{j1} > 2.4$ or $ \eta^{j2} > 2.4$) $\Delta\phi_{\text{jj}} < 1$, no requirement on $E_T^{\text{jet,no-jvt}}$	no	Multijet (R+S) normalisation Estimate non-closure uncertainty
mid- m_{jj} CR	$160 \text{ GeV} < E_T^{\text{miss}} < 200 \text{ GeV}$ $N_{\text{jet}} = 2$, $800 \text{ GeV} < m_{\text{jj}} < 1500 \text{ GeV}$ $\Delta\phi_{\text{jj}} < 1$, no requirement on $E_T^{\text{jet,no-jvt}}$	no	Same as low- m_{jj} CR
pile-up CR	$ \eta^{j1} > 2.4$ and j1 is PU tagged no pile-up-tagging requirement for j2 $2 \leq N_{\text{jet}} \leq 4$ no m_i^{rel} requirement for $1 < \Delta\phi_{\text{jj}} < 2$	yes	Scaled by R_{MJ} to obtain multijet yield in SR
low-MET CR	$100 \text{ GeV} < E_T^{\text{miss}} < 160 \text{ GeV}$	yes	Numerator of R_{MJ}
low-MET PU-CR	same as pile-up CR, but $100 \text{ GeV} < E_T^{\text{miss}} < 160 \text{ GeV}$	yes	Denominator of R_{MJ}
low-MET VR	$110 \text{ GeV} < E_T^{\text{miss}} < 150 \text{ GeV}$ loose fJVT requirement no requirement on $E_T^{\text{jet,no-jvt}}$	no	Performance check of pile-up CR method

 Table 6.2: Control regions used for the multijet background estimation. Only changes relative to the SR selection are given. The third column shows if a the control region is binned in $\Delta\phi_{\text{jj}}$ and m_{jj} like the signal region. Except for the MJ CR, which uses single-jet-triggered data, all control regions use E_T^{miss} -triggered data.

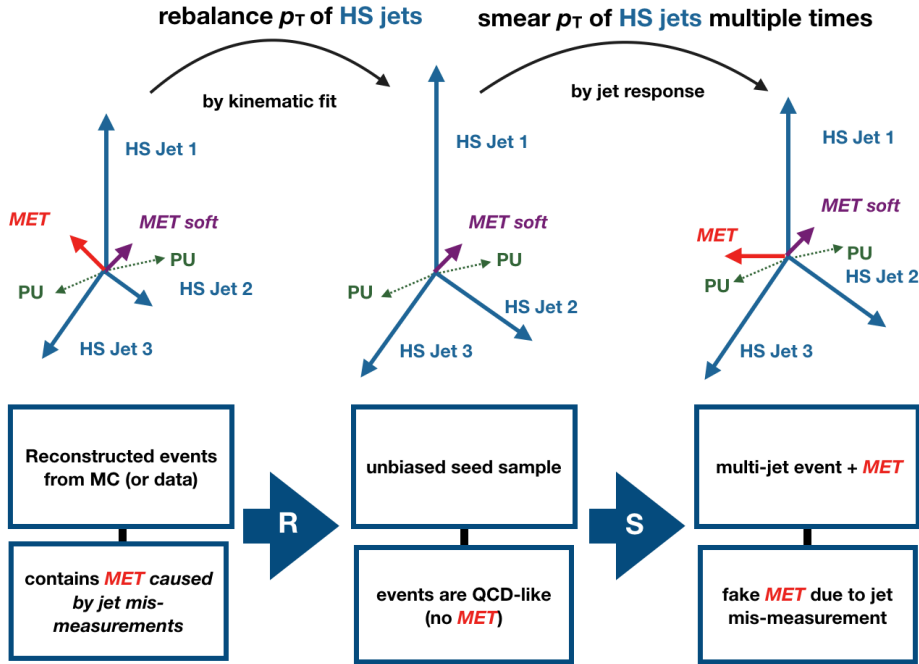


Figure 6.1: Sketch of MC-based R+S multijet background prediction technique as used in the analysis [162].

6.1.1 Rebalance and Smear estimate of multijet background

The Rebalance and Smear (R+S) is a sampling technique that emulates the experimental effects causing multijet events to enter the VBF signal region [22]. R+S emulates the detector response of each jet of a multijet seed sample multiple times to predict the full event kinematics of a QCD multijet sample. In its simplest version, the R+S method uses events from unrescaled single jet triggered data, rebalance them to account for p_T imbalance and smear them to emulate the effect of the detector response. In addition, each seed event is smeared several times in order to increase the statistical precision. This has been used for the multijet estimate in previous iterations of this analysis. For the full Run 2 analysis an improved version of the technique was developed. A separate rebalancing of the hard scatter (HS) and pile-up (PU) jets in the event was introduced, and two variations are defined by the seed sample used (data or Monte Carlo).

The modified Monte Carlo based R+S works as follows. It starts with an inclusive MC multijet sample which may have some E_T^{miss} at reconstruction level. The momentum imbalance on the HS part of the event is removed in a rebalancing step by a kinematic fit while the PU part is kept fixed. At this point, the HS corresponds to a multijet process at truth level. Then, the HS jets of each event are smeared multiple times (reducing the event weight accordingly) with detector response distributions. The PU part of the event remains constant. This procedure is illustrated in Figure 6.1. It is important to mention that since the R+S method changes the event kinematics, the pile-up tagging needs to be re-evaluated.

6.1.2 R+S systematic uncertainties on the m_{jj} shape

In order to account for potential differences between the data and the simulation, the smearing is repeated with systematically varied jet energy response distributions. A 15% wider jet energy resolution (“core”) and a 50% increase of the non-Gaussian “tails” of the jet energy response are produced. The differences to the nominal on the m_{jj} shape are taken as systematic uncertainties. Also, two variations of the R+S estimate are produced. In one the seed samples are taken from data and in the other from MC. The difference between the m_{jj} shapes of the two predictions is taken as an additional systematic uncertainty. A comparison of the m_{jj} shapes in the SR between the data driven and the MC based R+S estimates is shown in Figure 6.2. A comparison of the m_{jj} shapes in the SR between the nominal and the core-up and tail-up variations is shown in Figure 6.3.

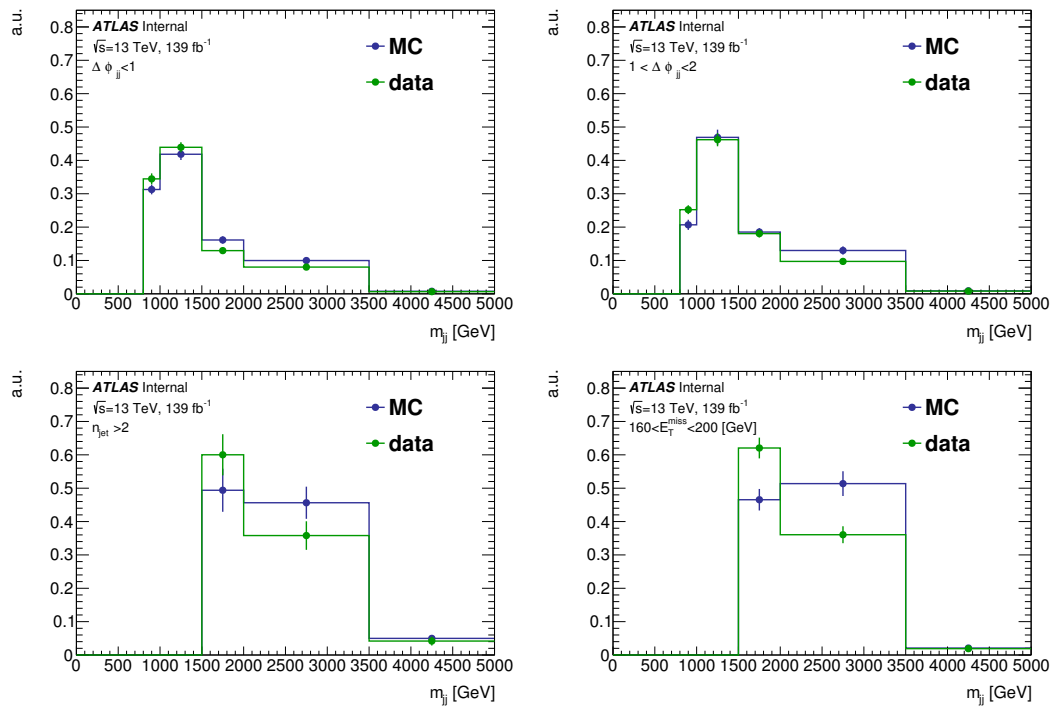


Figure 6.2: Comparison of the SR m_{jj} shapes between the data driven and MC based R+S estimates. The difference between these shapes is taken as a systematic uncertainty on the multijet estimate.

6.1.3 Normalisation in mid E_T^{miss} mid m_{jj} and low m_{jj} control regions and non-closure uncertainty

Due to the complexity of the method, a non-closure correction with a corresponding systematic uncertainty is assigned. In E_T^{miss} triggered data, we determine normalisation factors in two multijet control regions. A mid E_T^{miss} -mid m_{jj} control region is defined by $160 \text{ GeV} < E_T^{\text{miss}} < 200 \text{ GeV}$ and $800 \text{ GeV} < m_{jj} < 1500 \text{ GeV}$, and a low m_{jj} region is defined as $200 \text{ GeV} < m_{jj} < 800 \text{ GeV}$ and $E_T^{\text{miss}} > 150 \text{ GeV}$ (See Figure 6.4). In order to increase the contribution from multijet background

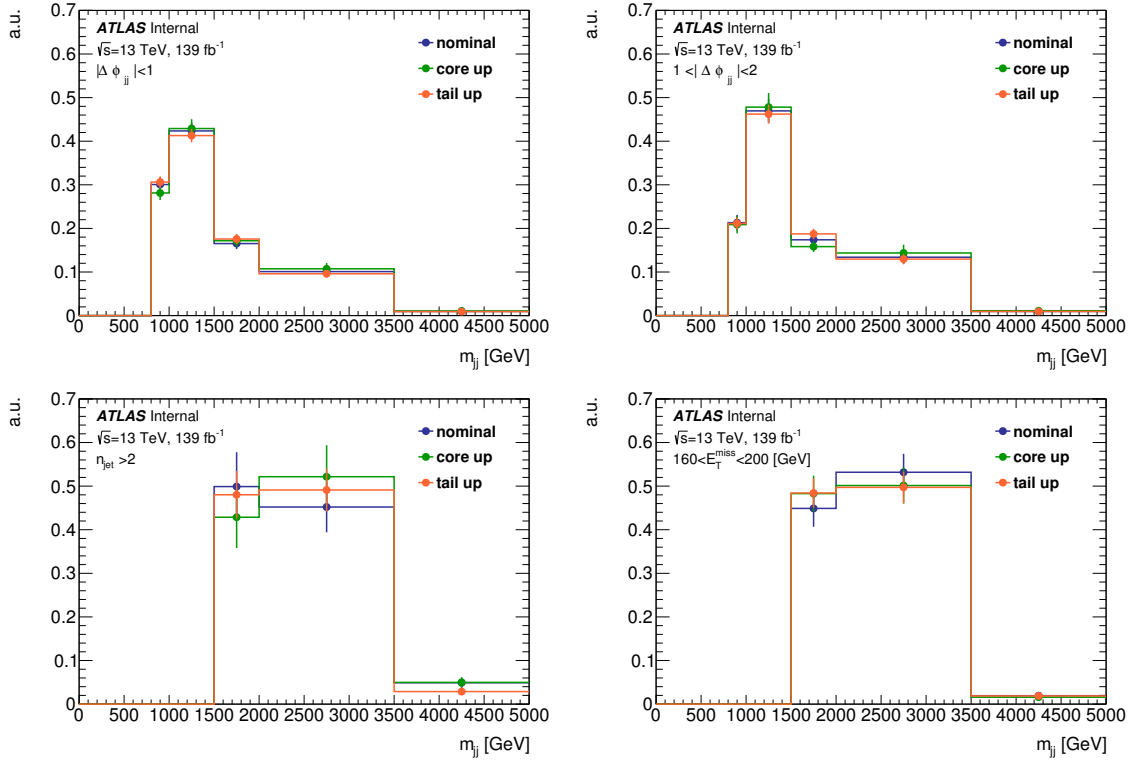


Figure 6.3: Comparison of the SR m_{jj} shapes between the nominal prediction and the tail-up and core-up systematic variations. The difference between these shapes is taken as a systematic uncertainty on the multijet estimate.

in the low m_{jj} region, the $\Delta\eta_{jj}$ cut is loosened from 3.8 to 2.5 while adding the requirement that one of the two leading jets is forward ($|\eta| > 2.5$). The $E_T^{\text{jet,no-jvt}}$ cut in both normalisation regions was dropped to avoid effects of mismodelling of this variable in these regions. All other kinematic cuts are left as in the SR. The non-QCD backgrounds are subtracted and V +jets contributions are scaled to fit the corresponding single and di-lepton control regions. The non-closure correction is computed as the ratio between the data minus the non-QCD contributions and the R+S multijet prediction. In the low m_{jj} CR, only the low $\Delta\phi_{jj}$ region ($\Delta\phi_{jj} < 1.0$) is used because it has a larger contribution from multijet.

The average normalisation factor between the two regions is used as a correction, individually for each data taking period. Half of the spread (max correction - min correction) / 2 is used as a systematic (non-closure) uncertainty. Both the normalisation factors and the systematic uncertainty are applied in the two $\Delta\phi_{jj}$ bins. A summary of the normalisation and non-closure uncertainties are given in Tab. 6.3. Comparisons of the data and the background estimates in the multijet CRs, for each data taking period and for the combined 139 fb^{-1} are presented in Figures 6.5 and 6.6.

Table 6.3: Multijet normalisation for each year for the two CR in low m_{jj} and mid E_T^{miss} -mid m_{jj} .

year(s)	Low m_{jj}	mid E_T^{miss} mid m_{jj}	Average \pm systematic
2015+2016	0.17	0.38	0.27 ± 0.11
2017	0.55	1.54	1.04 ± 0.49
2018	0.48	0.97	0.73 ± 0.25

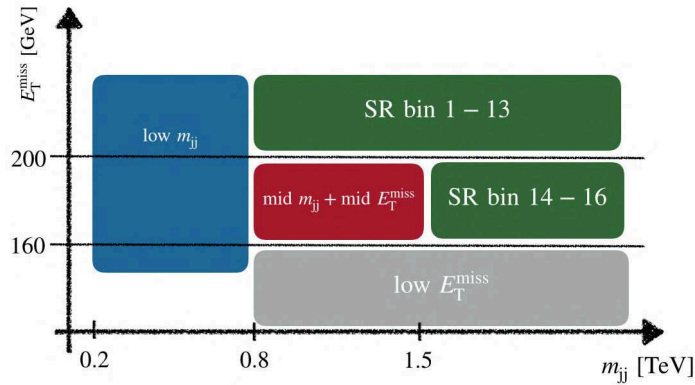
Figure 6.4: Visualization of the MJ CRs in the E_T^{miss} - m_{jj} plane.

Table 6.4: Comparison of multijet normalisation with fJVT<0.2 and fJVT<0.5

Year	normalisation	
	fJVT<0.2	fJVT<0.5
2016	0.27 ± 0.11	0.35 ± 0.13
2017	1.04 ± 0.49	1.11 ± 0.49
2018	0.73 ± 0.25	0.67 ± 0.27

6.1.4 Cross check of multijet normalisation using fJVT<0.5

In the analysis, a fJVT cut is applied on the two leading jets. Events with $E_T^{\text{miss}} > 200$ GeV are required to have jets with fJVT<0.5 while events with $E_T^{\text{miss}} < 200$ GeV are set to have fJVT<0.2. The normalisation regions described in Sec. 6.1.3 are below the threshold of 200 GeV in E_T^{miss} , therefore the fJVT<0.2 cut was applied. In contrast, the SR bins 1-13 use the looser fJVT cut. In order to cross check if the change in fJVT cut alters the normalisation, scale factors were computed using the same regions as in 6.1.3 but loosening the fJVT cut from 0.2 to 0.5. A comparison between the two sets of normalisation factors is shown in Table 6.4. We conclude that the normalisation is stable when changing the fJVT cut. The $\Delta\phi_{jj}$ and m_{jj} distributions in the low m_{jj} and mid m_{jj} mid E_T^{miss} regions with fJVT<0.5, after the normalisation is applied, are shown in Figures 6.7 and 6.8 respectively.

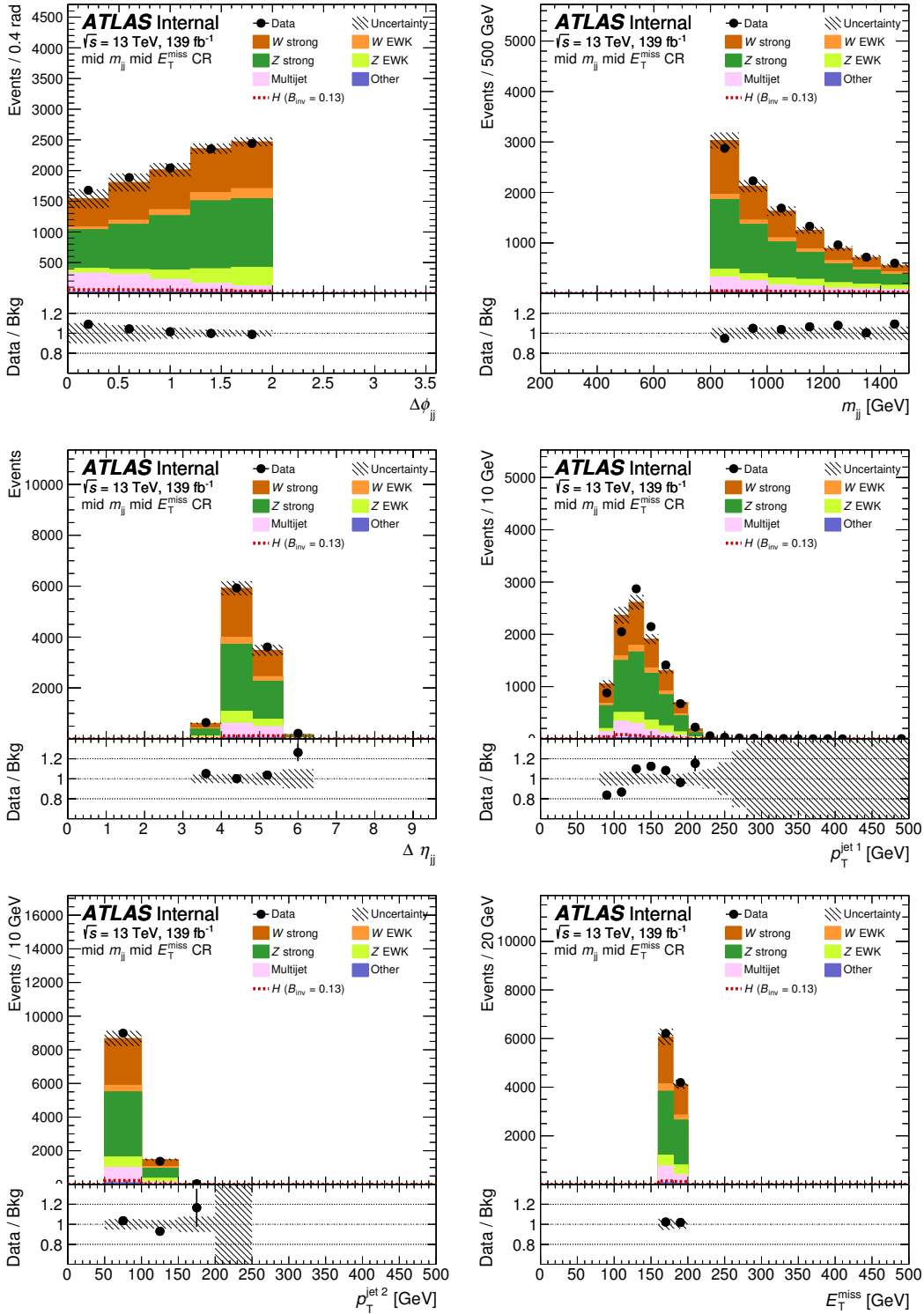


Figure 6.5: Distributions of kinematic variables in the mid E_T^{miss} -mid m_{jj} multijet CR (160 GeV < E_T^{miss} < 200 GeV & 800 GeV < m_{jj} < 1500 GeV). Data and background predictions correspond to the full LHC Run 2.

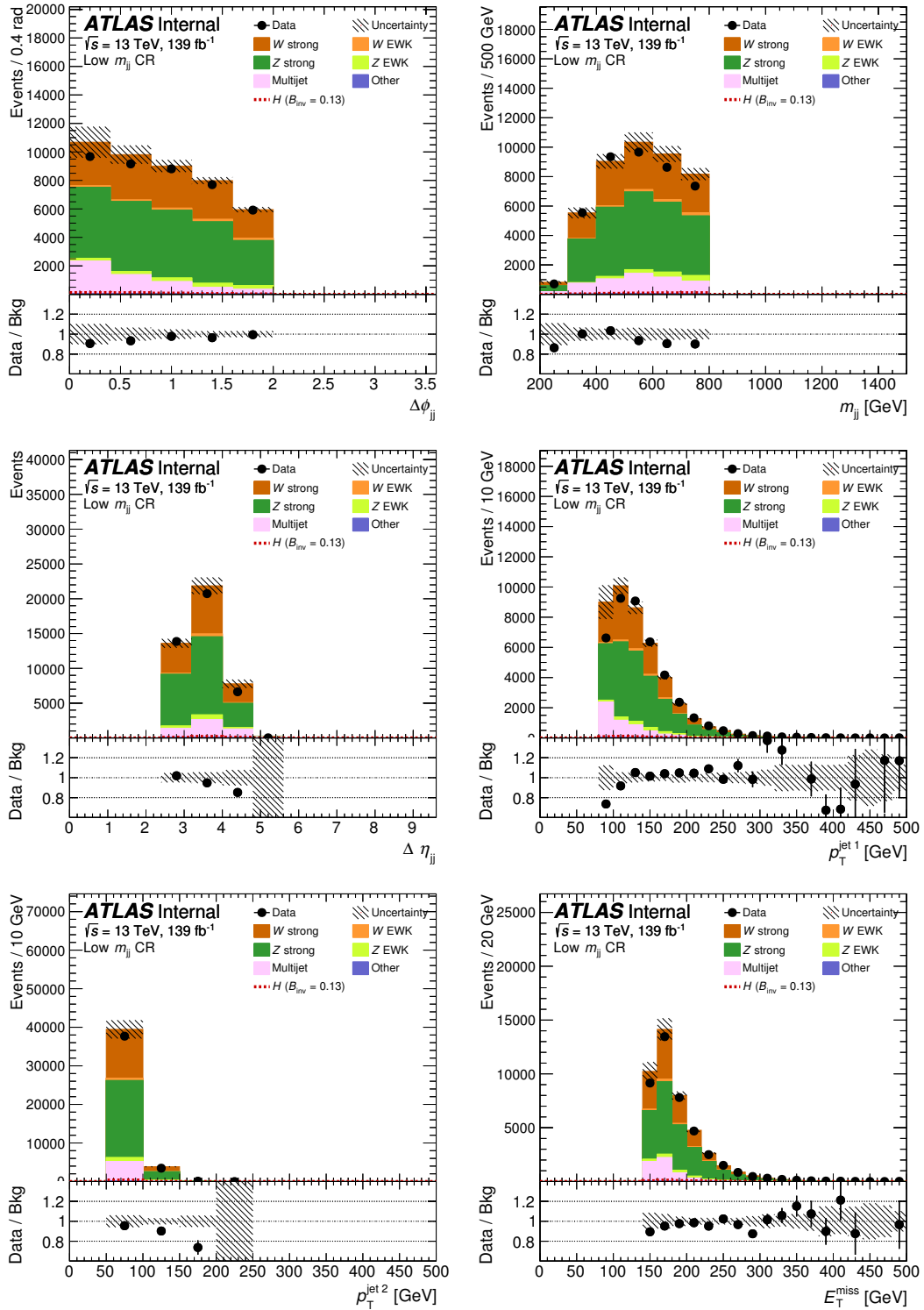


Figure 6.6: Distributions of kinematic variables in the low m_{jj} multijet CR ($E_T^{\text{miss}} > 150$ GeV, $200 \text{ GeV} < m_{jj} < 800$ GeV). Data and background predictions correspond to the full LHC Run 2.

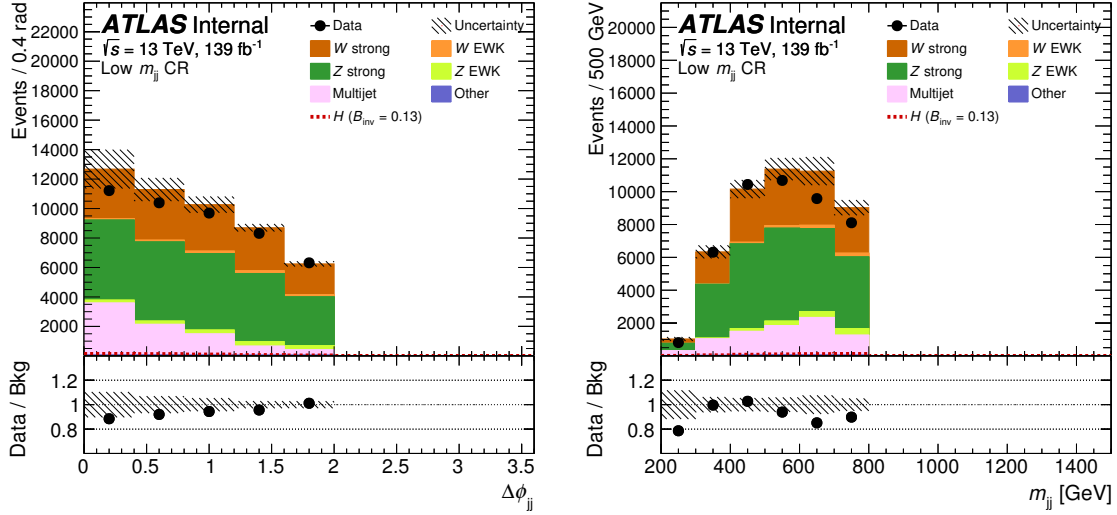


Figure 6.7: Closure plots in the low m_{jj} region with $f_{JVT} < 0.5$

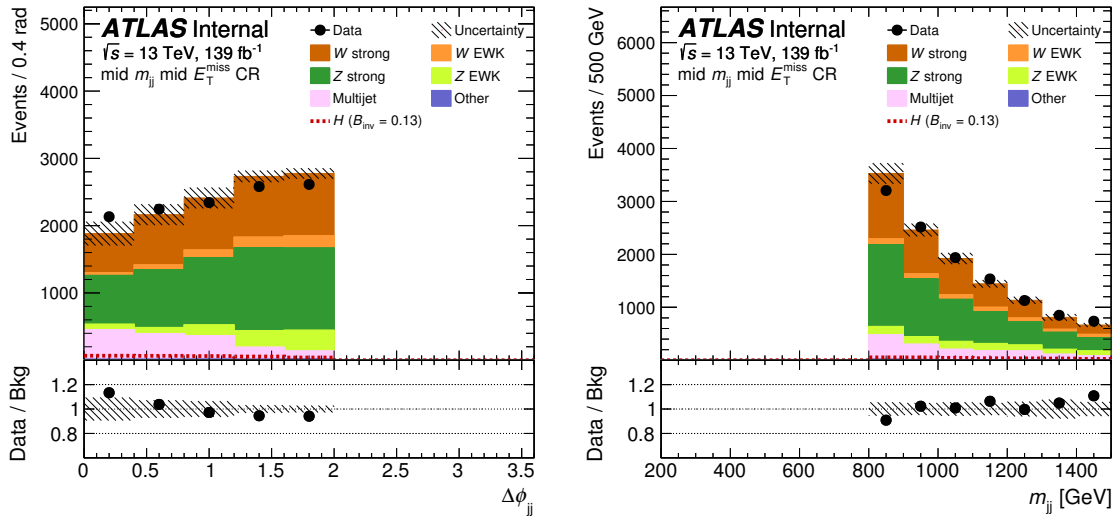


Figure 6.8: Closure plots in the mid E_T^{miss} -mid m_{jj} region with $f_{JVT} < 0.5$

Table 6.5: Predicted multijet (MJ) background in the signal region. The inclusive predictions and their relative contribution to the total background are reported separately for different data taking periods. The quoted errors on the fraction of the total background are statistical only. Average <core-up>, <tail-up>, and <Data vs MC> uncertainties are reported in this table, but they are evaluated per bin in the statistical treatment.

year(s)	MJ yield	fraction of tot. bg	stat	<core>	<tail>	<Data vs MC>	non-closure
2015+2016	112.8	2.8%	3.7%	3.9%	2.5%	2.4%	40%
2017	385.9	8.8%	4.9%	4.5%	5.8%	7.0%	47%
2018	414.6	7.0%	3.2%	8.7%	5.9%	-0.4%	34%

6.1.5 Multijet Prediction

Around 5% of the total background in the signal region corresponds to the multijet background. Most of that contribution is in the two lowest m_{jj} bins ($800 < m_{jj} < 1000$ GeV and $1 < m_{jj} < 1.5$ TeV). A summary of the multijet estimate in the SR and its uncertainties is given in table 6.5 for each data taking period. The average systematic uncertainties <core>, <tail>, and <Data vs MC> are reported. The relative systematic uncertainties are defined as nominal-variation/nominal, and the average is the sum of the systematic uncertainties over all SR bins divided by the number of bins (16). The per bin multijet predictions and their corresponding uncertainties are presented in Table 6.6. The core and tail uncertainties are treated as fully correlated across all analysis bins and all years. The non-closure systematic uncertainty is treated as fully correlated across analysis bins but uncorrelated between the different years. The statistical uncertainty is treated bin-by-bin as uncorrelated but fully correlated across years.

6.1.6 Multijet m_{jj} shape in the signal region

In the preliminary version of the analysis published in the conference note [24], the multijet m_{jj} shape was averaged between the data taking years to avoid statistical fluctuations. Given the improvements in statistical precision, this procedure is not needed anymore. The m_{jj} shape is now taken from the sum of the estimates of each MC campaign after the normalisation in the mid E_T^{miss} and mid m_{jj} regions presented in Sec. 6.1.3. A comparison between the average shape and the shape of the sum is shown in Fig 6.9 for the different SR bins. In general, the two shapes agree within statistical uncertainties.

Validation of the multijet m_{jj} shape in the low E_T^{miss} and mid E_T^{miss} - mid m_{jj} multijet CRs

The shape of the multijet m_{jj} distribution was cross checked in a low E_T^{miss} region ($100 \text{ GeV} < E_T^{\text{miss}} < 160 \text{ GeV}$) and a mid m_{jj} mid E_T^{miss} region ($160 \text{ GeV} < E_T^{\text{miss}} < 200 \text{ GeV}$ and $800 \text{ GeV} < m_{jj} < 1500 \text{ GeV}$). All other kinematic cuts are kept the same as in the SR. The shape of the R+S prediction is compared with the shape of the data minus the non-QCD backgrounds separately in low and high $\Delta\phi_{jj}$ bins. The V+jets background is normalized per m_{jj} bin from the corresponding single and di-lepton control regions. The data and non-QCD yields in the low E_T^{miss} CR are shown in Figure 6.10, the comparison of the shapes is shown in Figure 6.11. The data and non-QCD yields in the mid E_T^{miss} , mid m_{jj} CR are

Table 6.6: Bin by bin prediction of multijet (MJ) background, statistical, and relative systematic uncertainties for the full LHC Run 2.

SR bin	MJ yield	stat	non-closure	core	tail	data vs MC
1	107.944	7.815	43.425	0.064	-0.019	-0.102
2	152.075	9.001	61.281	-0.013	0.025	-0.050
3	59.318	6.896	24.370	-0.039	-0.063	0.198
4	36.243	6.135	15.019	-0.063	0.049	0.197
5	3.433	1.583	1.457	-0.109	0.042	0.156
6	36.638	4.476	14.913	0.021	0.009	-0.219
7	80.691	7.956	32.882	-0.018	0.016	0.015
8	29.879	3.351	12.059	0.090	-0.078	0.025
9	23.011	4.232	9.573	-0.073	0.032	0.252
10	1.64	0.568	0.683	-0.172	0.006	0.105
11	35.907	6.703	15.347	0.411	0.223	-0.215
12	32.532	5.103	13.712	0.209	0.122	0.215
13	3.527	1.514	1.478	0.303	0.526	0.161
14	139.043	16.931	56.451	-0.076	-0.079	-0.333
15	164.741	78.066	61.460	0.057	0.065	0.298
16	5.987	1.830	2.323	0.180	0.030	0.089

shown in Figure 6.12, the comparison of the shapes is shown in Figure 6.13. Overall there is a good agreement between the shapes.

Validation of the m_{jj} shape with fJVT<0.5

Some discrepancies in the m_{jj} shape between the R+S and the pile-up CR methods at low $\Delta\phi_{jj}$ were found. A test was performed in a region defined by $150 \text{ GeV} < E_T^{\text{miss}} < 200 \text{ GeV}$, $m_{jj} < 1.5 \text{ TeV}$, $\Delta\phi_{jj} < 1.0$, fJVT<0.5. The V+jets contribution is normalised per m_{jj} bin from the corresponding single and di-lepton control regions. No normalisation is applied on the multijet events. The m_{jj} closure plot in this region is shown in Figure 6.14. Some discrepancy is observed in the shape of the distribution at low m_{jj} values.

6.1.7 Pile up control region multijet estimate

The pile-up control region is a method that uses events with high fJVT score for the leading jet (pile-up CR) to extrapolate the multijet background to the signal region. This pile-up CR has the same kinematics as the SR but the fJVT requirement on the leading jet is inverted (see Figure 6.15). Two pile-up CRs are defined accordingly to the SR fJVT selection. Events with $E_T^{\text{miss}} > 200 \text{ GeV}$ or $160 < E_T^{\text{miss}} < 200 \text{ GeV}$ are required to have a leading jet with an fJVT score larger than 0.5 or 0.2, respectively. The CR with leading jet fJVT larger than 0.5 is shown in Figure 6.16 and the CR with leading jet fJVT larger than 0.2 is shown in Figure 6.17. The number of multijet events in a given signal region bin i (N_{MJ}^i) is given by:

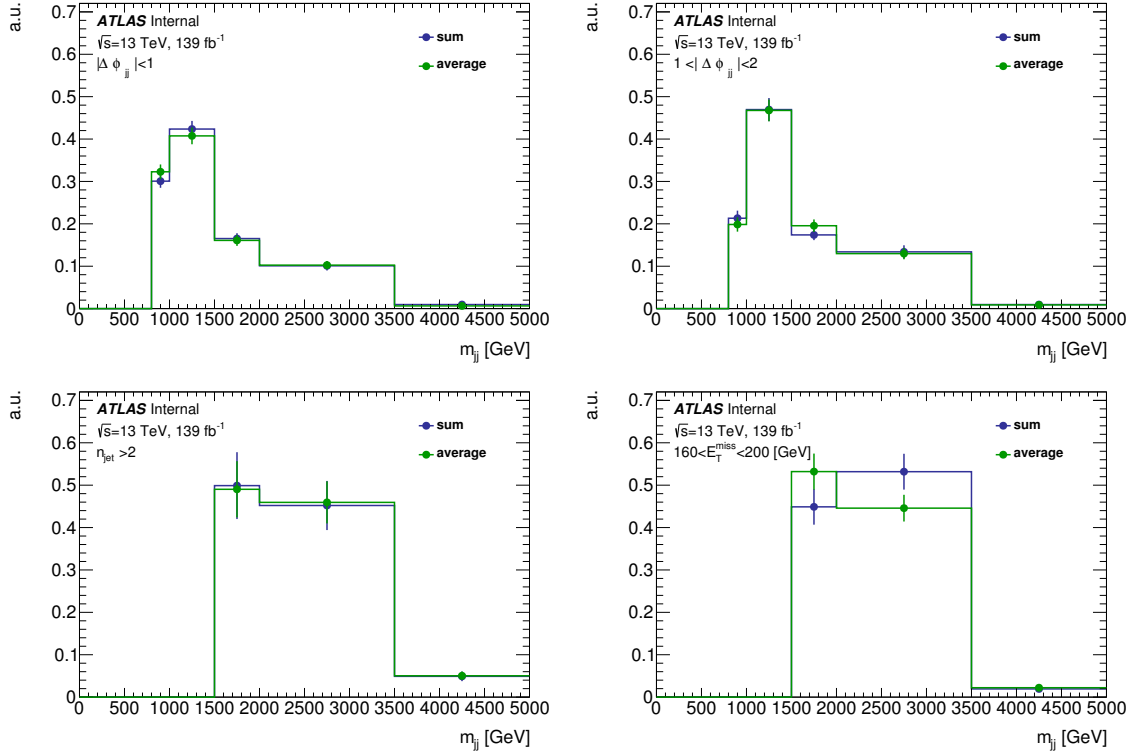


Figure 6.9: Comparison of the SR m_{jj} shapes when averaged between data taking years and when added over these years.

$$N_{MJ}^i = R_{MJ,i} \times \left(N_{\text{data}}^{\text{rev. fJVT},i} - N_{\text{non-MJ}}^{\text{rev. fJVT},i} \right), \quad (6.1)$$

where $R_{MJ,i}$ is the transfer factor between the CR and the SR, and the term in parentheses corresponds to the number of multijet events in the CR bin i computed as the difference between the data and the non-QCD events in the control region. Events with the leading jet passing the reverted fJVT selection are expected to have additional central pile-up jets needed to balance the leading jet. Thus, in order to gain statistics, events with $2 \leq N_j \leq 4$ are used to extrapolate to the $N_j = 2$ signal regions.

The transfer factor is defined as the ratio between the number of multijet events passing the fJVT selection and the number of events failing this selection:

$$R_{MJ,i} = \frac{N_{\text{data}}^{\text{pass fJVT},i} - N_{\text{non-QCD}}^{\text{pass fJVT},i}}{N_{\text{data}}^{\text{rev. fJVT},i} - N_{\text{non-QCD}}^{\text{rev. fJVT},i}}. \quad (6.2)$$

The transfer factor is measured at lower E_T^{miss} values ($100 < E_T^{\text{miss}} < 160$ GeV) and it is computed as a function of m_{jj} and $\Delta\phi_{jj}$. The dependence of this factor on kinematic variables as E_T^{miss} , jet p_T , jet η , and pile-up conditions was studied. It is shown in Figures 6.19, and 6.20, for leading jet fJVT<0.5, and in Figure 6.22 for leading jet fJVT<0.2. No strong dependence was found, potential

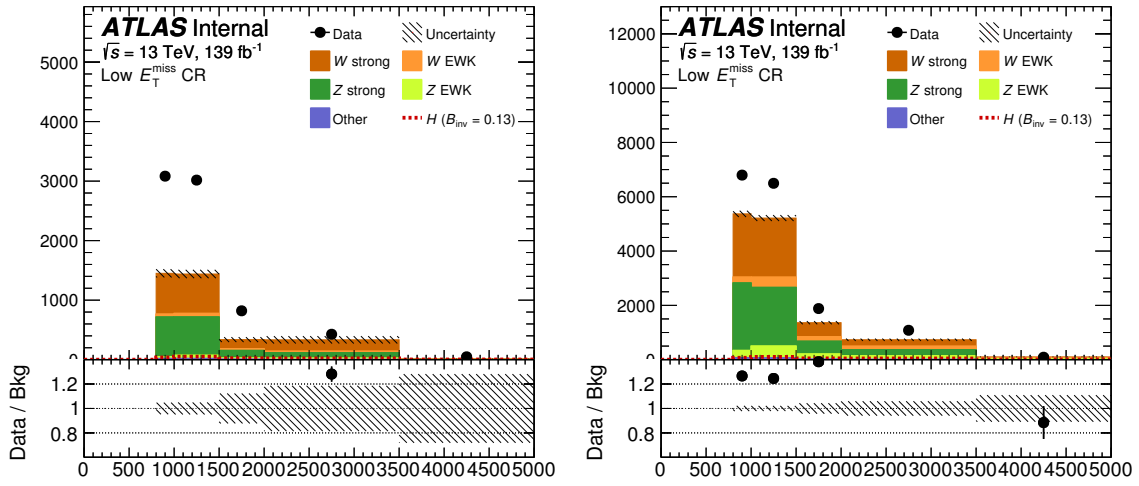


Figure 6.10: Data and non-QCD contributions in the low E_T^{miss} control region. Low $\Delta\phi_{jj}$ ($|\Delta\phi_{jj}| < 1.0$) on the left and high $\Delta\phi_{jj}$ ($1.0 < |\Delta\phi_{jj}| < 2.0$) on the right.

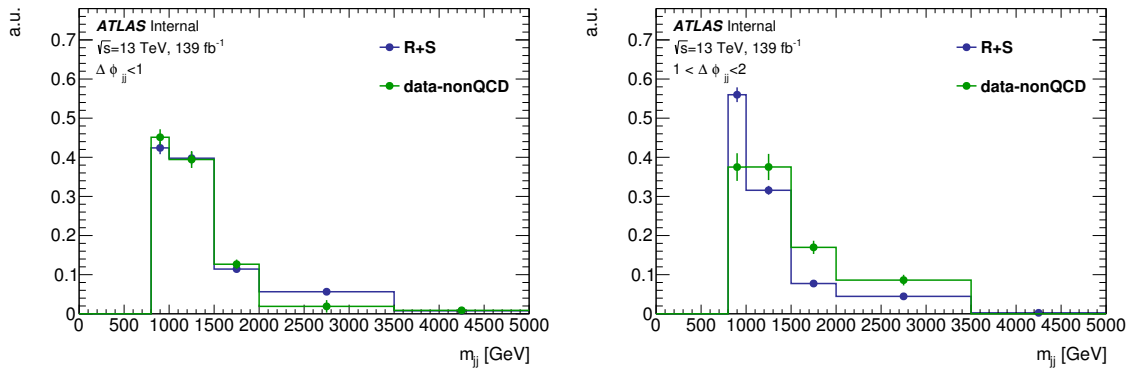


Figure 6.11: Comparison of the m_{jj} shapes in the low E_T^{miss} multijet CR between the R+S estimate and the data - non-QCD contributions. Low $\Delta\phi_{jj}$ ($|\Delta\phi_{jj}| < 1.0$) is shown on the left and high $\Delta\phi_{jj}$ ($1.0 < |\Delta\phi_{jj}| < 2.0$) on the right.

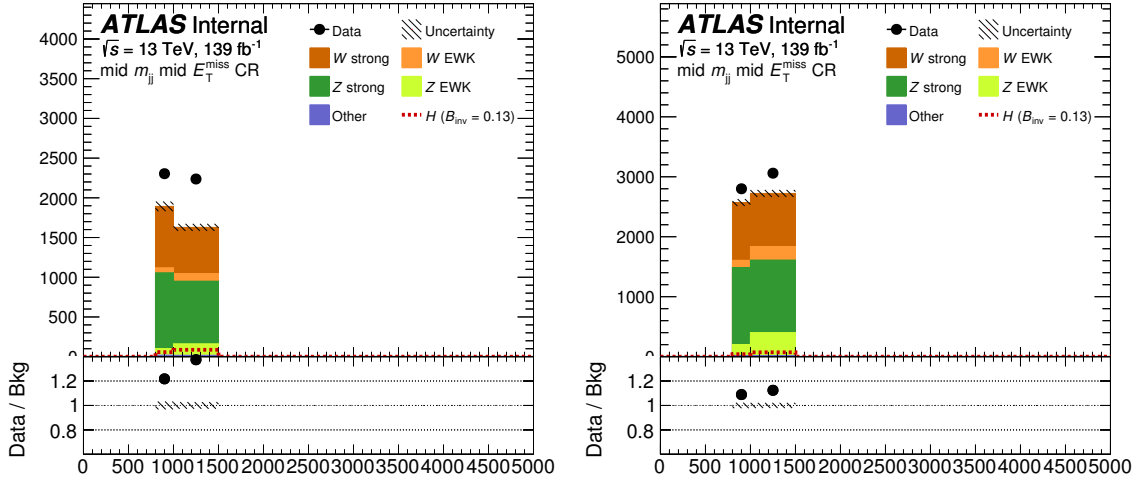


Figure 6.12: Data and non-QCD contributions in the mid E_T^{miss} , mid m_{jj} control region. Low $\Delta\phi_{jj}$ ($|\Delta\phi_{jj}| < 1.0$) on the left and high $\Delta\phi_{jj}$ ($1.0 < |\Delta\phi_{jj}| < 2.0$) on the right.

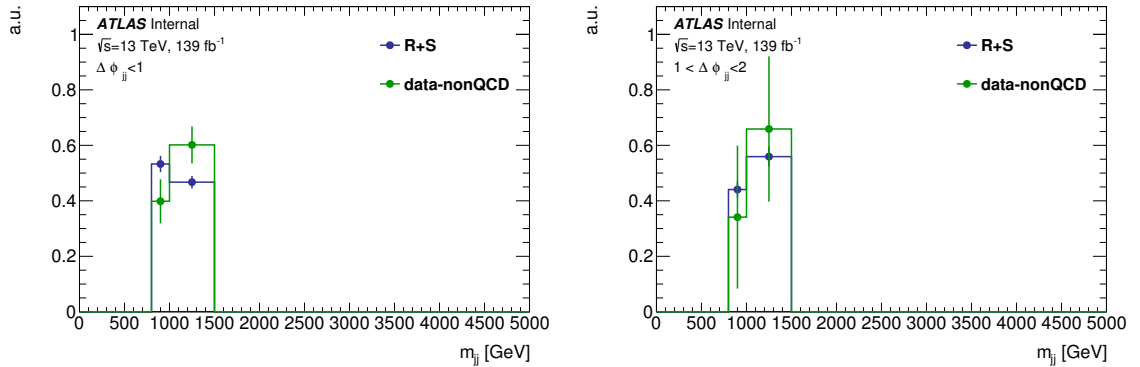


Figure 6.13: Comparison of the m_{jj} shapes in the mid E_T^{miss} - mid m_{jj} multijet CR between the R+S estimate and the data - non-QCD contributions. Low $\Delta\phi_{jj}$ ($|\Delta\phi_{jj}| < 1.0$) is shown on the left and high $\Delta\phi_{jj}$ ($1.0 < |\Delta\phi_{jj}| < 2.0$) on the right.

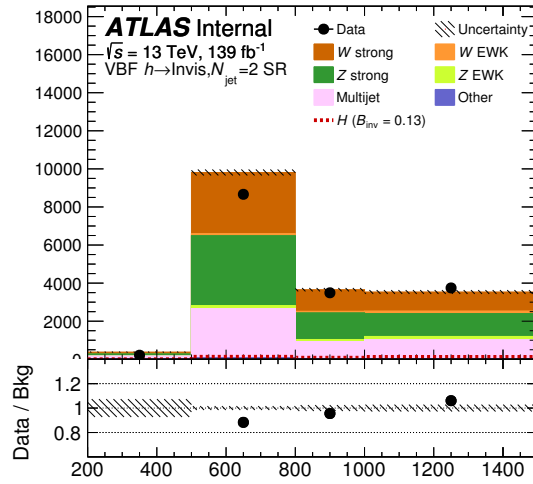


Figure 6.14: Test of the m_{jj} shape in $150 \text{ GeV} < E_T^{\text{miss}} < 200 \text{ GeV}$, $m_{jj} < 1.5 \text{ TeV}$, $\Delta\phi_{jj} < 1.0$, $f_{JVT} < 0.5$. The hashed band indicates the statistical uncertainty.

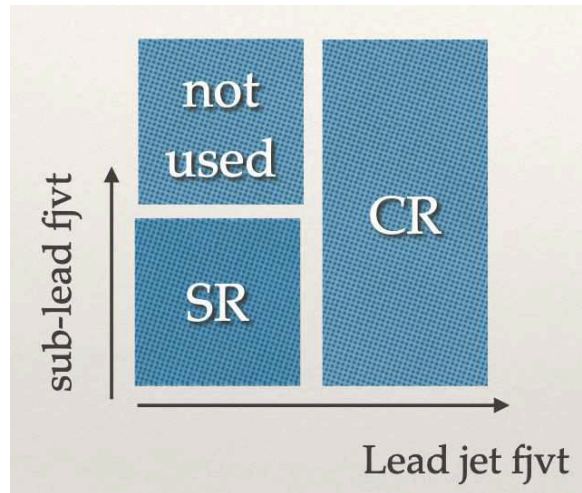


Figure 6.15: Schematic of the fJVT control region definition.

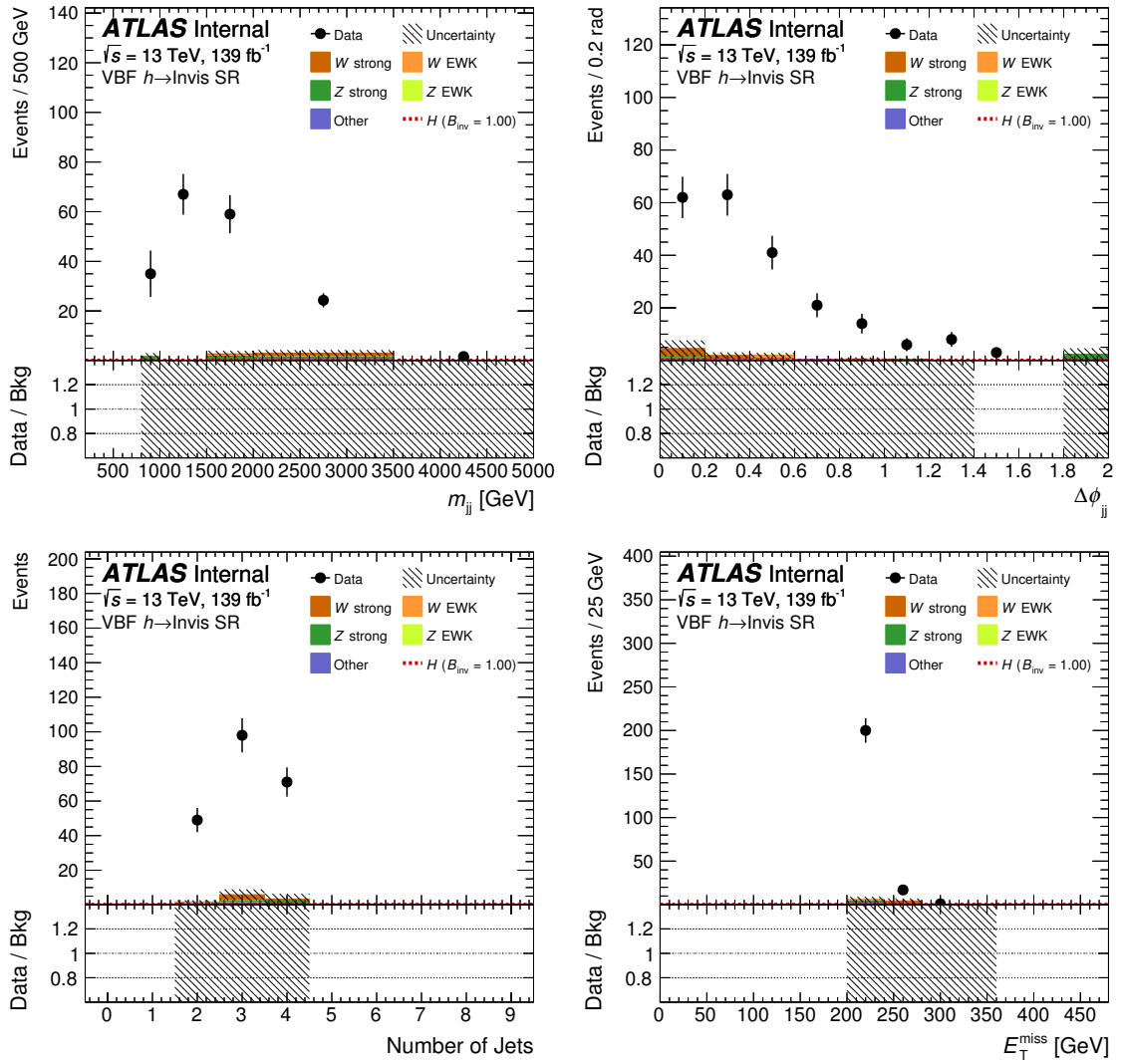


Figure 6.16: The sum of control regions with leading jet FJVT larger than 0.5 is shown for the m_{jj} , $\Delta\phi_{jj}$, N_{jet} , and E_T^{miss} for $E_T^{\text{miss}} > 200$ GeV. The multijet contribution is not shown, and it is the dominant contribution.

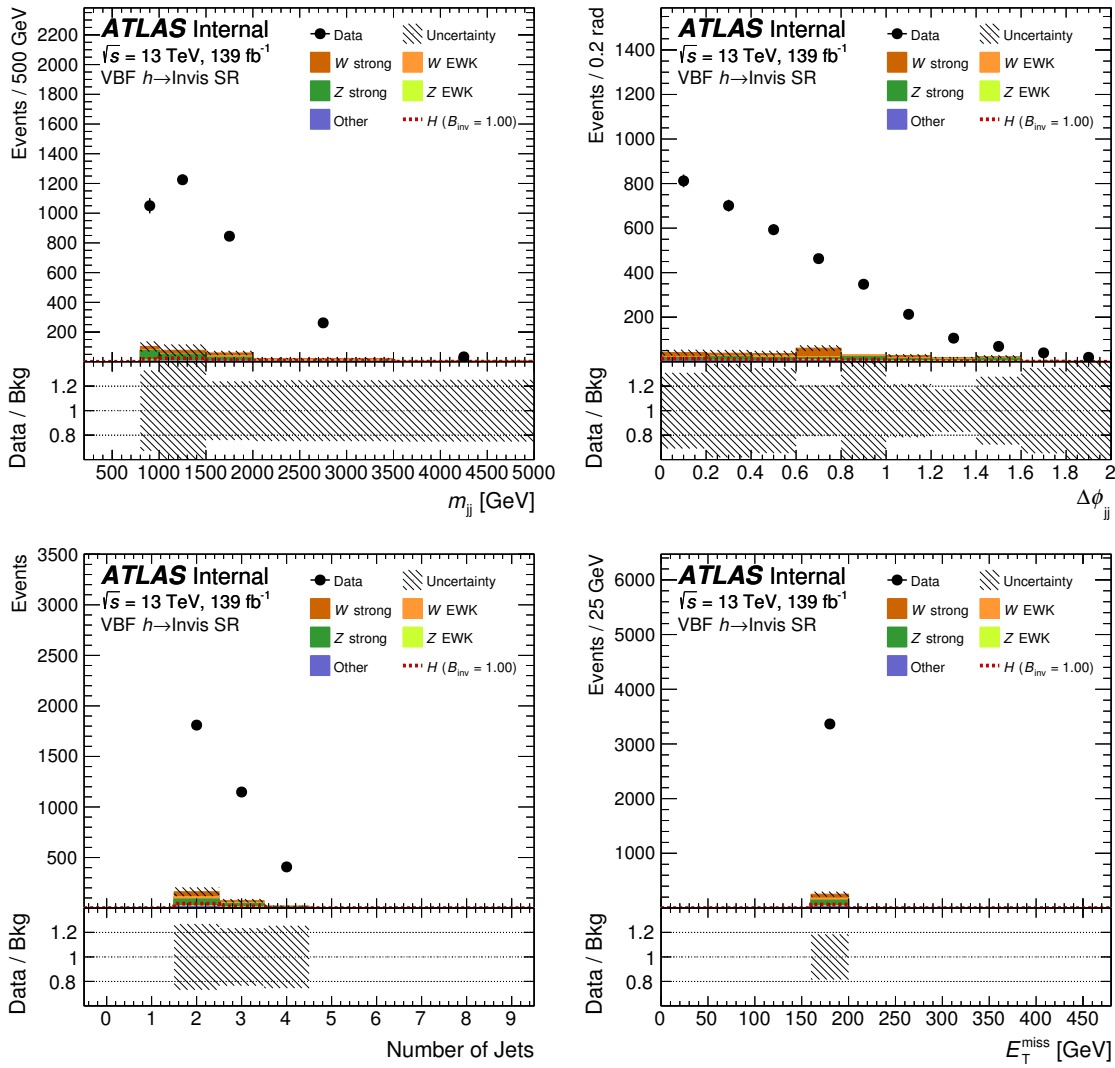


Figure 6.17: The sum of control regions with leading jet FJVT larger than 0.2 is shown for the m_{ij} , $\Delta\phi_{ij}$, N_{jet} , and E_T^{miss} for $160 < E_T^{\text{miss}} < 200 \text{ GeV}$. The multijet contribution is not shown, and it is the dominant contribution.

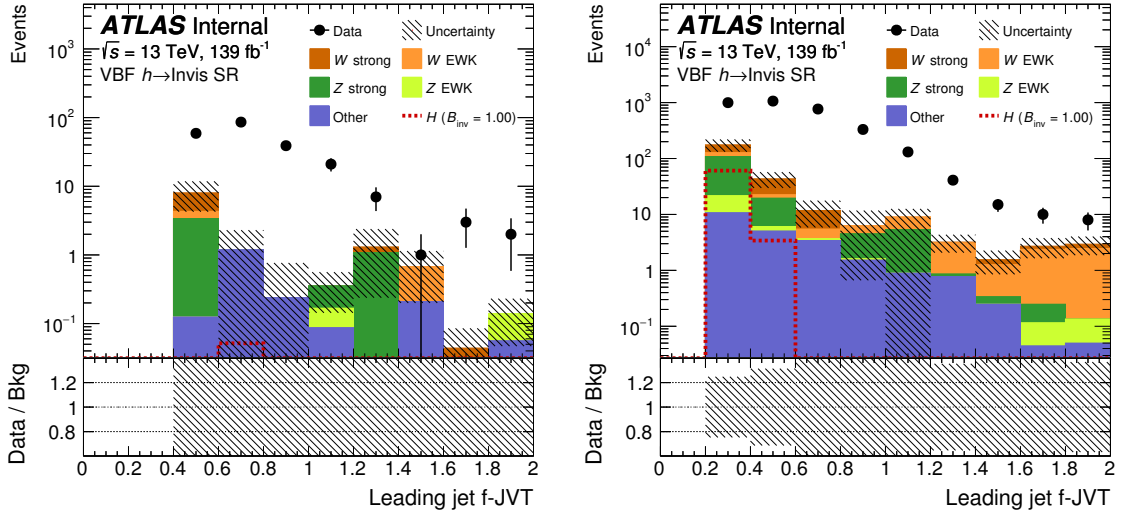


Figure 6.18: Leading jet fJVT score in the multijet CR for $E_T^{\text{miss}} > 200$ GeV (left) and $160 < E_T^{\text{miss}} < 200$ GeV (right).

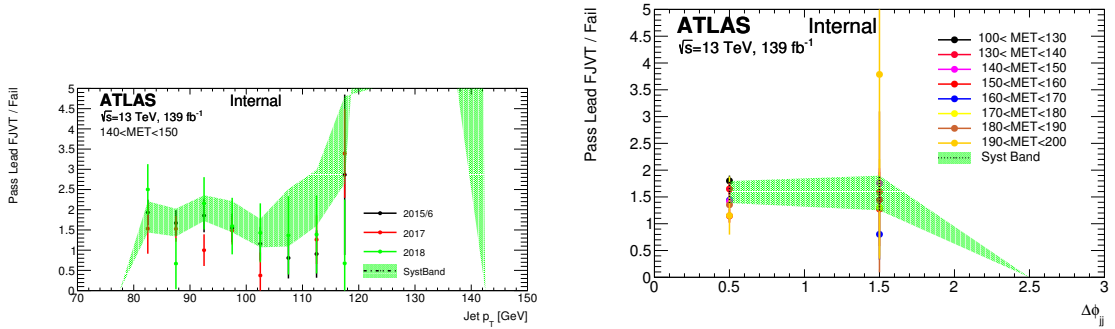


Figure 6.19: The transfer factor $f_{M_J}^i$ dependence on jet p_T and $\Delta\phi_{jj}$ are shown.

differences are covered by a 20% systematic uncertainty band. Also, a comparison of the transfer factors for the different data taking periods is shown in Figure 6.21. A summary of the transfer factor and their uncertainties is found in Table 6.7. A comparison between the background predictions and the observed data in a low E_T^{miss} CR ($100 < E_T^{\text{miss}} < 160$ GeV) is shown in Figure 6.23. Overall a good agreement within uncertainties is observed between the data and background.

6.2 V + jets estimate

The main backgrounds in the signal region are $Z \rightarrow \nu\nu$ and $W \rightarrow \ell\nu$ events where the lepton is lost (it will be notated as ℓ_{lost} from now). The main reasons that leptons are "lost" are tau leptons decaying hadronically and leptons falling outside the p_T or η acceptance. These processes are challenging to model, and in order to reduce the impact of theoretical and experimental uncertainties, a data driven

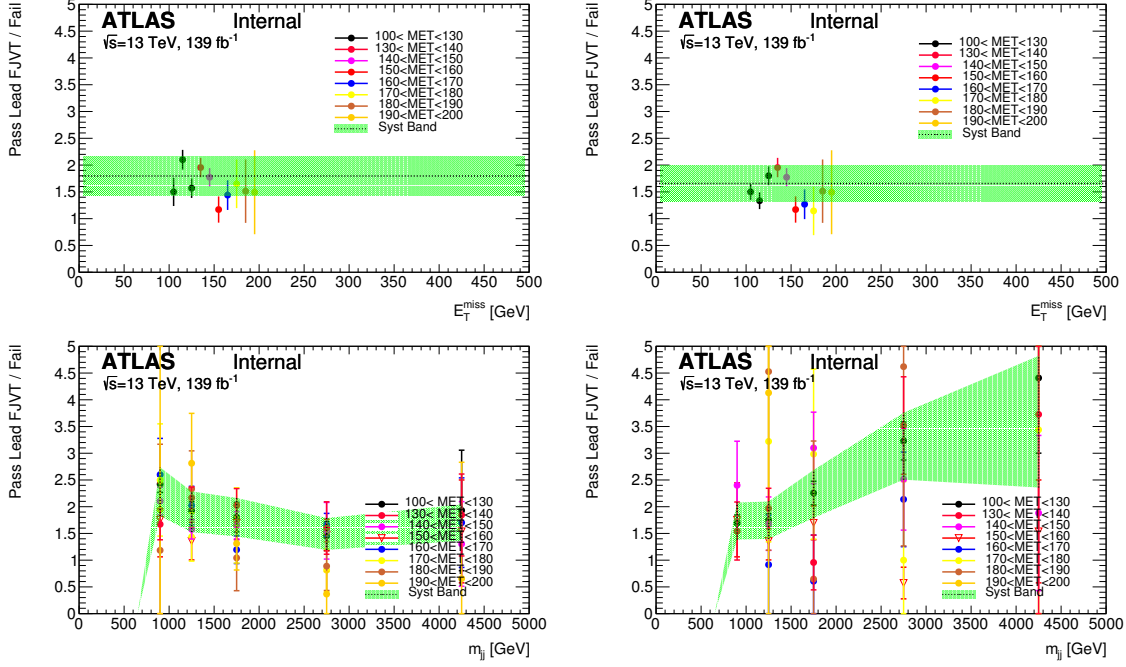


Figure 6.20: The transfer factor f_{MJ}^i dependence on E_T^{miss} and m_{jj} are shown for $|\Delta\phi_{jj}| < 1$ (left) and $1 < |\Delta\phi_{jj}| < 2$ (right).

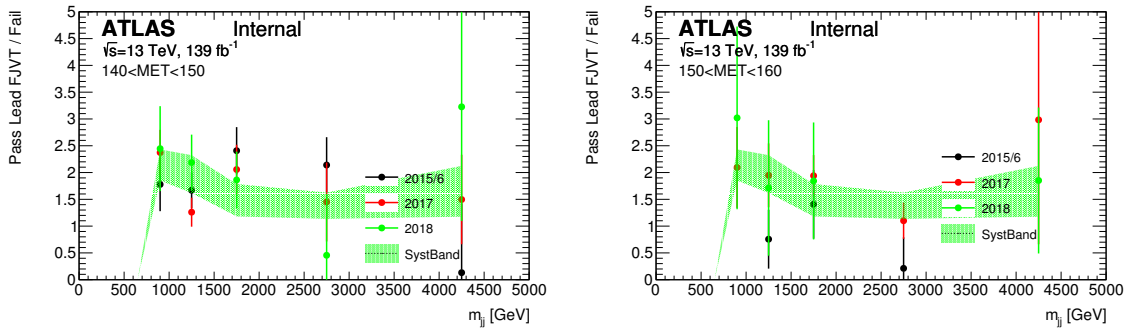
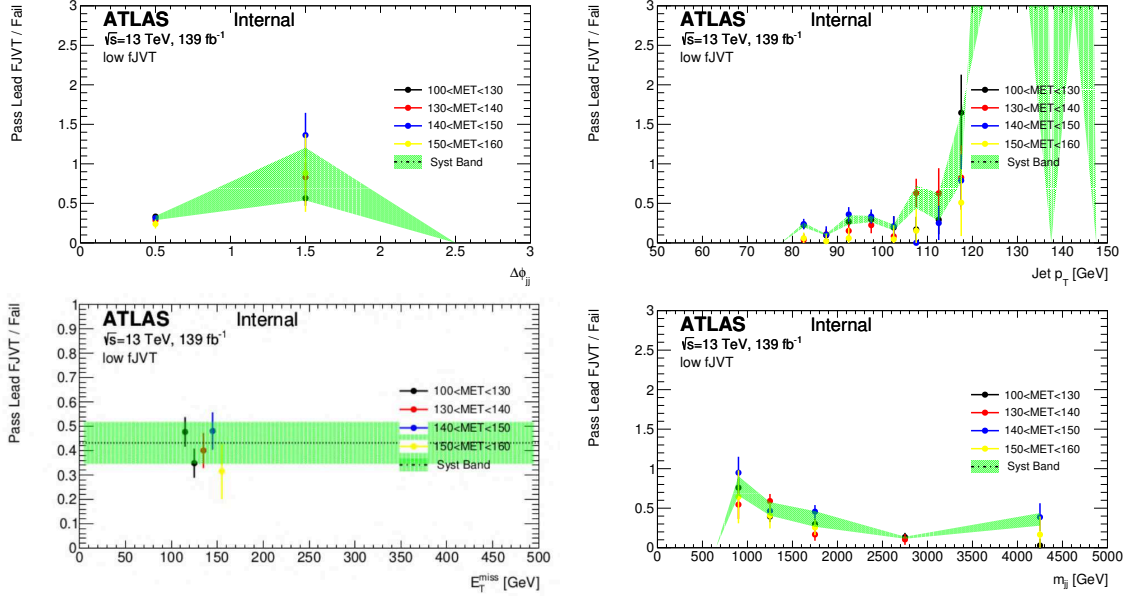


Figure 6.21: The transfer factor f_{MJ}^i dependence on different years of data taking are shown for $140 < E_T^{\text{miss}} < 150$ GeV (left) and $150 < E_T^{\text{miss}} < 160$ GeV (right) as a function of m_{jj} .


 Figure 6.22: The transfer factor f_{MJ}^i dependence on $\Delta\phi_{ij}$, leading jet p_T , E_T^{miss} , and m_{ij} for $\text{FJVT} < 0.2$.

SR Bin	m_{ij}	$\Delta\phi_{ij}$	E_T^{miss}	f_{MJ}^i	Stat. unc.	Systematic unc.
SR1	0.8-1.0 TeV	$ \Delta\phi_{ij} < 1$	> 200 GeV	2.29 (5.7 comb.)	± 0.23 (10%)	± 0.47 (21%) (60% comb.)
SR2	1.0-1.5 TeV	$ \Delta\phi_{ij} < 1$	> 200 GeV	2.19	± 0.39 (18%)	± 0.44 (20%)
SR3	1.5-2.0 TeV	$ \Delta\phi_{ij} < 1$	> 200 GeV	1.63	± 0.27 (17%)	± 0.32 (20%)
SR4	2.0-3.5 TeV	$ \Delta\phi_{ij} < 1$	> 200 GeV	1.52	± 0.15 (10%)	± 0.30 (20%)
SR5	> 3.5 TeV	$ \Delta\phi_{ij} < 1$	> 200 GeV	1.82	± 0.49 (27%)	± 0.36 (20%)
SR6	0.8-1.0 TeV	$1 < \Delta\phi_{ij} < 2$	> 200 GeV	1.75	± 0.21 (12%)	± 0.39 (22%)
SR7	1.0-1.5 TeV	$1 < \Delta\phi_{ij} < 2$	> 200 GeV	1.76	± 0.25 (14%)	± 0.35 (20%)
SR8	1.5-2.0 TeV	$1 < \Delta\phi_{ij} < 2$	> 200 GeV	2.10	± 0.54 (26%)	± 0.47 (22%)
SR9	2.0-3.5 TeV	$1 < \Delta\phi_{ij} < 2$	> 200 GeV	2.35	± 0.78 (33%)	± 0.28 (20%)
SR10	> 3.5 TeV	$1 < \Delta\phi_{ij} < 2$	> 200 GeV	3.38	± 1.42 (42%)	± 0.68 (20%)
SR6-10	< 0.8 TeV	$1 < \Delta\phi_{ij} < 2$	> 200 GeV	1.80	± 0.20 (11%)	± 0.36 (20%)
SR14	1.5-2.0 TeV	$ \Delta\phi_{ij} < 2$	160 – 200 GeV	0.28	± 0.027 (10%)	± 0.06 (27%)
SR15	2.0-3.5 TeV	$ \Delta\phi_{ij} < 2$	160 – 200 GeV	0.11	± 0.012 (10%)	± 0.022 (20%)
SR16	> 3.5 TeV	$ \Delta\phi_{ij} < 2$	160 – 200 GeV	0.28	± 0.065 (18%)	± 0.063 (23%)

 Table 6.7: The transfer factors f_{MJ}^i along with their statistical and systematic uncertainties. The discrepancy in SR1 between the FJVT and the R+S is handled by taking the average of the two predictions (labelled “comb.”) with an uncertainty that covers the difference.

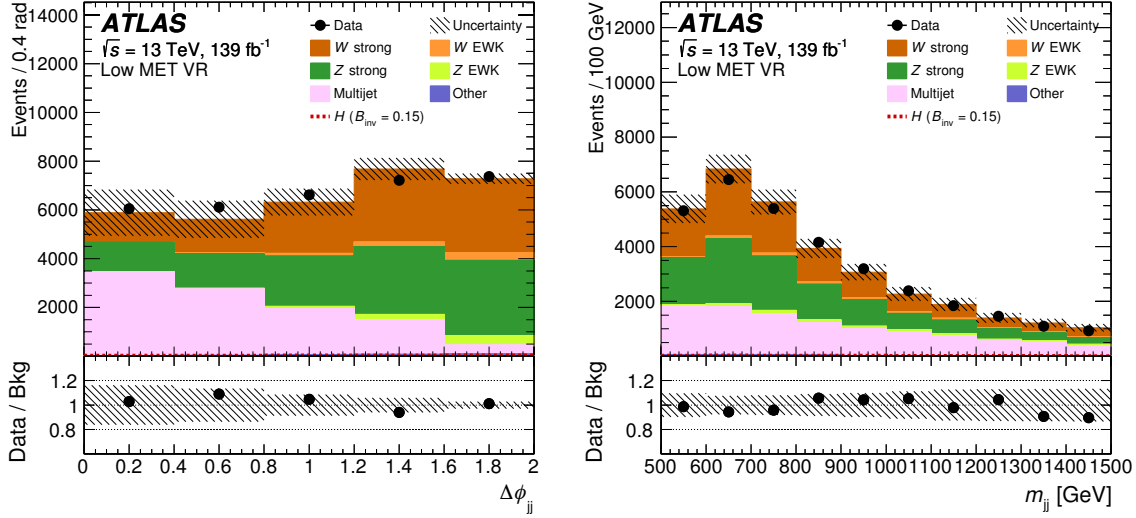


Figure 6.23: Comparison of data and predicted backgrounds in the multijet low E_T^{miss} CR.

estimate using control regions (CRs) is implemented. The CRs are defined with the same kinematic cuts as the signal region but with different number of leptons in the final state. A two lepton CR is used for $Z \rightarrow \ell\ell$ events and a one lepton CR is used for $W \rightarrow \ell\nu$ events. To obtain the W and Z background components, the MC prediction in a SR bin i is scaled by parameters $k_{i,W}$ ($k_{i,Z}$). These parameters are computed as the ratio data over MC in the W and Z CRs. The final estimate in the SR and the definition of the k-factors are given in Equation 6.3.

$$\begin{aligned}
 Z_{\text{SR}} &\approx \frac{Z_{\text{SR}}^{\text{MC}}}{Z_{\text{CR}}^{\text{MC}}} \cdot Z_{\text{CR}}^{\text{data}} = \frac{Z_{\text{CR}}^{\text{data}}}{Z_{\text{CR}}^{\text{MC}}} \cdot Z_{\text{SR}}^{\text{MC}} = \beta_Z \cdot Z_{\text{SR}}^{\text{MC}} \\
 W_{\text{SR}} &\approx \frac{W_{\text{SR}}^{\text{MC}}}{W_{\text{CR}}^{\text{MC}}} \cdot W_{\text{CR}}^{\text{data}} = \frac{W_{\text{CR}}^{\text{data}}}{W_{\text{CR}}^{\text{MC}}} \cdot W_{\text{SR}}^{\text{MC}} = \beta_W \cdot W_{\text{SR}}^{\text{MC}}
 \end{aligned} \tag{6.3}$$

The normalisation values $\beta_{Z,W}$ are obtained as parameters in the likelihood fit. Two alternatives have been tested using one normalisation factor for $W + \text{jets}$ and one for $Z + \text{jets}$ events, and using a common normalisation for both processes. The later benefits from larger statistics in the control W CR resulting in an improved sensitivity. This approach requires a precise understanding of the ratio between $Z + \text{jets}$ and $W + \text{jets}$ differential cross sections as discussed in Section 5.2.2 and it is used for the final results of this analysis.

6.2.1 Z CR

The $Z \rightarrow \ell\ell$ control region is defined in Section 5.3.8. There is one CR for each signal region bin. The sum of these control regions is shown in this section. The summed CR has a purity in $Z + \text{jets}$ events

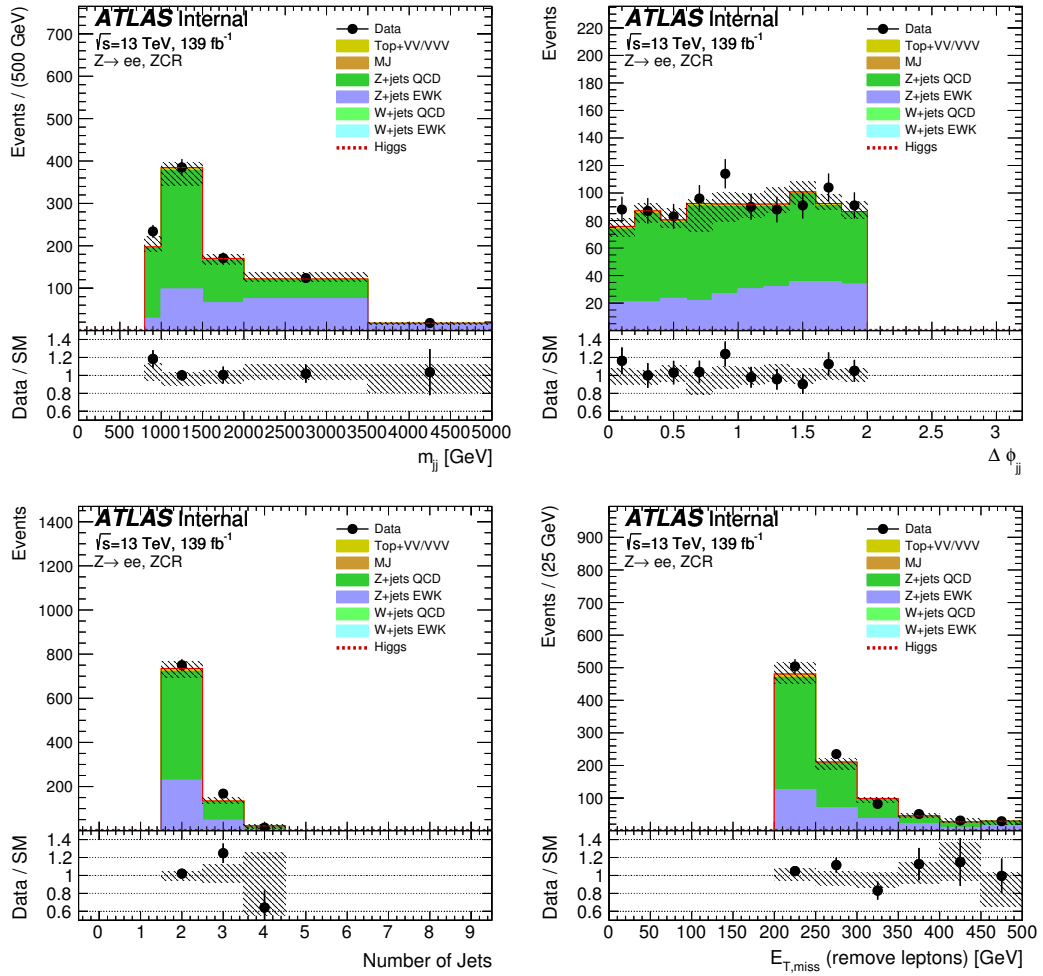


Figure 6.24: The distributions of m_{jj} , $\Delta\phi_{jj}$, N_{jet} , and E_T^{miss} are shown with the 139 fb^{-1} dataset from 2015 to 2018 in the summed $Z \rightarrow ee$ control regions. The hashed band indicates statistical and reconstruction systematic uncertainties.

greater than 90%. A comparison of the MC estimate and the experimental data is shown in Figures 6.24 and 6.25 for $Z \rightarrow ee$ and Figures 6.26 and 6.27 for $Z \rightarrow \mu\mu$. Overall no large disagreement with the data is observed.

6.2.2 W CR

The $W \rightarrow \ell\nu$ control region is defined in Section 5.3.8. There is one CR for each signal region bin. The sum of these control regions is shown in this section.

The $W \rightarrow e\nu$ control region has a contribution of events with a jet from multijet processes misidentified as an electron. To suppress this background the E_T^{miss} significance (see Section 5.3.6)

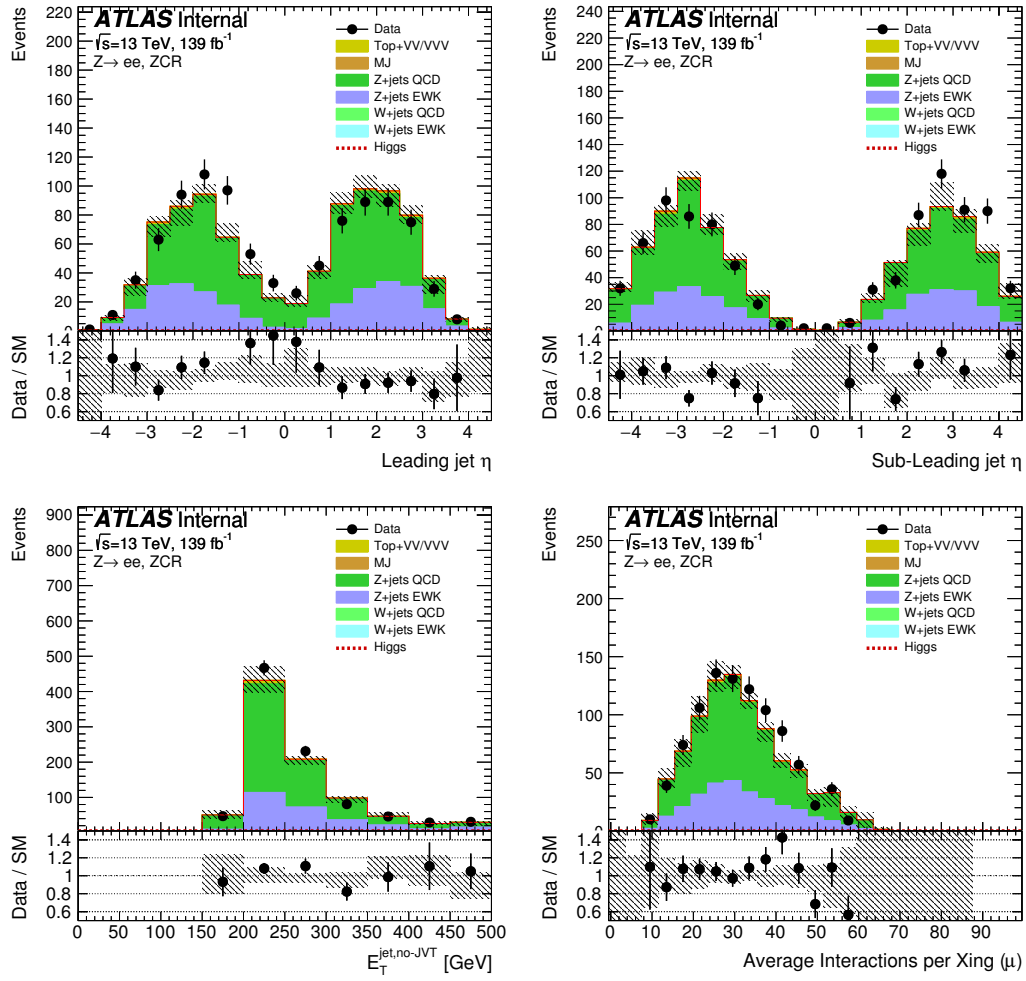


Figure 6.25: The distributions of leading jet η , sub-leading jet η , $E_T^{\text{jet,no-jvt}}$, and average pile-up per bunch crossing (μ) are shown with the 139 fb^{-1} dataset from 2015 to 2018 in the summed $Z \rightarrow ee$ control regions. The hashed band indicates statistical and reconstruction systematic uncertainties.

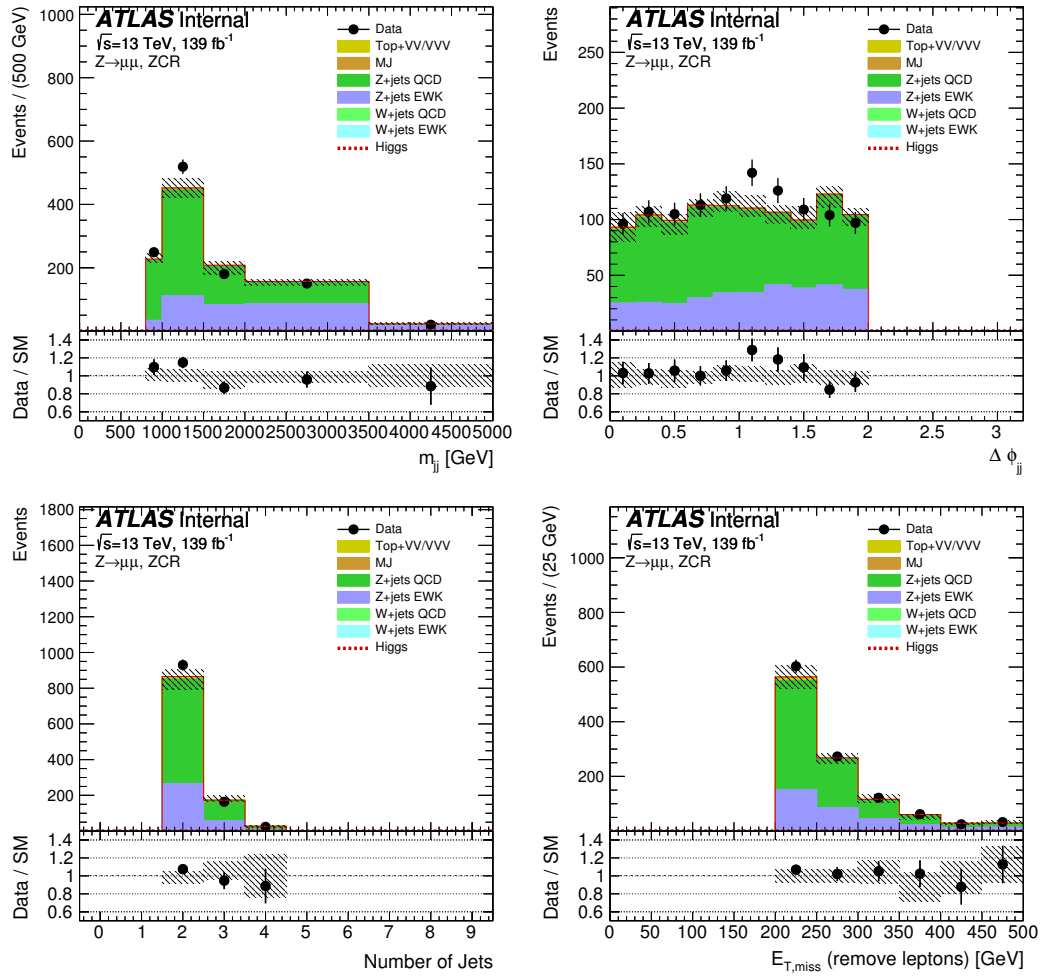


Figure 6.26: The distributions of m_{jj} , $\Delta\phi_{jj}$, N_{jet} , and E_T^{miss} are shown with the 139 fb^{-1} dataset from 2015 to 2018 in the summed $Z \rightarrow \mu\mu$ control regions. The hashed band indicates statistical and reconstruction systematic uncertainties.

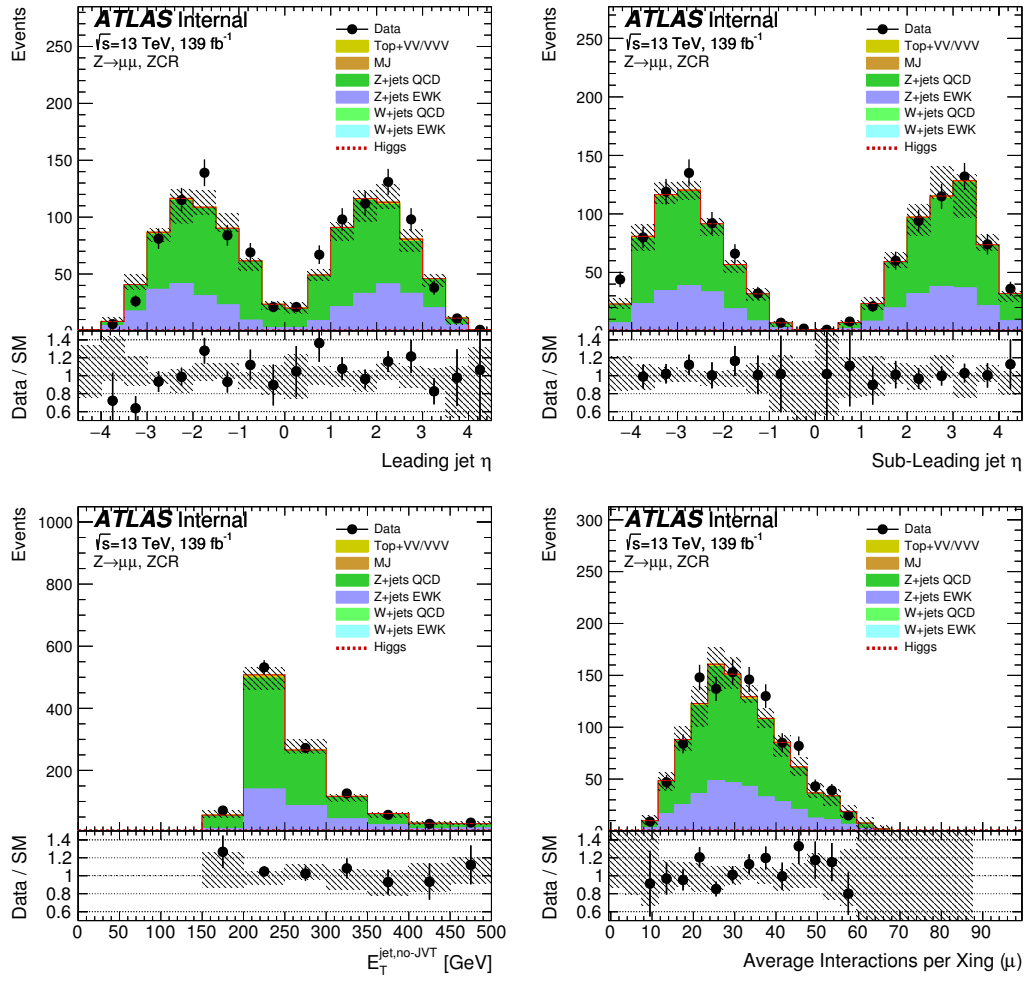


Figure 6.27: The distributions of leading jet η , sub-leading jet η , $E_T^{\text{jet,no-jvt}}$, and average pile-up per bunch crossing (μ) are shown with the 139 fb^{-1} dataset from 2015 to 2018 in the summed $Z \rightarrow \mu\mu$, ZCR control regions. The hashed band indicates statistical and reconstruction systematic uncertainties.

is required to be larger than $4\sqrt{\text{GeV}}$. The events that fail this selection define the "fake- e " CR. This region is enriched by fake electron and the amount of this background can be computed as the data minus the non fake- e events in the 16 bins analogous to the SR. A $W \rightarrow e\nu$ anti-ID region is defined by events with a signal lepton passing the loose identification requirement but not passing the tight one. The ratio of events with $S_{\text{MET}} > 4$ and $S_{\text{MET}} < 4$ is computed as a transfer factor R_S between the low E_T^{miss} significance and high E_T^{miss} significance regions. The final contribution of the fake- e background to the $W \rightarrow e\nu$ CR is the transfer factor times the event yields corresponding to the fake- e CR.

An analogous procedure is followed in the $W \rightarrow \mu\nu$ CR in order to compute the contribution from jets misidentified as muons. The key variable in this case is m_T (see Section 5.3.7). A cut $m_T > 20$ GeV is applied in order to reduce this background. Events not satisfying this cut define the fake- μ CR. An anti-ID region and a transfer factor R_M are defined analogous to the fake- e case. The final contribution of the fake- μ background to the $W \rightarrow \mu\nu$ CR is the transfer factor times the event yields corresponding to the fake- μ CR.

A comparison of the background estimates and the experimental data in the summed W CR is shown in Figures 6.28 and 6.29 for $W \rightarrow e\nu$, and in Figures 6.30 and 6.31 for $W \rightarrow \mu\nu$.

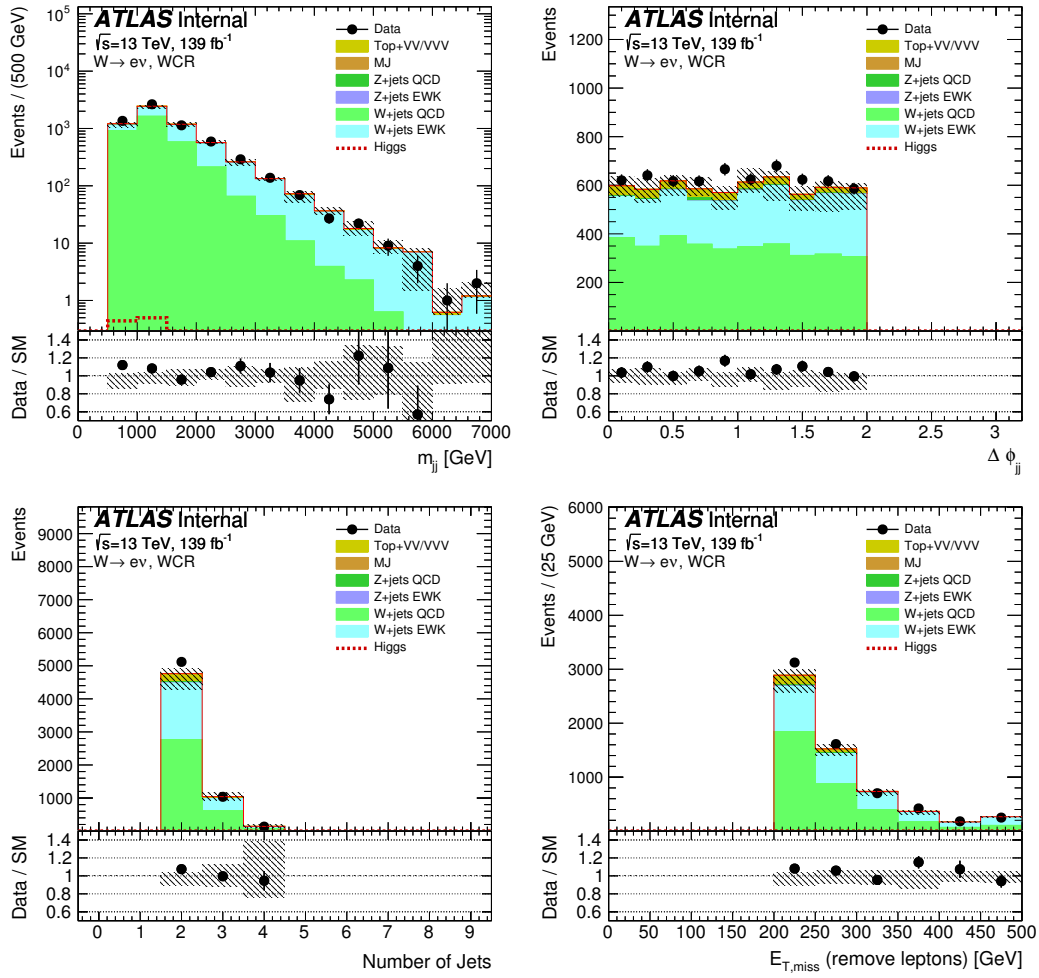


Figure 6.28: The distributions of m_{jj} , $\Delta\phi_{jj}$, N_{jet} , and $E_{T,miss}$ are shown with the 139 fb^{-1} dataset from 2015 to 2018 in the summed $W \rightarrow ev$ control regions. The hashed band indicates statistical and reconstruction systematic uncertainties.

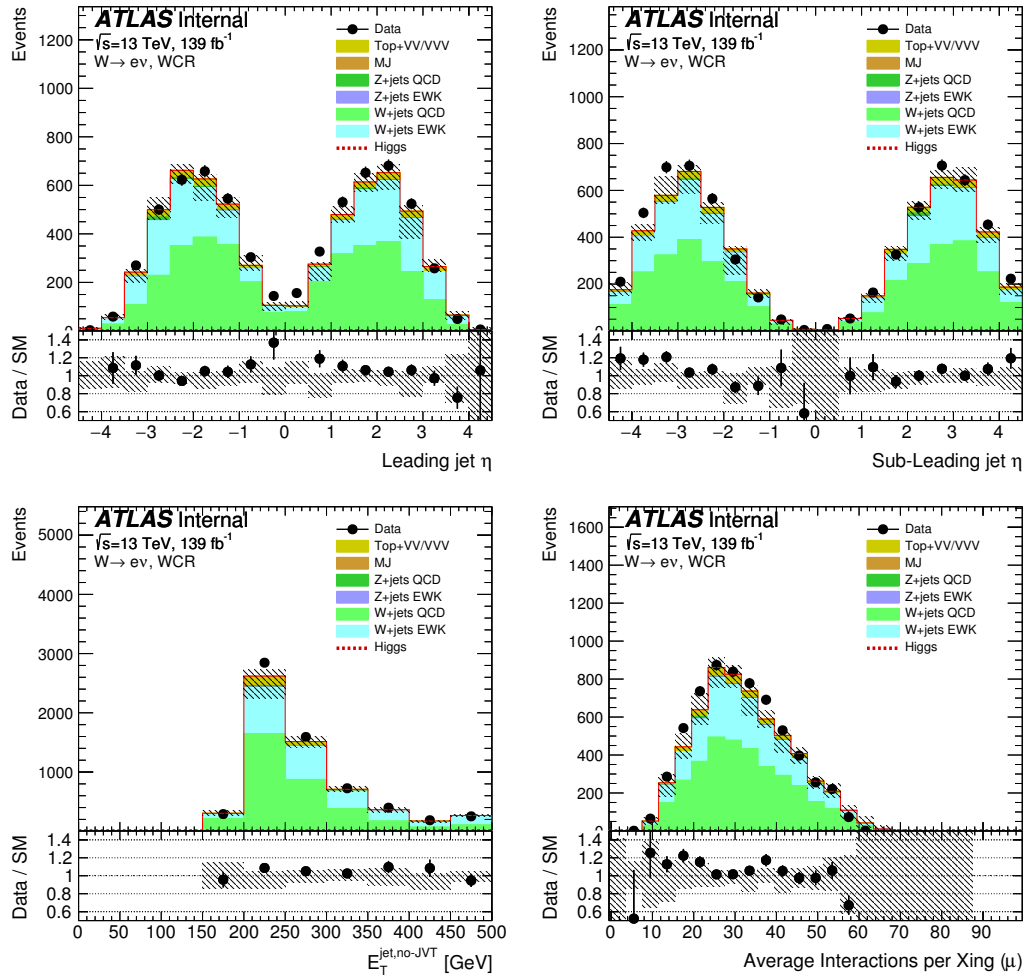


Figure 6.29: The distributions of leading jet η , sub-leading jet η , $E_T^{\text{jet,no-jvt}}$, and average pile-up per bunch crossing (μ) are shown with the 139 fb^{-1} dataset from 2015 to 2018 in the summed $W \rightarrow e\nu$ control regions. The hashed band indicates statistical and reconstruction systematic uncertainties.

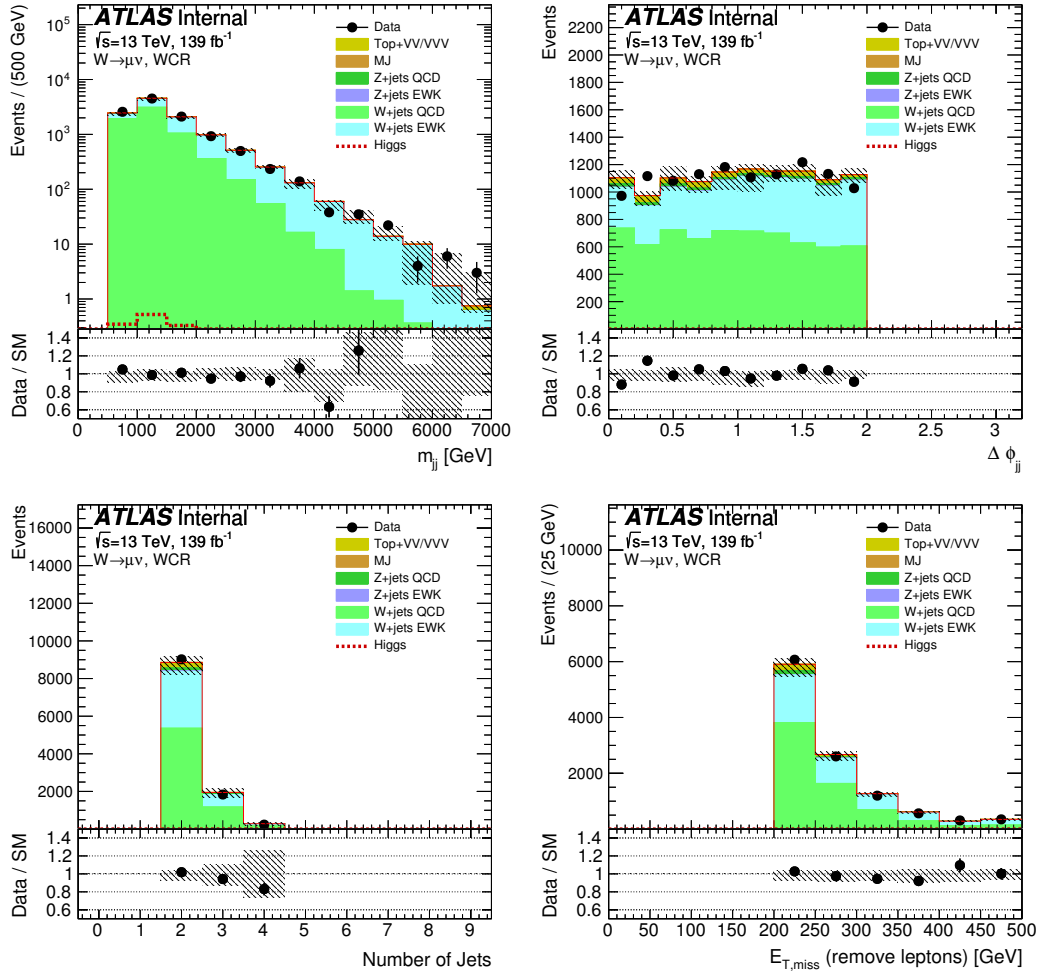


Figure 6.30: The distributions of m_{jj} , $\Delta\phi_{jj}$, N_{jet} , and $E_{T, \text{miss}}^{\text{miss}}$ are shown with the 139 fb^{-1} dataset from 2015 to 2018 in the summed $W \rightarrow \mu\nu$ control regions. The hashed band indicates statistical and reconstruction systematic uncertainties.

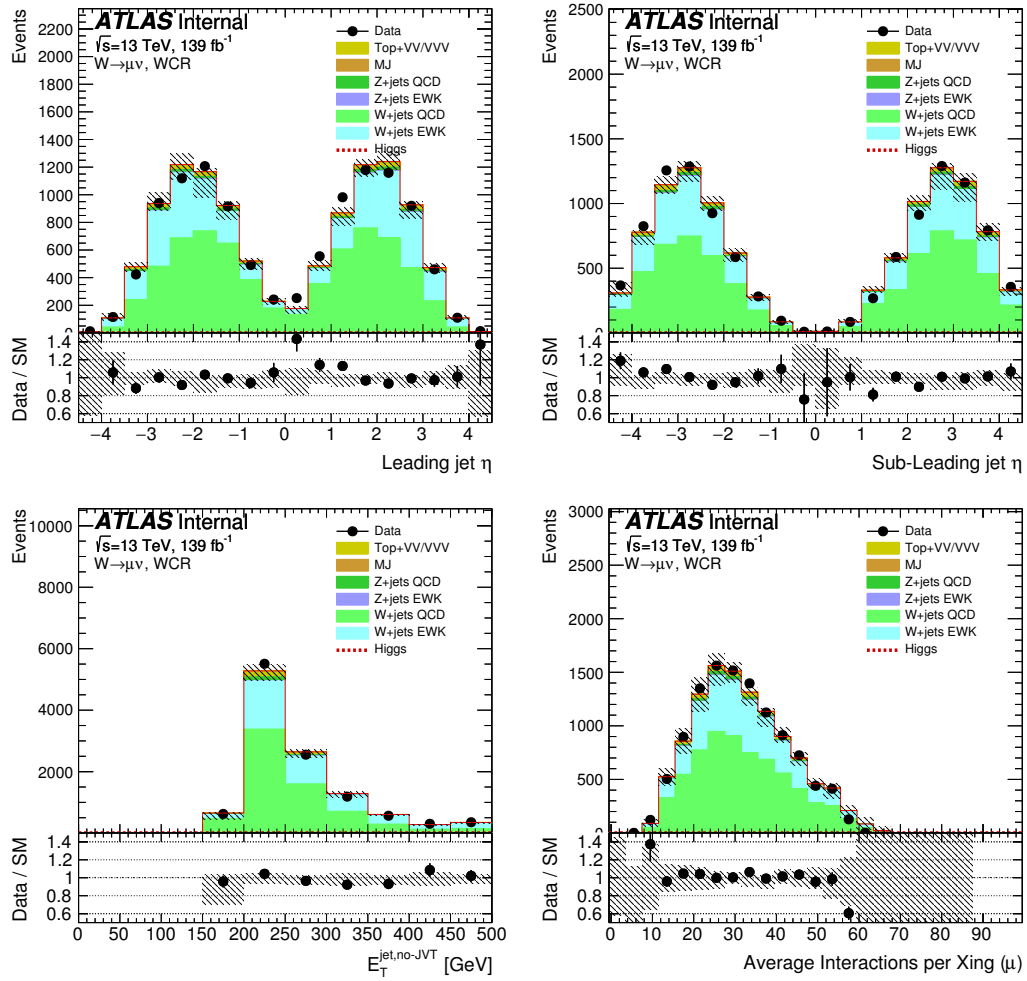


Figure 6.31: The distributions of leading jet η , sub-leading jet η , $E_T^{\text{jet,no-jvt}}$, and average pile-up per bunch crossing (μ) are shown with the 139 fb^{-1} dataset from 2015 to 2018 in the summed $W \rightarrow \mu\nu$ control regions. The hashed band indicates statistical and reconstruction systematic uncertainties.

Systematic uncertainties

There are three main sources of experimental uncertainties in the analysis: the luminosity, the trigger and the physics objects (leptons, jets and E_T^{miss}). In addition, there are several theory uncertainties caused by the finite precision of the Monte Carlo simulations, e.g. the limited order at which the matrix elements are computed. Sections 7.1.1 to 7.1.5 summarise the experimental systematic uncertainties and Section 7.2 summarises the theoretical uncertainties.

7.1 Experimental uncertainties

7.1.1 Luminosity

The precision on the integrated luminosity measurements changes over the data taking periods in ATLAS. For the years 2015, 2016, 2017 and 2018, the relative uncertainty on the luminosity was 2.1, 3.4, 2.4, and 2.0%, respectively. For the total dataset 2015-2018, the relative uncertainty is 1.7%, measured with the LUCID-2 sub-detector[86].

7.1.2 Trigger

In the SR ($E_T^{\text{miss}} > 160$ GeV), the E_T^{miss} trigger is not fully efficient. Systematic uncertainties are assigned comparing the trigger turn on curves in data and simulation to account for potential differences in the trigger efficiencies. These efficiencies agree within 1%. Additional uncertainties arise from possible differences in the trigger efficiency between Z + jets and W + jets events [142, 163]. This component is obtained comparing the trigger turn on curves in MC samples. It is found to be smaller than 0.5% in all SR bins.

7.1.3 Lepton reconstruction

Uncertainties related to the leptons and photons are particularly relevant in the V + jets CRs. These uncertainties arise from the reconstruction, identification and isolation efficiencies, and the energy scale and resolution [114, 164]. Additionally, an uncertainty on the electron reconstruction inefficiency

for the electron veto is taken into account.

7.1.4 Jets

Jets are the key objects in the analysis SR. Systematic uncertainties arise from the b -jet response, flavour composition and response, energy scale (JES) and resolution (JER), pile-up tagging efficiency, pile-up calibration and η -intercalibration [165]. The JES relative systematic uncertainties for central jets with $|\eta| < 1.2$ show a p_T dependence ranging from 5% at low jet p_T to 1% at high jet p_T . The JER uncertainty vary between 1.5% and 0.5% from low to high jet p_T values. The systematic uncertainties on jets are propagated to the calculation of E_T^{miss} to evaluate their impact on the predicted yields.

7.1.5 Missing transverse momentum

The uncertainties on the reconstructed objects used in the calculation of E_T^{miss} are propagated to the reconstruction of this variable. Additionally, the uncertainties on the soft track term scale and resolution measured in data to simulation comparisons [166] are propagated to the total E_T^{miss} uncertainty.

7.2 Theoretical uncertainties

The theoretical uncertainties affect both signal and background processes. They originate from fixed scale choices and modelling of the event generation, limited precision of perturbative calculations, and our description of parton showers and the proton substructure.

7.2.1 V + jets uncertainties

The simulation of the background processes is performed at fixed orders and requires the choice of fixed parameters related to higher-order matrix elements and parton shower matching uncertainties. These uncertainties are assessed by varying the four scale choices used in the event generation: the renormalisation, factorisation, resummation, and CKKW matching scales [167]. The CKKW matrix element matching scale is used for calculating the overlap between the parton shower and matrix element objects. The resummation scale is used for the resummation of gluon emission in parton shower calculations. The factorisation and renormalisation scales are choices in the fixed matrix element calculation related to the treatment of infrared and ultraviolet divergences.

The factorisation and renormalisation scales are varied up and down by a factor of two using on-the-fly event weights in the Sherpa MC simulation. As a consequence the nominal and varied samples are fully statistical correlated. The uncertainties are determined by taking an envelope of the seven factorisation/renormalisation scale variations: the central value, each scale independently varied up/down, and both scales coherently varied up/down. The effect of these uncertainties on the expected event yields for the strong V + jets background vary as a function of m_{jj} from $^{+27}_{-18}$ at low m_{jj} to $^{+43}_{-26}$ at high m_{jj} . For the electroweak V + jets processes, the uncertainties range from 2% – 4% for

Z + jets, and 1% – 8% for W + jets.

The resummation scale is also varied by a factor of two but in this case separated varied samples are needed. Because of computing limitations, these samples cannot be reconstructed and an alternative approach is followed. The effect of the variations is determined at truth level and a reweighting is applied on the fully-reconstructed nominal sample. The uncertainty in each analysis bin is computed as half the difference between the up and down variations at truth level:

$$\text{rel. unc.} = \frac{r_{\text{up}} - r_{\text{down}}}{r_{\text{up}} + r_{\text{down}}}, \quad (7.1)$$

where r_{up} and r_{down} are the up and down variations respectively. The relative resummation scale uncertainties range from 4% to 6%. The CKKW matching scale is varied up to 30 GeV and down to 15 GeV from the nominal value of 20 GeV and a reweighting procedure is applied in the same way as for the resummation scale. The CKKW uncertainties range between 4% to 6%.

The PDF uncertainties of the V + jets backgrounds are evaluated as the standard deviation of the yields obtained by using an ensemble of 100 PDF replicas of the NNPDF set, resulting in uncertainties ranging from 1% to 2%.

All theoretical uncertainties are treated as uncorrelated between strong and electroweak processes. Uncertainties on Z and W are assumed as fully correlated, allowing a cancellation of the uncertainties in the SR. To quantify that cancellation, the variation of the ratio of each background in the SR to the corresponding CR is calculated. The uncertainties on this ratio range from 1% to 3%.

The Z + jets MC is reweighted to a full NLO theoretical prediction on the ratio of Z and W cross sections as described in Section 5.2.2. The correction is derived separately for strong and electroweak V + jets production modes and there are several uncertainties associated to it. These systematic uncertainties are derived as a function of $x = m_{jj}$ as follows. There is a QCD and a mixed QCD-EWK component which is derived as the difference between LO and NLO calculations:

$$\delta\mathcal{R}_{\text{QCD}}^{Z/W}(x) = \left| \mathcal{R}_{\text{LO QCD}}^{Z/W}(x) - \mathcal{R}_{\text{TH}}^{Z/W}(x) \right|, \quad (7.2)$$

and

$$\delta\mathcal{R}_{\text{mix}}^{Z/W}(x) = \left| \mathcal{R}_{\text{NLO QCD+EWK}}^{Z/W}(x) - \mathcal{R}_{\text{TH}}^{Z/W}(x) \right|. \quad (7.3)$$

There is an uncertainty component due to the chosen parton shower (PS) model. For the EWK samples this is computed from the difference in the ratio Z/W using a dipole recoil model and an angular ordered parton shower model [168]:

$$\delta\mathcal{R}_{\text{PS}}^{Z/W}(x) = \left| \mathcal{R}_{\text{HERWIG 7,dipole}\times\text{EWK}}^{Z/W}(x) - \mathcal{R}_{\text{HERWIG 7,AO}}^{Z/W}(x) \right|. \quad (7.4)$$

For the strong V + jets samples, the PS uncertainty is obtained from the difference between the nominal ratio $\mathcal{R}_{\text{TH}}^{Z/W}$ and this ratio computed at NLO plus parton shower:

$$\delta\mathcal{R}_{\text{PS}}^{Z/W}(x) = \left| \mathcal{R}_{\text{NLOPS QCD}\times\text{EWK}}^{Z/W}(x) - \mathcal{R}_{\text{TH}}^{Z/W}(x) \right|. \quad (7.5)$$

Finally, there is a reweighting uncertainty due to differences between the analysis and the NLO theoretical predictions in the selection used to compute the Z/W ratio. In particular, the third jet veto (TJV) is not applied in the calculations. These uncertainties are obtained computing the difference in the ratio with and without the jet veto in the ATLAS MC:

$$\delta\mathcal{R}_{\text{Rew}}^{Z/W}(x) = \left| \mathcal{R}_{\text{SHERPA, TJV}}^{Z/W}(x) - \mathcal{R}_{\text{SHERPA}}^{Z/W}(x) \right|. \quad (7.6)$$

To account for potential differences in the correction as a function of $\Delta\phi_{\text{jj}}$ due to interference with EWK diboson production, the EWK Z/W ratio is computed in bins of $\Delta\phi_{\text{jj}}$ $[0, 1]$, $[1, 2]$ and > 2 , as well as inclusively. The inclusive correction is taken as the nominal correction and the difference to the corrections in the three bins are taken as a systematic uncertainty:

$$\delta\mathcal{R}_{\text{Rew } i}^{Z/W}(x) = \left| \mathcal{R}_{\text{TH, bin } i}^{Z/W}(x) - \mathcal{R}_{\text{TH}}^{Z/W}(x) \right|. \quad (7.7)$$

The systematic uncertainties on the Z/W ratio are shown in Figures 5.4 and 5.5. The QCD and mixed QCD-EWK uncertainties are in the range 2 – 5%, the parton shower uncertainty is in the range 3 – 5%, the reweighting uncertainty is between 2% at low m_{jj} values and 13% at high m_{jj} for the strong V + jets MC and between 1% to 11% for the EWK V + jets.

7.2.2 Signal uncertainties

The dominant uncertainties on the signal processes originate from the parton shower, PDF, QCD and EWK scale uncertainties. The VBF and ggF Higgs boson production cross sections and uncertainties are assigned following the recommendations from the LHC Higgs working group [21]. A p_{T} -dependant NLO electroweak correction from HAWK [169] is applied on the VBF process with an associated uncertainty of 2%. The renormalisation and factorisation uncertainties depend on m_{jj} and are computed varying individually the renormalisation and factorisation scale. The jet veto uncertainty is computed using the Stewart-Tackmann technique [170], resulting in uncertainties in a range between 1% and 3%. The parton shower uncertainty is determined in a comparison between VBF signal samples showered in PYTHIA and POWHEG +HERWIG 7. These uncertainties range from 1% - 3%. The PDF uncertainties assessed from variations of PDF replicas of the NNPDF set range from 1% - 2%.

The uncertainties on the ggF process are assigned in the same way as for the VBF signal. Renormalisation and factorization scales, PDF and parton shower uncertainties are assigned. A Stewart-Tackmann procedure is used to estimate the jet bin migration uncertainty, resulting in an uncertainty of 45% for $n_{\text{jet}} = 2$ and 41% for $n_{\text{jet}} = 3$ or 4.

Results

This section summarises the statistical treatment and the results of the different likelihood fits to the validation regions, control regions and signal regions. The pre-fit event yields for the background and signal processes, and the observed data are summarised in Table 8.1 for the inclusive SR and the different CRs. The background-only hypothesis is tested, in the absence of an excess over the SM prediction an upper limit on the branching ratio of invisible Higgs boson decays (\mathcal{B}_{inv}) is set at 95% CL using the Asymptotic formulae for the CLs frequentist approach [137–139]. The Statistical model is described in Section 8.1. A fit in the high $\Delta\phi_{\text{jj}}$ validation region used to test the background estimates is presented in Section 8.2. A control region only fit used to test the model across the different CRs is explained in Section 8.3. The SR+CR fits are presented in Section 8.4. The limit on \mathcal{B}_{inv} is translated as a limit on the spin-independent WIMP-nucleon cross section using Higgs-portal models and an interpretation for a search of invisible decays of a heavy scalar boson mediator with a mass different than the SM Higgs boson are presented in Section 8.5. The results of this analysis have been submitted to JHEP [25].

8.1 Statistical treatment

The signal and background event yields are obtained from a maximum profiled likelihood fit [139]. The likelihood function is a product of the Poisson probabilities to observe the data count $N_i^{\text{CR/SR}}$ in the analysis bin i , from a corresponding signal plus background model. In each bin, the model for the expected event count depends on the background and signal estimates and a set of nuisance parameters θ_j that represent experimental and theoretical uncertainties. The likelihood function for the complete analysis can be expressed as the product of different components corresponding to the SRs, the CRs, and the nuisance parameters. The $V + \text{jets}$ background estimates are normalised by common W and Z scale factors β_i for both strong and electroweak production modes. The multijet estimate is obtained from the transfer factors of the pile-up CRs as defined in Section 6.1.7 and the fake-lepton estimates are extracted using transfer factors of the corresponding CRs as defined in Sections 6.2. The signal normalisation is obtained from the signal strength μ .

The signal region yield likelihood is

Process	SR	$Z_{\ell\ell}$ CR	$W_{e\nu}$ CR	$W_{\mu\nu}$ CR	Fake- e CR	Fake- μ CR	Pile-up CR
Z strong	6030 ± 2050	1220 ± 440	42 ± 14	143 ± 21	160 ± 57	40 ± 14	$42 \pm^{59}_{42}$
Z EWK	2630 ± 260	618 ± 74	12.1 ± 1.8	28.3 ± 3.3	23.5 ± 3.3	15.3 ± 2.8	7.2 ± 3.1
W strong	3710 ± 1300	-	3260 ± 1180	5170 ± 1850	1810 ± 650	1010 ± 370	$49 \pm^{92}_{49}$
W EWK	1610 ± 150	-	2360 ± 190	3410 ± 240	1400 ± 140	822 ± 69	22.9 ± 7.7
Fake- e	-	-	191 ± 70	-	1100 ± 330	-	-
Fake- μ	-	-	-	43 ± 15	-	130 ± 51	-
Multijet	830 ± 190	-	-	-	-	-	1890 ± 110
Other	180 ± 46	46 ± 25	346 ± 82	351 ± 71	67 ± 13	89 ± 27	19.5 ± 9.0
Total bkg.	14990 ± 2990	1880 ± 510	6210 ± 1260	9150 ± 1890	4560 ± 760	2110 ± 390	2030 ± 110
H (VBF)	886 ± 81						3.9 ± 1.3
H (ggF)	106 ± 41						$1.0 \pm^{1.5}_{1.0}$
H (VH)	0.9 ± 0.2						-
Data	16490	2051	6361	9294	4563	2110	2033

Table 8.1: Observed and expected background event yields with associated uncertainties in the signal region (SR) and control regions ($Z_{\ell\ell}$ CR, $W_{e\nu}$ CR, $W_{\mu\nu}$ CR, fake- e CR, fake- μ CR, pile-up CR) prior to the likelihood fit. Minor backgrounds from $t\bar{t}$, VV , VVV , and VBF $H \rightarrow W^*W / \tau^+\tau^-$ are combined and labelled ‘other’. The uncertainties in the backgrounds include the statistical, experimental, and theoretical uncertainties, taking into account the correlations between the individual SR and CR bins. The predicted signal yields (VBF, ggF, and VH) for $\mathcal{B}_{\text{inv}} = 15\%$ (the observed limit) are presented for comparison. For all CRs with leptons, the contribution from the predicted signal is negligible.

$$\mathcal{L}^{\text{SR}} = \prod_i \mathcal{P} \left(N_i^{\text{SR}} | \beta_i \cdot B_{Z,i}^{\text{SR}} + \beta_i \cdot B_{W,i}^{\text{SR}} + B_{\text{MJ},i}^{\text{SR}} + B_{\text{other},i}^{\text{SR}} + \mu \cdot S_i^{\text{SR}} \right). \quad (8.1)$$

The factor β_i is used to scale the strong and electroweak components of the $V + \text{jets}$ estimates ($B_{Z,i}^{\text{SR}}$ and $B_{W,i}^{\text{SR}}$) in each SR bin i and in the corresponding CR bins. This has the effect of scaling the estimates by the appropriately weighted difference between the data counts and the estimates in the corresponding W and Z control regions bins.

The multijet pile-up CR likelihood is

$$\mathcal{L}^{\text{PU-CR}} = \prod_{i \in [1,5] \text{ or } \{6-10\} \text{ or } [14,16]} \mathcal{P} \left(N_i^{\text{PU-CR}} | B_{\text{non-MJ},i}^{\text{PU-CR}} + n_{\text{PU-MJ},i} \right), \quad (8.2)$$

where the product is done over each of the analysis bins $[1, 5]$ and $[14, 16]$, and an inclusive category for $\{6 - 10\}$. The background model consists on the estimates of the non-QCD backgrounds ($B_{\text{non-MJ},i}^{\text{PU-CR}}$) plus the multijet component $n_{\text{PU-MJ},i}$.

The multijet background estimate for a SR bin i is

$$B_{\text{MJ},i}^{\text{SR}} = \begin{cases} n_{\text{PU-MJ},i} \cdot R_{\text{MJ},i} & \text{for } i \in [1, 5] \text{ or } [14, 16] \\ n_{\text{PU-MJ},\{6-10\}} \cdot R_{\text{MJ},\{6-10\}} \cdot f_{\text{R+S},i} & \text{for } i \in [6, 10] \\ B_{\text{MJ-R+S},i}^{\text{SR}} & \text{for } i \in [11, 13] \end{cases} \quad (8.3)$$

where $R_{MJ,i}$ is the transfer factor from the pile-up multijet CR, $f_{R+S,i}$ is the m_{jj} shape factor from the R+S estimate, and $B_{MJ-R+S,i}^{SR}$ is the multijet estimate from the R+S method.

The $V + \text{jets}$ CR likelihood is split into the Z CR, the $W \rightarrow e\nu$, and $W \rightarrow \mu\nu$ CRs:

$$\begin{aligned} \mathcal{L}^{V+\text{jets-CR}} = & \prod_i \mathcal{P} \left(N_i^{Z\text{CR}} | \beta_i \cdot B_{Z,i}^{Z\text{CR}} + B_{\text{non-Z},i}^{Z\text{CR}} \right) \\ & \prod_i \mathcal{P} \left(N_i^{W\mu\nu\text{CR}} | \beta_i \cdot B_{W,i}^{W\mu\nu\text{CR}} + B_{\text{non-W},i}^{W\mu\nu\text{CR}} + R_M \cdot n_{\text{fake-}\mu,i} \right) \\ & \prod_i \mathcal{P} \left(N_i^{W e\nu\text{CR}} | \beta_i \cdot B_{W,i}^{W e\nu\text{CR}} + B_{\text{non-W},i}^{W e\nu\text{CR}} + R_S \cdot n_{\text{fake-}e,i} \right). \end{aligned} \quad (8.4)$$

The Z and W backgrounds are scaled by the same factor β_i as their components in the SR. The fake lepton contribution is equal to the transfer factor (R_S or R_M) times the fake lepton component obtained from the corresponding CR ($n_{\text{fake-}l,i}$).

The fake lepton CR likelihood is

$$\begin{aligned} \mathcal{L}^{\text{fake-CR}} = & \prod_i \mathcal{P} \left(N_i^{\text{fake-}\mu\text{CR}} | \beta_i \cdot B_{W,i}^{\text{fake-}\mu\text{CR}} + B_{\text{non-W},i}^{\text{fake-}\mu\text{CR}} + n_{\text{fake-}\mu,i} \right) \\ & \prod_i \mathcal{P} \left(N_i^{\text{fake-}e\text{CR}} | \beta_i \cdot B_{W,i}^{\text{fake-}e\text{CR}} + B_{\text{non-W},i}^{\text{fake-}e\text{CR}} + n_{\text{fake-}e,i} \right), \end{aligned} \quad (8.5)$$

the W background is scaled by the same normalisation factor β_i as in the other CRs and the non- W and non- Z are taken from the MC estimates.

The likelihood of the nuisance parameters is

$$\mathcal{L}^{\text{NP}} = \prod_j \mathcal{G} \left(0 | \theta_j \right), \quad (8.6)$$

where the $\mathcal{G} \left(0 | \theta_j \right)$ corresponds to a Gaussian distribution around 0 with a standard deviation given by the size of the systematic uncertainties.

Finally, the full likelihood is the product:

$$\mathcal{L} \left(\mu, \vec{\beta}_V, \vec{n}_{\text{PU-MJ/fake-}e/\text{fake-}\mu}, \vec{\theta} \right) = \mathcal{L}^{\text{SR}} \cdot \mathcal{L}^{\text{PU-CR}} \cdot \mathcal{L}^{V+\text{jets-CR}} \cdot \mathcal{L}^{\text{fake-CR}} \cdot \mathcal{L}^{\text{NP}}. \quad (8.7)$$

8.2 High $\Delta\phi_{jj}$ validation region fit

The high $\Delta\phi_{jj}$ validation region (VR) is used to test the background estimates and the corrections to the Z/W cross sections ratio discussed in Section 5.2.2. In the validation region only fit, the unblinded data and background estimates in the validation region is used, but no information from the signal

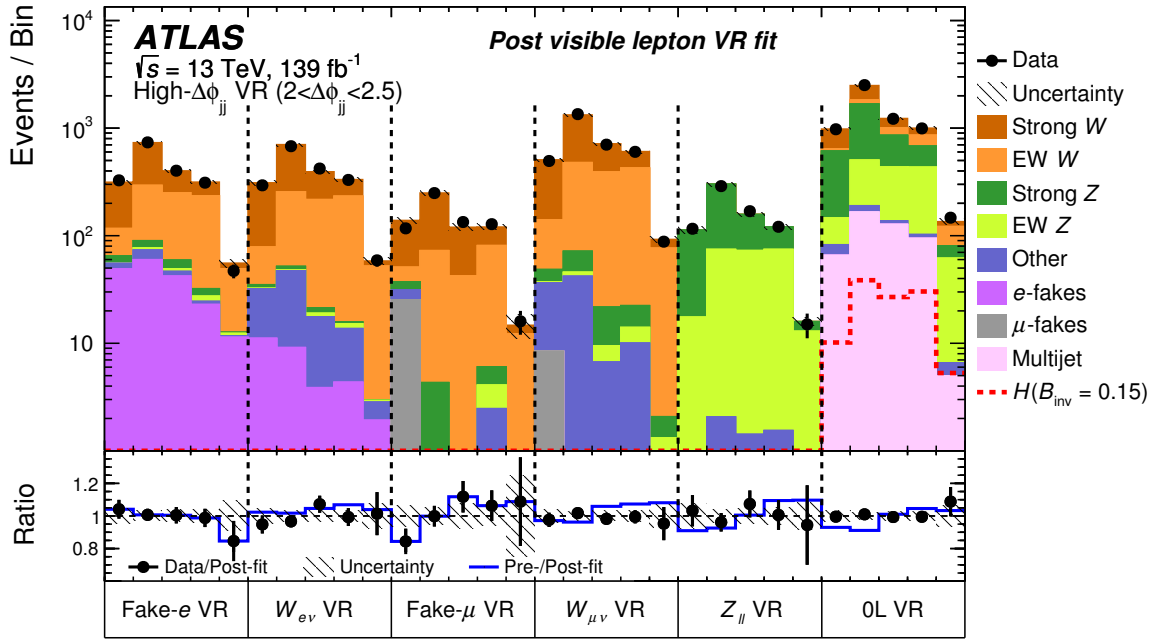


Figure 8.1: Comparison of data and background estimates in the high $\Delta\phi_{jj}$ VR after the likelihood fit.

region is used. The VR is split in five m_{jj} bins as the SR bins 1-5. The signal contribution is less than 13% of the signal to background which is below our blinding threshold. A background-only fit ($\mu = 0$) is performed excluding the 0-lepton bins. The background normalisation is extrapolated to the 0-lepton region and the post-fit estimates are shown in Figure 8.1. Overall a good agreement between the data and background estimates is observed. The normalisation factors for W and Z backgrounds (β_i) are shown in Table 8.2. These factors are defined to be around one unless there is an excess or deficit. All normalisation factors are compatible with one indicating a good agreement between the prediction and the experimental data.

m_{jj}	β_i $2 < \Delta\phi_{jj} < 2.5$
0.8–1.0 TeV	0.992 ± 0.351
1.0–1.5 TeV	0.956 ± 0.221
1.5–2.0 TeV	0.977 ± 0.180
2.0–3.5 TeV	0.948 ± 0.120
>3.5 TeV	0.885 ± 0.120

Table 8.2: The best fit values for β_i normalisation factors for W and Z using a VR only fit.

8.3 Control region only fit

The control region only fit is performed to ensure that the fit model is consistent between the different CRs. This fit makes use of the unblinded data and background estimates in the CRs, but no information from the SR is used in the fit. The signal strength μ is not floated in this fit. The post fit normalisations are propagated to the SR. The post fit data and background estimates are shown in Figure 8.2. The data is found to be compatible with the background-only prediction. The agreement is improved compared to the pre-fit agreement (blue line). The normalisation factors for W and Z backgrounds (β_i) are shown in Table 8.3. The resulting yields are expected to be relatively close to unity unless there is an excess or deficit in their corresponding bins.

Bin	m_{jj}	β_i
1	0.8–1.0 TeV	1.14 ± 0.02
2	1.0–1.5 TeV	1.11 ± 0.02
3	1.5–2.0 TeV	1.01 ± 0.03
4	2.0–3.5 TeV	0.97 ± 0.03
5	> 3.5 TeV	0.87 ± 0.08
6	0.8–1.0 TeV	1.18 ± 0.03
7	1.0–1.5 TeV	1.14 ± 0.02
8	1.5–2.0 TeV	0.97 ± 0.03
9	2.0–3.5 TeV	0.94 ± 0.03
10	> 3.5 TeV	0.81 ± 0.06
11	$2 < N_{\text{jet}} < 4, 1.5\text{--}2.0$ TeV	0.97 ± 0.03
12	$2 < N_{\text{jet}} < 4, 2.0\text{--}3.5$ TeV	0.86 ± 0.03
13	$2 < N_{\text{jet}} < 4, > 3.5$ TeV	0.96 ± 0.08
14	$160 < E_{\text{T}}^{\text{miss}} < 200$ GeV, 1.5–2.0 TeV	1.25 ± 0.03
15	$160 < E_{\text{T}}^{\text{miss}} < 200$ GeV, 2.0–3.5 TeV	1.00 ± 0.04
16	$160 < E_{\text{T}}^{\text{miss}} < 200$ GeV, > 3.5 TeV	0.52 ± 0.09

Table 8.3: The best fit values for β_i -normalisation factors for W and Z , in the SR bins using a CR only fit.

8.4 SR+CR fit

First, a background-only fit ($\mu = 0$) is performed in the unblinded SR+CR using the experimental data in both regions. The post-fit m_{jj} and $\Delta\phi_{jj}$ distributions are shown in Figure 8.4. Overall the data agrees with the background-only model with an excess larger than 1σ visible at high m_{jj} . At low m_{jj} the SR is dominated by strong V + jets background, at high m_{jj} the electroweak V + jets component dominates. A comparison between the post fit background estimates and the experimental data is shown in Figure 8.3. The comparison is shown in all SR and CR bins excluding the fake-leptons and pile-up CRs. The ratio between the pre-fit and post-fit estimates is shown with a blue line, it is observed that the agreement with the data is improved after the fit. The best fit values for the β_i normalisation factors are shown in Table 8.5.

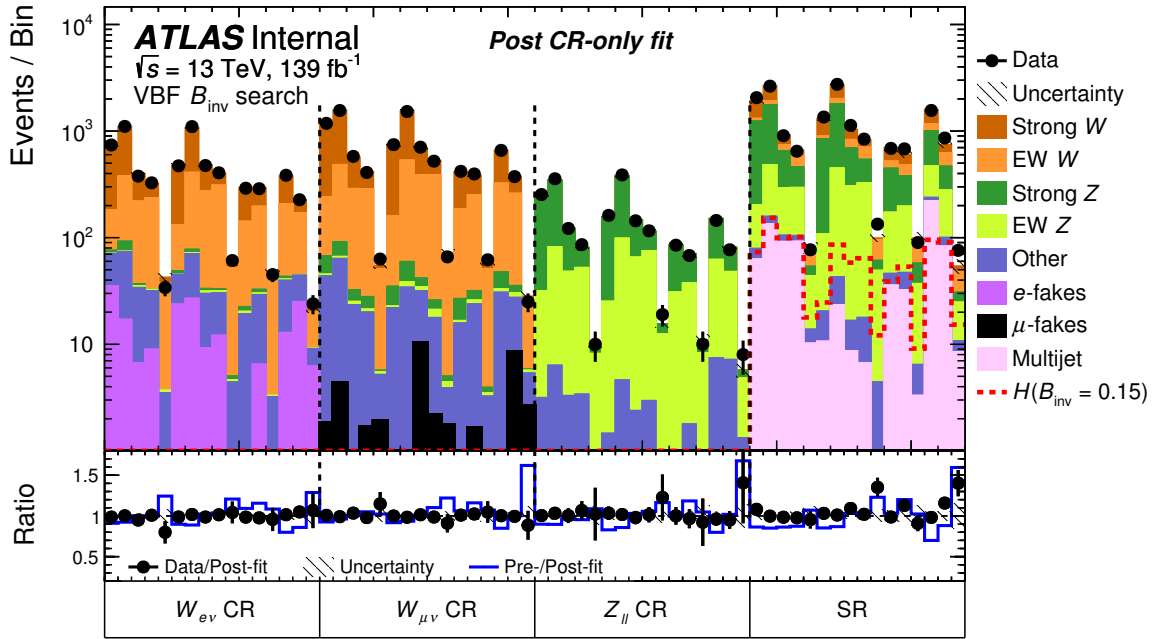


Figure 8.2: The unblinded control regions are shown for each of the 16 bins in a CR-only fit. The normalisations are propagated to the SR from the CR-only fit. The post-fit errors are statistical plus theory systematic uncertainties, and the normalisations are post fit.

In the absence of an excess over the Standard model prediction, exclusion limits on the branching ration of invisible Higgs boson decays are set at a 95% CL with the frequentist CLs approach. This limit is defined as the minimum value of the signal strength for which the signal is distinguishable from the background. The expected limit is computed using the V + jets normalised to the best fit parameters and the SR event yields are set to the prediction of the background-only model. The observed limit is computed using the signal + background model, simultaneously finding the best fit values for all the fit parameters including the signal strength μ and using the experimental data in the SRs and CRs. The best value for μ is 0.053 ± 0.052 . The observed and expected limit with its uncertainty band are shown in Table 8.4, an observed (expected) upper limit of 0.145 (0.103) is found. This corresponds to an excess slightly larger than 1σ which is in agreement with the excess observed at high m_{jj} .

Expected	Observed	+1 σ	-1 σ	+2 σ	-2 σ
0.103	0.145	0.144	0.075	0.195	0.056

Table 8.4: Expected and observed limits from full statistics plus systematic uncertainties fit with an control regions and signal regions unblinded, calculated at the 95% CL with 139 fb^{-1} .

The contributions to the 68% confidence interval of the fitted signal strength μ from different sources of systematic uncertainty are shown in Table 8.6. They are evaluated in a fit with a particular group of systematic uncertainties set to their best fit values, performing independent fits and removing the 1σ uncertainty quadratically from the nominal uncertainty that includes all systematic uncertainties.

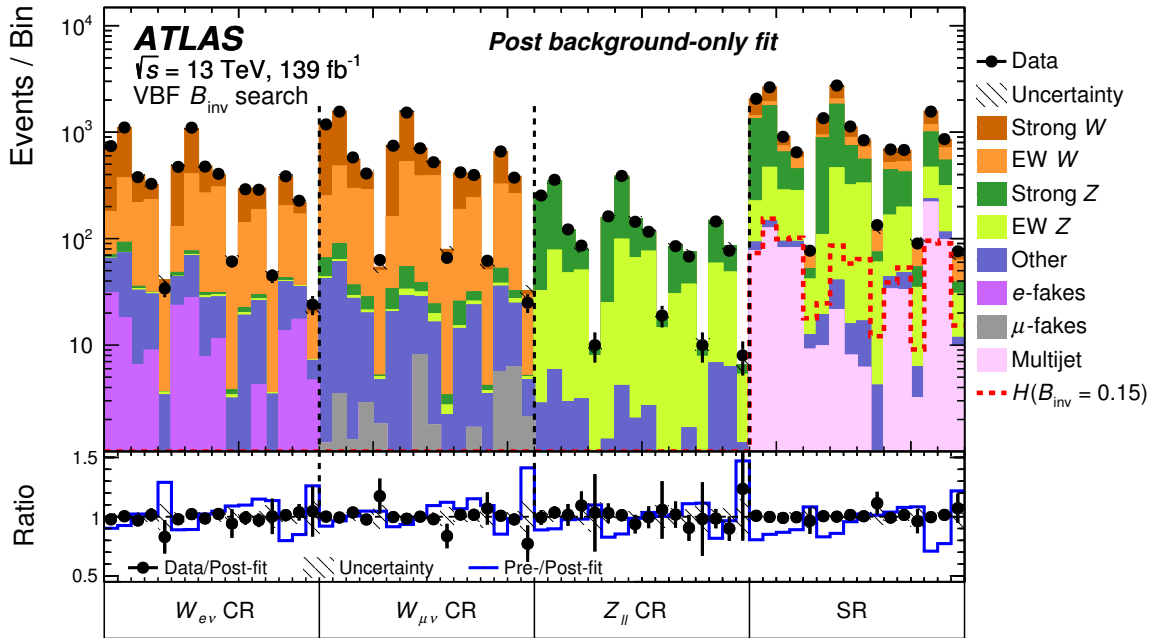


Figure 8.3: The unblinded signal regions and the main unblinded control regions are shown for each of the 16 bins in a background only fit. The post-fit errors are statistical plus theory systematic uncertainties, and the normalisations are post fit.

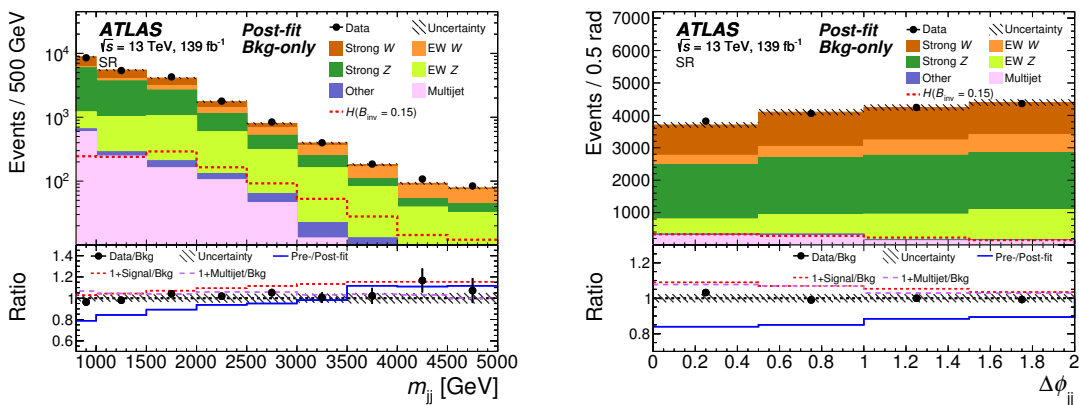


Figure 8.4: Post-fit distribution of m_{jj} (left) and $\Delta\phi_{jj}$ (right) in the inclusive SR.

Bin	m_{jj}	β_i
1	0.8–1.0 TeV	1.21 ± 0.02
2	1.0–1.5 TeV	1.09 ± 0.01
3	1.5–2.0 TeV	1.03 ± 0.02
4	2.0–3.5 TeV	0.97 ± 0.03
5	> 3.5 TeV	0.85 ± 0.07
6	0.8–1.0 TeV	1.23 ± 0.02
7	1.0–1.5 TeV	1.16 ± 0.01
8	1.5–2.0 TeV	0.99 ± 0.02
9	2.0–3.5 TeV	0.95 ± 0.02
10	> 3.5 TeV	0.94 ± 0.05
11	$2 < N_{\text{jet}} < 4, 1.5\text{--}2.0$ TeV	1.01 ± 0.03
12	$2 < N_{\text{jet}} < 4, 2.0\text{--}3.5$ TeV	0.86 ± 0.02
13	$2 < N_{\text{jet}} < 4, > 3.5$ TeV	0.93 ± 0.06
14	$160 < E_{\text{T}}^{\text{miss}} < 200$ GeV, 1.5–2.0 TeV	1.24 ± 0.03
15	$160 < E_{\text{T}}^{\text{miss}} < 200$ GeV, 2.0–3.5 TeV	1.06 ± 0.03
16	$160 < E_{\text{T}}^{\text{miss}} < 200$ GeV, > 3.5 TeV	0.62 ± 0.07

Table 8.5: The best fit values for β_i -normalisation factors for V + jets using a fit to the unblinded control regions and signal regions

The leading uncertainties are the data and MC statistic uncertainties, and the systematic uncertainties on the multijet and the fake lepton estimates. Alternatively, one can follow the same approach but removing quadratically the limit with one group of uncertainties set to their best fit values from the nominal limit. The ratio between this quadratic difference and the nominal limit can be taken as a measure of the impact of the uncertainties on the limit. This is reported in Table 8.7.

The improvements on the \mathcal{B}_{inv} upper limit caused by the different changes studied over the analysis optimization are shown in Table 8.8. Extrapolating the previous ATLAS result [22] of an expected upper limit on \mathcal{B}_{inv} of 0.28 fb^{-1} to 139 fb^{-1} , the expected limit is 18%. The split of the SR into m_{jj} , $\Delta\phi_{jj}$ and $E_{\text{T}}^{\text{miss}}$ bins of, increment of MC statistics, innovations in the multijet background estimate and the use of W boson to constrain the Z events are shown to have sizable impacts between 3 and 17 % on the limit.

8.5 Interpretation of the \mathcal{B}_{inv} upper limit

The upper limit on invisible Higgs boson decays can be connected to the nucleon-WIMP interaction cross section ($\sigma_{\text{WIMP-nucleon}}$). This allows for a direct comparison between the analysis result and direct detection experiments. In order to compare with direct detection experiments, the 90% CL limit on the \mathcal{B}_{inv} was computed. The obtained observed (expected) limit is 12.7% (8.7 %). The \mathcal{B}_{inv} upper limit is translated into a limit on $\sigma_{\text{WIMP-nucleon}}$ using the effective field theory (EFT) framework with a BSM physics scale at $O(1)$ TeV which is well above the Higgs boson mass (see Section 2.6.1).

Table 8.6: The contributions to the 68% confidence interval of the fitted signal strength μ from different sources of systematic uncertainty. Due to residual correlations between categories, the sum in quadrature of the individual contributions only approximately equals the total uncertainty. The entry ‘V+ jets data stats.’ is the statistical uncertainty originating from data yields for the W and Z normalisation. The ‘Remaining’ category contains $E_{\text{T}}^{\text{miss}}$, luminosity, and pile-up uncertainties, and a diboson uncertainty in the $Z_{\ell\ell}$ CR.

Source	Contribution to $\pm 1\sigma$ (= 0.052)
Data stats.	0.029
V+ jets data stats.	0.022
MC stats.	0.014
Multijet	0.021
μ/e -fakes	0.019
Lepton	0.017
(Lepton – muon only)	0.0049
(Lepton – electron only)	0.016
JER	0.015
JES	0.011
Remaining	0.012
V+ jets – theory	0.015
Signal – theory	0.0056

Source	Δ [%]
Jet energy scale	2.1
Jet energy resolution	4.2
Fake leptons	6.5
Lepton ID	5.3
Multijet	5.0
Other	2.8
V+ jets theory	4.2
Signal theory	0.6
MC stats.	3.8
V+ jets data stats.	9.4
Remaining data stats.	8.7

Table 8.7: Relative impact Δ of the 95% CL expected upper limit on \mathcal{B}_{inv} if a group of uncertainties is ‘removed’, i.e. if the corresponding nuisance parameters are fixed to their best fit values. Fixing all nuisance parameters to their best fit values and subtracting the resulting value in quadrature from the expected limit provides an estimate of the impact of the data statistical uncertainties, which is shown in the last row.

Description	Expected limit	% Change Rel. Prev. Step
3-bin $E_T^{\text{miss}} > 180$ GeV no fjvt	18%	–
3-bin $E_T^{\text{miss}} > 180$ GeV with fjvt	15%	17%
11-bin $E_T^{\text{miss}} > 200$ GeV	13.2%	13%
Increased MC stats	12.5%	5%
Additional binning ($160 < E_T^{\text{miss}} < 200$ GeV)	12.1%	3%
MJ updates	10.9%	10.0%
W to constrain Z	10.3%	6%

Table 8.8: The improvement compared to the previous ATLAS publication to the 95% CL limits from the increased MC sample size, the additional SR binning, the MJ updates, and lastly the W to constrain Z .

The exclusion limits on the WIMP-nucleon scattering cross section are compared with other experiments in Figure 8.5. Different WIMP scenarios are shown: a scalar, Majorana, and a vector EFT and a full UV complete model. The Lagrangians for these models are shown in Section 2.6.1. Because of the different couplings between the scalar, fermion or vector DM particles and the Higgs boson, the exclusion limits depend on the spin of the DM candidate. The weakest limit is for a scalar particle and the strongest is for a vector DM candidate. For the UV complete model, the introduction of a "Dark Higgs" particle is needed and the WIMP-nucleon interaction cross section depends on the mass of this new particle m_2 . A conservative case ($m_2 = 0.1$ GeV), a moderate one ($m_2 = 10$ GeV), and an optimistic scenario ($m_2 = 100$ GeV) are shown to illustrate how this exclusion limits vary as a function of m_2 . Our result excludes cross section values ranging from $\mathcal{O}(10^{-42} \text{ cm}^2)$ to $\mathcal{O}(10^{-46} \text{ cm}^2)$. The neutrino floor corresponds to a limit at which the background from solar neutrinos is irreducible defining a sensitivity edge for current direct detection experiments. Only the best limits from the direct detection experiments are shown. They correspond to the DarkSide-50, PandaX-4T, LUX and CRESST-III experiments. The ATLAS result is complementary with results from direct searches, while direct searches are sensitive to higher mass values ($\mathcal{O}(100)$ GeV) of the DM particle, the ATLAS search is sensitive to lower values ($m_{\text{WIMP}} < m_H/2$).

A second possible interpretation is to search for invisible decays of a Higgs-like scalar boson with a mass different from the SM Higgs boson. This interpretation assumes that the scalar boson couples to the weak vector bosons, and it can be produced via VBF. All kinematic cuts, SR and CR categories, and background estimates are set as in the nominal analysis. A set of alternative signal samples are generated for a mass range between 50 GeV and 2 TeV. The production cross section of the scalar boson is unknown, thus an upper limit on the product of production cross section time branching ratio of invisible decays ($\sigma^{\text{VBF}} \cdot \mathcal{B}_{\text{inv}}$) is computed as a function of the scalar boson mass at 95% CL. These limits are presented in Figure 8.6. The limit is 1.0 pb for a mediator mass of 50 GeV and improves to a value of 0.1 pb for a mass of 2 TeV. The sensitivity improves as a function of mass due to a larger signal over background ratio at high m_{jj} values compared to the nominal analysis.

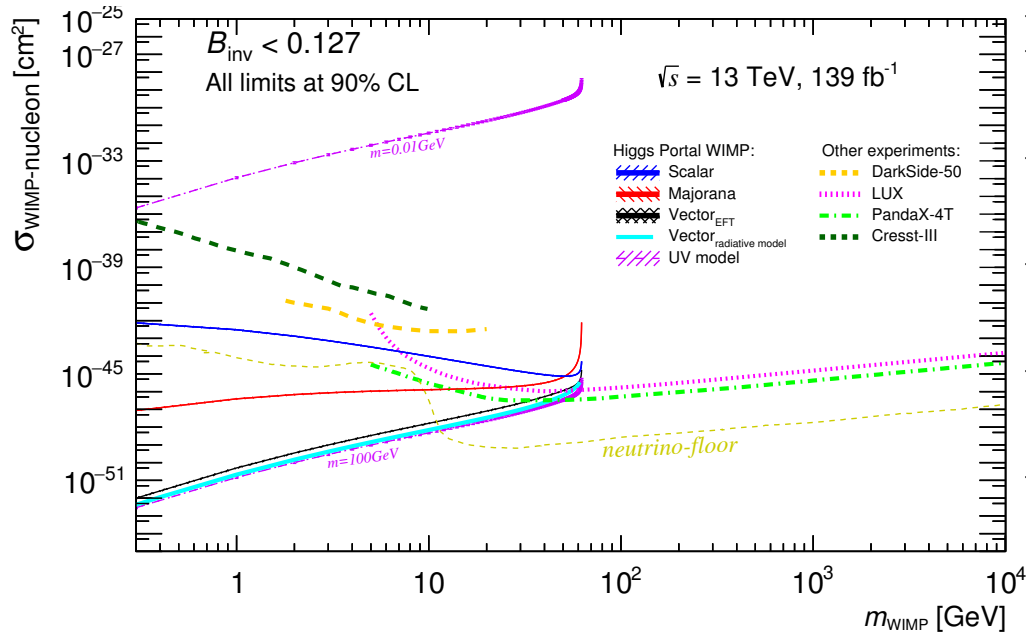


Figure 8.5: The 90% CL exclusion limits are shown for a fermionic and bosonic dark matter candidates. These results are overlaid with the strongest direct detection exclusions. The neutrino floor corresponds to a limit at which the background from solar neutrinos is irreducible defining a sensitivity edge for current direct detection experiments.

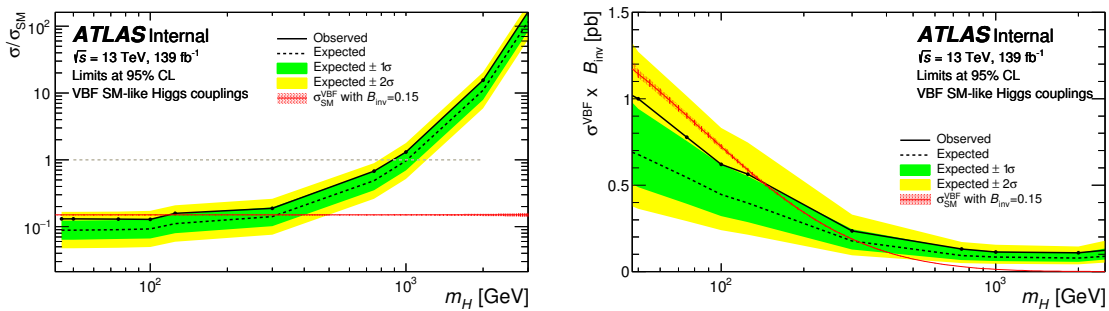


Figure 8.6: The 95% CL exclusion limits are also checked for VBF produced Higgs-like boson with masses from 50 to 2000 GeV.

8.6 Sensitivity projections for the HL-LHC

The sensitivity of the search for invisible Higgs boson decays can be projected to the HL-LHC conditions. The 139 fb^{-1} background and signal predictions are scaled as a function of integrated luminosity, except for the multijet background which requires a special treatment. The multijet background can be separated in two contributions, one contribution where one of the two leading jets belong to a pileup interaction, called “HS+PU” topology, and one for which the two leading jets originate from the same scattering process, this is called “HS-only” topology. The dependence of these components as a function of the mean number of interactions μ differs between them and need to be understood. In a set of dedicated dijet simulated samples produced with PYTHIA for different μ values, the HS+PU component was found to increase linearly with μ , while no dependence was found for the HS-only topology. A factor of 3.25 was derived to correct for the total multijet background at the HL-LHC conditions with μ values of 200.

Upper limits on \mathcal{B}_{inv} are computed as a function of integrated luminosity in order to estimate the sensitivity of the analysis at the HL-LHC. This approach has the advantage that no new simulation of background and signal estimates are needed. However, no effects of the detector upgrade are considered in this extrapolation. Different cases were studied for the upper limit considering different sources of systematic uncertainties:

- Data stats only.
- Data stats + V + jets theory systematic uncertainties.
- Data stats + V + jets + multijet + luminosity systematic uncertainties.
- Data stats + V + jets + multijet + luminosity + reconstruction systematic uncertainties.
- Data stats + V + jets + multijet + luminosity + reconstruction systematic uncertainties in a shape fit.

The dependence of the upper limit on \mathcal{B}_{inv} as a function of integrated luminosity for the three first cases is shown in Figure 8.7. At 3 ab^{-1} , the data stats only limit is around 1%, adding the V + jets theory systematic uncertainties the limit raises up to 2%, and if we include the multijet systematic uncertainties the limit is around 2.7%. For the last two cases under study, the dependence as a function of luminosity is not fully studied yet but the expected limits for 3 ab^{-1} are available. For a fit including data statistics, V + jets theory uncertainties, multijet uncertainties, luminosity uncertainty and reconstruction uncertainties, the upper limit on \mathcal{B}_{inv} is 3.1%. In an optimistic scenario where the fit benefits from information of the shape of the m_{jj} distribution, the upper limit is 2.1%.

There is an alternative approach to obtain independent signal and background estimates from the smearing of the MC at truth scale. However, the studies on this technique are not yet finished. It is worth mentioning that the final sensitivity projections will come from this method since it includes the effects of the upgrade of the experiment.

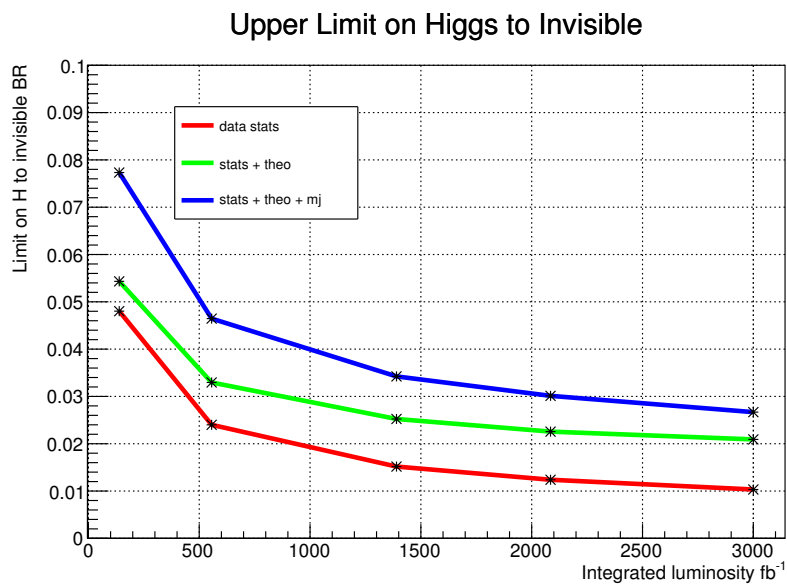


Figure 8.7: Upper limit on \mathcal{B}_{inv} as a function of integrated luminosity.

Conclusions

A search for invisible Higgs boson boson boson boson decays is presented using 139 fb^{-1} of pp collision data with a center-of-mass energy of $\sqrt{s} = 13 \text{ TeV}$ collected from 2015 until 2018 by the ATLAS detector at the LHC. The VBF signature is exploited by requiring two energetic jets with a wide separation in η and which are not back-to-back in the azimuthal plane. In addition, large values of m_{jj} and E_T^{miss} are required. The dominant V+jets backgrounds are estimated using MC reweighted at next-to-leading order and a common control region for W+jets and Z+jets events. Two techniques were developed for the prediction of the QCD multijet background and MC estimates are used for other minor backgrounds ($t\bar{t}$, VV, VVV).

No excess over the Standard Model prediction was found. The post-fit distributions agree within uncertainties with the background only model. Assuming the Standard Model cross section for the Higgs boson an observed upper limit on the branching ratio of invisible Higgs boson decays of 14.5% was set at 95% CL while 10.3% was expected. This is the best limit reported so far and corresponds to an improvement of almost a factor of 3 with respect to the previous ATLAS publication of an observed (expected) limit of 0.37 (0.28). A compatible result for this search has been recently reported by the CMS collaboration with an observed (expect) upper limit of 18% (10%). The improved sensitivity in the analysis comes mainly from increased data and MC statistics, an improved estimate of the multijet background, and the theory corrections on the $V + \text{jets}$ background.

The upper limit is interpreted using Higgs-portal models to exclude regions in the parameter space of $\sigma_{\text{WIMP-nucleon}}$ and m_{WIMP} . Different WIMP scenarios are shown in Figure 8.5, a scalar, Majorana, and a vector EFT and a full UV complete model. For the latter, the introduction of a "Dark Higgs" particle is needed and the WIMP-nucleon interaction cross section depends on the mass of this new particle m_2 . A conservative case ($m_2 = 0.1 \text{ GeV}$), a moderate one ($m_2 = 10 \text{ GeV}$), and an optimistic scenario ($m_2 = 100 \text{ GeV}$) are shown to illustrate how this exclusion limits vary as a function of m_2 . The presented result excludes cross section values ranging from $\mathcal{O}(10^{-42} \text{ cm}^2)$ to $\mathcal{O}(10^{-46} \text{ cm}^2)$.

The result can also be interpreted as a search for invisible decays of a Higgs-like heavy scalar particle acting as a mediator to DM. The limit on the product of Higgs production cross section times branching ratio to invisible particles ($\sigma^{\text{VBF}} \cdot \mathcal{B}_{\text{inv}}$) is computed at 95% CL for a mass range between 50 GeV and 2 TeV. The sensitivity improves as a function of mass due to a larger signal over

background ratio at high m_{jj} values. The limit on $\sigma^{\text{VBF}} \cdot \mathcal{B}_{\text{inv}}$ is 1.0 pb at a mediator mass of 50 GeV and improves to a value of 0.1 pb for a mass of 2 TeV.

With the upcoming of the high luminosity LHC and the PHASE-II upgrades of the ATLAS detector, an improved sensitivity to invisible Higgs boson decays is expected. Two different approaches to estimate this sensitivity were developed: an extrapolation of the Run-2 analysis, and an independent estimate based on the smearing of the MC at truth scale. For the extrapolation of the Run-2 analysis, the background and signal estimates corresponding to the 139 fb^{-1} analysis were scaled as a function of luminosity. The increase in the pile-up conditions also affects the multijet background which is corrected by a factor of 3.25 obtained from studies on dedicated simulated samples. The systematic uncertainties were scaled according to the recommendations provided by the various working groups within the ATLAS collaboration. An upper limit of 3% is expected for an integrated luminosity of 3 ab^{-1} . In an optimistic scenario where information from the shape of the m_{jj} distribution can be used in the likelihood fit, an upper limit of 2% is expected.

The additional pile-up activity at the HL-LHC could also contribute to larger uncertainties on the jet energy scale. To face this complication, different approaches for an upgraded pile-up correction in the ATLAS jet energy calibration chain were studied and presented in Section 4.5. The p_T of the jets is corrected simultaneously as a function of N_{PV} , μ , p_T , and η . The correction is derived by comparing truth and reconstructed information in dijet simulated samples. An improvement on the pile-up uncertainty of the jets of a factor of 2 is expected with this new correction at low p_T values around 20 GeV.

Direct and indirect DM searches are expected to improve their sensitivity in the following years as well. Currently, the best exclusion limits come from the DarkSide-50, PandaX-4T, LUX and Cresst-III experiments. These experiments are complementary to collider searches in the region $m_{\text{WIMP}} > m_{\text{Higgs}}/2$, and they exclude cross sections down to $\mathcal{O}(10^{-46} \text{ cm}^2)$. In the following years, the sensitivity of these experiments is expected to increase by more than a factor of 10 in the m_{WIMP} range down to a few GeV/c^2 . Due to the experimental differences xenon and argon detectors are more sensitive to the lower and higher side of this mass range, respectively. In the sub- GeV/c^2 regime the biggest advances are expected to come from bolometers and possible DM-electron interactions.

Elucidating the nature of dark matter remains one of the most intense research areas in the particle physics and astrophysics community. So far most experimental efforts are concentrated on the mass range between a few GeV/c^2 and in the sub- GeV/c^2 . Big efforts are being made both on the experimental and theoretical side of DM searches in order to increase the sensitivity on these mass ranges. A detection of a DM particle will open a new window in the exploration of the Universe and the outcome of DM searches will have strong implications in the field of particle physics and beyond.

Bibliography

- [1] F. Zwicky, *On the Masses of Nebulae and of Clusters of Nebulae*, *Astrophys. J.* **86** (1937) 217 (cit. on pp. 1, 19).
- [2] S. W. Allen, A. E. Evrard and A. B. Mantz, *Cosmological Parameters from Observations of Galaxy Clusters*, *Annual Review of Astronomy and Astrophysics* **49** (2011) 409, eprint: <https://doi.org/10.1146/annurev-astro-081710-102514>, URL: <https://doi.org/10.1146/annurev-astro-081710-102514> (cit. on p. 1).
- [3] Planck Collaboration et al., *Planck 2015 results - XIII. Cosmological parameters*, *A&A* **594** (2016) A13, URL: <https://doi.org/10.1051/0004-6361/201525830> (cit. on p. 1).
- [4] H. Goldberg, *Constraint on the Photino Mass from Cosmology*, *Phys. Rev. Lett.* **50** (1983) 1419, [Erratum: *Phys. Rev. Lett.* 103,099905(2009); ,219(1983)] (cit. on p. 1).
- [5] J. R. Ellis et al., *Supersymmetric Relics from the Big Bang*, *Nucl. Phys.* **B238** (1984) 453, [,223(1983)] (cit. on p. 1).
- [6] R. E. Shrock and M. Suzuki, *Invisible Decays of Higgs Bosons*, *Phys. Lett.* **110B** (1982) 250 (cit. on pp. 1, 27).
- [7] D. Choudhury and D. P. Roy, *Signatures of an invisibly decaying Higgs particle at LHC*, *Phys. Lett.* **B322** (1994) 368, arXiv: [hep-ph/9312347](https://arxiv.org/abs/hep-ph/9312347) [[hep-ph](https://arxiv.org/abs/hep-ph/9312347)] (cit. on pp. 1, 27).
- [8] N. Arkani-Hamed et al., *Neutrino masses from large extra dimensions*, *Phys. Rev.* **D65** (2001) 024032, arXiv: [hep-ph/9811448](https://arxiv.org/abs/hep-ph/9811448) [[hep-ph](https://arxiv.org/abs/hep-ph/9811448)] (cit. on pp. 1, 27).
- [9] O. J. P. Eboli and D. Zeppenfeld, *Observing an invisible Higgs boson*, *Phys. Lett.* **B495** (2000) 147, arXiv: [hep-ph/0009158](https://arxiv.org/abs/hep-ph/0009158) [[hep-ph](https://arxiv.org/abs/hep-ph/0009158)] (cit. on pp. 1, 27).
- [10] R. M. Godbole et al., *Search for 'invisible' Higgs signals at LHC via associated production with gauge bosons*, *Phys. Lett.* **B571** (2003) 184, arXiv: [hep-ph/0304137](https://arxiv.org/abs/hep-ph/0304137) [[hep-ph](https://arxiv.org/abs/hep-ph/0304137)] (cit. on pp. 1, 27).
- [11] I. Antoniadis, M. Tuckmantel and F. Zwirner, *Phenomenology of a leptonic goldstino and invisible Higgs boson decays*, *Nucl. Phys.* **B707** (2005) 215, arXiv: [hep-ph/0410165](https://arxiv.org/abs/hep-ph/0410165) [[hep-ph](https://arxiv.org/abs/hep-ph/0410165)] (cit. on pp. 1, 27).
- [12] H. Davoudiasl, T. Han and H. E. Logan, *Discovering an invisibly decaying Higgs at hadron colliders*, *Phys. Rev.* **D71** (2005) 115007, arXiv: [hep-ph/0412269](https://arxiv.org/abs/hep-ph/0412269) [[hep-ph](https://arxiv.org/abs/hep-ph/0412269)] (cit. on pp. 1, 27).

- [13] B. Patt and F. Wilczek, *Higgs-field portal into hidden sectors*, (2006), arXiv: [hep-ph/0605188 \[hep-ph\]](#) (cit. on pp. 1, 27).
- [14] S. Kanemura et al., *Can WIMP Dark Matter overcome the Nightmare Scenario?*, *Phys. Rev.* **D82** (2010) 055026, arXiv: [1005.5651 \[hep-ph\]](#) (cit. on pp. 1, 27).
- [15] A. Djouadi et al., *Implications of LHC searches for Higgs–portal dark matter*, *Phys. Lett.* **B709** (2012) 65, arXiv: [1112.3299 \[hep-ph\]](#) (cit. on pp. 1, 27, 28).
- [16] D. Ghosh et al., *Looking for an Invisible Higgs Signal at the LHC*, *Phys. Lett.* **B725** (2013) 344, arXiv: [1211.7015 \[hep-ph\]](#) (cit. on pp. 1, 27).
- [17] G. Belanger et al., *Status of invisible Higgs decays*, *Phys. Lett.* **B723** (2013) 340, arXiv: [1302.5694 \[hep-ph\]](#) (cit. on pp. 1, 27).
- [18] D. Curtin et al., *Exotic decays of the 125 GeV Higgs boson*, *Phys. Rev.* **D90** (2014) 075004, arXiv: [1312.4992 \[hep-ph\]](#) (cit. on pp. 1, 27).
- [19] S. Dittmaier et al., *Handbook of LHC Higgs Cross Sections: 1. Inclusive Observables*, (2011), arXiv: [1101.0593 \[hep-ph\]](#) (cit. on p. 2).
- [20] S. Dittmaier et al., *Handbook of LHC Higgs Cross Sections: 2. Differential Distributions*, (2012), arXiv: [1201.3084 \[hep-ph\]](#) (cit. on pp. 2, 17).
- [21] D. de Florian et al., *Handbook of LHC Higgs Cross Sections: 4. Deciphering the Nature of the Higgs Sector*, (2016), arXiv: [1610.07922 \[hep-ph\]](#) (cit. on pp. 2, 76, 118).
- [22] ATLAS Collaboration, *Search for invisible Higgs boson decays in vector boson fusion at $\sqrt{s} = 13$ TeV with the ATLAS detector*, *Phys. Lett. B* **793** (2019) 499, arXiv: [1809.06682 \[hep-ex\]](#) (cit. on pp. 2, 87, 126).
- [23] CMS Collaboration, *Search for invisible decays of the Higgs boson produced via vector boson fusion in proton-proton collisions at $\sqrt{s} = 13$ TeV*, (2022), arXiv: [2201.11585 \[hep-ex\]](#) (cit. on pp. 2, 73).
- [24] ATLAS Collaboration, *Search for invisible Higgs boson decays with vector boson fusion signatures with the ATLAS detector using an integrated luminosity of 139 fb^{-1}* , ATLAS-CONF-2020-008, 2020, URL: <https://cds.cern.ch/record/2715447> (cit. on pp. 3, 94).
- [25] ATLAS Collaboration, *Search for invisible Higgs-boson decays in events with vector-boson fusion signatures using 139 fb^{-1} of proton-proton data recorded by the ATLAS experiment*, (2022), submitted to JHEP, arXiv: [2202.07953 \[hep-ex\]](#) (cit. on pp. 3, 119).
- [26] S. L. Glashow, *Partial-symmetries of weak interactions*, *Nuclear Physics* **22** (1961) 579, ISSN: 0029-5582, URL: <https://www.sciencedirect.com/science/article/pii/0029558261904692> (cit. on p. 5).
- [27] S. Weinberg, *A Model of Leptons*, *Phys. Rev. Lett.* **19** (21 1967) 1264, URL: <https://link.aps.org/doi/10.1103/PhysRevLett.19.1264> (cit. on pp. 5, 9).
- [28] A. Salam and J. C. Ward, *Weak and electromagnetic interactions*, *Nuovo Cim.* **11** (1959) 568 (cit. on p. 5).

-
- [29] G. 't Hooft and M. Veltman, *Regularization and renormalization of gauge fields*, *Nuclear Physics B* **44** (1972) 189, ISSN: 0550-3213, URL: <https://www.sciencedirect.com/science/article/pii/0550321372902799> (cit. on p. 5).
- [30] G. Arnison et al., *Experimental observation of isolated large transverse energy electrons with associated missing energy at $s=540$ GeV*, *Physics Letters B* **122** (1983) 103, ISSN: 0370-2693, URL: <https://www.sciencedirect.com/science/article/pii/0370269383911772> (cit. on p. 5).
- [31] G. Arnison et al., *Experimental observation of lepton pairs of invariant mass around 95 GeV/c² at the CERN SPS collider*, *Physics Letters B* **126** (1983) 398, ISSN: 0370-2693, URL: <https://www.sciencedirect.com/science/article/pii/0370269383901880> (cit. on p. 5).
- [32] C. Berger et al., *Jet analysis of the $Y(9.46)$ decay into charged hadrons*, *Physics Letters B* **82** (1979) 449, ISSN: 0370-2693, URL: <https://www.sciencedirect.com/science/article/pii/037026937990265X> (cit. on p. 5).
- [33] S. Abachi et al., *Observation of the Top Quark*, *Phys. Rev. Lett.* **74** (14 1995) 2632, URL: <https://link.aps.org/doi/10.1103/PhysRevLett.74.2632> (cit. on p. 5).
- [34] F. Abe et al., *Observation of Top Quark Production in $\bar{p}p$ Collisions with the Collider Detector at Fermilab*, *Phys. Rev. Lett.* **74** (14 1995) 2626, URL: <https://link.aps.org/doi/10.1103/PhysRevLett.74.2626> (cit. on p. 5).
- [35] J. J. Aubert et al., *Experimental Observation of a Heavy Particle J* , *Phys. Rev. Lett.* **33** (23 1974) 1404, URL: <https://link.aps.org/doi/10.1103/PhysRevLett.33.1404> (cit. on p. 5).
- [36] J. -E. Augustin et al., *Discovery of a Narrow Resonance in e^+e^- Annihilation*, *Phys. Rev. Lett.* **33** (23 1974) 1406, URL: <https://link.aps.org/doi/10.1103/PhysRevLett.33.1406> (cit. on p. 5).
- [37] G. Aad et al., *Observation of a new particle in the search for the Standard Model Higgs boson with the ATLAS detector at the LHC*, *Physics Letters B* **716** (2012) 1, ISSN: 0370-2693, URL: <https://www.sciencedirect.com/science/article/pii/S037026931200857X> (cit. on p. 5).
- [38] S. Chatrchyan et al., *Observation of a new boson at a mass of 125 GeV with the CMS experiment at the LHC*, *Physics Letters B* **716** (2012) 30, ISSN: 0370-2693, URL: <https://www.sciencedirect.com/science/article/pii/S0370269312008581> (cit. on p. 5).
- [39] U. of Zurich, *Standard Model*. URL: <https://www.physik.uzh.ch/en/researcharea/lhcb/outreach/StandardModel.html> (visited on 16/06/2021) (cit. on p. 6).
- [40] A. Salam, *Weak and Electromagnetic Interactions*, *Conf. Proc. C* **680519** (1968) 367 (cit. on p. 9).

- [41] S. L. Glashow, *The renormalizability of vector meson interactions*, *Nuclear Physics* **10** (1959) 107, ISSN: 0029-5582, URL: <https://www.sciencedirect.com/science/article/pii/0029558259901968> (cit. on p. 9).
- [42] W. Murray and V. Sharma, *Properties of the Higgs Boson Discovered at the Large Hadron Collider*, *Annual Review of Nuclear and Particle Science* **65** (2015) 515, eprint: <https://doi.org/10.1146/annurev-nucl-102313-025603>, URL: <https://doi.org/10.1146/annurev-nucl-102313-025603> (cit. on pp. 15, 16).
- [43] Y. Fukuda et al., *Evidence for oscillation of atmospheric neutrinos*, *Phys. Rev. Lett.* **81** (1998) 1562, arXiv: [hep-ex/9807003](https://arxiv.org/abs/hep-ex/9807003) (cit. on p. 18).
- [44] Q. R. Ahmad et al., *Measurement of the rate of $\nu_e + d \rightarrow p + p + e^-$ interactions produced by ^8B solar neutrinos at the Sudbury Neutrino Observatory*, *Phys. Rev. Lett.* **87** (2001) 071301, arXiv: [nucl-ex/0106015](https://arxiv.org/abs/nucl-ex/0106015) (cit. on p. 18).
- [45] P. Zyla et al., *Review of Particle Physics*, *PTEP* **2020** (2020) 083C01 (cit. on pp. 18, 21).
- [46] P. A. R. Ade et al., *Planck 2015 results. XIII. Cosmological parameters*, *Astron. Astrophys.* **594** (2016) A13, arXiv: [1502.01589](https://arxiv.org/abs/1502.01589) [[astro-ph.CO](https://arxiv.org/abs/1502.01589)] (cit. on p. 18).
- [47] ESA and the Planck Collaboration, *Best Map Ever of the Universe*, URL: https://www.nasa.gov/mission_pages/planck/multimedia/pia16873.html (visited on 25/08/2021) (cit. on p. 19).
- [48] K. Begeman, *HI rotation curves of spiral galaxies. I. NGC 3198.*, *Astron. Astrophys.* **223** (1989) 47 (cit. on p. 20).
- [49] C. Tao, *Dark Matter searches: an overview*, *Journal of Instrumentation* **15** (2020), URL: <https://doi.org/10.1088/1748-0221/15/06/c06054> (cit. on p. 21).
- [50] J. Billard et al., *Direct Detection of Dark Matter – APPEC Committee Report*, (2021), arXiv: [2104.07634](https://arxiv.org/abs/2104.07634) [[hep-ex](https://arxiv.org/abs/2104.07634)] (cit. on pp. 21–23).
- [51] R. K. Leane, “Indirect Detection of Dark Matter in the Galaxy”, *3rd World Summit on Exploring the Dark Side of the Universe*, 2020, arXiv: [2006.00513](https://arxiv.org/abs/2006.00513) [[hep-ph](https://arxiv.org/abs/2006.00513)] (cit. on p. 21).
- [52] R. Bernabei et al., *First model independent results from DAMA/LIBRA-phase2*, *Nucl. Phys. Atom. Energy* **19** (2018) 307, arXiv: [1805.10486](https://arxiv.org/abs/1805.10486) [[hep-ex](https://arxiv.org/abs/1805.10486)] (cit. on p. 23).
- [53] L. Goodenough and D. Hooper, *Possible Evidence For Dark Matter Annihilation In The Inner Milky Way From The Fermi Gamma Ray Space Telescope*, (2009), arXiv: [0910.2998](https://arxiv.org/abs/0910.2998) [[hep-ph](https://arxiv.org/abs/0910.2998)] (cit. on p. 23).
- [54] A. Cuoco, M. Krämer and M. Korsmeier, *Novel Dark Matter Constraints from Antiprotons in Light of AMS-02*, *Phys. Rev. Lett.* **118** (2017) 191102, arXiv: [1610.03071](https://arxiv.org/abs/1610.03071) [[astro-ph.HE](https://arxiv.org/abs/1610.03071)] (cit. on p. 24).
- [55] M.-Y. Cui et al., *Possible Dark Matter Annihilation Signal in the AMS-02 Antiproton Data*, *Phys. Rev. Lett.* **118** (19 2017) 191101, URL: <https://link.aps.org/doi/10.1103/PhysRevLett.118.191101> (cit. on p. 24).

-
- [56] E. Bulbul et al.,
Detection of an unidentified emission line in the stacked X-ray spectrum of galaxy clusters,
The Astrophysical Journal **789** (2014) 13,
URL: <https://doi.org/10.1088/0004-637x/789/1/13> (cit. on p. 24).
- [57] C. A. Argüelles et al., *Dark Matter Annihilation to Neutrinos*, (2019),
arXiv: [1912.09486](https://arxiv.org/abs/1912.09486) [[hep-ph](#)] (cit. on p. 24).
- [58] O. Buchmueller, C. Doglioni and L. T. Wang, *Search for dark matter at colliders*,
Nature Phys. **13** (2017) 217, arXiv: [1912.12739](https://arxiv.org/abs/1912.12739) [[hep-ex](#)] (cit. on p. 25).
- [59] ATLAS Collaboration, *Search for Dark Matter Produced in Association with a Higgs Boson Decaying to $b\bar{b}$ using 36fb^{-1} of pp collisions at $\sqrt{s} = 13$ TeV with the ATLAS Detector*,
Phys. Rev. Lett. **119** (2017) 181804, arXiv: [1707.01302](https://arxiv.org/abs/1707.01302) [[hep-ex](#)] (cit. on p. 25).
- [60] CMS Collaboration, *Search for dark matter particles produced in association with a Higgs boson in proton-proton collisions at $\sqrt{s} = 13$ TeV*, *JHEP* **03** (2020) 025,
arXiv: [1908.01713](https://arxiv.org/abs/1908.01713) [[hep-ex](#)] (cit. on p. 25).
- [61] V. Kitali, *Search for invisible decays of the Higgs boson produced in vector-boson fusion in final states with jets and large missing transverse energy with the ATLAS detector*, PhD thesis, 2019, URL: <https://ediss.sub.uni-hamburg.de/handle/ediss/6100> (cit. on p. 25).
- [62] ATLAS Collaboration, *Search for dark matter and other new phenomena in events with an energetic jet and large missing transverse momentum using the ATLAS detector*,
JHEP **01** (2018) 126, arXiv: [1711.03301](https://arxiv.org/abs/1711.03301) [[hep-ex](#)] (cit. on pp. 25, 77).
- [63] CMS Collaboration, *Search for new physics in final states with an energetic jet or a hadronically decaying W or Z boson and transverse momentum imbalance at $\sqrt{s} = 13$ TeV*,
Phys. Rev. D **97** (2018) 092005, arXiv: [1712.02345](https://arxiv.org/abs/1712.02345) [[hep-ex](#)] (cit. on p. 25).
- [64] ATLAS Collaboration, *Search for dark matter at $\sqrt{s} = 13$ TeV in final states containing an energetic photon and large missing transverse momentum with the ATLAS detector*,
Eur. Phys. J. C **77** (2017) 393, arXiv: [1704.03848](https://arxiv.org/abs/1704.03848) [[hep-ex](#)] (cit. on p. 25).
- [65] CMS Collaboration, *Search for new physics in the monophoton final state in proton-proton collisions at $\sqrt{s} = 13$ TeV*, *JHEP* **10** (2017) 073, arXiv: [1706.03794](https://arxiv.org/abs/1706.03794) [[hep-ex](#)] (cit. on p. 25).
- [66] ATLAS Collaboration,
Search for an invisibly decaying Higgs boson or dark matter candidates produced in association with a Z boson in pp collisions at $\sqrt{s} = 13$ TeV with the ATLAS detector,
Phys. Lett. B **776** (2018) 318, arXiv: [1708.09624](https://arxiv.org/abs/1708.09624) [[hep-ex](#)] (cit. on p. 25).
- [67] CMS Collaboration, *Search for new physics in events with a leptonically decaying Z boson and a large transverse momentum imbalance in proton-proton collisions at $\sqrt{s} = 13$ TeV*,
Eur. Phys. J. C **78** (2018) 291, arXiv: [1711.00431](https://arxiv.org/abs/1711.00431) [[hep-ex](#)] (cit. on p. 25).
- [68] ATLAS Collaboration,
Search for dark matter in events with a hadronically decaying vector boson and missing transverse momentum in pp collisions at $\sqrt{s} = 13$ TeV with the ATLAS detector,
JHEP **10** (2018) 180, arXiv: [1807.11471](https://arxiv.org/abs/1807.11471) [[hep-ex](#)] (cit. on p. 25).

- [69] X. Lou, *Search for Dark Matter Produced in Association with Heavy Standard Model Particles at $\sqrt{s} = 13$ TeV with the ATLAS Detector at the LHC*, PhD thesis, 2020, URL: <https://cds.cern.ch/record/2725607> (cit. on p. 25).
- [70] ATLAS Collaboration, *Search for dark matter produced in association with bottom or top quarks in $\sqrt{s} = 13$ TeV pp collisions with the ATLAS detector*, *Eur. Phys. J. C* **78** (2018) 18, arXiv: [1710.11412](https://arxiv.org/abs/1710.11412) [[hep-ex](#)] (cit. on p. 25).
- [71] CMS Collaboration, *Search for dark matter produced in association with a single top quark or a top quark pair in proton-proton collisions at $\sqrt{s} = 13$ TeV*, *JHEP* **03** (2019) 141, arXiv: [1901.01553](https://arxiv.org/abs/1901.01553) [[hep-ex](#)] (cit. on p. 25).
- [72] ATLAS Collaboration, *Dark matter summary plots*, URL: <https://atlas.web.cern.ch/Atlas/GROUPS/PHYSICS/PUBNOTES/ATL-PHYS-PUB-2021-045/> (visited on 15/02/2022) (cit. on p. 26).
- [73] M. Zaazoua et al., *Higgs portal vector dark matter interpretation: review of Effective Field Theory approach and ultraviolet complete models*, (2021), arXiv: [2107.01252](https://arxiv.org/abs/2107.01252) [[hep-ph](#)] (cit. on p. 27).
- [74] O. S. Brüning et al., eds., *LHC Design Report. 1. The LHC Main Ring*, CERN-2004-003-V-1, 2004, URL: <https://cdsweb.cern.ch/record/782076> (cit. on p. 31).
- [75] O. Buning et al., eds., *LHC Design Report. 2. The LHC infrastructure and general services*, CERN-2004-003-V-2, 2004, URL: <https://cds.cern.ch/record/815187> (cit. on p. 31).
- [76] M. Benedikt et al., eds., *LHC Design Report. 3. The LHC injector chain*, CERN-2004-003-V-3, 2004, URL: <https://cds.cern.ch/record/823808> (cit. on p. 31).
- [77] *LEP Design Report Vol.1: The LEP Injector Chain*, 1983, URL: <https://cds.cern.ch/record/98881> (cit. on p. 31).
- [78] *LEP Design Report: Vol.2. The LEP Main Ring*, 1984, URL: <https://cds.cern.ch/record/102083> (cit. on p. 31).
- [79] *ALICE: Technical proposal for a Large Ion collider Experiment at the CERN LHC*, LHC technical proposal, CERN, 1995, URL: <https://cds.cern.ch/record/293391> (cit. on p. 31).
- [80] *LHCb : Technical Proposal*, CERN, 1998, URL: <https://cds.cern.ch/record/622031> (cit. on p. 31).
- [81] *CMS, the Compact Muon Solenoid: Technical proposal*, LHC technical proposal, CERN, 1994, URL: <https://cds.cern.ch/record/290969> (cit. on p. 31).
- [82] ATLAS Collaboration, *The ATLAS Experiment at the CERN Large Hadron Collider*, *JINST* **3** (2008) S08003 (cit. on pp. 31, 35, 41, 42).
- [83] E. Mobs, *The CERN accelerator complex - 2019. Complexe des accélérateurs du CERN - 2019*, (2019), General Photo, URL: <https://cds.cern.ch/record/2684277> (cit. on p. 32).
- [84] W. Herr and B. Muratori, *Concept of luminosity*, (2006), URL: <https://cds.cern.ch/record/941318> (cit. on p. 32).

-
- [85] G. Avoni et al., *The new LUCID-2 detector for luminosity measurement and monitoring in ATLAS*, *JINST* **13** (2018) P07017 (cit. on p. 33).
- [86] ATLAS Collaboration, *Luminosity determination in pp collisions at $\sqrt{s} = 13$ TeV using the ATLAS detector at the LHC*, ATLAS-CONF-2019-021, 2019, URL: <https://cds.cern.ch/record/2677054> (cit. on pp. 33, 115).
- [87] ATLAS Collaboration, *Total Integrated Luminosity and Data Quality in 2015-2018*, URL: <https://twiki.cern.ch/twiki/bin/view/AtlasPublic/LuminosityPublicResultsRun2> (visited on 18/06/2021) (cit. on p. 34).
- [88] ATLAS Collaboration, *Number of Interactions per Crossing*, URL: <https://twiki.cern.ch/twiki/bin/view/AtlasPublic/LuminosityPublicResultsRun2> (visited on 18/06/2021) (cit. on p. 34).
- [89] A. Yamamoto et al., *The ATLAS central solenoid*, *Nuclear Instruments and Methods in Physics Research Section A: Accelerators, Spectrometers, Detectors and Associated Equipment* **584** (2008) 53, ISSN: 0168-9002, URL: <https://www.sciencedirect.com/science/article/pii/S0168900207020414> (cit. on p. 36).
- [90] J. Pequeno, “Computer generated image of the ATLAS inner detector”, 2008, URL: <https://cds.cern.ch/record/1095926> (cit. on pp. 36, 37).
- [91] G. Aad et al., *ATLAS pixel detector electronics and sensors*, *JINST* **3** (2008) P07007, URL: <https://cds.cern.ch/record/1119279> (cit. on p. 37).
- [92] ATLAS Collaboration, *ATLAS Insertable B-Layer Technical Design Report*, ATLAS-TDR-19; CERN-LHCC-2010-013, 2010, URL: <https://cds.cern.ch/record/1291633> (cit. on p. 37).
- [93] B. Abbott et al., *Production and integration of the ATLAS Insertable B-Layer*, *JINST* **13** (2018) T05008, arXiv: 1803.00844 [physics.ins-det] (cit. on p. 37).
- [94] ATLAS Collaboration, *Operation and performance of the ATLAS semiconductor tracker*, *JINST* **9** (2014) P08009, arXiv: 1404.7473 [hep-ex] (cit. on p. 38).
- [95] ATLAS Collaboration, *Performance of the ATLAS Transition Radiation Tracker in Run 1 of the LHC: tracker properties*, *JINST* **12** (2017) P05002, arXiv: 1702.06473 [hep-ex] (cit. on p. 38).
- [96] V. A. Mitsou, “The ATLAS transition radiation tracker”, *8th International Conference on Advanced Technology and Particle Physics (ICATPP 2003): Astroparticle, Particle, Space Physics, Detectors and Medical Physics Applications*, 2003, arXiv: hep-ex/0311058 (cit. on p. 38).
- [97] J. Pequeno, “Computer Generated image of the ATLAS calorimeter”, 2008, URL: <https://cds.cern.ch/record/1095927> (cit. on p. 39).
- [98] ATLAS Collaboration, *ATLAS Liquid Argon Calorimeter: Technical Design Report*, ATLAS-TDR-2; CERN-LHCC-96-041, 1996, URL: <https://cds.cern.ch/record/331061> (cit. on p. 39).

- [99] ATLAS Collaboration, *ATLAS Liquid Argon Calorimeter Phase-I Upgrade: Technical Design Report*, ATLAS-TDR-022; CERN-LHCC-2013-017, 2013, URL: <https://cds.cern.ch/record/1602230> (cit. on p. 39).
- [100] ATLAS Collaboration, *ATLAS Tile Calorimeter: Technical Design Report*, ATLAS-TDR-3; CERN-LHCC-96-042, 1996, URL: <https://cds.cern.ch/record/331062> (cit. on p. 40).
- [101] ATLAS Collaboration, *ATLAS Tile Calorimeter Phase-II Upgrade: Technical Design Report*, ATLAS-TDR-028; CERN-LHCC-2017-019, 2017, URL: <https://cds.cern.ch/record/2285583> (cit. on p. 40).
- [102] ATLAS Collaboration, *ATLAS Muon Spectrometer: Technical Design Report*, ATLAS-TDR-10; CERN-LHCC-97-022, CERN, 1997, URL: <https://cds.cern.ch/record/331068> (cit. on p. 41).
- [103] ATLAS Collaboration, *ATLAS Muon Spectrometer Phase-II Upgrade: Technical Design Report*, ATLAS-TDR-026; CERN-LHCC-2017-017, 2017, URL: <https://cds.cern.ch/record/2285580> (cit. on p. 41).
- [104] K. Nagai, *Thin gap chambers in ATLAS*, *Nucl. Instrum. Meth. A* **384** (1996) 219, ed. by F. Ferroni and P. Schlein (cit. on p. 41).
- [105] G. Cattani, *The Resistive Plate Chambers of the ATLAS experiment: performance studies*, *Journal of Physics: Conference Series* **280** (2011) 012001, URL: <https://doi.org/10.1088/1742-6596/280/1/012001> (cit. on p. 42).
- [106] M. Livan, *Monitored drift tubes in ATLAS*, tech. rep., CERN, 1996, URL: <https://cds.cern.ch/record/319197> (cit. on p. 42).
- [107] J. Pequeno, “Computer generated image of the ATLAS Muons subsystem”, 2008, URL: <https://cds.cern.ch/record/1095929> (cit. on p. 43).
- [108] ATLAS Collaboration, *Expected performance of the ATLAS detector at the High-Luminosity LHC*, ATL-PHYS-PUB-2019-005, 2019, URL: <https://cds.cern.ch/record/2655304> (cit. on p. 46).
- [109] R. Atkin, *Review of jet reconstruction algorithms*, *Journal of Physics: Conference Series* **645** (2015) 012008, URL: <https://doi.org/10.1088/1742-6596/645/1/012008> (cit. on p. 48).
- [110] M. Cacciari, G. P. Salam and G. Soyez, *The anti-kt jet clustering algorithm*, *Journal of High Energy Physics* **2008** (2008) 063, URL: <https://doi.org/10.1088/1126-6708/2008/04/063> (cit. on pp. 49, 57).
- [111] ATLAS Collaboration, *Topological cell clustering in the ATLAS calorimeters and its performance in LHC Run 1*, *Eur. Phys. J. C* **77** (2017) 490, arXiv: 1603.02934 [hep-ex] (cit. on p. 49).

-
- [112] ATLAS Collaboration, *Jet reconstruction and performance using particle flow with the ATLAS Detector*, *Eur. Phys. J. C* **77** (2017) 466, arXiv: 1703.10485 [hep-ex] (cit. on p. 49).
- [113] W. Lampl et al., *Calorimeter Clustering Algorithms: Description and Performance*, tech. rep., CERN, 2008, URL: <https://cds.cern.ch/record/1099735> (cit. on p. 50).
- [114] ATLAS Collaboration, *Electron reconstruction and identification in the ATLAS experiment using the 2015 and 2016 LHC proton–proton collision data at $\sqrt{s} = 13$ TeV*, *Eur. Phys. J. C* **79** (2019) 639, arXiv: 1902.04655 [hep-ex] (cit. on pp. 51, 115).
- [115] ATLAS Collaboration, *Electron and photon energy calibration with the ATLAS detector using data collected in 2015 at $\sqrt{s} = 13$ TeV*, ATL-PHYS-PUB-2016-015, 2016, URL: <https://cds.cern.ch/record/2203514> (cit. on p. 52).
- [116] ATLAS Collaboration, *Muon reconstruction performance of the ATLAS detector in proton–proton collision data at $\sqrt{s} = 13$ TeV*, *Eur. Phys. J. C* **76** (2016) 292, arXiv: 1603.05598 [hep-ex] (cit. on pp. 53, 62).
- [117] ATLAS Collaboration, *Tagging and suppression of pileup jets with the ATLAS detector*, ATLAS-CONF-2014-018, 2014, URL: <https://cds.cern.ch/record/1700870> (cit. on p. 54).
- [118] B. Andersson et al., *Parton fragmentation and string dynamics*, *Physics Reports* **97** (1983) 31, ISSN: 0370-1573, URL: <https://www.sciencedirect.com/science/article/pii/0370157383900807> (cit. on p. 55).
- [119] X. Artru and G. Mennessier, *String model and multiproduction*, *Nuclear Physics B* **70** (1974) 93, ISSN: 0550-3213, URL: <https://www.sciencedirect.com/science/article/pii/0550321374903605> (cit. on p. 55).
- [120] S. Weinzierl, *Introduction to Monte Carlo methods*, (2000), arXiv: hep-ph/0006269 (cit. on p. 55).
- [121] S. Alioli et al., *Monte Carlo event generators for high energy particle physics event simulation*, (2019), ed. by A. Buckley et al., arXiv: 1902.01674 [hep-ph] (cit. on p. 55).
- [122] S. Höche, “Introduction to parton-shower event generators”, *Theoretical Advanced Study Institute in Elementary Particle Physics: Journeys Through the Precision Frontier: Amplitudes for Colliders*, 2015 235, arXiv: 1411.4085 [hep-ph] (cit. on p. 55).
- [123] P. J. Clark, *The ATLAS detector simulation*, *Nucl. Phys. B Proc. Suppl.* **215** (2011) 85, ed. by P. Govoni et al. (cit. on p. 55).
- [124] S. Agostinelli et al., *Geant4—a simulation toolkit*, *Nuclear Instruments and Methods in Physics Research Section A: Accelerators, Spectrometers, Detectors and Associated Equipment* **506** (2003) 250, ISSN: 0168-9002, URL: <https://www.sciencedirect.com/science/article/pii/S0168900203013688> (cit. on p. 56).

- [125] W. Lukas, *Fast Simulation for ATLAS: Atlfast-II and ISF*, *Journal of Physics: Conference Series* **396** (2012) 022031, URL: <https://doi.org/10.1088/1742-6596/396/2/022031> (cit. on p. 56).
- [126] A. Basalaev and Z. M. and, *The Fast Simulation Chain for ATLAS*, *Journal of Physics: Conference Series* **898** (2017) 042016, URL: <https://doi.org/10.1088/1742-6596/898/4/042016> (cit. on p. 56).
- [127] ATLAS Collaboration, *Jet energy scale and resolution measured in proton–proton collisions at $\sqrt{s} = 13$ TeV with the ATLAS detector*, *Eur. Phys. J. C* **81** (2020) 689. 73 p, arXiv: [2007.02645](https://arxiv.org/abs/2007.02645) [[hep-ex](#)] (cit. on pp. 58, 62, 64).
- [128] ATLAS Collaboration, *Jet energy scale measurements and their systematic uncertainties in proton–proton collisions at $\sqrt{s} = 13$ TeV with the ATLAS detector*, *Phys. Rev.* **D96** (2017) 072002, arXiv: [1703.09665](https://arxiv.org/abs/1703.09665) [[hep-ex](#)] (cit. on p. 58).
- [129] ATLAS Collaboration, *Pile-up subtraction and suppression for jets in ATLAS*, ATLAS-CONF-2013-083, 2013, URL: <https://cds.cern.ch/record/1570994> (cit. on pp. 58, 60).
- [130] ATLAS Collaboration, *Pile-up corrections for jets from proton–proton collisions at $\sqrt{s} = 7$ TeV in ATLAS in 2011*, ATLAS-CONF-2012-064, 2012, URL: <https://cds.cern.ch/record/1459529> (cit. on p. 58).
- [131] S. D. Ellis and D. E. Soper, *Successive combination jet algorithm for hadron collisions*, *Phys. Rev. D* **48** (1993) 3160, arXiv: [hep-ph/9305266](https://arxiv.org/abs/hep-ph/9305266) (cit. on p. 59).
- [132] S. Catani et al., *Longitudinally invariant K_t clustering algorithms for hadron hadron collisions*, *Nucl. Phys. B* **406** (1993) 187 (cit. on p. 59).
- [133] ATLAS Collaboration, *Jet energy measurement with the ATLAS detector in proton–proton collisions at $\sqrt{s} = 7$ TeV*, *Eur. Phys. J. C* **73** (2013) 2304, arXiv: [1112.6426](https://arxiv.org/abs/1112.6426) [[hep-ex](#)] (cit. on p. 61).
- [134] ATLAS Collaboration, *Electron and photon performance measurements with the ATLAS detector using the 2015–2017 LHC proton–proton collision data*, *JINST* **14** (2019) P12006, arXiv: [1908.00005](https://arxiv.org/abs/1908.00005) [[hep-ex](#)] (cit. on p. 62).
- [135] ATLAS Collaboration, *Combination of Searches for Invisible Higgs Boson Decays with the ATLAS Experiment*, *Phys. Rev. Lett.* **122** (2019) 231801, arXiv: [1904.05105](https://arxiv.org/abs/1904.05105) [[hep-ex](#)] (cit. on p. 73).
- [136] CMS Collaboration, *Search for invisible decays of a Higgs boson produced through vector boson fusion in proton–proton collisions at $\sqrt{s} = 13$ TeV*, *Phys. Lett. B* **793** (2019) 520, arXiv: [1809.05937](https://arxiv.org/abs/1809.05937) [[hep-ex](#)] (cit. on p. 73).
- [137] T. Junk, *Confidence level computation for combining searches with small statistics*, *Nucl. Instrum. Meth. A* **434** (1999) 435, arXiv: [hep-ex/9902006](https://arxiv.org/abs/hep-ex/9902006) (cit. on pp. 75, 119).
- [138] A. L. Read, *Presentation of search results: the CLs technique*, *Journal of Physics G: Nuclear and Particle Physics* **28** (2002) 2693, URL: <https://doi.org/10.1088/0954-3899/28/10/313> (cit. on pp. 75, 119).

-
- [139] G. Cowan et al., *Asymptotic formulae for likelihood-based tests of new physics*, *Eur. Phys. J. C* **71** (2011) 1554, arXiv: 1007.1727 [physics.data-an] (cit. on pp. 75, 119), Erratum: *Eur. Phys. J. C* **73** (2013) 2501.
- [140] ATLAS Collaboration, *Performance of the missing transverse momentum triggers for the ATLAS detector during Run-2 data taking*, *JHEP* **08** (2020) 080, arXiv: 2005.09554 [hep-ex] (cit. on p. 75).
- [141] ATLAS Collaboration, *Performance of the ATLAS muon trigger in pp collisions at $\sqrt{s} = 8$ TeV*, *Eur. Phys. J. C* **75** (2015) 120, arXiv: 1408.3179 [hep-ex] (cit. on p. 75).
- [142] ATLAS Collaboration, *Performance of electron and photon triggers in ATLAS during LHC Run 2*, *Eur. Phys. J. C* **80** (2020) 47, arXiv: 1909.00761 [hep-ex] (cit. on pp. 75, 115).
- [143] ATLAS Collaboration, *The performance of the jet trigger for the ATLAS detector during 2011 data taking*, *Eur. Phys. J. C* **76** (2016) 526, arXiv: 1606.07759 [hep-ex] (cit. on p. 75).
- [144] CERN, *SM Higgs production cross sections at 13 TeV*, 2019, URL: <https://twiki.cern.ch/twiki/bin/view/LHCPhysics/CERNYellowReportPageAt13TeV> (visited on 20/09/2021) (cit. on p. 76).
- [145] T. Gleisberg et al., *Event generation with SHERPA 1.1*, *JHEP* **02** (2009) 007, arXiv: 0811.4622 [hep-ph] (cit. on p. 76).
- [146] R. D. Ball et al., *Parton distributions for the LHC Run II*, *JHEP* **04** (2015) 040, arXiv: 1410.8849 [hep-ph] (cit. on p. 76).
- [147] T. Gleisberg and S. Höche, *Comix, a new matrix element generator*, *JHEP* **12** (2008) 039, arXiv: 0808.3674 [hep-ph] (cit. on p. 76).
- [148] F. Cascioli, P. Maierhofer and S. Pozzorini, *Scattering Amplitudes with Open Loops*, *Phys. Rev. Lett.* **108** (2012) 111601, arXiv: 1111.5206 [hep-ph] (cit. on p. 76).
- [149] S. Höche et al., *QCD matrix elements + parton showers: The NLO case*, *JHEP* **04** (2013) 027, arXiv: 1207.5030 [hep-ph] (cit. on p. 76).
- [150] C. Anastasiou et al., *High-precision QCD at hadron colliders: Electroweak gauge boson rapidity distributions at next-to-next-to leading order*, *Phys. Rev. D* **69** (9 2004) 094008, URL: <https://link.aps.org/doi/10.1103/PhysRevD.69.094008> (cit. on p. 76).
- [151] M. Bahr et al., *Herwig++ physics and manual*, *Eur. Phys. J. C* **58** (2008) 639, arXiv: 0803.0883 [hep-ph] (cit. on p. 77).
- [152] K. Arnold et al., *VBFNLO: A Parton level Monte Carlo for processes with electroweak bosons*, *Comput. Phys. Commun.* **180** (2009) 1661, arXiv: 0811.4559 [hep-ph] (cit. on p. 77).
- [153] J. M. Lindert et al., *Precise predictions for V+ jets dark matter backgrounds*, *Eur. Phys. J. C* **77** (2017) 829, arXiv: 1705.04664 [hep-ph] (cit. on p. 77).
- [154] J. M. Lindert, S. A. Pozzorini and M. Schönherr, *NLO predictions for V+multijet backgrounds in searches for invisible Higgs decays*, To appear (2022) (cit. on p. 77).

- [155] J. Baglio et al., *VBFNLO: A Parton Level Monte Carlo for Processes with Electroweak Bosons – Manual for Version 2.7.0*, (2011), arXiv: [1107.4038 \[hep-ph\]](#) (cit. on p. 78).
- [156] W. Buttinger, *Using Event Weights to account for differences in Instantaneous Luminosity and Trigger Prescale in Monte Carlo and Data*, tech. rep. ATL-COM-SOFT-2015-119, CERN, 2015, URL: <https://cds.cern.ch/record/2014726> (cit. on p. 78).
- [157] ATLAS Collaboration, *Observation and measurement of Higgs boson decays to WW^* with the ATLAS detector*, *Phys. Rev. D* **92** (2015) 012006, arXiv: [1412.2641 \[hep-ex\]](#) (cit. on p. 80).
- [158] ATLAS Collaboration, *Identification and rejection of pile-up jets at high pseudorapidity with the ATLAS detector*, *Eur. Phys. J. C* **77** (2017) 580, arXiv: [1705.02211 \[hep-ex\]](#) (cit. on p. 80), Erratum: *Eur. Phys. J. C* **77** (2017) 712.
- [159] *Characterisation and mitigation of beam-induced backgrounds observed in the ATLAS detector during the 2011 proton-proton run*, *Journal of Instrumentation* **8** (2013) P07004, URL: <https://doi.org/10.1088/1748-0221/8/07/p07004> (cit. on p. 81).
- [160] ATLAS Collaboration, *Selection of jets produced in 13 TeV proton–proton collisions with the ATLAS detector*, ATLAS-CONF-2015-029, 2015, URL: <https://cds.cern.ch/record/2037702> (cit. on p. 81).
- [161] ATLAS Collaboration, *E_T^{miss} performance in the ATLAS detector using 2015–2016 LHC pp collisions*, ATLAS-CONF-2018-023, 2018, URL: <https://cds.cern.ch/record/2625233> (cit. on pp. 82, 83).
- [162] A. Linss, *Search for Dark Matter in Invisible Higgs Boson Decays with the ATLAS Detector at the LHC*, PhD thesis, 2021, URL: <https://ediss.sub.uni-hamburg.de/handle/ediss/9464> (cit. on p. 87).
- [163] ATLAS Collaboration, *Performance of the ATLAS muon triggers in Run 2*, *JINST* **15** (2020) P09015, arXiv: [2004.13447 \[hep-ex\]](#) (cit. on p. 115).
- [164] ATLAS Collaboration, *Muon reconstruction and identification efficiency in ATLAS using the full Run 2 pp collision data set at $\sqrt{s} = 13$ TeV*, (2020), arXiv: [2012.00578 \[hep-ex\]](#) (cit. on p. 115).
- [165] ATLAS Collaboration, *Search for dark matter in association with an energetic photon in pp collisions at $\sqrt{s} = 13$ TeV with the ATLAS detector*, (2020), arXiv: [2011.05259 \[hep-ex\]](#) (cit. on p. 116).
- [166] ATLAS Collaboration, *Performance of missing transverse momentum reconstruction with the ATLAS detector using proton–proton collisions at $\sqrt{s} = 13$ TeV*, *Eur. Phys. J. C* **78** (2018) 903, arXiv: [1802.08168 \[hep-ex\]](#) (cit. on p. 116).
- [167] L. Lonnblad and S. Prestel, *Matching Tree-Level Matrix Elements with Interleaved Showers*, *JHEP* **03** (2012) 019, arXiv: [1109.4829 \[hep-ph\]](#) (cit. on p. 116).

-
- [168] J. Bellm et al., *Parton Shower Uncertainties with Herwig 7: Benchmarks at Leading Order*, *Eur. Phys. J. C* **76** (2016) 665, arXiv: [1605.01338 \[hep-ph\]](#) (cit. on p. [117](#)).
- [169] A. Denner et al., *HAWK 2.0: A Monte Carlo program for Higgs production in vector-boson fusion and Higgs strahlung at hadron colliders*, *Comput. Phys. Commun.* **195** (2015) 161, arXiv: [1412.5390 \[hep-ph\]](#) (cit. on p. [118](#)).
- [170] I. W. Stewart and F. J. Tackmann, *Theory Uncertainties for Higgs and Other Searches Using Jet Bins*, *Phys. Rev. D* **85** (2012) 034011, arXiv: [1107.2117 \[hep-ph\]](#) (cit. on p. [118](#)).

List of triggers

A.1 Lepton triggers

The single lepton triggers used in the analysis are listed in Table A.1. The di-lepton triggers used in the analysis are listed in Table A.1.

Table A.1: List of single lepton triggers.

Period	Electron	Muon
All 2015	HLT_e24_lhmedium_L1EM20VH HLT_e60_lhmedium HLT_e120_lhloose	HLT_mu20_loose_L1MU15 HLT_mu50
2016 Runs \leq 304008	HLT_e24_lhtight_nod0_ivarloose HLT_e60_lhmedium_nod0 HLT_e140_lhloose_nod0	HLT_mu50 HLT_mu26_ivarmedium
2016 Runs $>$ 304008	HLT_e26_lhtight_nod0_ivarloose HLT_e60_lhmedium_nod0 HLT_e140_lhloose_nod0	HLT_mu50 HLT_mu26_ivarmedium
2017 Runs	HLT_e26_lhtight_nod0_ivarloose HLT_e60_lhmedium_nod0 HLT_e140_lhloose_nod0 HLT_e300_etcut	HLT_mu26_ivarmedium HLT_mu50 HLT_mu60_0eta105_msonly
2018 Runs	HLT_e26_lhtight_nod0_ivarloose HLT_e26_lhtight_nod0 HLT_e60_lhmedium_nod0 HLT_e140_lhloose_nod0 HLT_e300_etcut	HLT_mu26_ivarmedium HLT_mu50 HLT_mu60_0eta105_msonly

Table A.2: List of di-lepton triggers.

Period	Electron	Muon
2015	HLT_2e12_lhloose_L12EM10VH	HLT_mu18_mu8noL1
2016	HLT_2e17_lhvloose_nod0	HLT_mu22_mu8noL1
2017	HLT_2e24_lhvloose_nod0	HLT_mu22_mu8noL1
2018	HLT_2e17_lhvloose_nod0_L12EM15VHI	HLT_mu22_mu8noL1

A.2 E_T^{miss} triggers

E_T^{miss} triggers used in the analysis are listed in Table A.3.

Table A.3: Triggers used for 2015-2018 data taking. The years and run numbers in which HLT thresholds were changed are noted.

Period	Trigger
All 2015	HLT_xe70_mht
2016, Runs \leq 302872	HLT_xe90_mht_L1XE50
2016, Runs $>$ 302872	HLT_xe110_mht_L1XE50
2015–2016	HLT_noalg_J400
2017 Runs	HLT_xe110_pufit_L1XE55
2018 Runs	HLT_xe110_xe70_L1XE50

ABCD multijet estimate

B.1 ABCD method

Given the difficulties of predicting the QCD multijet background, an ABCD estimate was developed as a cross-check of the Rebalance and Smear method. This method uses two discriminating variables to extrapolate the multijet contribution from QCD enriched regions to the signal region. Two pairs of variables were tested: m_{jj} vs E_T^{miss} , and m_{jj} vs fJVT.

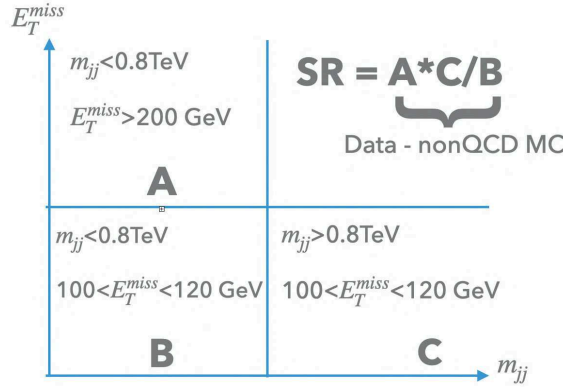
In general, the SR is designed to reject the background through a set of kinematic cuts. Considering a set of two variables: $var1$ and $var2$, the signal region would be defined from respective selections $cut1$ and $cut2$. These cuts split the phase space in 4 regions: A,B,C and D being the SR. All other kinematic cuts are set as in the signal region. The different regions for the m_{jj} vs E_T^{miss} case are illustrated in Figure B.1, and in Figure B.2 for the m_{jj} vs fJVT approach.

The excess data minus non-QCD background can be taken as the multijet contribution in regions A, B and C. To account for possible mismodelling in the V+jets Monte Carlo, scale factors are derived from corresponding W and Z control regions. Considering no correlations between $var1$ and $var2$, the number of multijet events in the SR can be estimated from Eq B.1. Correlations between the two discriminating variables need to be studied independently. A systematic correction together with a corresponding uncertainty can be assigned depending on the case.

$$SR = A \cdot \frac{C}{B} \tag{B.1}$$

B.2 m_{jj} vs E_T^{miss}

As a first test, m_{jj} and E_T^{miss} were chosen as discriminating variables. Low and high m_{jj} regions are defined as $200 \text{ GeV} < m_{jj} < 800$ and $m_{jj} > 800 \text{ GeV}$, respectively. Low and high E_T^{miss} regions are defined as $100 < E_T^{\text{miss}} < 120 \text{ GeV}$ and $E_T^{\text{miss}} > 200 \text{ GeV}$, respectively. The resulting multijet estimates using equation B.1 for years 2017 and 2018 are summarised in Table B.1. For 2015-2016, it is not possible to compute an estimate because of null data minus non-QCD excess in the low m_{jj} high E_T^{miss} region.


 Figure B.1: Sketch of phase space for m_{jj} vs E_T^{miss} ABCD estimate.

To understand the correlation between m_{jj} and E_T^{miss} , the dependence of the ratio of multijet events C/B (high over low m_{jj}) as function of E_T^{miss} was studied in Monte Carlo simulations. A linear fit was applied on this ratio. Using this linear fit, one can extrapolate the value of the ratio C/B from a E_T^{miss} value of 120 GeV (low E_T^{miss}) to 200 GeV (high E_T^{miss}), and the fit error can be used as a systematic uncertainty. The predictions after applying this correction are shown in Table B.1. Because of the low statistics, the fit error was found to be larger than 100%. For this reason, we conclude that the ABCD estimate is in the same order of magnitude as the R+S method ($O(10^2)$), but a reasonable level of precision cannot be achieved in this approach due to statistical limitations.

	SR yield \pm stat unc.	
	2017	2018
No correlation	76.31 ± 32.89	192.80 ± 44.14
Linear correlation	261.74 ± 112.81	661.30 ± 151.40

Table B.1: MultiJet prediction from an ABCD method.

B.3 m_{jj} vs fJVT

Due to the limitations to study the correlation between m_{jj} and E_T^{miss} , a different approach was tested with m_{jj} and fJVT as discriminating variables. Low and high m_{jj} regions are defined as in the previous section. Pass and fail fJVT regions are defined as $\text{fJVT}(j_0) < 0.5 \wedge \text{fJVT}(j_1) < 0.5$ and $\text{fJVT}(j_0) > 0.5 \vee \text{fJVT}(j_1) > 0.5$ respectively. Here $\text{fJVT}(j_0)$ is the fJVT score of the leading jet and $\text{fJVT}(j_1)$ is the fJVT score of the subleading jet.

Leading fJVT distributions for 2017 and 2018 at low m_{jj} are shown in Figure B.3. The excess data minus non-QCD in these cases is negligible (< 10 events), and the statistical uncertainty from the difference can be larger than 100%. For this reason it was not possible to compute a reasonable estimate.

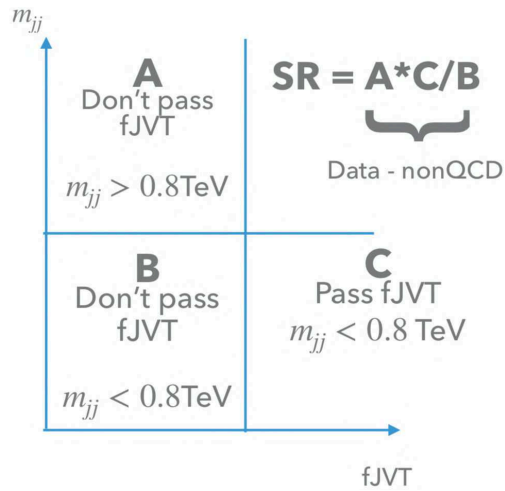


Figure B.2: Sketch of phase space for m_{jj} vs fJVT ABCD estimate.

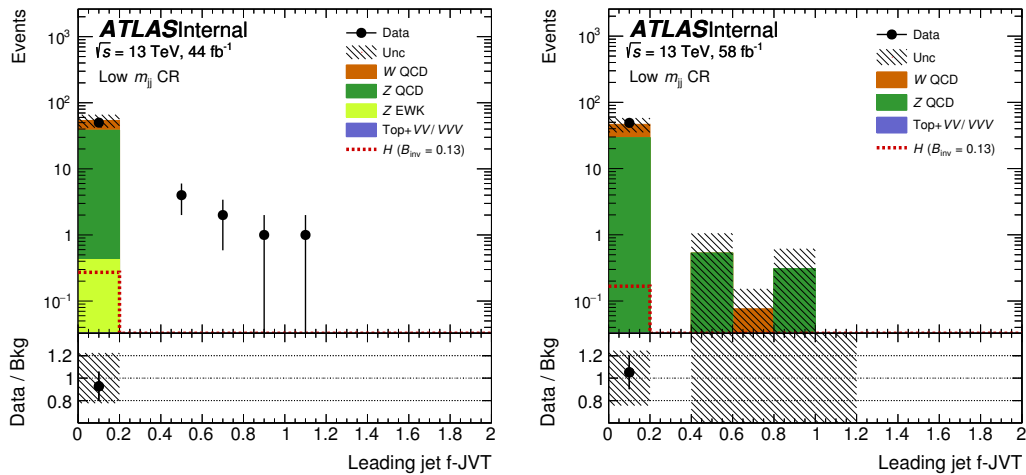


Figure B.3: Leading fJVT distributions at low m_{jj} for 2017 (left) and 2018 (right).

List of Figures

2.1	Elementary particles of the Standard Model [39]	6
2.2	Interaction vertex of quantum electrodynamics.	10
2.3	Example of a QED process. An electron and an anti-electron annihilate to produce a photon which later decays into a electron anti-electron pair.	10
2.4	Example of one loop QED processes.	11
2.5	Tree level Feynman diagram for the interaction between two quarks mediated by a gluon.	15
2.6	Feynman diagrams for the coupling between three gluons (left) and four gluons (right).	15
2.7	Lowest level Feynman diagrams of the Higgs production modes at the LHC [42].	16
2.8	Higgs boson production cross section as a function of the center-of-mass energy in pp collisions for $m_H = 125$ GeV[20].	17
2.9	Summary of the branching fractions for the main Higgs decay modes at the LHC [20].	17
2.10	Map of the cosmic microwave background. It shows tiny temperature fluctuations that correspond to regions of slightly different densities [47].	19
2.11	Rotational velocity v versus distance r from the galactic centre, for the galaxy NGC 3198. Squares (\square) are the velocities determined from HI observations [48] while the dashed line is the prediction from visible matter.	20
2.12	Picture of the bullet cluster taken by the Chandra X-ray observatory. Baryonic matter is illustrated in pink and the DM distribution deduced from gravitational lensing is displayed in blue.	20
2.13	Illustration of DM searches. If one take the direction of time from up to down we have the vertex for direct detection, if the time arrow points to the left we have the indirect detection vertex, and if the time arrow points to the right we have the collider search vertex.	21
2.14	Working principle of common detector types for the direct WIMP search: (a) scintillating crystal, (b) bolometer (here with additional charge-readout), (c) single-phase and (d) dual-phase liquid noble gas detectors, (e) bubble chamber, (f) directional detector [50].	22
2.15	Current status of searches for spin-independent elastic WIMP-nucleus scattering assuming the standard parameters for an isothermal WIMP halo. The neutrino floor (ν – floor) corresponds to a limit at which the background from solar neutrinos is irreducible defining a sensitivity edge for current direct detection experiments [50].	23
2.16	Summary of 90% C.L. limits (shaded) and projected sensitivities (dashed) to the dark matter annihilation cross section, assuming s-wave annihilation [57].	24
2.17	Illustration of the signal generated in $E_T^{\text{miss}} + X$ events. The visible particles recoil against the E_T^{miss} produced by the invisibles particles scaping the detector [58].	25

2.18	DM constrains in a scenario with couplings $g_q = 0.25$, $g_l = 0$, $g_x = 1$ on top and $g_q = 0.1$, $g_l = 0.01$, $g_x = 1$ on the bottom [72].	26
3.1	Illustration of the CERN LHC accelerator complex [83].	32
3.2	Integrated luminosity as a function of time delivered by the LHC (green), recorded by ATLAS (yellow), and Good for physics (blue) [87].	34
3.3	Mean number of interaction per bunch crossing at LHC Run 2 [88].	34
3.4	Illustration of the ATLAS detector [82] with its different subsystems.	35
3.5	Illustration of the ATLAS magnet system composed of the Central Solenoid, the Barrel Toroid and the End-Cap Toroids [89].	36
3.6	Illustration of the ATLAS inner detector and its subcomponents [90].	36
3.7	Illustration of the central region of the ATLAS Inner Detector showing the Pixel Detector (PD), the Semi-Conductor Tracker (SCT), the Transition Radiation Tracker (TRT), and the new Insertable B-Layer (IBL) [90].	37
3.8	Illustration of the ATLAS calorimeter [97].	39
3.9	Illustration of the LAr calorimeter layers in the barrel [82].	41
3.10	Sketch of the structure and readout system of the tile calorimeter [82].	42
3.11	Illustration of the ATLAS muon spectrometer [107].	43
3.12	Schematic representation of the ATLAS trigger and data acquisition system. The level-1 trigger consist of the L1 Calo, the L1 Muon, and the L1 Topo. Events passing the L1 trigger are passed to the software based high-level trigger to be finally saved in the Data Storage.	45
3.13	Plan for the development of the HL-LHC. Run 3 is expected to start in 2022 followed by a long shutdown (LS3) for the installation of the HL-LHC. Physics runs at HL-LHC are expected to start in 2027.	46
3.14	A schematic illustration of the path of an electron through the detector [114]. The red trajectory shows the hypothetical path of an electron, which first traverses the tracking system (pixel detectors, then silicon-strip detectors and lastly the TRT) and then enters the electromagnetic calorimeter. The dashed red trajectory indicates the path of a photon produced by the interaction of the electron with the material in the tracking system	51
3.15	Illustration of the different processes occurring (and simulated) in a pp collision [122]. The hard scatter event is shown as a red blob in the center, the purple blob indicates a secondary hard scatter event, the red and purple tree structures represent the parton shower, the hadronisation processes are represented with green blobs and hadron decays with dark green blobs. Soft photon radiation is illustrated as yellow lines.	55
4.1	ATLAS jet energy calibration chain [127]	58
4.2	Jet transverse momentum dependence on μ (left) and N_{PV} (right) before the pile-up correction, after the area-based correction and after the residual correction [127]	58
4.3	Mean number of primary vertices as a function of μ for Z+jets in data and MC [129].	60
4.4	Illustration of the residual calibration. In a given $(p_T^{\text{truth}}, \eta^{\text{truth}})$ bin, the p_T of the jets corresponding to different N_{PV} , μ bins are shifted to the truth scale as a common reference, and they can be shifted back to a pile-up scale in a second step.	63
4.5	$\partial p_T / \partial \mu$ and $\partial p_T / \partial N_{PV}$ dependence on p_T^{truth} after the pile-up correction [127].	64

4.6	Fractional jet energy scale systematic uncertainty components for R=0.4 jets as a function of η at $p_T = 60$ GeV, reconstructed from particle-flow objects. The total uncertainty, determined as the quadrature sum of all components, is shown as a filled region topped by a solid black line. Flavour-dependant components shown here assume a dijet flavour composition. Taken from [127].	64
4.7	Comparison of the pile-up dependence after the residual correction between the old and the new ρ definition. It can be seen that the two definitions produce compatible results in terms of pile-up dependence.	65
4.8	Dependence of p_T on μ (left) and N_{PV} (right) after the different residual corrections. In the legend, option 1 corresponds to the first term of the correction, option 2 corresponds to the inclusive N_{PV} , μ method, and option 3 is the $\langle\mu\rangle$, $\langle N_{PV}\rangle$ method. The previous method described in Section 4.1 is labeled as 1D.	67
4.9	Examples of p_T^{calib} distribution in the forward region. Option 0 shows a large amount of jets with negative p_T^{calib} . Option 4 has less amount of jet with negative p_T^{calib} . 1D correction does not have jets with negative p_T^{calib}	68
4.10	Distribution of the calorimeter energy deposits in time. It can be observed that applying a timing cut would remove the contributions from out-of-time pile-up.	69
4.11	Pile-up dependence before any pile-up correction in the different time cut variations.	70
4.12	Pile-up dependence after area-based correction in the different time cut variations.	71
4.13	Pile-up dependence after residual pile-up correction in the different time cut variations.	72
5.1	Higgs production via Vector-Boson Fusion.	74
5.2	Example Feynman diagrams for the $Z \rightarrow \nu\nu$ background in the signal region from (left) strong production of order α_{EWK}^2 and (right) electroweak production of order α_{EWK}^4	74
5.3	Orders of α_{EWK} and α_s up to NLO production of $V + \text{jets}$ processes.	77
5.4	Correction applied on strong $V + \text{jets}$ MC (left) and its systematic uncertainties (right). "QCD" refers to the change of the ratio induced by the NLO QCD corrections, "Mix" shows the difference of additive and multiplicative application of the NLO QCD and NLO electroweak corrections, "PS" stands for the uncertainties attributed to the parton shower, and "Sherpa jet veto" denotes the difference between the ratios with and without a jet veto being applied.	79
5.5	Correction applied on electroweak $V + \text{jets}$ MC (left) and its systematic uncertainties (right). "QCD" refers to the change of the ratio induced by the NLO QCD corrections, "Mix" shows the difference of additive and multiplicative application of the NLO QCD and NLO electroweak corrections, "PS" stands for the uncertainties attributed to the parton shower, and the three " $\Delta\phi_{jj} - [1, 2, 3]$ " uncertainties quantify the impact of the $\Delta\phi_{jj}$ dependence on the correction and are evaluated in the ranges of (0-1,1-2,>2).	79
5.6	Illustration of the binning strategy in the signal region. The shading indicates the signal-to-background ratio, assuming a branching fraction of the invisible Higgs boson decays of $\mathcal{B}_{\text{inv}} = 0.15$. In each bin, the relative contribution of the invisibly decaying Higgs boson signal with respect to the total signal yield in the SR is reported as a percentage.	82

6.1	Sketch of MC-based R+S multijet background prediction technique as used in the analysis [162].	87
6.2	Comparison of the SR m_{jj} shapes between the data driven and MC based R+S estimates. The difference between these shapes is taken as a systematic uncertainty on the multijet estimate.	88
6.3	Comparison of the SR m_{jj} shapes between the nominal prediction and the tail-up and core-up systematic variations. The difference between these shapes is taken as a systematic uncertainty on the multijet estimate.	89
6.4	Visualization of the MJ CRs in the $E_T^{\text{miss}}-m_{jj}$ plane.	90
6.5	Distributions of kinematic variables in the mid E_T^{miss} -mid m_{jj} multijet CR ($160 \text{ GeV} < E_T^{\text{miss}} < 200 \text{ GeV} \& 800 \text{ GeV} < m_{jj} < 1500 \text{ GeV}$). Data and background predictions correspond to the full LHC Run 2.	91
6.6	Distributions of kinematic variables in the low m_{jj} multijet CR ($E_T^{\text{miss}} > 150 \text{ GeV}$, $200 \text{ GeV} < m_{jj} < 800 \text{ GeV}$). Data and background predictions correspond to the full LHC Run 2.	92
6.7	Closure plots in the low m_{jj} region with $\text{fJVT} < 0.5$	93
6.8	Closure plots in the mid E_T^{miss} -mid m_{jj} region with $\text{fJVT} < 0.5$	93
6.9	Comparison of the SR m_{jj} shapes when averaged between data taking years and when added over these years.	96
6.10	Data and non-QCD contributions in the low E_T^{miss} control region. Low $\Delta\phi_{jj}$ ($ \Delta\phi_{jj} < 1.0$) on the left and high $\Delta\phi_{jj}$ ($1.0 < \Delta\phi_{jj} < 2.0$) on the right.	97
6.11	Comparison of the m_{jj} shapes in the low E_T^{miss} multijet CR between the R+S estimate and the data - non-QCD contributions. Low $\Delta\phi_{jj}$ ($ \Delta\phi_{jj} < 1.0$) is shown on the left and high $\Delta\phi_{jj}$ ($1.0 < \Delta\phi_{jj} < 2.0$) on the right.	97
6.12	Data and non-QCD contributions in the mid E_T^{miss} , mid m_{jj} control region. Low $\Delta\phi_{jj}$ ($ \Delta\phi_{jj} < 1.0$) on the left and high $\Delta\phi_{jj}$ ($1.0 < \Delta\phi_{jj} < 2.0$) on the right.	98
6.13	Comparison of the m_{jj} shapes in the mid E_T^{miss} - mid m_{jj} multijet CR between the R+S estimate and the data - non-QCD contributions. Low $\Delta\phi_{jj}$ ($ \Delta\phi_{jj} < 1.0$) is shown on the left and high $\Delta\phi_{jj}$ ($1.0 < \Delta\phi_{jj} < 2.0$) on the right.	98
6.14	Test of the m_{jj} shape in $150 \text{ GeV} < E_T^{\text{miss}} < 200 \text{ GeV}$, $m_{jj} < 1.5 \text{ TeV}$, $\Delta\phi_{jj} < 1.0$, $\text{fJVT} < 0.5$. The hashed band indicates the statistical uncertainty.	99
6.15	Schematic of the fJVT control region definition.	99
6.16	The sum of control regions with leading jet FJVT larger than 0.5 is shown for the m_{jj} , $\Delta\phi_{jj}$, N_{jet} , and E_T^{miss} for $E_T^{\text{miss}} > 200 \text{ GeV}$. The multijet contribution is not shown, and it is the dominant contribution.	100
6.17	The sum of control regions with leading jet FJVT larger than 0.2 is shown for the m_{jj} , $\Delta\phi_{jj}$, N_{jet} , and E_T^{miss} for $160 < E_T^{\text{miss}} < 200 \text{ GeV}$. The multijet contribution is not shown, and it is the dominant contribution.	101
6.18	Leading jet fJVT score in the multijet CR for $E_T^{\text{miss}} > 200 \text{ GeV}$ (left) and $160 < E_T^{\text{miss}} < 200 \text{ GeV}$ (right).	102
6.19	The transfer factor f_{MJ}^i dependence on jet p_T and $\Delta\phi_{jj}$ are shown.	102
6.20	The transfer factor f_{MJ}^i dependence on E_T^{miss} and m_{jj} are shown for $ \Delta\phi_{jj} < 1$ (left) and $1 < \Delta\phi_{jj} < 2$ (right).	103

6.21	The transfer factor f_{MJ}^i dependence on different years of data taking are shown for $140 < E_T^{\text{miss}} < 150$ GeV (left) and $150 < E_T^{\text{miss}} < 160$ GeV (right) as a function of m_{jj} .	103
6.22	The transfer factor f_{MJ}^i dependence on $\Delta\phi_{jj}$, leading jet p_T , E_T^{miss} , and m_{jj} for $FJVT < 0.2$.	104
6.23	Comparison of data and predicted backgrounds in the multijet low E_T^{miss} CR.	105
6.24	The distributions of m_{jj} , $\Delta\phi_{jj}$, N_{jet} , and E_T^{miss} are shown with the 139 fb^{-1} dataset from 2015 to 2018 in the summed $Z \rightarrow ee$ control regions. The hashed band indicates statistical and reconstruction systematic uncertainties.	106
6.25	The distributions of leading jet η , sub-leading jet η , $E_T^{\text{jet,no-jvt}}$, and average pile-up per bunch crossing (μ) are shown with the 139 fb^{-1} dataset from 2015 to 2018 in the summed $Z \rightarrow ee$ control regions. The hashed band indicates statistical and reconstruction systematic uncertainties.	107
6.26	The distributions of m_{jj} , $\Delta\phi_{jj}$, N_{jet} , and E_T^{miss} are shown with the 139 fb^{-1} dataset from 2015 to 2018 in the summed $Z \rightarrow \mu\mu$ control regions. The hashed band indicates statistical and reconstruction systematic uncertainties.	108
6.27	The distributions of leading jet η , sub-leading jet η , $E_T^{\text{jet,no-jvt}}$, and average pile-up per bunch crossing (μ) are shown with the 139 fb^{-1} dataset from 2015 to 2018 in the summed $Z \rightarrow \mu\mu$ control regions. The hashed band indicates statistical and reconstruction systematic uncertainties.	109
6.28	The distributions of m_{jj} , $\Delta\phi_{jj}$, N_{jet} , and E_T^{miss} are shown with the 139 fb^{-1} dataset from 2015 to 2018 in the summed $W \rightarrow e\nu$ control regions. The hashed band indicates statistical and reconstruction systematic uncertainties.	111
6.29	The distributions of leading jet η , sub-leading jet η , $E_T^{\text{jet,no-jvt}}$, and average pile-up per bunch crossing (μ) are shown with the 139 fb^{-1} dataset from 2015 to 2018 in the summed $W \rightarrow e\nu$ control regions. The hashed band indicates statistical and reconstruction systematic uncertainties.	112
6.30	The distributions of m_{jj} , $\Delta\phi_{jj}$, N_{jet} , and E_T^{miss} are shown with the 139 fb^{-1} dataset from 2015 to 2018 in the summed $W \rightarrow \mu\nu$ control regions. The hashed band indicates statistical and reconstruction systematic uncertainties.	113
6.31	The distributions of leading jet η , sub-leading jet η , $E_T^{\text{jet,no-jvt}}$, and average pile-up per bunch crossing (μ) are shown with the 139 fb^{-1} dataset from 2015 to 2018 in the summed $W \rightarrow \mu\nu$ control regions. The hashed band indicates statistical and reconstruction systematic uncertainties.	114
8.1	Comparison of data and background estimates in the high $\Delta\phi_{jj}$ VR after the likelihood fit.	122
8.2	The unblinded control regions are shown for each of the 16 bins in a CR-only fit. The normalisations are propagated to the SR from the CR-only fit. The post-fit errors are statistical plus theory systematic uncertainties, and the normalisations are post fit.	124
8.3	The unblinded signal regions and the main unblinded control regions are shown for each of the 16 bins in a background only fit. The post-fit errors are statistical plus theory systematic uncertainties, and the normalisations are post fit.	125
8.4	Post-fit distribution of m_{jj} (left) and $\Delta\phi_{jj}$ (right) in the inclusive SR.	125

List of Figures

8.5	The 90% CL exclusion limits are shown for a fermionic and bosonic dark matter candidates. These results are overlaid with the strongest direct detection exclusions. The neutrino floor corresponds to a limit at which the background from solar neutrinos is irreducible defining a sensitivity edge for current direct detection experiments.	129
8.6	The 95% CL exclusion limits are also checked for VBF produced Higgs-like boson with masses from 50 to 2000 GeV.	129
8.7	Upper limit on \mathcal{B}_{inv} as a function of integrated luminosity.	131
B.1	Sketch of phase space for m_{jj} vs E_T^{miss} ABCD estimate.	152
B.2	Sketch of phase space for m_{jj} vs fJVT ABCD estimate.	153
B.3	Leading fJVT distributions at low m_{jj} for 2017 (left) and 2018 (right).	153

List of Tables

2.1	List of bosons in the Standard Model and their fundamental properties.	7
5.1	Inclusive cross section for the production of the Higgs boson. Taken from the LHC Higgs Yellow Report [144].	76
5.2	Lepton selections	84
6.1	The usage of MJ estimates by SR bins. A - indicates that the method is not used.	86
6.2	Control regions used for the multijet background estimation. Only changes relative to the SR selection are given. The third column shows if a the control region is binned in $\Delta\phi_{jj}$ and m_{jj} like the signal region. Except for the MJ CR, which uses single-jet-triggered data, all control regions use E_T^{miss} -triggered data.	86
6.3	Multijet normalisation for each year for the two CR in low m_{jj} and mid E_T^{miss} -mid m_{jj}	90
6.4	Comparison of multijet normalisation with fJVT<0.2 and fJVT<0.5	90
6.5	Predicted multijet (MJ) background in the signal region. The inclusive predictions and their relative contribution to the total background are reported separately for different data taking periods. The quoted errors on the fraction of the total background are statistical only. Average <core-up>, <tail-up>, and <Data vs MC> uncertainties are reported in this table, but they are evaluated per bin in the statistical treatment.	94
6.6	Bin by bin prediction of multijet (MJ) background, statistical, and relative systematic uncertainties for the full LHC Run 2.	95
6.7	The transfer factors f_{MJ}^i along with their statistical and systematic uncertainties. The discrepancy in SR1 between the FJVT and the R+S is handled by taking the average of the two predictions (labelled “comb.”) with an uncertainty that covers the difference.	104
8.1	Observed and expected background event yields with associated uncertainties in the signal region (SR) and control regions ($Z_{\ell\ell}$ CR, $W_{e\nu}$ CR, $W_{\mu\nu}$ CR, fake- e CR, fake- μ CR, pile-up CR) prior to the likelihood fit. Minor backgrounds from $t\bar{t}$, VV , VVV , and $\text{VBF } H \rightarrow W^*W / \tau^+\tau^-$ are combined and labelled ‘other’. The uncertainties in the backgrounds include the statistical, experimental, and theoretical uncertainties, taking into account the correlations between the individual SR and CR bins. The predicted signal yields (VBF, ggF, and VH) for $\mathcal{B}_{\text{inv}} = 15\%$ (the observed limit) are presented for comparison. For all CRs with leptons, the contribution from the predicted signal is negligible.	120
8.2	The best fit values for β_i normalisation factors for W and Z using a VR only fit.	122
8.3	The best fit values for β_i -normalisation factors for W and Z , in the SR bins using a CR only fit.	123

8.4	Expected and observed limits from full statistics plus systematic uncertainties fit with an control regions and signal regions unblinded, calculated at the 95% CL with 139 fb^{-1} .	124
8.5	The best fit values for β_i -normalisation factors for $V + \text{jets}$ using a fit to the unblinded control regions and signal regions	126
8.6	The contributions to the 68% confidence interval of the fitted signal strength μ from different sources of systematic uncertainty. Due to residual correlations between categories, the sum in quadrature of the individual contributions only approximately equals the total uncertainty. The entry ‘ $V + \text{jets}$ data stats.’ is the statistical uncertainty originating from data yields for the W and Z normalisation. The ‘Remaining’ category contains E_T^{miss} , luminosity, and pile-up uncertainties, and a diboson uncertainty in the $Z_{\ell\ell}$ CR.	127
8.7	Relative impact Δ of the 95% CL expected upper limit on \mathcal{B}_{inv} if a group of uncertainties is ‘removed’, i.e. if the corresponding nuisance parameters are fixed to their best fit values. Fixing all nuisance parameters to their best fit values and subtracting the resulting value in quadrature from the expected limit provides an estimate of the impact of the data statistical uncertainties, which is shown in the last row.	127
8.8	The improvement compared to the previous ATLAS publication to the 95% CL limits from the increased MC sample size, the additional SR binning, the MJ updates, and lastly the W to constrain Z .	128
A.1	List of single lepton triggers.	149
A.2	List of di-lepton triggers.	150
A.3	Triggers used for 2015-2018 data taking. The years and run numbers in which HLT thresholds were changed are noted.	150
B.1	MultiJet prediction from an ABCD method.	152

Eidesstattliche Versicherung

Hiermit versichere ich an Eides statt, die vorliegende Dissertationsschrift selbst verfasst und keine anderen als die angegebenen Hilfsmittel und Quellen benutzt zu haben.

Hamburg, den 11th May 2022
Pablo Andres Rivadeneira Bracho

A handwritten signature in black ink that reads "Pablo Rivadeneira". The signature is written in a cursive style with a large initial 'P'.

Acknowledgements

Special thanks to Krisztian Peters for the supervision and for helping me to get settled in the PhD environment.

Thanks to Elisabetta Gallo for being a supportive co-supervisor.

Many thanks to DESY and the DESY-ATLAS group for the good working environment and the help provided over these years. Also, for providing us with a great infrastructure that empower the scientific work. Thanks to my close colleagues and collaborators Janik, Jonas, Alicia, Arthur, Othmane, Michaela, Christian, and Xuanhong. I admire your scientific spirit and your expertise. Thanks to Ingrid for taking care of the full group.

Thanks to CERN and the ATLAS collaboration. Special thanks to Doug Schaefer, Jennifer Roloff, Matt LeBlanc, and Dilia Portillo.

Finally, thanks to Alba, my beloved partner. Whose love was my support and motivation over these years.